Evaluation for Solidification Cracking Susceptibility of Type 310S Stainless Steel using Laser Trans-Varestraint Test and Prediction of Solidification Microstructure using Multi-Phase Field Modeling

（レーザトランスバレストレイン試験法を用いたステンレス鋼 SUS 310S の凝固割れ感受性の評価とマルチフェーズフィールド法を用いた凝固組織予測）

November, 2016

王　丹

Department of Mechanical Science and Engineering
Graduate School of Engineering
Hiroshima University

Abstract

With the development of science and technology, laser beam welding (LBW), owning high power density, high efficiency, and ability to provide high welding speeds and lower distortions, has been widely used in the various fields. For the welding of austenite stainless steel, such as type 310S, solidification crack occurs as a contribution of solidification behavior and thermal strain which is determined by welding conditions, especially welding speed. At present, there are lots of studies regarding solidification crack, however, the research on the effect of high welding speed on solidification cracking susceptibility quantitatively during the LBW is few. Therefore, the solidification cracking susceptibility need to be under the discussion during LBW at different welding speeds.

High temperature ductility curve composed of the local critical strain and brittle temperature range (BTR) can quantitative evaluate solidification cracking susceptibility. In general, the occurrence of solidification crack is in the BTR where the ductility of material deteriorates in mushy zone. Therefore, it is necessary to study both the local critical strain and BTR in order to evaluate solidification cracking susceptibility comprehensively and precisely.

Until now, Shinozaki group has already developed U type hot cracking test with LBW to measure the local critical strain. However, an effective evaluation method to measure the BTR precisely is few during LBW. Thus, the author et al. develop laser Trans-Varestaint test in order to measure the BTR during LBW. In addition, the local critical strain and BTR are considered to be influenced by the morphology and distribution of the residual liquid metal at the terminal of solidification. Thus, it is necessary to obtain these indexes, like the morphology and distribution of the residual liquid, to understand solidification cracking mechanism. However, through experimental method, it is hard to measure these values due to high cooling rate. Therefore, the multi-phase field method as one of candidates can be employed to simulate the residual liquid distribution for predicting solidification phenomenon. In this thesis, the purpose is to develop a systematic method to evaluate solidification cracking susceptibility quantitatively and

predict the real solidification phenomenon in order to under solidification cracking mechanism during LBW.

First, the Trans-Varestraint test during LBW is developed and evaluation method is investigated for measuring the BTR and further evaluating solidification cracking susceptibility quantitatively. For comparison, the traditional Trans-Varestraint test during gas tungsten arc welding (GTAW) is also carried out at welding speed of 0.2 m/min, same as that using LBW. The number density of solidification crack and total crack length per bead width using LBW are nearly the same as that using GTAW. The result shows the heat source between LBW and GTAW has a little influence on solidification cracking susceptibility. In order to further measure the BTR during LBW, temperature profile is measured by inserting an optical fiber radiation thermometer into the molten pool and the liquidus temperature is obtained under the help of in-situ observation method at welding speed of 0.2 m/min. However, the problem of temperature measurement using a thermometer is presented at high welding speed. Thus, measurement method of 2D temperature distribution by using a multi-sensor camera is introduced and used in order to measure the BTR during LBW. The method to measure the temperature range of the crack is illustrated in detail. Finally, the temperature range of each solidification crack can be measured and the BTR is the maximum temperature range of the crack by using 2D temperature distribution. In addition, the ductility curve tendency is obtained by drawing the curve covering all of the temperature range of the crack.

Next, the influence of welding speed from 0.2 to 2.0 m/min on solidification cracking susceptibility is evaluated for type 310S stainless steel during LBW. The longest solidification crack occurs at the rear center of the molten pool at low welding speed of 0.2 m/min, however, it tends to appear at the side of molten pool at high welding speeds from 1.0 to 2.0 m/min. The number density of solidification crack and total crack length per bead width have a tendency to first increase and then keep stable with increasing welding speed. In order to measure a true BTR, the applicability and accuracy of measurement method of the 2D temperature distribution for measuring the temperature range of the crack are evaluated quantitatively. And the BTR is the average value under saturated augmented strain of 2.8 and 4.3 %. The result shows the BTR is almost the same at around 102 °C during LBW at welding speeds from 0.2 to 2.0 m/min. Finally,

solidification cracking susceptibility could be evaluated comprehensively using the CST' calculated using the minimum local critical strain (ε_{min}) divided by the BTR. The CST' tends to decrease with increasing laser welding speed as a result of the same BTR and a decrease of ε_{min}. The result shows that solidification cracking susceptibility has a tendency of increase during LBW at different welding speeds from 0.2 to 2.0 m/min.

Then, the morphology and distribution of the residual liquid under different cooling rates are simulated using the multi-phase field method to predict real solidification phenomenon and understand solidification cracking mechanism during LBW at different welding speeds. The secondary dendrite arm spacing and primary dendrite tip radius in the calculation result by adjusting the calculation parameters, such as interfacial mobility and anisotropy of interfacial mobility, have agreement with those of liquid Sn quenched microstructure and KGT modeling, respectively. The effect of the parameters, such as interfacial mobility, interfacial energy, anisotropies of interfacial mobility and interfacial stiffness, on the length of the residual liquid region is investigated quantitatively. In order to verify the calculation result, the length of the residual liquid region is compared with that of the fracture surface of the solidification crack. The result shows the calculated length of the residual liquid is nearly the same as that of fracture surface by adjusting calculation parameters, like interfacial mobility and anisotropy of interfacial mobility. Therefore, the residual liquid distribution could be predicted precisely by verifying with experiment and optimizing calculation parameters.

According to the predicted result, the distribution of the similar residual liquid dot at the terminal of solidification under different cooling rates contributes to the same BTR during LBW at different welding speeds. However, the appearance of the relatively long residual liquid film in the region under higher cooling rates leads to a decrease in the minimum local critical strain during LBW at higher welding speeds. Therefore, comprehensively these factors cause an increase in the solidification cracking susceptibility of type 310S stainless steel during LBW at different welding speeds from 0.2 to 2.0 m/min. Moreover, based on this and previous calculation, the result shows the interfacial mobility tends to increase and anisotropy of interfacial mobility tends to decrease with increasing cooling rate. And it is possible to apply the recommended calculation parameters to predict real solidification phenomenon under various cooling rates.

Table of Contents

Chapter 1

Introduction

1.1 Research Background

Stainless steel is one of the important classes of engineering materials due to their high temperature corrosion resistance and high strength, thus they have already been widely used in various industries, such as the electric power generation, the petrochemical industry and so on [1]. In these fields, it is inevitable to utilize welding technology for joining the tubes and completing the large components. As is well known, any defect of the weld joint, especially the crack, maybe induce a serious accident during manufacturing and transportation. Therefore, in order to ensure the industry security and increase the production efficiency, welding technology of stainless steel should be concerned, especially the welding of austenitic stainless steel, such as type 310S stainless steel.

With the development of science and technology, laser was invented, improved and applied for welding field. Compared with the traditional welding technology, laser beam welding (LBW) has incomparable superiority in the respect of the welding quality, precision, efficiency, automation and so on. Therefore, LBW is considered as one of the most promising manufacturing technology in the 21st century. So far, LBW with high power, high efficiency, and owning ability to achieve high welding speeds and lower distortions, have been widely applied in industry [2]. In order to enhance production efficiency and improve the level of automation, welding speed as one of the most important welding parameters should be increased. However, it is considered that the welding conditions, such as welding speed, play an important role in affecting solidification behavior and thermal strain which correspond to solidification cracking susceptibility. Thus, the effect of welding speed (from low to high speed) on solidification cracking susceptibility should be evaluated quantitatively during LBW for austenitic stainless steel in order to prevent from the occurrence of solidification cracking.

Figure 1.1 indicates a schematic illustration of a high temperature ductility curve for evaluating solidification cracking susceptibility quantitatively. The high temperature ductility curve is composed of local critical strain and brittle temperature range (BTR). It is well known solidification crack occurs in the BTR where the ductility of the material deteriorates in mushy zone [3]. During solidification, when tensile strain in the solidifying weld metal is lower than the critical strain, the crack does not occur. However, when higher than the critical strain, solidification crack will appear. Thus, the BTR and local critical strain should be measured in order to evaluate solidification cracking susceptibility comprehensively and quantitatively. At present, Shinozaki group has already developed U type hot cracking test for the measurement of the local critical strain during LBW [4]. However, there is few evaluating method to measure the BTR during LBW.

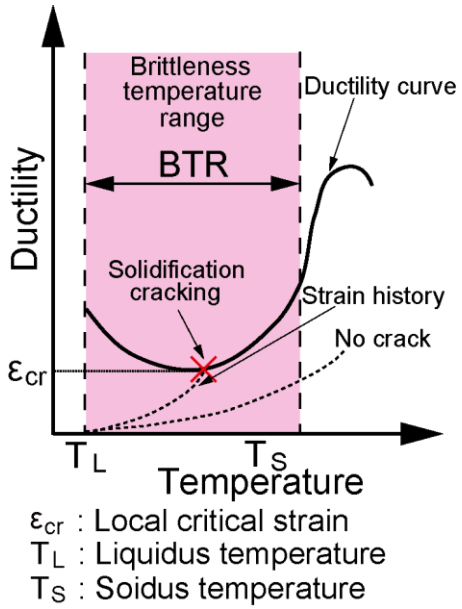

Fig. 1.1 Schematic illustration of a high temperature ductility curve

Previously, Trans-Varestraint test is one of the most effective and common test method to investigate hot cracking susceptibility during welding and has the capacity to measure the BTR through a combination of the maximum crack length and temperature profile [5-7]. However, gas tungsten arc welding (GTAW) with low welding speed is applied as a heat source for the Trans-Varestraint test conventionally. Therefore, it is necessary to apply LBW to the Trans-Varestraint test in order to measure the BTR for evaluating

solidification cracking susceptibility. What's more, it is required to improve the conventional evaluation method in the respect of the measurement of the temperature profile and so on, because cooling rate during LBW is much higher than that of GTAW.

According to the solidification theory, the solidification crack always occurs along the solidification grain boundary in the BTR during solidification, because the solute redistribution can cause a high concentration of the solute and impurity elements along this boundary, resulting in the formation of the low-melting residual liquid film along the boundary and further inducing the solidification cracking [8]. In addition, it is well known the BTR and critical strain are the two most important factors to affect solidification cracking susceptibility. While, the morphology and distribution of the residual liquid mainly influence these factors at the terminal of solidification. For instance, a residual liquid film can lower the critical strain and cause a high solidification cracking susceptibility as a result of the formation of a continuous interface [5]. Thus, it is necessary to obtain these indexes, like the morphology and distribution of the residual liquid, to understand solidification cracking mechanism. However, through experimental method, it is hard to measure these data due to high cooling rate during LBW. While, multi-phase field method (MPFM) which is a mathematical model for solving the interfacial problems can simulate microstructure evolution [9-11] and further predict the morphology and distribution of the residual liquid during solidification. Therefore, the MPFM as one of the reasonable candidates could be employed to simulate the residual liquid distribution for predicting solidification phenomenon. Until now, the MPFM was carried out under the condition of low cooling rate, such as casting [12, 13] and GTAW [14, 15]. In addition, there is little researches on verifying the simulation result with that of experiment quantitatively, resulting in hard to fit suitable calculation parameters to predict real solidification phenomenon. Thus, the residual liquid distribution would be predicted using the MPFM based on verifying with experiment and optimizing calculation parameters under the condition of high cooling rate, like LBW, for understanding solidification cracking mechanism. Moreover, the effect of cooling rate on the calculation parameters would also be investigated in order to reveal the suitable parameters to predict real solidification phenomenon under various cooling rates.

1.2 Objective and Construction of Thesis

The objective of this search is to establish a new test method to evaluate solidification cracking susceptibility quantitatively and systematically, and to predict real solidification phenomenon in order to understand solidification cracking mechanism during LBW. Firstly, the Trans-Varestaint test during LBW is developed. And the effect of the heat source between LBW and GTAW on solidification cracking susceptibility is investigated. Then, the influence of welding speed on solidification cracking susceptibility for type 310S stainless steel is evaluated by using the developed Trans-Varestraint test during LBW. Measurement method of 2D temperature distribution as one of the suitable candidates is used to measure temperature range of each crack. Finally, the BTR could be measured precisely by combining the Trans-Varestraint test during LBW and 2D temperature distribution. In addition, with the help of the MPFM, the residual liquid distribution is predicted and verified with that of experimental result during LBW at different welding speeds. Finally, the predicted morphology and distribution of the residual liquid metal is used to understand solidification cracking mechanism. Figure 1.2 shows the flow chart of the construction of this thesis.

Chapter 1 introduces the scientific background of this research, points out the objective and illustrates the overall construction of the thesis.

Chapter 2 reviews the previous studies on solidification cracking during welding. To beginning with, the widely used testing methods for evaluating solidification cracking susceptibility are summarized for explaining the necessity of developing a new testing method. Next, the relative reports on the influence of welding speed on solidification cracking for stainless steel during LBW are reviewed and discussed, moreover, the shortcomings are proposed in order to illustrate the necessity of further study. Finally, the phase field method is introduced and some relative researches on the simulation of solidification microstructure are summarized and discussed to propose the original research using the MPFM.

Chapter 3 introduces the Trans-Varestraint test during LBW for studying solidification cracking quantitatively and systematically. First is to develop the Trans-Varestraint test during LBW. Next is to compare the solidification cracking susceptibility based on the number and length of the crack between LBW and GTAW at the same welding speed of

0.2 m/min. Then, the problem of the temperature measurement method using an optical fiber radiation thermometer will be described simply, and then the measurement method of 2D temperature distribution using a multi-sensor camera is introduced. Meanwhile, the method for measuring the temperature range of the crack is illustrated in detail. Finally, the BTR is obtained using 2D temperature distribution. Moreover, the ductility curve tendency is tried to be obtained by drawing the curve covering all of the temperature range of the crack.

In chapter 4, the Trans-Varestraint test during LBW and measurement method of 2D temperature distribution are employed to evaluate the influence of welding speed on solidification cracking susceptibility for type 310S stainless steel during LBW. Firstly, the different solidification cracking distributions are discussed and explained by using solidifying microstructure obtained by liquid Sn quenching during LBW at different welding speeds. Then, the variation tendency of the number density of solidification crack and total crack length per bead width are discussed for each welding speed. The problem of the temperature measurement using an optical fiber radiation thermometer is discussed in detail. Next, the applicability and accuracy of the measurement method of 2D temperature distribution are investigated quantitatively to verify the temperature range of the crack and to obtain the true BTR. Finally, the solidification cracking susceptibility for type 310S stainless steel during LBW at different welding speeds is evaluated quantitatively and comprehensively by combining the measured BTR (this work data) with the local critical strain (Kadoi et al. data [16]).

Chapter 5 predicts the residual liquid distribution using the MPFM in order to understand solidification cracking mechanism during LBW at different welding speeds. The influence of the important parameters, such as interfacial mobility, interfacial energy, anisotropies of interfacial mobility and interfacial stiffness, on the residual liquid distribution is investigated quantitatively. Then, the residual liquid distribution is verified with that of experiment. Finally, the predicted morphology and distribution of the residual liquid metal are used to make a comprehensive understanding for solidification cracking mechanism during LBW at different welding speeds. Moreover, the effect of cooling rate on the calculation parameters would be evaluated to give a reference to fit the suitable

calculation parameters to predict real solidification phenomenon under various cooling rates.

Chapter 6 summaries this thesis and proposes the future work.

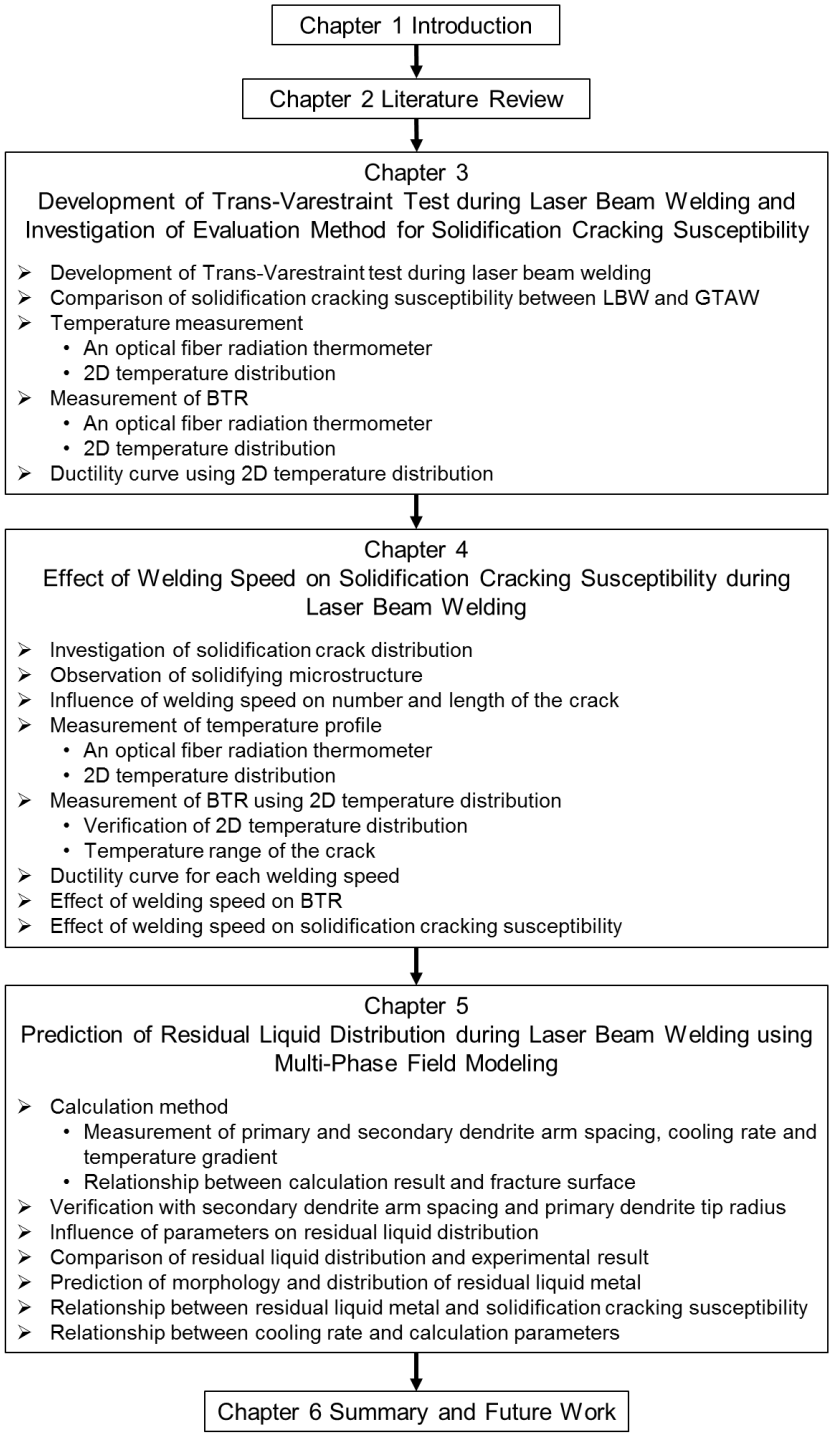

Fig. 1.2 Construction of the thesis

Chapter 2

Literature Review

2.1 Introduction

This chapter reviews the relative researches on the solidification cracking and phenomenon during welding. To beginning with, the cracking test methods for evaluating solidification cracking susceptibility are summarized, and some important and widely used test methods are introduced in detail. Next, the researches on the effect of welding speed on the solidification cracking susceptibility for stainless steel during laser beam welding (LBW) are reviewed. Finally, phase filed method is introduced and some relative studies on the simulation of solidification microstructure during welding are summarized.

2.2 Evaluation Methods for Solidification Cracking Susceptibility

At present, lots of test methods are developed and modified for evaluating solidification cracking susceptibility. Generally speaking, these testing methods can be classified as a self-restraint cracking test and an external-restraint cracking test.

Self-restraint cracking test is used to reproduce the actual welding conditions as closely as possible in practical work. By designing specimen and fixture, the different restraints could be induced. Currently, these test methods mainly includes FISCO hot cracking test [17-20], Houldcroft test [21-24] and circular patch test [25-27]. However, in the case of these tests, it is difficult to distinguish the effects of material factor and mechanical factors. In addition, most of self-restraint cracking tests are no capability of reproducing cracking in some materials with low cracking susceptibility.

While, external-restraint cracking test can implement an external augmented strain or stress to the specimen during welding. The effect of material factor on the solidification cracking can be clearly distinguished from that of the mechanical factor. Therefore, the external-restraint cracking test is considered as the effective and quantitative evaluation method for solidification cracking susceptibility. Until now, there are various external-restraint cracking test for evaluating solidification cracking susceptibility quantitatively,

such as Varestraint test [28-40], Sigmajig test [41, 42], Rapid tensile test [43, 44] and U-type hot cracking test [45, 46], etc.

The Varestraint test is one of the most widely used external-restraint cracking tests, which was developed by Savage and Lundin [47]. The augmented strain can be applied to the specimen by using bending block with different radii of the surface during welding, inducing the occurrence of hot cracking. Additionally, the Varestraint test has three basic types to investigate the hot cracking. First type is the Longitudinal Varestraint test. The external stain is applied along the welding direction. By carrying out one test, not only solidification cracking but also heat affected zone (HAZ) liquation cracking can be evaluated in the specimen. Secondary type is the Trans-Varestraint test. The external strain is applied transverse to the welding direction. During testing, the longest solidification crack always occurs at the rear center of molten pool and the HAZ liquation cracking would not appear. Thus, it can evaluate solidification cracking susceptibility quantitatively. Third type is the Spot Varestraint test which can only evaluate the cracking susceptibility in the HAZ.

Therefore, in order to evaluate solidification cracking susceptibility quantitatively, the Trans-Varestaint test is employed and a schematic illustration is shown in Fig. 2.1 [48]. Traditionally, the heat source is gas tungsten arc welding (GTATW). When the tailing edge of the molten pool moves to the center of the specimen, the augmented strain will apply to the specimen by bending, leading to the occurrence of the solidification cracking. Moreover, the different augmented strain can be obtained by changing the bending block (die block) with different surface radii. After testing, some important indexes, such as the number of crack and total crack length, are used to evaluate solidification cracking susceptibility quantitatively, as shown in Fig. 2.2. With increasing augmented strain, there was a tendency of increasing in the number of crack and total crack length for each material. In addition, both values gave the same ordering as AISI 310 > AISI 316 > AISI 321 > AISI 304. Then, by combining the maximum crack length and temperature profile, the BTR can be determined, which is the most important index to evaluate solidification cracking susceptibility. Meanwhile, the ductility curve tendency could be obtained by multiple tests, as shown in Fig. 2.3. The maximum wide temperature range in the ductility curve is the BTR. By comparison, the variation tendency of the BTR is the same as those

of the number of crack and total crack length. Therefore, the solidification cracking susceptibility tends to decrease from AISI 310 to AISI 304 during GTAW.

Recently, with the development of technology, LBW which possesses a high energy density, a high welding speed and causes the lower distortion has already been widely used in the industry field. Because the solidification behavior and thermal strain depends on the welding condition, the solidification cracking will also occur during LBW. However, at present there are few studies of the Trans-Varestraint test during LBW [49, 50]. Chun et al. applied LBW to the Trans-Varestraint test to evaluate solidification cracking susceptibility of stainless steel [49]. However, the BTR was measured using a thermocouple with a relative low response rate, providing a result that was less accurate. Therefore, the author et al. also developed the Trans-Varestraint test during LBW and applied an optical fiber radiation thermometer with a relative high response rate to measure temperature profile [50]. However, the BTR could not be obtained at high welding speed because the stable temperature profile could not be measured under the high cooling rate. Therefore, a new temperature measurement method needs to be developed to measure stable temperature profile for obtaining the BTR during LBW.

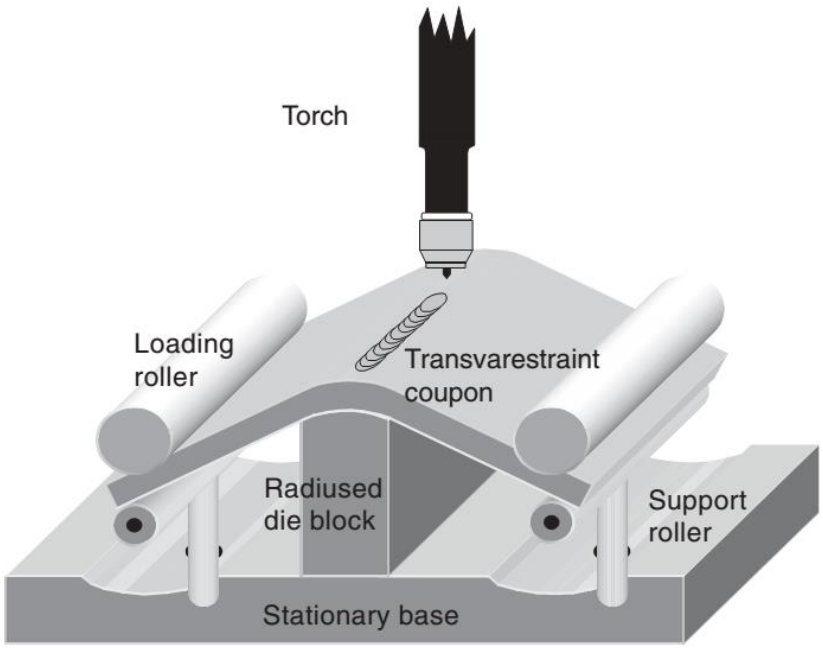

Fig. 2.1 Schematic illustration of Trans-Varestraint test [48]

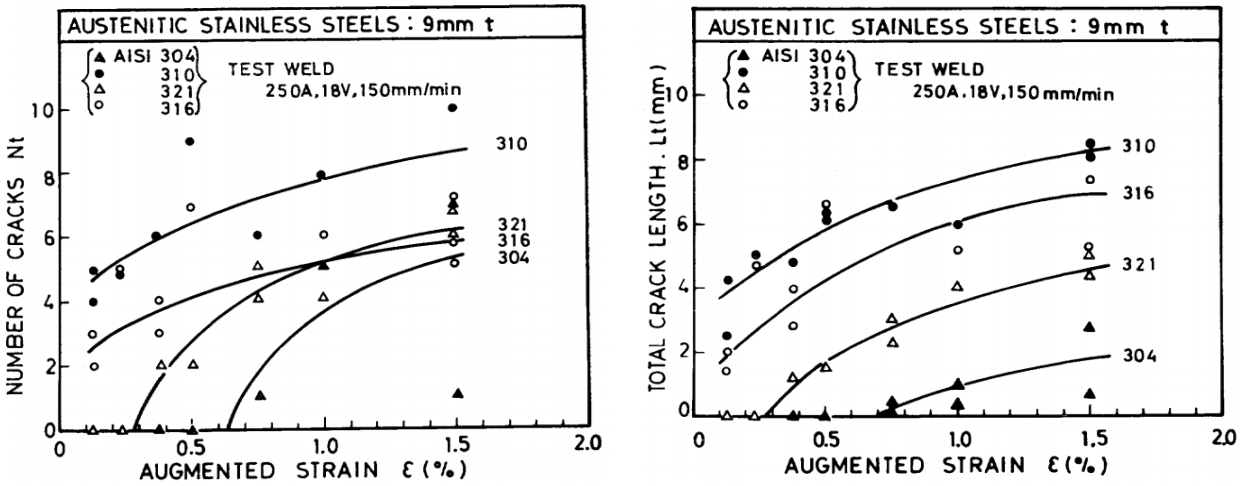

(a) Number of crack (b) Total crack length

Fig. 2.2 Number of crack and total crack length [38]

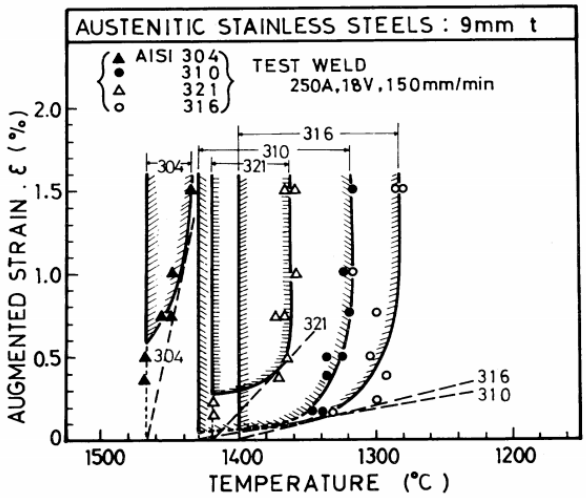

Fig. 2.3 Ductility curve tendency [38]

Moreover, Matsuda et al. developed the means of in-situ observation (MISO) to evaluate solidification cracking susceptibility and a schematic illustration is shown in Fig. 2.4 [43]. With the aid of an optical microscope and a high speed camera, the dynamic movement of reference points at the tail of the molten pool could be recorded during the initiation and propagation of solidification crack. The local strain could be calculated when solidification crack initiates, as shown in Fig. 2.5 a). By combining the temperature profile

at the rear center of the molten pool, the ductility curve could be obtained. Figure 2.5 b) shows the ductility curves of different austenitic stainless steels and Inconel alloy [44]. Compared with the ductility curves of the Trans-Varestraint test in Fig. 2.3, the minimum local strain measured using MISO is much higher. This is because the macro augmented strain in the Trans-Varestraint test ignores the strain concentration at the trailing edge of the molten pool where the local critical strain for the occurrence of the solidification crack always occurs.

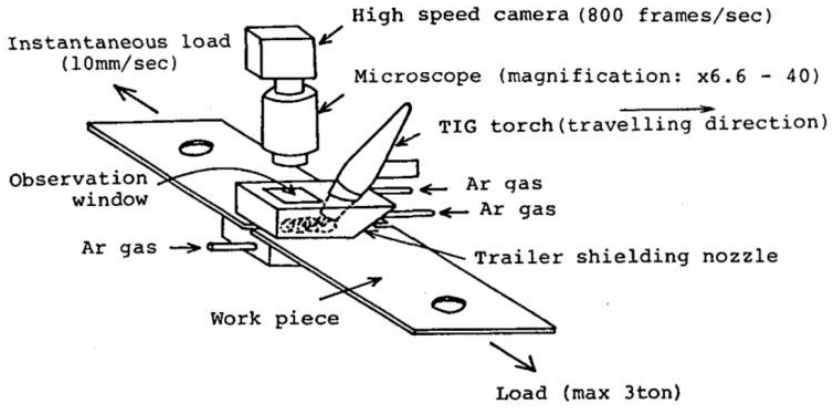

Fig. 2.4 Hot cracking test by means of in-situ observation [43]

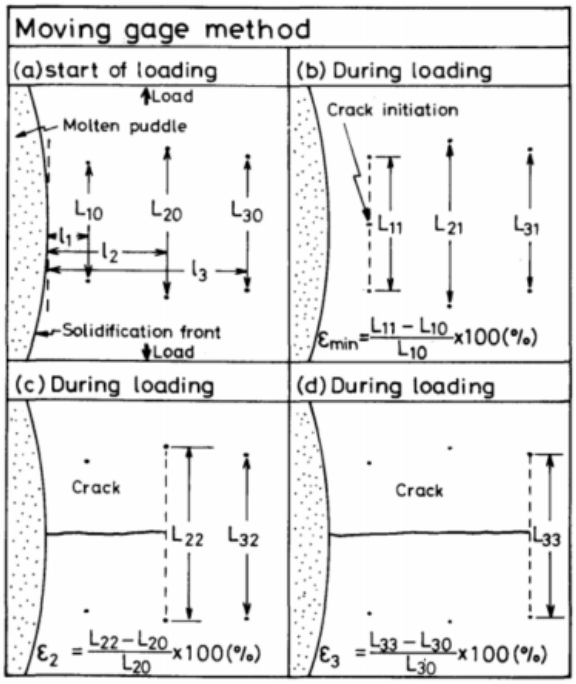

(a) Measurement method of local strain [43]

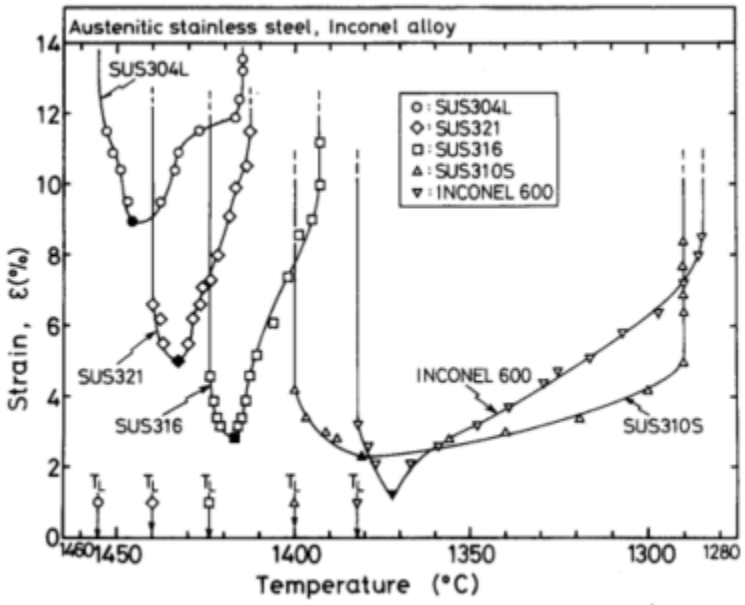

(b) Ductility curves of different materials [44]

Fig. 2.5 Measurement method of local strain and ductility curves [43, 44]

In addition, Shinozaki et al. developed U type hot cracking test with in-situ observation based on the hot cracking test by Matsuda [45]. The schematic illustration and experimental setup are shown in Fig. 2.6. The external load is applied by fixing the specimen on the restraint beams with initial deflection. During LBW, the specimen is stretched by the transverse tensile load, causing the occurrence of solidification cracking at the centerline of weld bead. In addition, a high speed camera is employed to record the dynamic deformation at the trailing edge of the molten pool, a macro lens is used to observe magnified image and a metal halide lamp is applied for supplying strengthened lightening. Figure 2.7 shows the measurement method of local critical strain. At time t_1, two reference points with a distance L_1 across crack initiation point is captured. By rewinding the movie to the time t_0, when these two reference points cross the edge of molten pool, the distance is measured as L_0. By using the equation in Fig. 2.7, the local critical strain could be calculated. Further, by combining the temperature profile along the centerline of molten pool and local critical strain, the high temperature ductility curve could be obtained. Figure 2.8 shows the high temperature ductility curve of type 347 stainless steel during LBW. However, it is difficult to measure the critical stain at the temperature

near liquidus temperature and solidus temperature as a result of the healing of residual liquid metal and the recovery of ductility, respectively. Moreover, the true BTR is hard to be obtained by only using U type hot cracking during LBW.

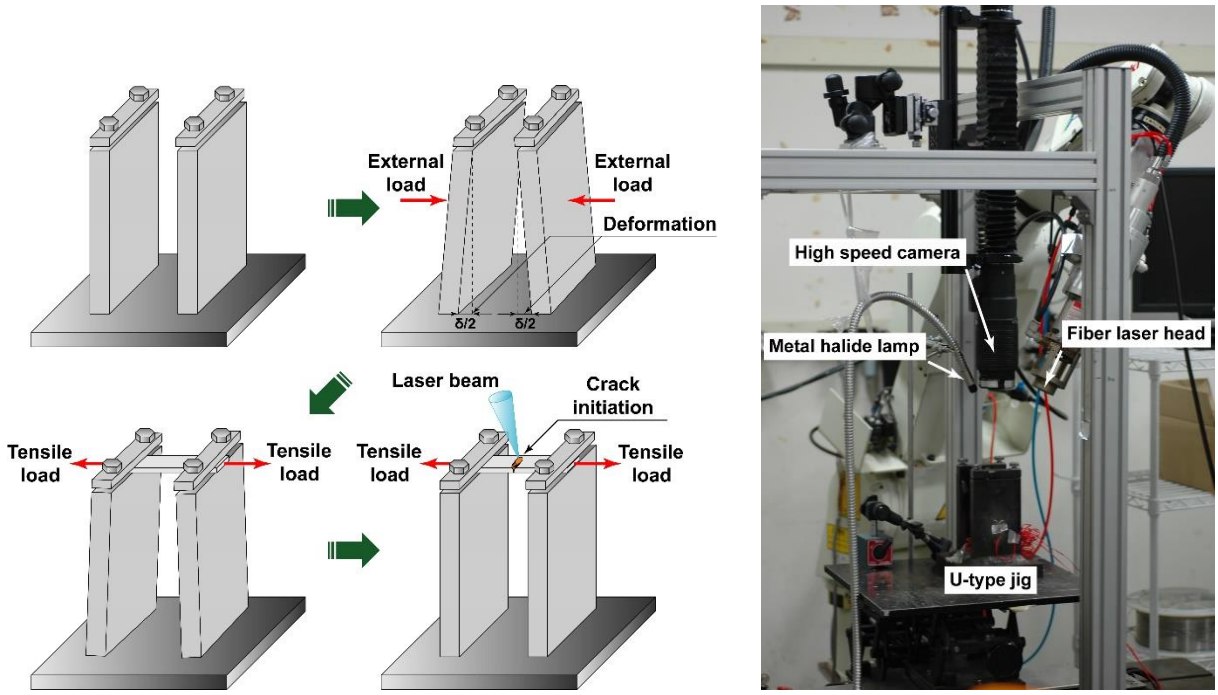

(a) Schematic illustration of U type hot cracking test (b) Experimental setup

Fig. 2.6 U type hot cracking test with in-situ observation [51]

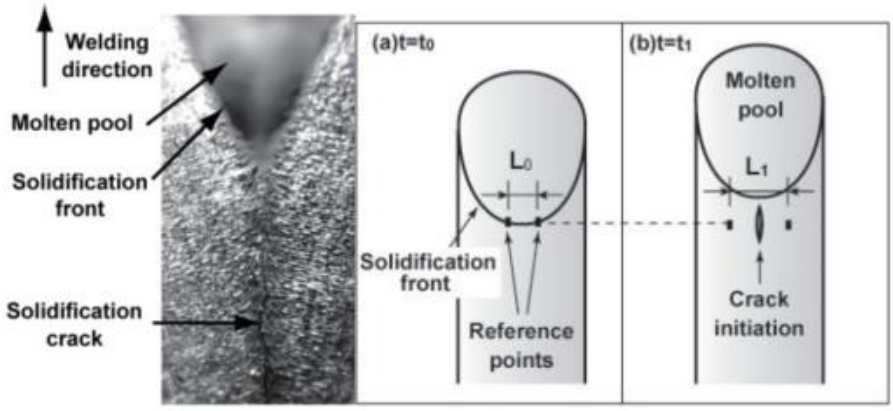

$$\varepsilon_{cr} = \frac{L_1 - L_0}{L_0} \times 100\% \quad \text{Equation 1}$$

Fig. 2.7 Measurement method of critical strain [45]

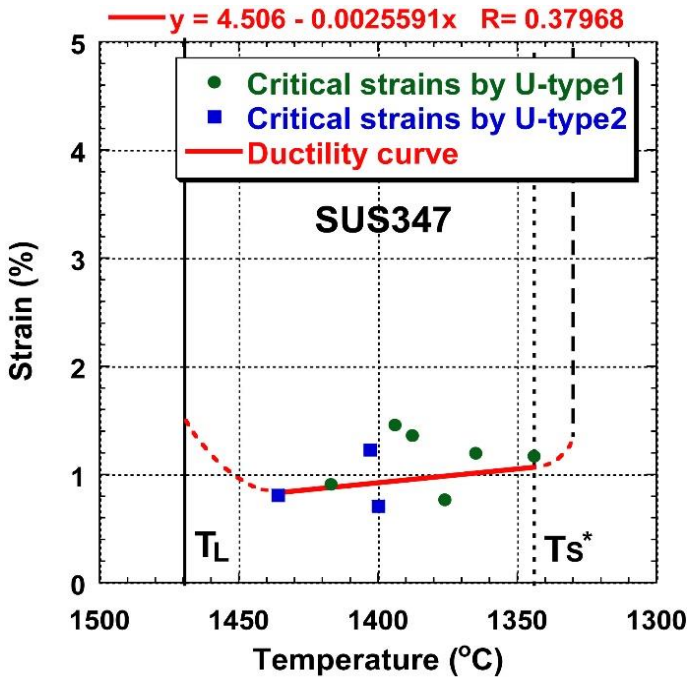

Fig. 2.8 High temperature ductility curve of type 347 stainless steel [51]

2.3 Effect of Welding Speed on Solidification Cracking Susceptibility for Stainless Steel during Laser Beam Welding

Stainless steel has been widely used in various industries because of its high temperature corrosion resistance and high strength. Meanwhile, LBW owning high power, high efficiency and ability to provide high welding speed and lower distortion has also be widely applied in the heavy industries at present. While, welding speed plays an important role in affecting solidification behavior and thermal strain which are corresponding to solidification cracking susceptibility. Therefore, it is necessary to evaluate the effect of welding speed on solidification cracking susceptibility for stainless steel during LBW. High temperature ductility curve composed of the local critical strain and BTR can evaluate the solidification cracking susceptibility comprehensively and quantitatively. Especially, CST which indicates the critical strain rate of temperature drop in the high temperature ductility curve is regarded as the most important and comprehensive index to evaluate solidification cracking susceptibility quantitatively and precisely because it reflects the both effects of the local critical strain and BTR. Therefore, it is essential to obtain both the

value of the local critical strain and BTR for investigating solidification cracking susceptibility of stainless steel precisely during LBW at different welding speeds.

Kadoi et al. evaluated the effect of high welding speed on the solidification cracking susceptibility of type 310S stainless steel during LBW using the local critical strain measured by U type hot cracking test with in-situ observation [16]. Figure 2.9 shows the local critical strain at different welding speeds. At higher welding speeds of 0.8 and 1.6 m/min, the tendencies of the critical stain changing with temperature are nearly the same. Additionally, the minimum local critical strain is a little lower at welding speed of 1.6 m/min. While, at welding speed of 0.4 m/min, the values of the local critical strain are much higher than those at other welding speeds. Thus, from the aspects of the local critical strain, the solidification cracking susceptibility tends to enhance with increasing welding speed during LBW. By applying in-situ observation with a high speed camera, the residual liquid droplet distributes between solidification grain boundaries along the centerline of the molten pool at low welding speed, however, the residual liquid morphology changes into a film in the wide range of solidification at high welding speed, causing high solidification cracking susceptibility. As is mentioned, the advantage of U type hot cracking test during LBW is to measure the local critical strain but it is no capable of measuring the BTR. Therefore, only if obtaining the BTR, the solidification cracking susceptibility just can be evaluated comprehensively and precisely using the CST.

Thus, Chun et al. [49] and the author et al. [50] developed the Trans-Varestraint during LBW to measure the BTR of type 310S stainless steel for evaluating solidification cracking susceptibility, respectively. Chun et al. [49] reported that the solidification crack with the maximum length occurred at the backend center of molten pool, however it had a relatively large angle (60- 70°) with the bead centerline during Trans-Varestraint test with LBW at high welding speed. Thus, in order to obtain the BTR, firstly the maximum crack length is converted to the distance from the end point of crack to the fusion boundary along the welding direction. And then, the temperature profile is measured or estimated based on the actual temperature values obtained by positioning several thermocouples at some measurement points from bead centerline to the weld toe line, as shown in Fig. 2.10 a). Finally, the BTR is obtained by combining the conversion maximum solidification crack length with the corresponding measured or estimated temperature profile, and the

values decreases with increasing welding speed from 0.6 to 2.4 m/min, as shown in Fig. 2.10 b). However, the temperature profile is measured by employing a thermocouple with relative lower response rate. Especially, at high welding speeds, the data points of the temperature profile become rare in the solidifying temperature range resulting in less accurate result. In addition, the measurement size of the thermocouple is relatively large, therefore, it is hard to ensure the designated insertion positions of the thermocouple during LBW, especially at high welding speed due to very narrow weld bead. Thus, the BTR is less accurate by using this method.

Meanwhile, the author et al. [50] also developed the Trans-Varestraint test during LBW and applied an optical fiber radiation thermometer with a relative high response rate to measure temperature profile. However, at high welding speeds the stable temperature profile could not be measured and the longest crack always occurs at the sides of the molten pool during LBW. Therefore, it is difficult to measure the true BTR using conventional temperature measurement method. The measurement method of a 2D temperature distribution needs to be employed and under discussion to measure the true BTR during LBW at different welding speeds.

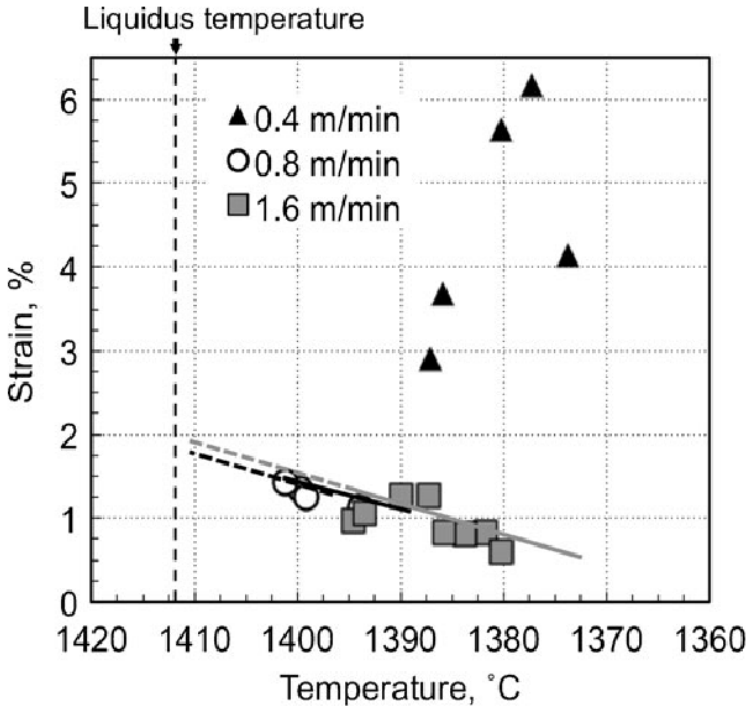

Fig. 2.9 High temperature ductility curves at different welding speeds [16]

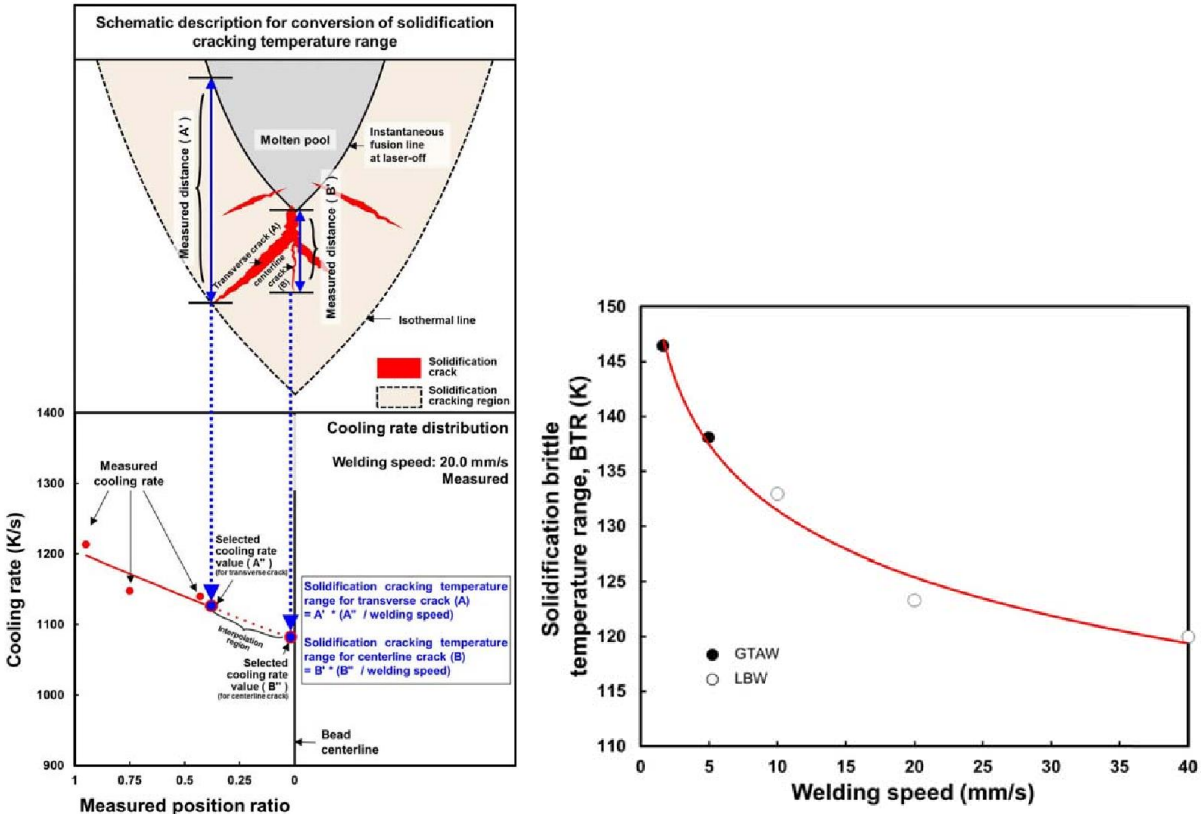

(a) Measurement method of the BTR (b) Effect of welding speed on the BTR

Fig. 2.10 Measurement method of the BTR and effect of welding speed on the BTR [49]

2.4 Simulation of Solidification Microstructure

Solidification cracking susceptibility depends on the morphology and distribution of the residual liquid. While, simulation can predict solidification phenomenon, such as dendrite morphology, micro-segregation, and morphology and distribution of the residual liquid metal. Therefore, the simulation can be regarded as one of the suitable candidates to study and predict the solidification cracking susceptibility. At present, there are several popular methods for the simulation of solidification microstructure, such as Deterministic method [52], Probabilistic method [53-57] and Phase field method [58-71].

Deterministic method is based on the solidification kinetics and physical background of crystal growth [52]. The nucleation and growth are decided by the deterministic function. However, this method does not consider the probabilistic phenomena and ignores the crystallographic morphology during dendrite growth. Therefore, it is hard to simulate

dendrite morphology precisely. In the case of Probabilistic method, the nucleation and growth are described by the probabilistic model. This method can be divided into two types which are Monte Carlo (MC) and Cellular Automaton (CA), respectively [55]. MC method is based on minimization of interfacial energy and probability and statistics theory. However, this method lacks of physical basic, such as nucleation and growth of crystalline [54], resulting in the difficulty to analyze physical phenomena quantitatively [55]. CA method is based on not only probabilistic model but also the physical mechanism in the nucleation and growth. However, due to consider little macro factors, the simulation result may be a little different from that of experiment using CA method.

Phase field method based on Ginsberg-Landau theory [58] and giving expression to the influence of diffusion, ordering potential and thermodynamic driving force in terms of differential equations can simulate microstructure evaluation in time and space, thus it is expected as one of the most useful methods to simulate the development of dendrite growth and predict solidification behavior. The interface is described by a steep, but continuous and transition of the phase filed variable ϕ between two states. Phase variable ϕ is an ordering variable embodying the physical state of liquid, solid or interface. The variation range of ϕ commonly could be set from 0 to 1. $\phi = 0$ represents the liquid phase and $\phi = 1$ represents the solid phase [59]. The diffuse interface is defined as variable from 0 to 1. Phase filed method can simulate solidification microstructure precisely, which is based on the coupling of phase field, solute field, temperature field or thermodynamics database.

Usually, the MPFM was proposed for simulating dendrite growth under low cooling rate, like casting [12, 13] and GTAW [14, 15]. However, at present, there is few studies on verifying simulation result with that of experimental result. Zheng et al. developed a phase field model to simulate the dendrite growth in the molten pool during GTA welding of aluminum alloy 2A14 [14]. The dendrite morphology obtained from the simulation is the nearly the same as that of experiment qualitatively, such as the growth direction of the primary and secondary dendrites, however, it is hard to obtain a complete quantitative agreement with that of experiment, as shown in Fig. 2.11. Additionally, Fukumoto et al. simulated solidification microstructure of type 304 stainless steel during GTAW [15]. During solidification, dendrite morphology is simulated successfully, and some indexes,

such as primary dendrite tip radius and temperature, are in agreement with KGT model. However, the solidifying microstructure obtained from the simulation still does not verify with that of experiment quantitatively. Thus, at present it is hard to fit suitable calculation parameters to predict real solidification phenomenon. It is well known that the calculation parameters, such as interfacial mobility and anisotropies, are important in affecting the dendrite growth and morphology during solidification simulation. Even though there are some studies on the influences of anisotropies and thermal noise on dendrite morphology [70, 71], the simulation results are still not compared with those of experiment.

Thus, to date, there is no accurate calculation parameters in the MPFM to simulate the real solidification microstructure which is in agreement with that of experiment quantitatively. Moreover, the effect of calculation parameters on the residual liquid distribution is not clear using the MPFM. Additionally, it is not established the relationship between calculation parameters and experimental condition, like cooling rate. Therefore, these problems need to be under discussion in this thesis.

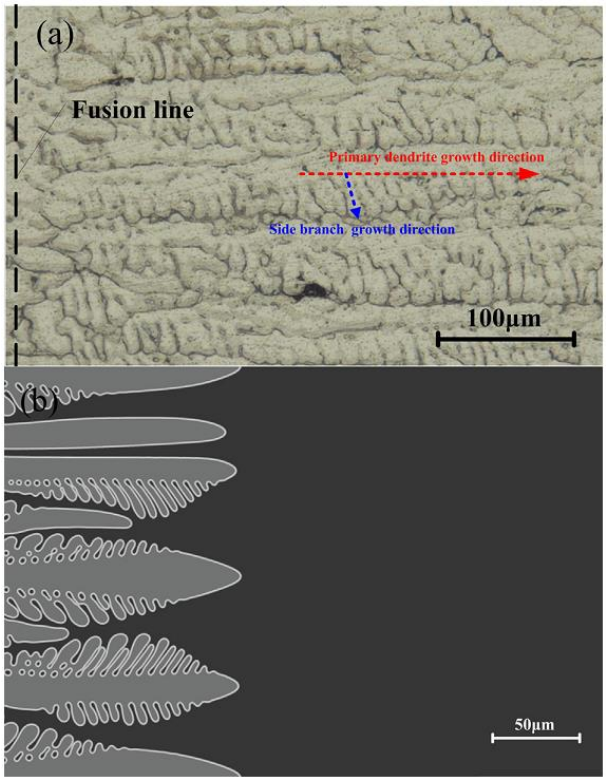

Fig. 2.11 Comparison of dendrite morphology, (a) experimental result and (b) simulation result [14]

Fig. 2.12 Simulation of dendrite growth by multi-phase field method in Fe-18%Cr-8%Ni-0.05%C-0.5%Si-1.0%Mn alloy [15]

Chapter 3

Development of Trans-Varestraint Test during Laser Beam Welding and Investigation of Evaluation Method for Solidification Cracking Susceptibility

3.1 Introduction

With the development of science and technology, laser beam welding (LBW) has already been applied in the practical productions due to its high power, high efficiency and the ability to provide high welding speed and lower distortion. However, LBW tends to produce rapid solidification resulting in the change of temperature gradient and cooling rate, etc., compared with that of gas tungsten arc welding (GTAW). Thus, the solidification behavior and thermal strain that correspond to solidification cracking susceptibility could be influenced using different heat sources. Therefore, the solidification cracking susceptibility should be understood and discussed during LBW.

It is well known that solidification crack occurs in the brittleness temperature range (BTR) where the ductility of the material deteriorates in mushy zone. Thus, the BTR is one of the important factors for quantitative evaluation of the susceptibility. The Trans-Varestraint test is one of the most common test method to evaluate hot cracking susceptibility during welding. The number and length of the crack, and the BTR can be measured as important indexes to evaluate solidification cracking susceptibility quantitatively. Conventionally, GTAW with low welding speed has been applied as a heat source during testing. There is little evaluation method to measure the BTR quantitatively during LBW. Thus, it is necessary to develop the Trans-Varestraint test during LBW and also to improve the conventional evaluation methods, such as the measurement of the temperature profile, because the cooling rate during LBW is much higher than that of GTAW.

Type 310S stainless steel is used for developing the Trans-Varestraint test during LBW. Firstly, the process of the Trans-Varestraint test during LBW at welding speed of 0.2

m/min is illustrated in detail. Moreover, the Trans-Varestraint test during GTAW is also carried out at the same welding speed of 0.2 m/min compared with that of LBW. Solidification crack distribution, number of the crack and total crack length are investigated and compared for evaluating the effect of different heat sources on solidification cracking susceptibility. While, in order to further evaluate the cracking susceptibility quantitatively during LBW, it is necessary to measure the BTR calculated using the crack length and temperature profile. Thus, temperature measurement using an optical fiber radiation thermometer is illustrated, and then the relative problem during measuring temperature is described and discussed simply (detail discussion in Chapter 4). Therefore, the measurement method of 2D temperature distribution using a multi-sensor camera as one of candidates is employed to measure temperature distribution around the molten pool. Next, the temperature range of each crack is measured using 2D temperature distribution. Finally, the BTR can be obtained using the developed Trans-Varestraint during LBW and 2D temperature distribution, which is the average value of the maximum temperature range under saturated augmented strain. Furthermore, ductility curve tendency is also tried to be obtained by drawing the curve covering all of the temperature range of the crack.

3.2 Materials Used

Type 310S stainless steel was used for developing the Trans-Varestraint test during LBW with in-situ observation and comparing with that of traditional Trans-Varestraint test during GTAW. In addition, type 304L stainless steel was employed to measure the augmented strain at the room temperature by changing bending blocks with different surface radii. Table 3.1 shows the chemical compositions of the used materials with a dimension of $110^{l} \times 110^{w} \times 5^{t}$ mm.

Table 3.1 Chemical compositions of used stainless steels (mass %)

Material	Elements								
	C	Si	Mn	P	S	Ni	Cr	Co	Fe
310S	0.04	0.43	0.96	0.019	0.001	20.13	25.19	0.09	Bal.
304L	0.006	0.69	1.42	0.034	0.002	10.06	18.14	0.18	Bal.

3.3 Development of Trans-Varestraint Test during LBW

3.3.1 Trans-Varestraint test method

Figure 3.1 shows the feature of Varestraint test machine (Type VF-09-17F, produced by Japan Special Machine). In this study, only Trans-Varestraint test method is applied due to focus on the investigation of solidification cracking susceptibility. In order to evaluate solidification cracking susceptibility during LBW, a fiber laser (Type YLR-3000S, produced by IPG) is used as a welding heat source, as shown in Fig. 3.2. The wavelength of this fiber laser is 1070 nm, and the laser beam parameter product (BPP) is 5.4 mm*mrad. For comparison, GTAW is also applied as a heat source and Fig. 3.3 shows the appearance of GTA welding machine (Type 500A DT-NP_3K, produced by Hitachi Industrial Equipment Systems Co., Ltd).

Table 3.2 shows the LBW conditions. Welding speed is 0.2 m/min and laser power is adjusted in order to obtain half penetration in the thickness direction. The spot diameter of laser is 0.4 mm with just focus length of 382.5 mm and defocus length of 0 mm. In addition, laser head is 25° to the welding direction for avoiding interference of other equipment. In order to provide a strong shielding atmosphere, Ar gas is blown at 50 l/min onto the surface and rear of the specimen during LBW. Table 3.3 shows GATW conditions. The main parameters are welding speed of 0.2 m/min (the same as that of LBW), arc current of 180 A, arc length of 2.0 mm, electrode extension length of 9.0 mm, torch tilting angle of 20° and flow rate of Ar shielding gas of 20 l/min.

The detail test process of the Trans-Varestraint test during LBW is illustrated in Fig. 3.4. First, the specimen is fixed on the bending block with screwing the front and back ends of the specimen along the centerline of welding direction. Then, the specimen with bending bock is moved up until the top sides of the specimen touches the bottom of two yokes tightly. Next step is to set the welding speed and distance, and the stroke (the distance of moving down of the two yokes). During testing, when the trailing edge of the molten pool moves to the center of specimen, the bending strain is applied on the specimen by moving down the two yokes as heat source stopes, leading to the occurrence of the cracking. The cooling rate becomes quite high during LBW, especially at high welding speed, thus the fast bending is required because the initiation and propagation of the cracks have to be completed before the specimen solidified completely.

In this research, the testing machine and fiber laser are accurately synchronized and a fast bending speed, approximately 350 mm/s (yoke movement), is applied. The test procedure of the Trans-Varestaint test during GTAW is similar as that of LBW.

Fig. 3.1 Varestraint test machine

(a) Fiber laser oscillator

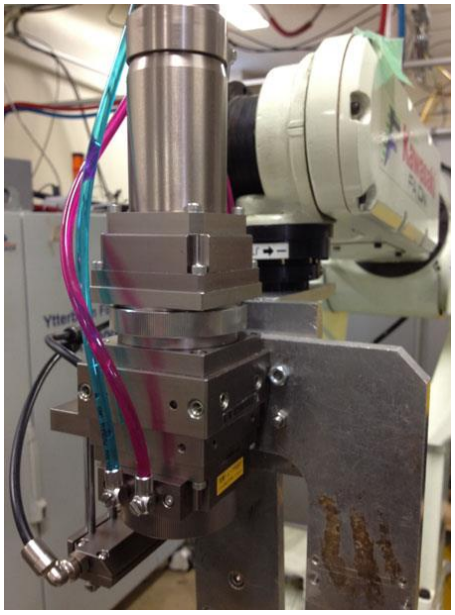

(b) Fiber laser head for welding

Fig. 3.2 Appearance of fiber laser equipment

Fig. 3.3 Appearance of GTA welding machine

Table 3.2 LBW conditions

Welding speed, m/min	0.2
Laser power, kW	1.0
Laser spot diameter, mm	0.4 (just focus)
Laser irradiation angle, deg	25
Ar shielding gas, l/min	50

Table 3.3 GTAW conditions

Welding speed, m/min	0.2
Arc current, A	180
Arc length, mm	2.0
Electrode extension length, mm	9
Torch tilting angle, deg	20
Ar shielding gas, l/min	20

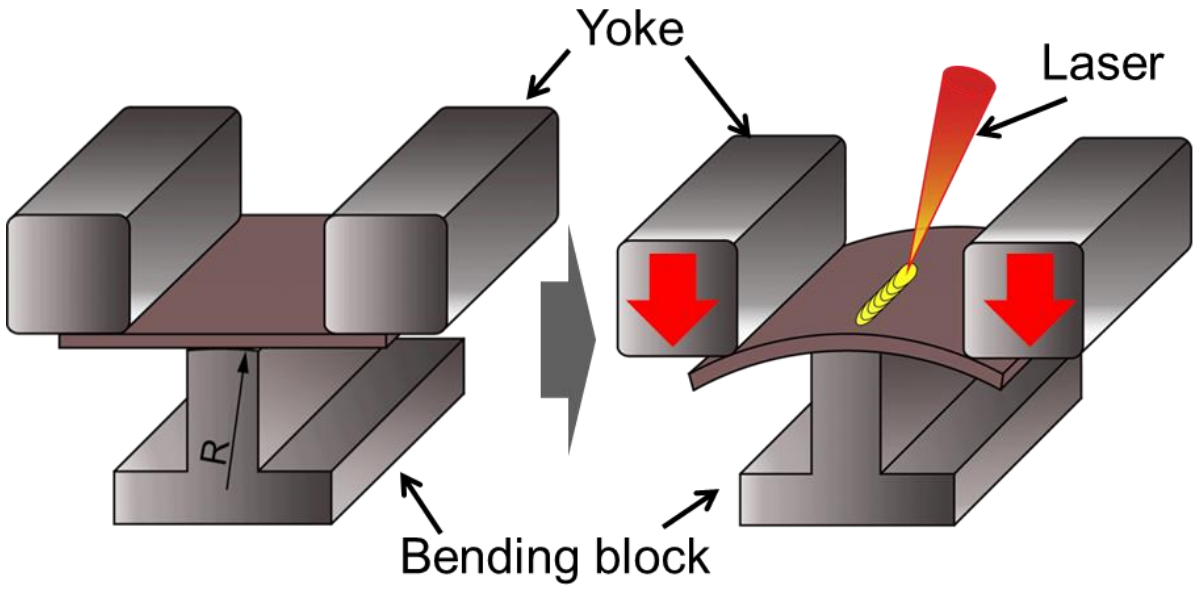

Fig. 3.4 Schematic illustration of Trans-Varestraint test during LBW

3.3.2 Trans-Varestraint test with in-situ observation

Figure 3.5 shows the experimental setup of the Trans-Varestraint during LBW with in-situ observation. A high speed camera (Type Memrecam HX-3, produced by nac) is set up vertical to the center of the specimen for capturing the molten pool shape after the occurrence of solidification crack during Trans-Varestraint. Meanwhile, laser lighting with the wavelength of 980 nm is used in order to obtain clear image. For the purpose of observing molten pool shape clearly, a macro lens (AF Micro-Nikkor ED 200 mm F/4D IP, produced by Nikon) with focus length of 200 mm is employed to obtain magnified image, a 980 nm band-pass filter (produced by M Square) is fixed on the macro lens in order to let 980 nm laser lighting pass and cut off 1070 nm laser beam. Finally, a protect lens is fixed on the outside in order to prevent spatter and metal vapor from damaging the filter. Table 3.4 shows the shooting conditions during LBW.

In the case of GTAW, in-situ observation method is nearly the same as that of LBW. A 980 nm laser lighting, a macro lens with focus length of 200 mm, a 980 nm band-pass filter and a protect lens are also employed to obtain clear and high magnification image during Trans-Varestraint test during GTAW. The shooting conditions during GTAW are shown in Table 3.5.

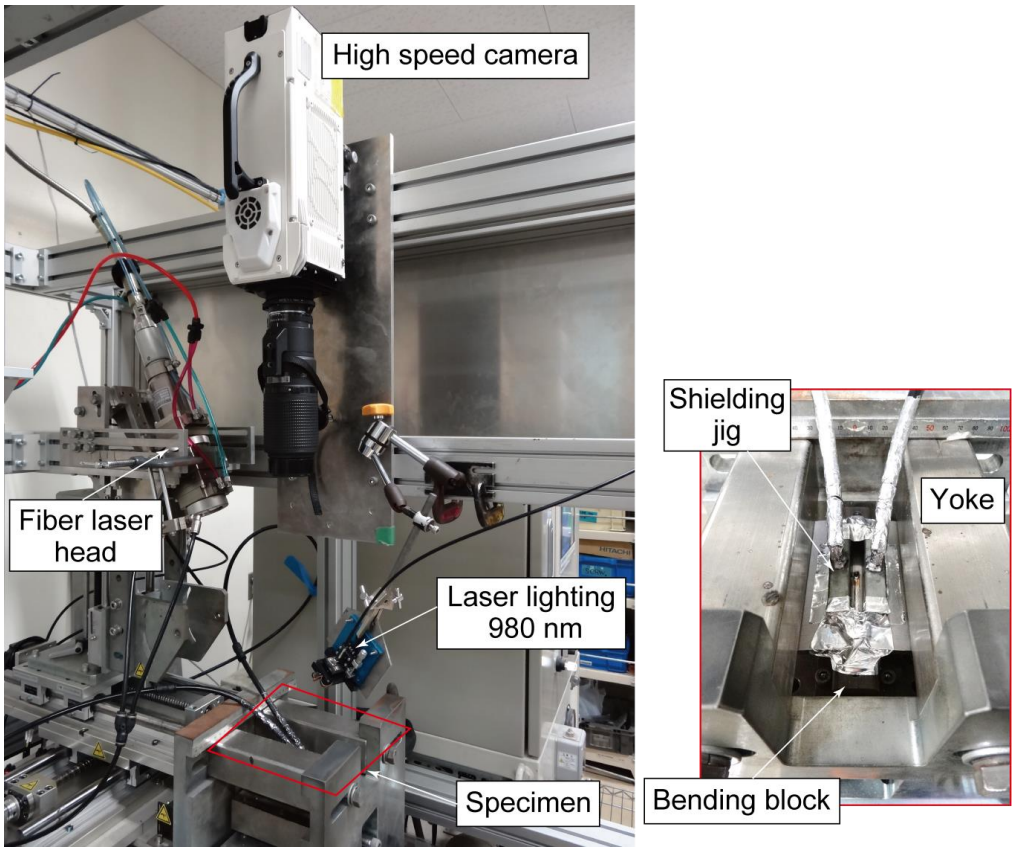

Fig. 3.5 Experimental setup of Trans-Varestraint during LBW with in-situ observation

Table 3.4 Shooting conditions during LBW

Frame rate, fps	5000
Resolution, pixel	1792×512
Shutter speed, sec	1/10000

Table 3.5 Shooting conditions during GTAW

Frame rate, fps	5500
Resolution, pixel	1344×1248
Shutter speed, sec	1/100000

3.3.3 Relationship between augmented strain and bending block

Equation (3.1) shows the relationship among the thickness of the specimen [6], the radius of bending block and theoretical calculated strain vertical to the welding direction.

$$\varepsilon = \frac{t}{2R} \times 100\ \% \tag{3.1}$$

where ε is the theoretical calculating strain, %;

t is the thickness of specimen, mm;

R is the radius of bending block, mm.

The above equation is deduced based on the phenomenon that the bottom of the specimen just totally touches the curvature surface of the bending block after bending. Therefore, according to above phenomenon, the corresponding stroke can be calculated for each bending block.

During Trans-Varestraint test, the different augmented strain could be applied by changing bending blocks with different surface radii. In this study, the augmented strain is measured by using a strain gage (Type KFEL-2-120-C1L5M2R, produced by Kyowa Electronic Instruments Co., LTD) which can measure strain in the elastic to plastic region. The strain measurement process is as follows: first, the center of the specimen is polished by using sandpaper and cleared by using acetone in order to remove impurity and residual oil. Then, the two centerlines is made crossing with each other on the specimen for positioning strain gage. Next, the strain gage is fixed on the center of the specimen, the back of which is painted with instant adhesive (Type CC-36, produced by Kyowa Electronic Instruments Co., LTD). In order to protect strain gage lead, strain gage is connected with lead line by using terminal which is attached to the specimen by instant adhesive (Type CC-33A, produced by Kyowa Electronic Instruments Co., LTD). Finally, a voltage measurement instrument (EDX-200A, produced by Kyowa Electronic Instruments Co., LTD) with sampling frequency of 5000 Hz is employed to measure a change of conversion voltage caused by the variation of electrical resistance as a result of the deformation of the specimen that corresponds to the augmented strain. In this study, the augmented strain is measured parallel and vertical to the welding direction, respectively.

For each bending block, the strain need to be measured at least twice successfully in order to obtain stable value. Figure 3.6 shows the strain history by using bending block with the surface radius of 70 mm. In Fig. 3.6, before bending, the value is around 0 due to no deformation. Then, the strain rises abruptly from 0 to the peak value (average value 4.26 %) in a very short period of about 0.01 s due to rapid fall of the bending block. After bending, there is a little and fast decrease from the peak value to the stable value (average value 3.93 %). In the case of Trans-Varestraint test, the solidification crack occurs before reaching to the peak value during bending. Therefore, the augmented strain is considered as the peak value. Table 3.6 shows the measured augmented strain corresponding to each bending block for the Trans-Varestraint test in this research. The augmented strain vertical to the welding direction is directly and strongly contributed by bending and the value increases with decreasing radius of bending block. In addition, if no special instructions, the augmented strain mentioned in this thesis defaults to the augmented strain vertical to the welding direction.

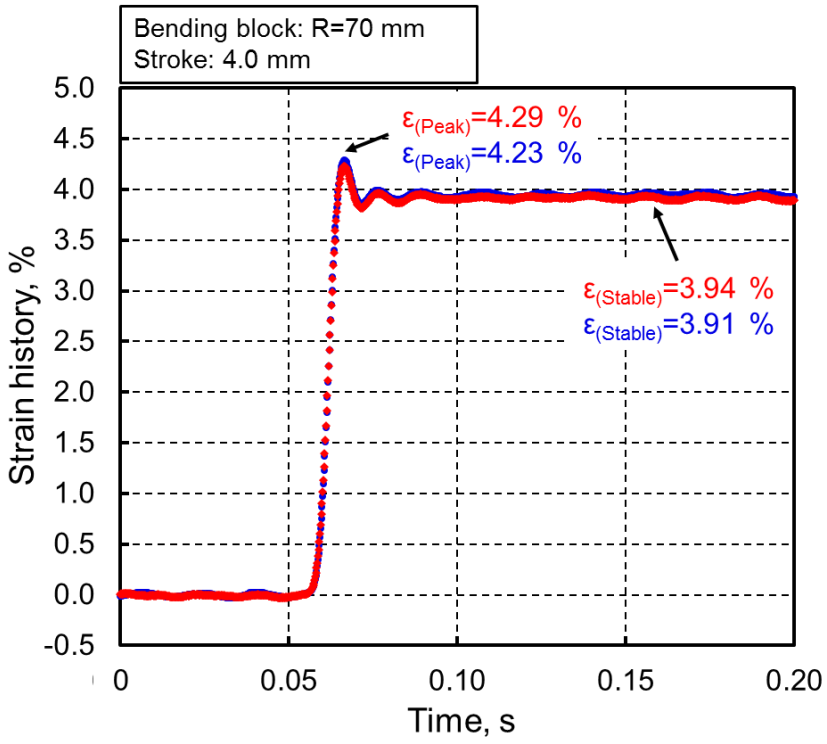

Fig. 3.6 Strain history using bending block with surface radius of 70 mm

Table 3.6 Augmented strain for Trans-Varestraint test

Radius of bending block, mm		400	300	200	125	70
Augmented strain, %	Vertical to welding direction	0.8	1.0	1.9	2.8	4.3
	Parallel to welding direction	0	0	0.1	0.1	0.1

3.3.4 Evaluation method of solidification crack during Trans-Varestraint test

Figure 3.7 shows the SEM image of the molten pool after Trans-Varestraint test during LBW at welding speed of 0.2 m/min under augmented strain of 4.3 %. The solidification crack distribution around the rear of the molten pool can be observed from the SEM image clearly, as shown in Fig. 3.7. However, the precise fusion boundary could not be drawn only from the SEM image. It is well known that the position of the fusion boundary can affect the actual length of each crack and further determine the value of the BTR strongly during measurement. While, under the acid of the in-situ observation image captured by a high speed camera, the precise fusion boundary can be drawn, as shown in Fig. 3.8. The solidified metal enhances the reflection of the light forming the high brightness and the liquid metal within the molten pool presents the low brightness, thus, the boundary between solidified and liquid metal could be distinguished and drawn precisely and easily, as marked by a red line in Fig. 3.8. Keep in the same scale, the fusion boundary of the in-situ observation image is moved and superimposed on the SEM image based on the same rear center of the molten pool. In this study, all of the fusion boundaries are measured from the in-situ observation image.

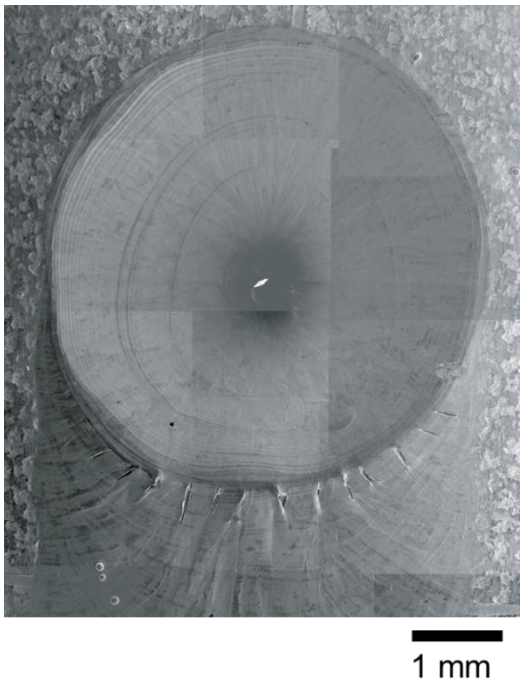

Fig. 3.7 SEM image of the molten pool after Trans-Varestraint test during LBW at welding speed of 0.2 m/min under augmented strain of 4.3 %

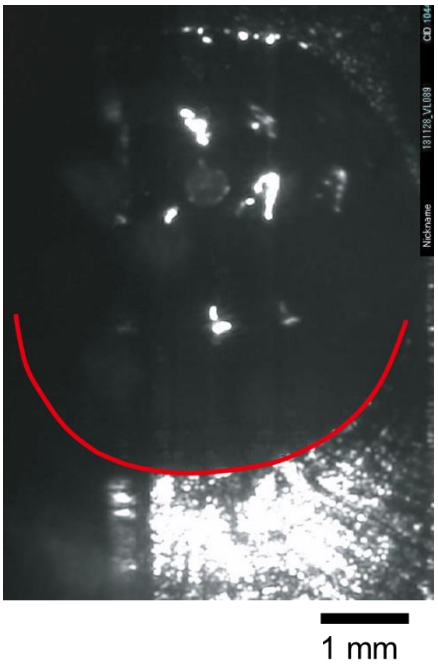

Fig. 3.8 In-situ observation image of the molten pool after Trans-Varestraint test during LBW at welding speed of 0.2 m/min under augmented strain of 4.3 %

Thus, the complete image of solidification crack distribution could be obtained including precise fusion boundary and the number of solidification crack, as shown in Fig. 3.9. As is mentioned, the red line is the fusion boundary and the yellow number presents the number of solidification crack. Figure 3.10 shows the graph of solidification crack distribution corresponding to that of the SEM image in Fig. 3.9. The molten pool shape looks like a smooth curve and the relatively longer solidification crack appears at the rear center of the molten pool. During Trans-Varestraint test, some cracks initiate from the fusion boundary and the length is the distance from initial point crossing the fusion boundary to the end point of this crack, as marked by the red bar. While, although a number of cracks initiate from the fusion boundary, the portion of the crack near the molten pool could be healed by the liquid metal, therefore, the healing part is marked by the light upward bar and the crack length is marked by the red bar. In addition, a few cracks initiate far away from the fusion boundary, thus, the white bar represents the distance from the fusion boundary to the crack initiation position. In Fig. 3.10, No. 17 crack with the maximum length occurs at the rear center of the molten pool during LBW at welding speed of 0.2 m/min. The similar result also appears in that of GTAW.

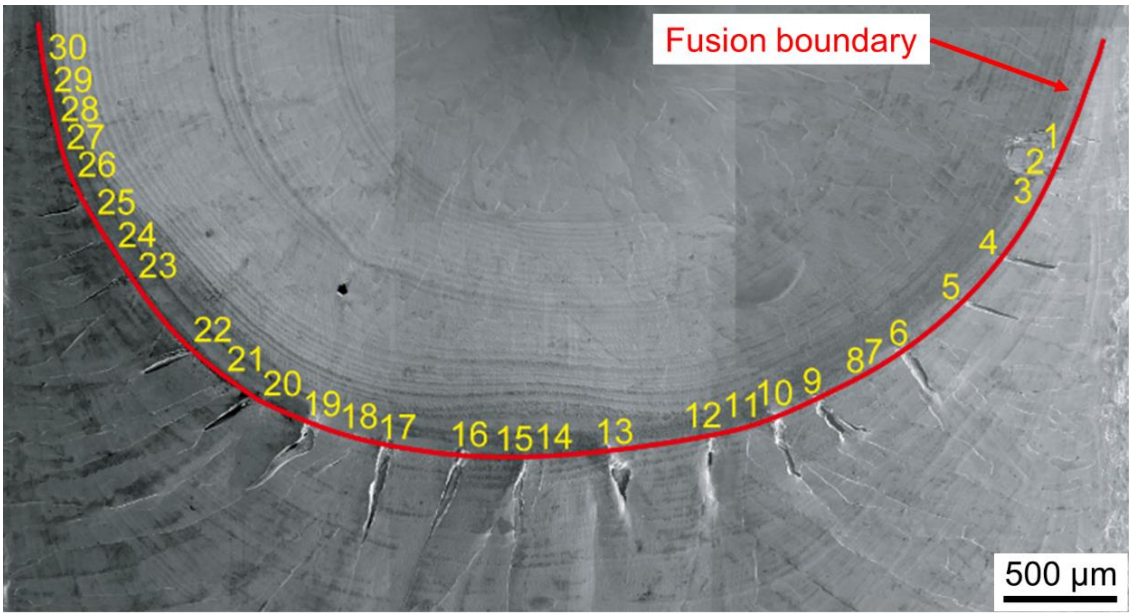

Fig. 3.9 SEM image of solidification crack distribution during LBW at welding speed of 0.2 m/min under augmented strain of 4.3 %

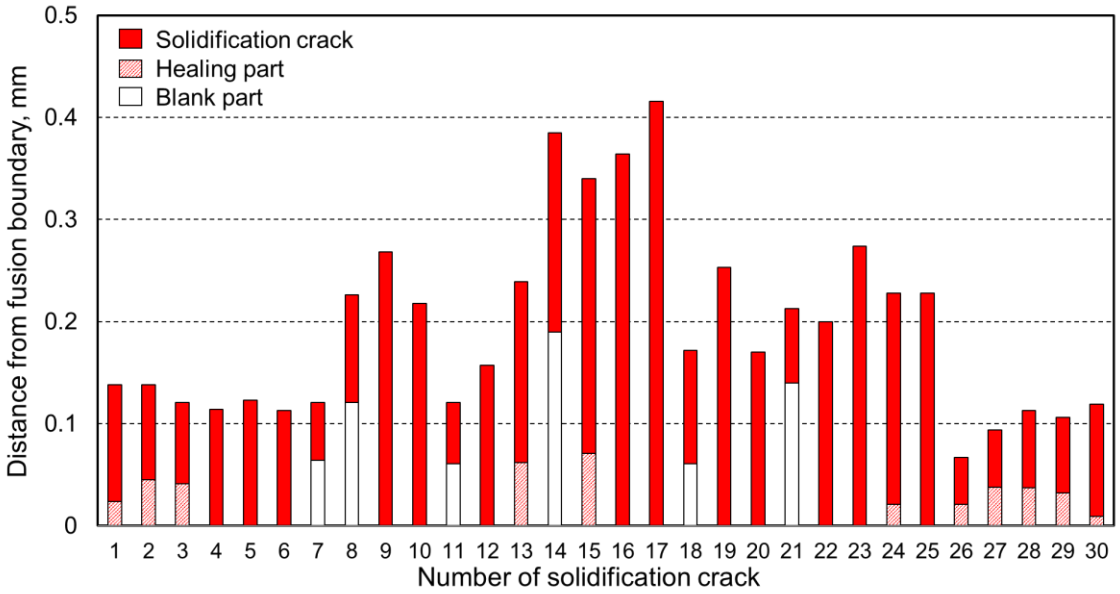

Fig. 3.10 Graph of solidification crack distribution during LBW at welding speed of 0.2 m/min under augmented strain of 4.3 %

Additionally, in order to confirm the types of the hot crack, it is necessary to observe the fracture surface of the crack. Figure 3.11 shows a SEM image of the fracture surface during LBW. On the high-temperature side, dendrite morphology is observed obviously, as shown in Fig. 3.11 a). Along the direction from the high- to low-temperature side, the dendrite arms become obscure and tiny hollows form gradually, as shown in Fig. 3.11 b) and c). On the low temperature side, an intergranular fracture surface can be observed in Fig. 3.11 d). The presence of hollows is consider as a proof of solidification crack [31], therefore, the region from the high-temperature side to where the hollow exist is identified as solidification crack and the region of intergranular fracture is identified as ductility-dip crack. Finally, it can be confirmed that ductility-dip crack combines with solidification crack along the temperature gradient in the type of this crack. In this study, all of the crack length is measured with distinguishing the solidification crack and the ductility-dip crack.

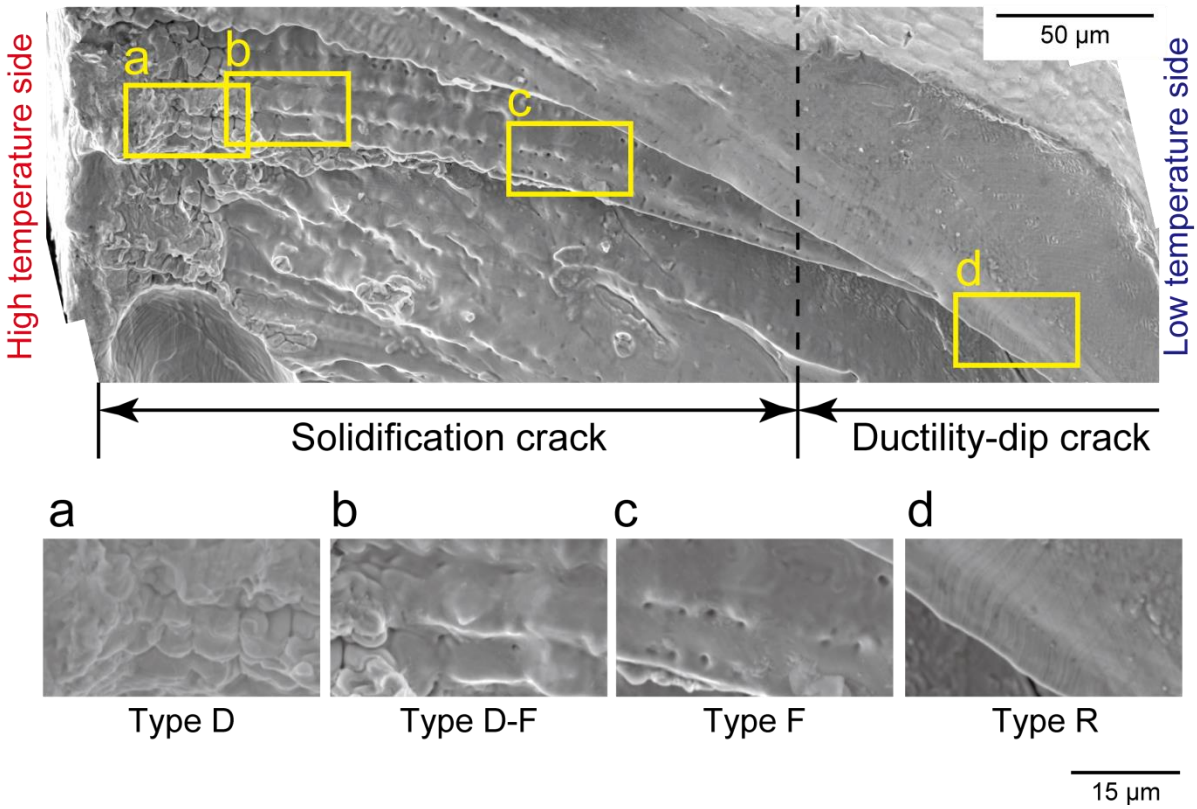

Fig. 3.11 Fracture surface of the crack

3.4 Comparison of Solidification Cracking Susceptibility between LBW and GTAW

In order to evaluate solidification cracking susceptibility quantitatively, the number of the crack should be counted carefully and the solidification crack length should be measured preciously by using Image-J software from the higher magnification image of the SEM. Figure 3.12 shows the number of the crack and the total crack length after Trans-Varestraint test during LBW and GTAW at welding speed of 0.2 m/min under augmented strain from 0.8 to 4.3 %. The variation tendencies in the number of the crack and the total crack length are expressed by a green solid line and a pink dash line for LBW and GTAW, as shown in Fig. 3.12. With increasing the augmented strain, the number of the solidification crack and the total crack length increase firstly and then both the values saturate at about 2.0 % of the augmented strain. Under the saturated strain, the number of the solidification crack is about 30 using LBW, however the value is more than 40 using GTAW. In addition, total crack length is around 5 mm using LBW, which is

a half of that using GTAW. As a whole, both values are much lower using LBW than those using GTAW.

However, it is considered that the difference in weld bead width gives an inaccurate evaluation of solidification cracking susceptibility parameters, such as the number and length of the crack, therefore, the influence of the bead width should be eliminated to clearly evaluate the effect of different heat sources on solidification cracking susceptibility. Figure 3.13 shows the bead width after Trans-Varestraint test during LBW and GTAW under the saturated augmented strain of 2.8 and 4.3 %. The value of the bead width using GTAW is the double of that using LBW. Therefore, the number of the crack and the total crack length using GTAW is much higher than those using LBW. In order to evaluate solidification cracking susceptibility accurately, the number of crack and total crack length should be divided by the bead width. Figure 3.14 shows the number density of solidification crack and total crack length per bead width under the saturated augmented strain of 2.8 and 4.3 %. Both values are nearly the same, which means the different heat sources between LBW and GTAW have a relatively small influence on solidification cracking susceptibility at welding speed of 0.2 m/min.

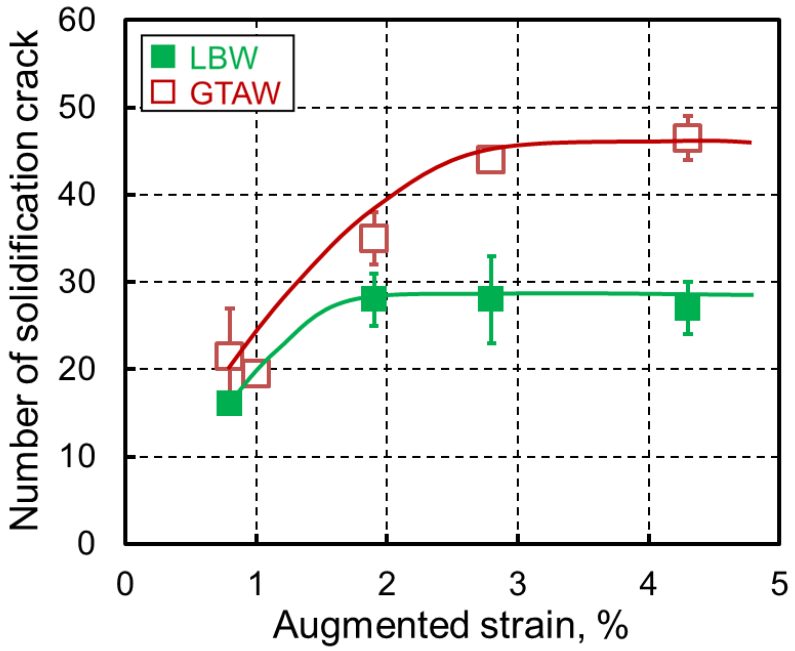

(a) Number of solidification crack

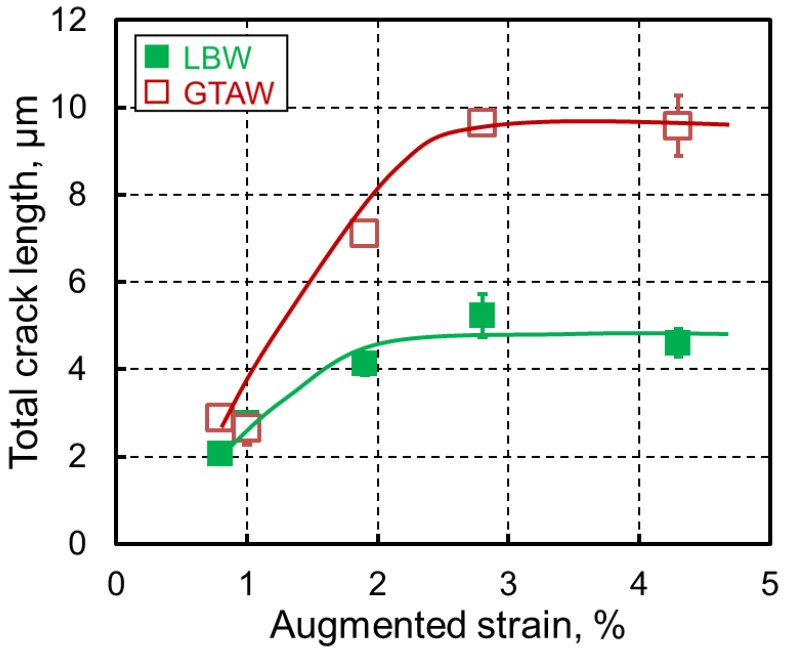

(b) Total crack length

Fig. 3.12 Number of solidification crack and total crack length during LBW and GTAW

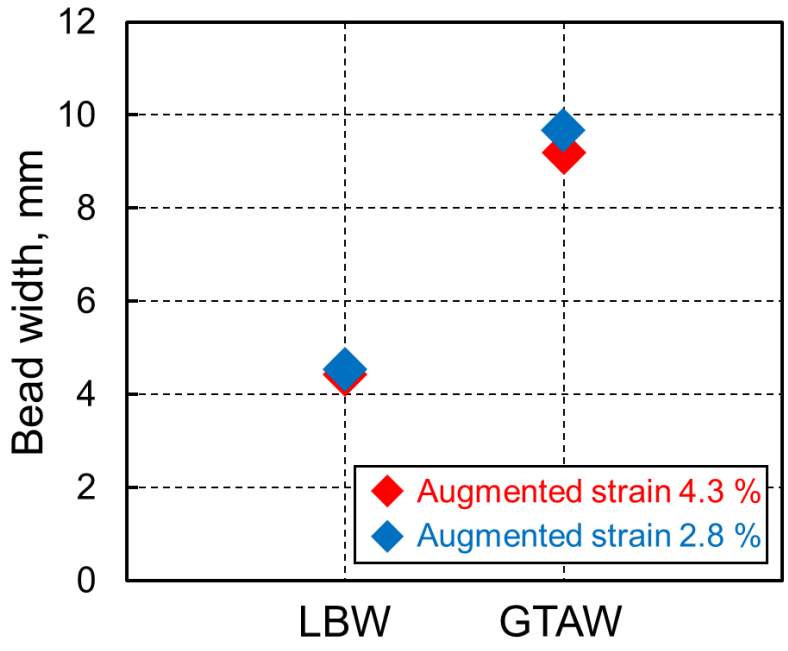

Fig. 3.13 Bead width after Trans-Varestraint test during LBW and GTAW

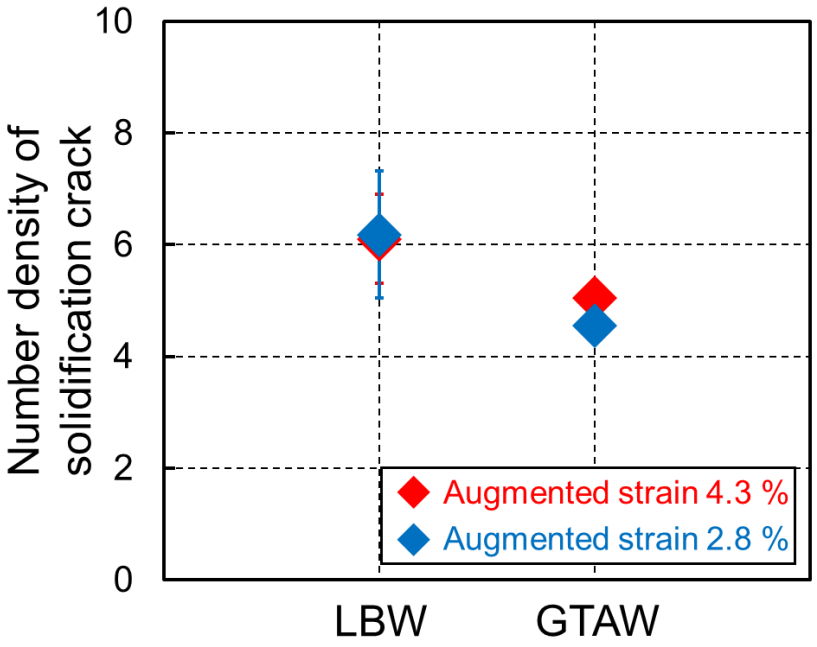

(a) Number density of solidification crack

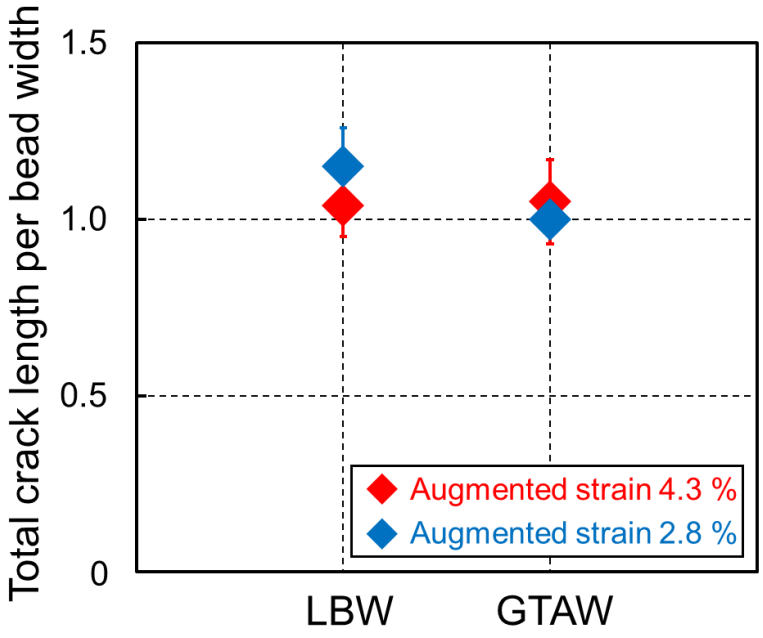

(b) Total crack length per bead width

Fig. 3.14 Number density of solidification crack and total crack length per bead width during LBW and GTAW

3.5 Measurement of Temperature Profile

3.5.1 Meaning of temperature measurement

According to the solidification theory, the weld metal becomes more ‘brittle’ in the sense that it is much less ductility in the BTR than either the molten pool or the completely solidified weld motel [5]. In other words, the solidification crack tends to occur easier when the solidifying weld metal is less ductile. Therefore, the BTR as a very important index for evaluating solidification cracking susceptibility quantitatively needs to be obtained. Conventionally, the BTR can be calculated by using temperature profile and the maximum crack length. Thus, it is necessary to measure precise temperature profile in order to obtain the accurate BTR.

The schematic illustration of calculating BTR using the conventional temperature measurement is shown in Fig. 3.15. The temperature profile is measured along the centerline of the molten pool parallel to the welding direction. At low welding speed, the longest crack always initiates at the trailing edge of molten pool and propagates approximately along welding direction. Therefore, the maximum crack length can be used to the temperature profile multiplying welding speed in order to obtain the BTR. Theoretically, the start point of the BTR is liquidus temperature where the solidification crack initiates, and the end point of the BTR is defined as the solidus temperature at which the longest solidification crack stops. The above method illustrates the conventional temperature measurement method to obtain the BTR, which is suitable to the low welding speed, such as 0.2 m/min.

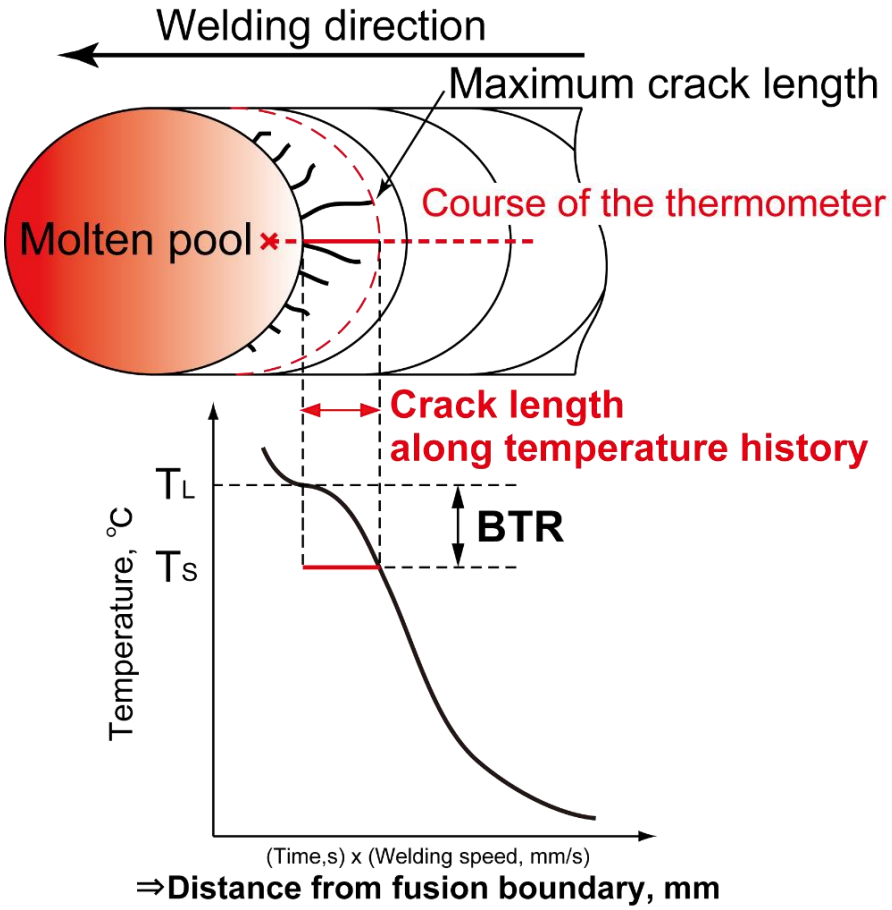

Fig. 3.15 Schematic illustration of calculating the BTR using conventional temperature measurement

3.5.2 Temperature profile using an optical fiber radiation thermometer

In this research, an optical fiber radiation thermometer (Type FIMTHERM-H, produced by JFE Techno-Research Ltd) is employed to measure the temperature profile along the centerline of the molten pool during LBW. Appearance of this optical fiber radiation thermometry is shown in Fig. 3.16, and Fig. 3.17 illustrates the schematic illustration of measurement tip of the thermometry. Quartz fiber with a diameter of 0.25 mm is for measuring temperature, and two stainless steel tubes with different diameters of 0.7 and 1.4 mm respectively cover the quartz fiber for double protection. The probe type is Indium gallium arsenide (InGaAs). In addition, in the case of this optical fiber radiation thermometer, the measured wavelength is 1.5 μm and the sampling frequency is 100 Hz.

The measurement principle of the optical fiber radiation thermometer is based on blackbody radiation. A blackbody is an idealized object which can absorb and emit all of incident electromagnetic radiation but never has the phenomenon of reflection and transmission. And the blackbody radiation intensity only depends on the temperature of the object. When the thermometer is inserted into the molten pool, an approximately ideal blackbody will form on the measurement tip of the thermometer because this tip is in a perfectly insulated enclosure inside the metal. Thus, the precise temperature could be measured by using the optical fiber radiation thermometer. Further, it also considers the correction of the emission during temperature measurement. Equation (3.2) expresses corrected temperature calculation transformed from measured voltage by using voltage measuring instrument (Type PCD-320A, produced by KYOWA).

$$T(℃) = 375V + 125 \tag{3.2}$$

where T is the actual temperature of the object;

V is the measured voltage from the instrument.

Fig. 3.16 Appearance of an optical fiber radiation thermometry

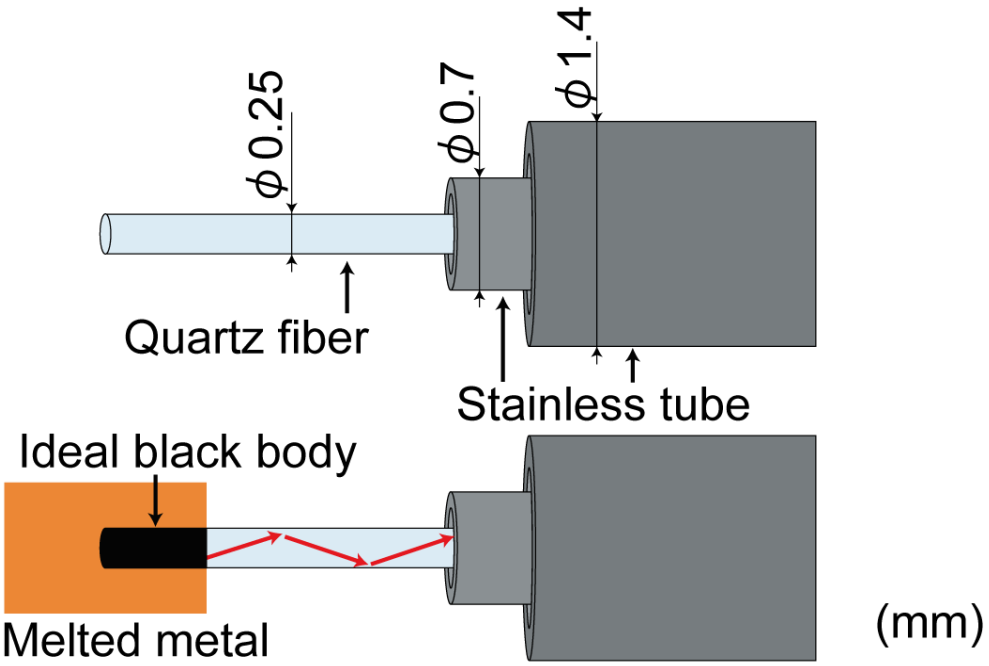

Fig. 3.17 Schematic illustration of the measurement tip of the thermometry

Figure 3.18 shows the experiment setup of the temperature measurement using the optical fiber radiation thermometer during LBW. The welding conditions are same as those during Trans-Varestraint test, but no applied bending. During welding, the optical fiber radiation thermometer is inserted at the trailing edge of the molten pool. The tube jig is applied to guide the thermometer directly into the designated position. The laser lighting is to provide brightness for the in-situ observation. The in-situ observation method with a high speed camera is used to make sure the precise time and position of inserting the thermometer. Moreover, in order to decide the liquidus temperature, the high speed camera is set synchronization with the optical fiber radiation thermometer, as shown in Fig. 3.19. During the temperature measurement, the high speed camera and optical fiber radiation thermometer will record the movie and temperature data at the same time when receiving the trigger of stabilized direct-current power supply of 5 V voltage.

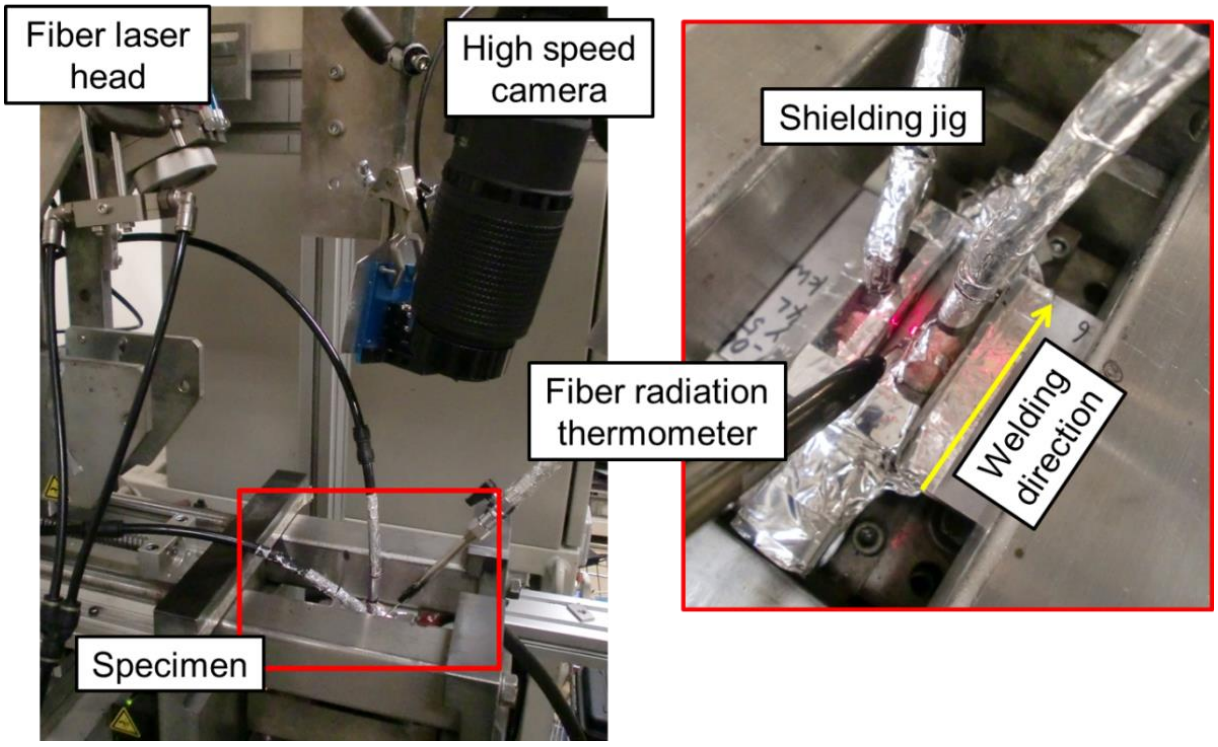

Fig. 3.18 Experiment setup for temperature measurement using an optical fiber radiation thermometer

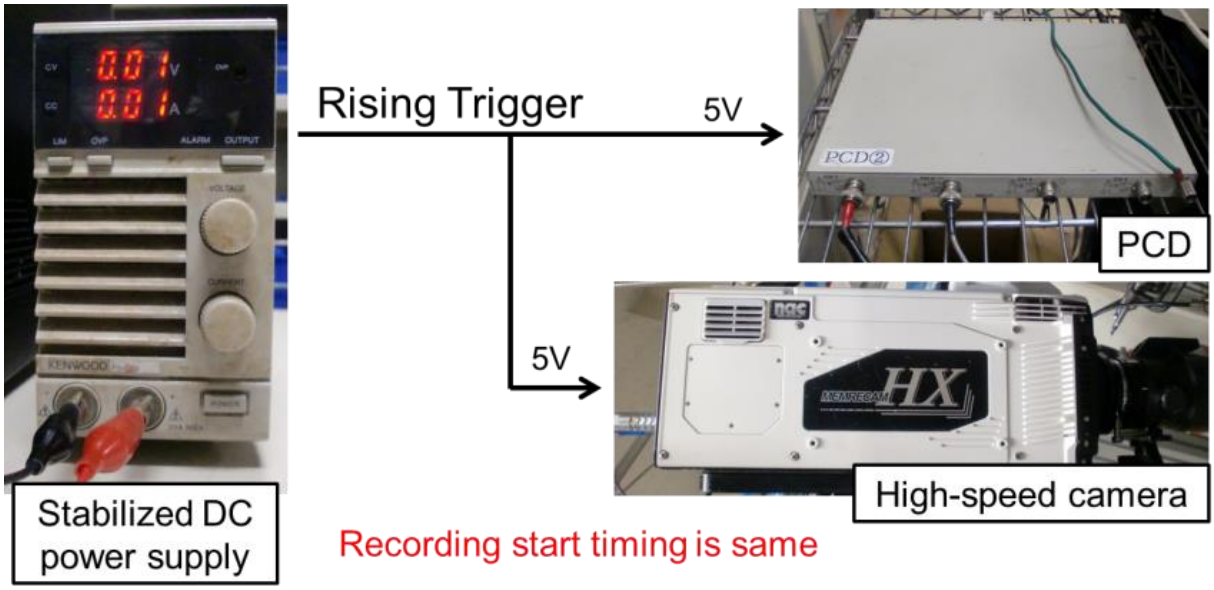

Fig. 3.19 Synchronization setting

Figure 3.20 shows the method to measure the temperature profile and judge the liquidus temperature using the high speed camera during LBW at welding speed of 0.2 m/min. The molten pool is represented by a white line, the shape of the thermometer is indicated by red line and the measurement tip is expressed by a red circle, as shown in Fig. 3.20. The detail produce is as follows: At the time t = t_0, the thermometer is just inserted into the terminal center of the molten pool between laser spot position and trailing edge of molten pool for preventing the laser beam from damaging the measurement tip of the thermometer, as shown in Fig. 3.20 a). Then, as time goes on and the molten pool moves, when the trailing edge of the molten pool just touches the center of the measurement tip by observing the high magnification movie frame by frame, the liquidus temperature could be derived by judging the time t = t_1, as shown in Fig. 3.20 b). Finally, at the time t = t_2, the measured temperature profile experiences a period that covers the total solidification range, as shown in Fig. 3.20 c).

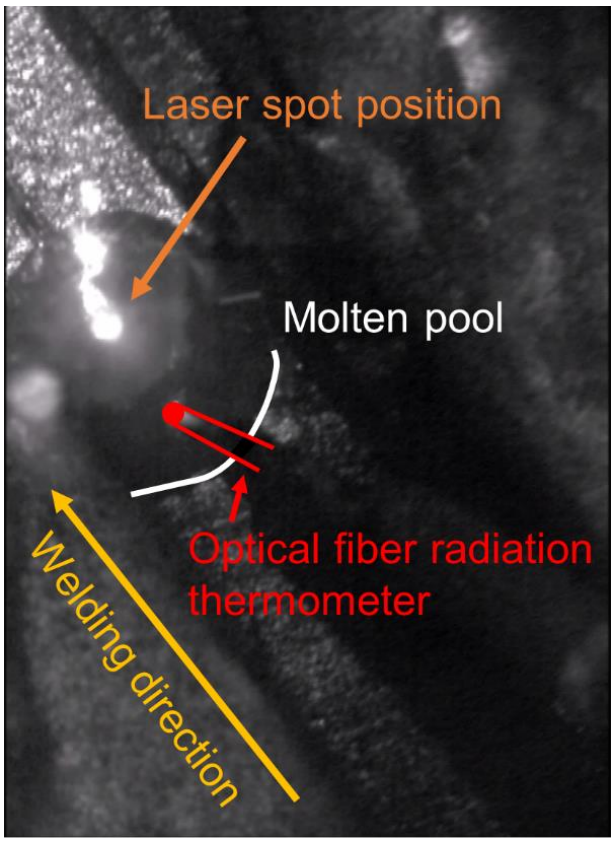

(a) Time t = t_0

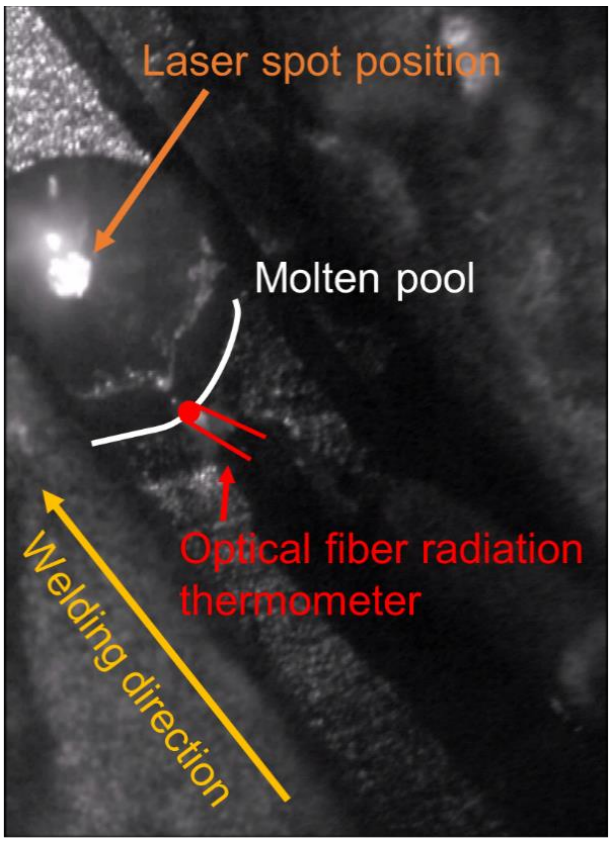

(b) Time t = t_1

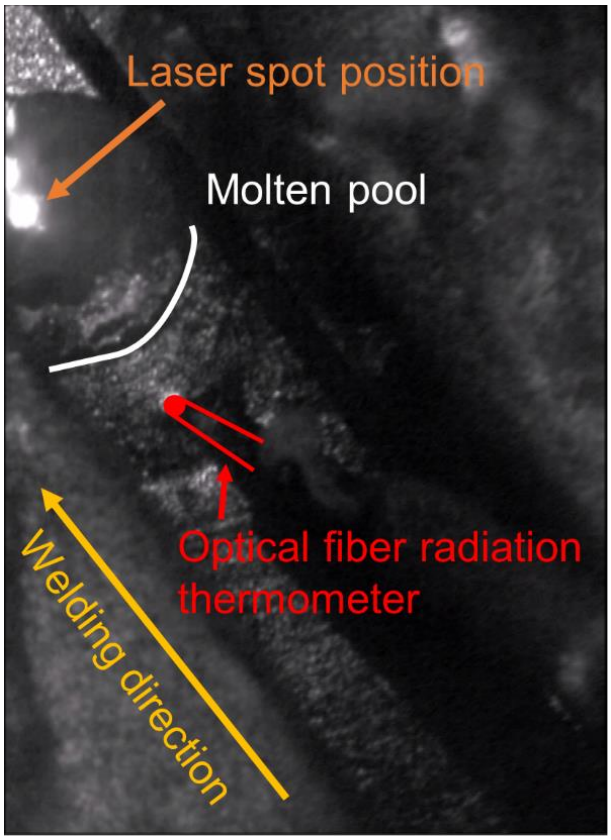

(c) Time t = t_2

Fig. 3.20 Method to measure temperature profile and judge liquidus temperature by combining the optical fiber radiation thermometer with a high speed camera

Conventionally, the liquidus temperature is derived using differential curve. Figure 3.21 shows the temperature profile and differential curve during LBW at welding speed of 0.2 m/min. The liquidus temperature judged from the high speed camera is 1385 °C, as indicated in Fig. 3.21 a) marked by red color, while the value judged by the inflection of differential curve is 1378 °C, as shown in Fig. 3.21 marked by green color. In the case of the evaluation of solidification cracking susceptibility, the temperature profile and liquidus temperature are the very important indexes. When using differential curve, the plot number of the temperature profile which influences the accuracy of the inflection point can directly affect the precision of the liquidus temperature. However, at relatively higher cooling rate, the temperature profile is steeper, thus, the plot number of the temperature profile in the solidification temperature range becomes much less, resulting in the

inconspicuous inflection point. This is due to the limitation of the sampling frequency of the optical fiber radiation thermometer. It is difficult to obtain the precious liquidus temperature using differential curve during LBW, especially at high welding speed. Therefore, at present it is reasonable to judge the liquidus temperature with the assistance of the high speed camera. The average temperature profile and liquidus temperature can be obtained based on several stable trials by using above method.

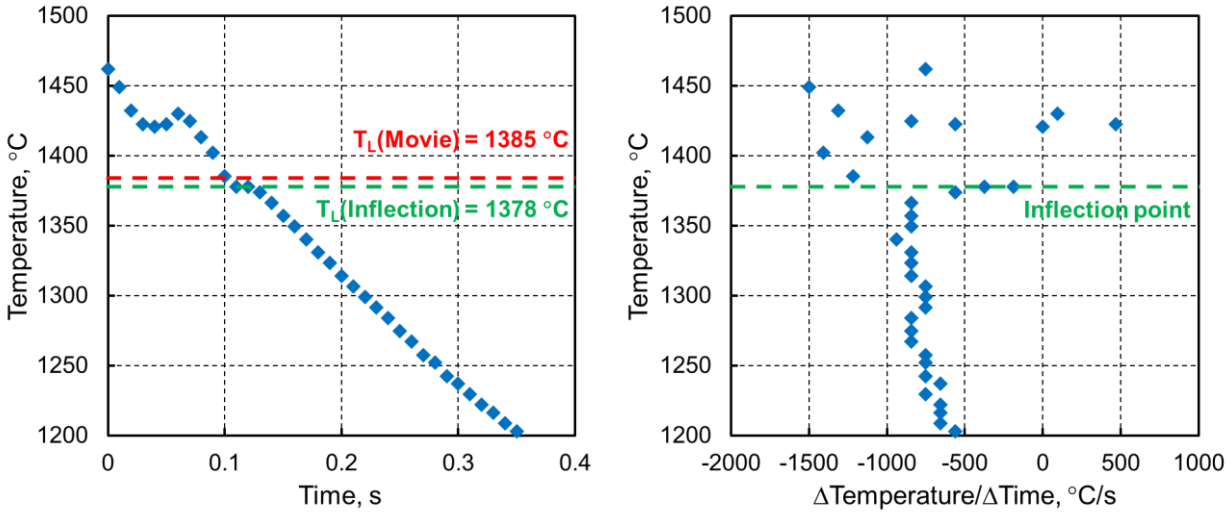

(a) Temperature profile (b) Differential curve

Fig. 3.21 Temperature profile and differential curve during LBW at welding speed of 0.2 m/min

However, when welding speed is more than 1.5 m/min, it is hard to judge the liquidus temperature because the fusion boundary becomes much unobvious as a contribution of the long teardrop molten pool. Moreover, the measured temperature profile is always unstable using the optical fiber radiation thermometer. This phenomenon will be describe and the reason will be discussed in detail in Chapter 4. In addition, some other problems using this thermometer will also be elaborated in Chapter 4. Therefore, the measurement method of 2D temperature distribution using a multi-sensor camera as one of candidates is developed and employed in order to measure the precise temperature and further obtain the true BTR.

3.5.3 2D temperature distribution using a multi-sensor camera

In this research, the measurement method of 2D temperature distribution is employed to measure the temperature range of each crack and finally to obtain the true BTR by using a multi-sensor camera based on two-color thermometry [72]. The temperature could be calculated by using intensity ratio of two different but close wavelengths of radiation light emitted from the object. The basic principle of two-color thermometry is as follows:

According to Planck' law, radiation intensity M_λ of a wavelength λ at a given temperature can be written

$$M_\lambda = \frac{c_1 \varepsilon \tau}{\lambda^5 \left(e^{\frac{c_2}{\lambda T}} - 1\right)} \tag{3.3}$$

where c_1 is first radiation constant (c_1 = 3.74×10^{-16} Wm^2);

ε is the emissivity of the object which is the radiation intensity ratio of the object and blackbody ($\varepsilon = \frac{E_{Object}}{E_{Blackbody}}$);

τ is the transmissivity from the object to sensor system;

λ is wavelength (μm);

c_2 is secondary radiation constant (c_2 = 1.44×10^{-2} mK);

T is actual temperature (K).

If two different wavelengths λ_1 and λ_2 with radiation intensity M_1 and M_2 are given respectively, the intensity ratio R of this two different wavelengths can be written

$$R = \frac{M_1}{M_2} = \frac{\varepsilon_1 \tau_1}{\varepsilon_2 \tau_2} \cdot \frac{\lambda_2^5 \left(e^{\frac{c_2}{\lambda_2 T}} - 1\right)}{\lambda_1^5 \left(e^{\frac{c_2}{\lambda_1 T}} - 1\right)} = \frac{\varepsilon_1 \tau_1}{\varepsilon_2 \tau_2} \cdot \frac{\beta_1}{\beta_2} \cdot \frac{\lambda_2^5}{\lambda_1^5} \cdot \frac{e^{\frac{c_2}{\lambda_2 T}}}{e^{\frac{c_2}{\lambda_1 T}}} = \frac{\lambda_2^5}{\lambda_1^5} \cdot \frac{e^{\frac{c_2}{\lambda_2 T}}}{e^{\frac{c_2}{\lambda_1 T}}} \tag{3.4}$$

where β is proportional constant ($\frac{\beta_1}{\beta_2} = 1$).

Two different wavelengths both radiate from the object to sensor system, thus transmissivity is the same ($\frac{\tau_1}{\tau_2} = 1$).

Figure 3.22 shows the schematic illustration of radiation intensity of an object and blackbody at a hypothesized temperature of 1400 °C. Even though the emissivity of an

object ε depends on materials, temperature, surface condition and so on, if two different wavelengths λ_1 and λ_2 are close, $\varepsilon_1 \approx \varepsilon_2$, thus, $\frac{\varepsilon_1}{\varepsilon_2} = 1$.

The general solution of Equation (3.4) can be written

$$log\, R = C_3 + \frac{C_4}{T} \tag{3.5}$$

where C_3 and C_4 are constants,

$$C_3 = 5\, log\left(\frac{\lambda_1}{\lambda_2}\right) \tag{3.6}$$

$$C_4 = C_2\left(\frac{1}{\lambda_2} - \frac{1}{\lambda_1}\right) \tag{3.7}$$

According to equation (3.5), the actual temperature is inversely proportional to the intensity ratio R of two different but close wavelengths, and does not depend on the emissivity and transmissivity. Therefore, the precious actual temperature could be calculated by measuring the intensity ratio R of two different but close wavelengths.

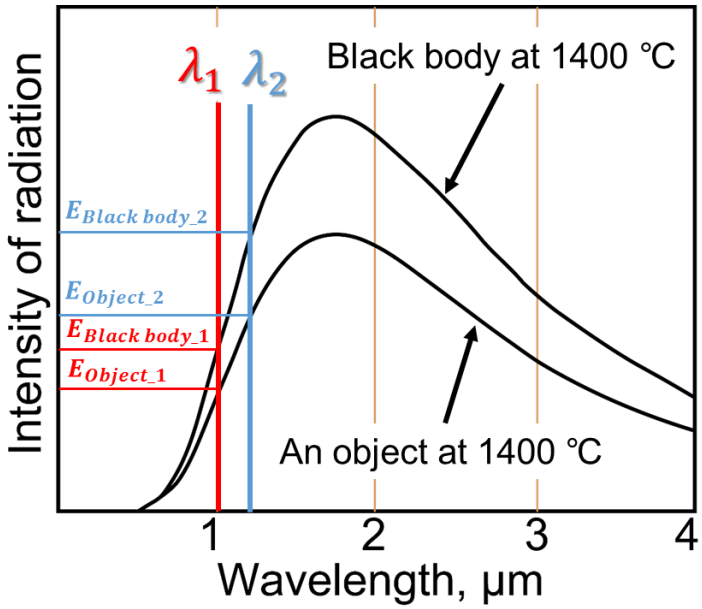

Fig. 3.22 Schematic illustration of radiation intensity of an object and blackbody

Figure 3.23 shows the schematic illustration of a multi-sensor camera (Type DensitoCam-multi, produced by Mitsui Photonics. Ltd) developed by Shinozaki group for temperature measurement. The advantage of this type multi-sensor camera is 2D

temperature measurement, in-situ observation, small measurement size, high temperature range and so on. This camera includes two beam splitters and three sensors. The beam splitters are responsible to split the incoming image from the molten pool to pass through three different band-pass filters into the sensors for capturing the molten pool shape and for measuring the temperature distribution at the same time during LBW. The in-situ observation image could be obtained by using one sensor and its corresponding 980 nm band-pass filter. And 2D temperature distribution image could be obtained by using two sensors which are set up with 650 and 800 nm band-pass filters respectively, and the temperature is calculated based on the two-color radiation thermometry method.

As is mentioned, the difference of the two selected wavelengths for the temperature measurement should be relative smaller in order to eliminate the effect of the emissivity. However, it is note that the temperature distribution becomes a large scatter and unstable if only considering to use the close wavelengths because a CCD sensor has a finite resolution for detecting the brightness and the radiation intensity ratio is too small. Moreover, through the spectroscopic analysis during LBW for type 310S stainless steel, some strong neutral line spectra of Fe with high intensity distributes on the continuous spectrum in the wavelengths from 510-610 nm and at around 770 nm [73]. Thus, the two selected wavelengths should avoid inside this range. Taking into account the above conditions, the 650 and 800 nm wavelengths are selected for the temperature measurement.

Figure 3.24 shows the experiment setup of the temperature measurement using a multi-sensor camera. The welding conditions are the same as that of the Trans-Varestraint test during LBW. The fiber laser is set with the titling 25° to the welding direction. The multi-sensor camera is fixed vertical to the specimen for capturing the molten pool. A macro lens (Type AF Micro-Nikkor ED 200 mm f/4D IF, produced by Nikon) is employed for providing high magnification image. Meanwhile, several extension rings (Type PK-13, produced by Nikon) are employed to further expand magnification. The 980 nm laser lighting is to supply the brightness for the in-situ observation. In addition, the surface of the shield jig is painted with blackbody spray in order to decrease the disturbance of laser reflection. To lower the interference of fume, an air knife is applied to remove it.

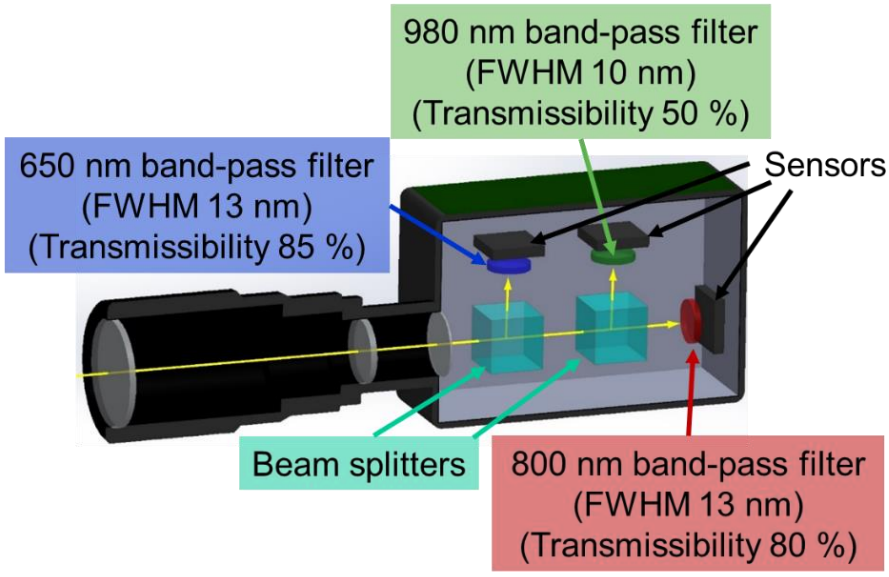

Fig. 3.23 Schematic illustration of a multi-sensor camera

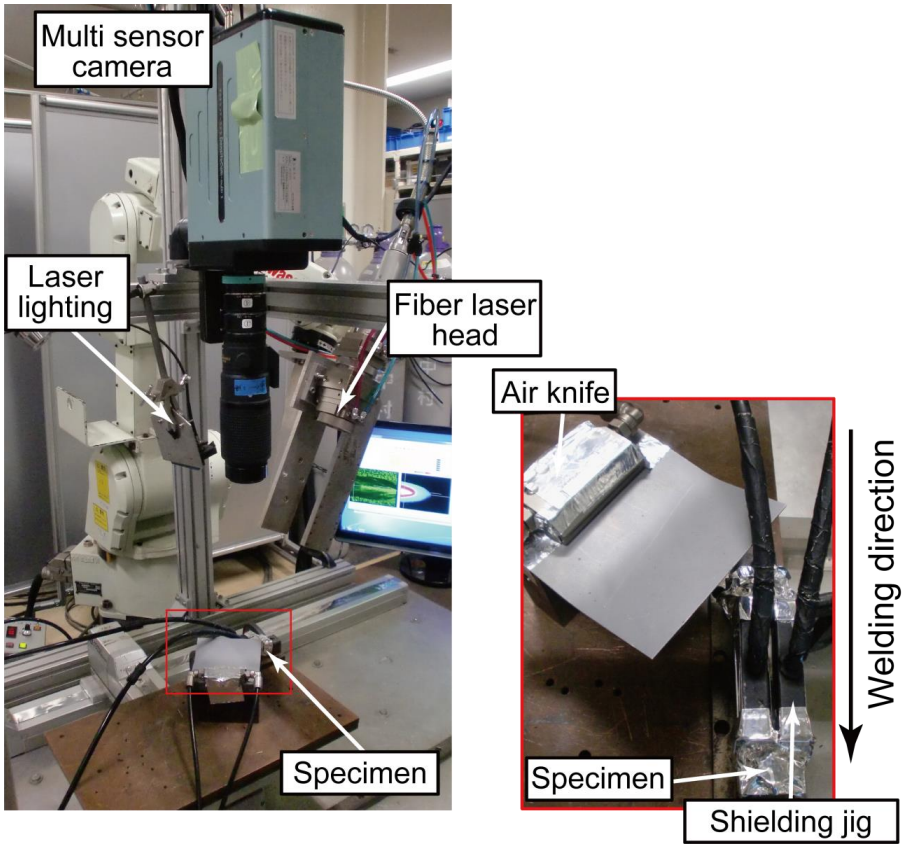

Fig. 3.24 Experiment setup of temperature measuring using a multi-sensor camera

Table 3.7 shows the shooting conditions during the temperature measurement using a multi-sensor camera. The frame rate is 50 fps and resolution is 640 × 480 pixel. Binning which is to group a number of more or less continuous pixel into a minimum unit to display temperature is 2 × 2 pixel in order to reduce the effect of minor observation errors. Finally, a two-color radiation temperature analysis software (Type Thermera, produced by Mitsui Photonics. Ltd) is used to calculate the temperature and the measurable temperature range is from 1000 to 1600 °C. However, due to the limitation of frame rate of 50 fps, it is different to obtain instant temperature when solidification crack just occurs during Trans-Varestraint test with LBW. Meanwhile, lots of investigations, such as the effect of bending on 2D temperature distribution, need to be done quantitatively. Thus, in this work 2D temperature distribution is measured during LBW on the condition of no applied strain.

Table 3.7 Shooting conditions of temperature measurement

<table>
<tr><td colspan="2">Frame rate, fps</td><td colspan="2">50</td></tr>
<tr><td colspan="2">Resolution, pixel</td><td colspan="2">640 × 480</td></tr>
<tr><td colspan="2">Magnification, μm/pixel</td><td colspan="2">7.8</td></tr>
<tr><td colspan="2">Shutter speed, ms</td><td colspan="2">2</td></tr>
<tr><td colspan="2">Aperture</td><td colspan="2">Open</td></tr>
<tr><td colspan="2">Binning</td><td colspan="2">2 × 2</td></tr>
<tr><td rowspan="3">Band-pass filter</td><td rowspan="2">Two-color thermometry</td><td>650 nm</td><td>FWHM 13 nm
Transmissibility 85 %</td></tr>
<tr><td>800 nm</td><td>FWHM 13 nm
Transmissibility 80 %</td></tr>
<tr><td>In-situ observation</td><td>980 nm</td><td>FWHM 10 nm
Transmissibility 50 %</td></tr>
</table>

Figure 3.25 shows the in-situ observation image, 2D temperature distribution image and different temperature gradients by using the multi-sensor camera during LBW at welding speed of 0.2 m/min. During the temperature measurement, the backend of the molten pool and 2D temperature distribution could be obtained at the same time. The fusion boundary of the molten pool is determined from the in-situ observation image, as

shown in Fig. 3.25 a) expressed by a white line. The temperature gradients along different directions around the molten pool are measured by using 2D temperature distribution image, as shown in Fig. 3.25 b). And Fig. 3.25 c) shows the comparison result of different temperature gradients along the centerline (line a) and the side (line b) of the molten pool. The temperature gradients of line a and b are 254 °C/mm and 401 °C/mm, respectively. Thus, this method can measure different temperature gradients around the molten pool in one frame. In the case of low welding speed of 0.2 m/min, the measurement area of the temperature distribution is just a half of molten pool due to the relative larger molten pool size. In this study, only one side of 2D temperature distribution is used to measure the temperature range of solidification crack.

In addition, the temperature profiles using the optical fiber radiation thermometer and 2D temperature distribution are compared during LBW at welding speed of 0.2 m/min, as shown in Fig. 3.26. Both the temperature profile directions are along the centerline of the molten pool. Although the average liquidus temperature based on several trials using the optical fiber radiation thermometer is 1385 °C which is the same as that using 2D temperature distribution at welding speed of 0.2 m/min, the cooling rate is a little lower using the optical fiber radiation thermometer than those using 2D temperature distribution. This difference comes from different measurement positions: the temperature is measured inside the specimen using the optical fiber radiation thermometer, however, it is obtained on the surface of the specimen using 2D temperature distribution.

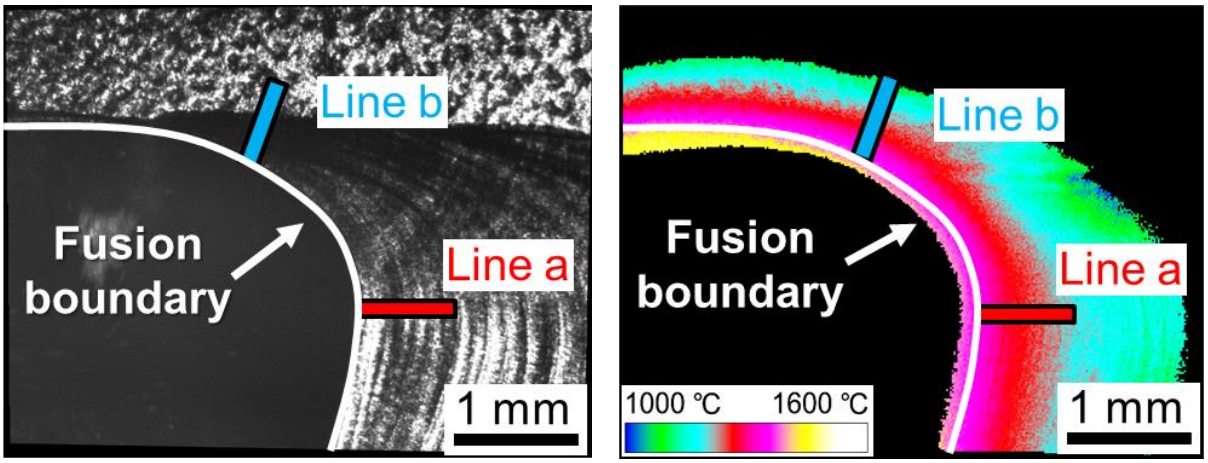

(a) In-situ observation image (b) 2D temperature distribution

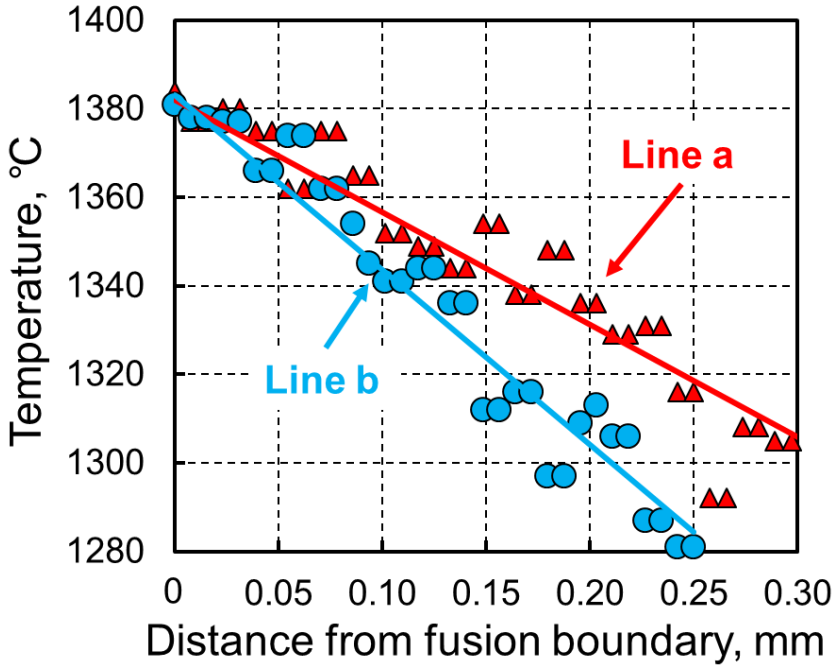

(c) Temperature gradients

Fig. 3.25 In-situ observation image, 2D temperature distribution image and temperature gradient during LBW at welding speed of 0.2 m/min

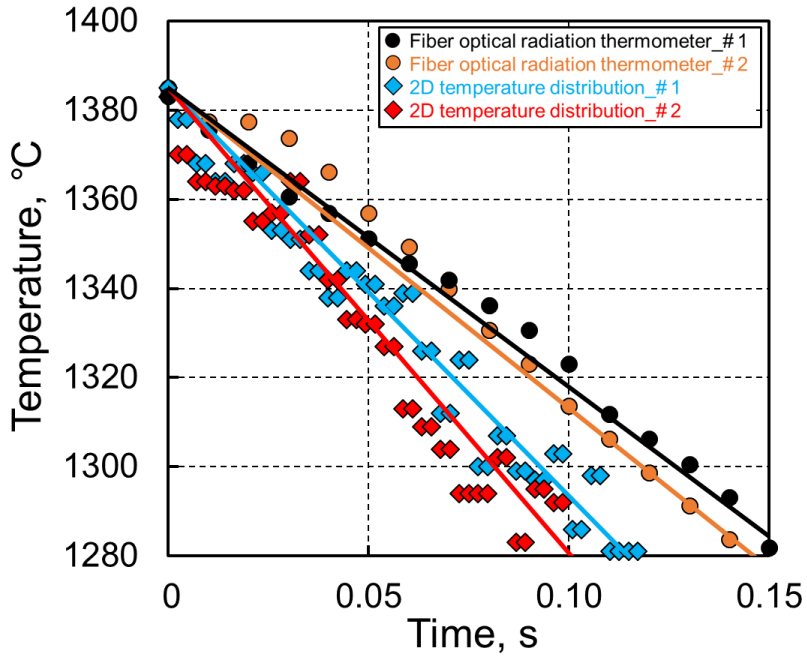

Fig. 3.26 Comparison of temperature profile between fiber optical radiation thermometer and 2D temperature distribution during LBW at welding speed of 0.2 m/min

3.6 Measurement of BTR

3.6.1 Using an optical fiber radiation thermometer

Figure 3.27 shows the measurement of the BTR using the optical fiber radiation thermometer during LBW at welding speed of 0.2 m/min. The average temperature gradient (based on the several trials) is obtained by the temperature profile multiplying welding speed and average liquidus temperature is 1385 °C. The maximum crack length along the centerline of the molten pool is expressed by a red bar, as shown in Fig. 3.27. Then, the BTR can be calculated that is the difference of the temperature of crack initial point (liquidus temperature) to crack end point (solidus temperature). Therefore, the average BTR is 88 °C under the saturated augmented strain of 2.8 and 4.3 % during LBW at welding speed of 0.2 m/min using the optical fiber radiation thermometer.

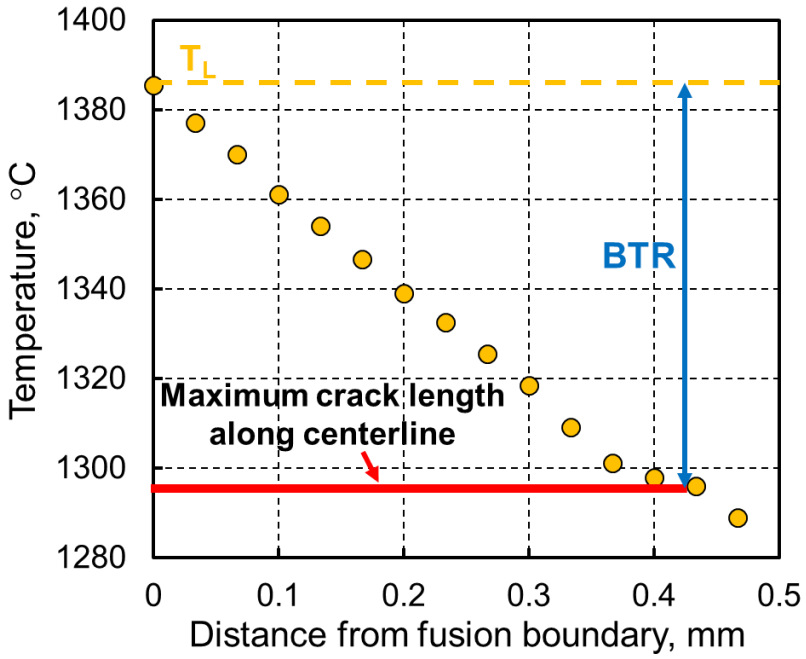

Fig. 3.27 Measurement of BTR using the optical fiber radiation thermometer during LBW at welding speed of 0.2 m/min

3.6.2 Using 2D temperature distribution

Using the measurement method of 2D temperature distribution, not only the crack along the centerline of the molten pool can be used to measure the temperature range,

but also the temperature range of each crack can be measured. And the BTR is the maximum temperature range for each crack. Figure 3.28 shows how to measure the temperature range for each solidification crack during LBW at welding speed of 0.2 m/min. The number of the solidification crack is counted using white number. Yellow line and black line are the fusion boundaries during Trans-Varestraint test and temperature measurement, respectively. Figure 3.28 a) shows solidification crack distribution and molten pool shape on the SEM image after Trans-Varestraint test during LBW. Because of no bending during the temperature measurement, the molten pool shape is different, as shown in Fig. 3.28 b). Therefore, in order to measure the temperature range of each crack, the crack should move due to different molten pool shapes. First, solidification crack distribution image superimposes on 2D temperature distribution image based on the same molten pool rear center, as shown in Fig. 3.28 c). Then, each solidification crack moves along vertical direction with the centerline of the molten pool until crack initial point touches the fusion boundary of 2D temperature distribution, as shown in Fig. 3.28 d). Finally, the temperature difference between initial and end points of the crack is the temperature range of each crack.

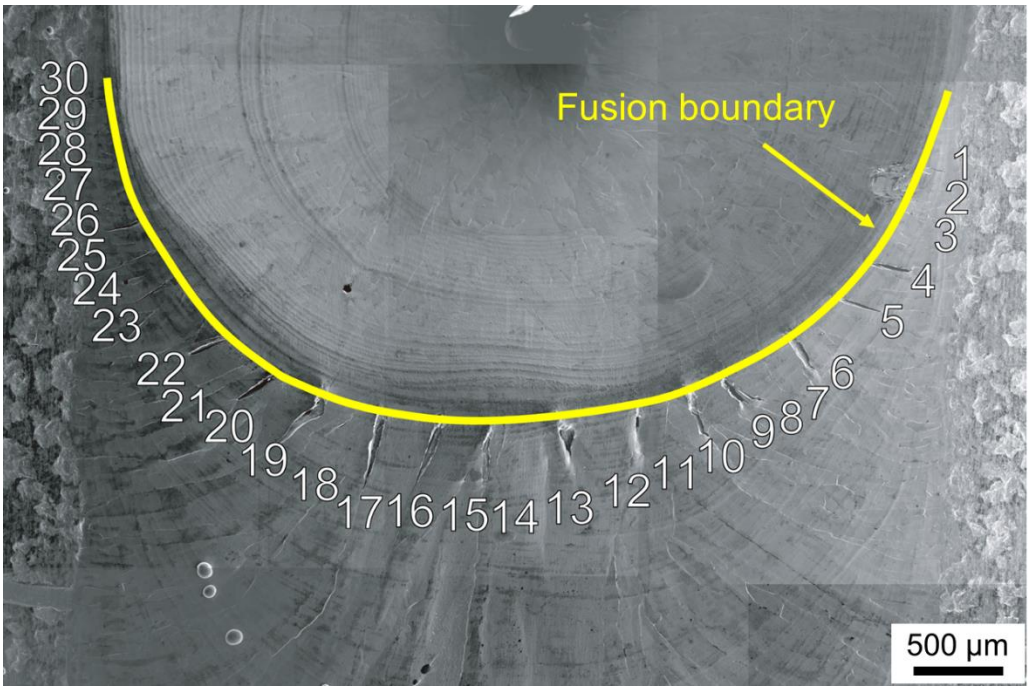

(a) SEM image of solidification crack distribution

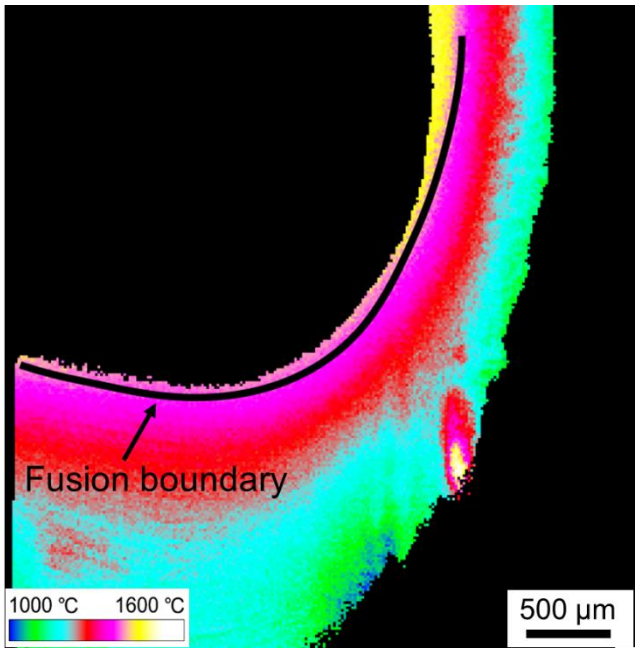

(b) 2D temperature distribution

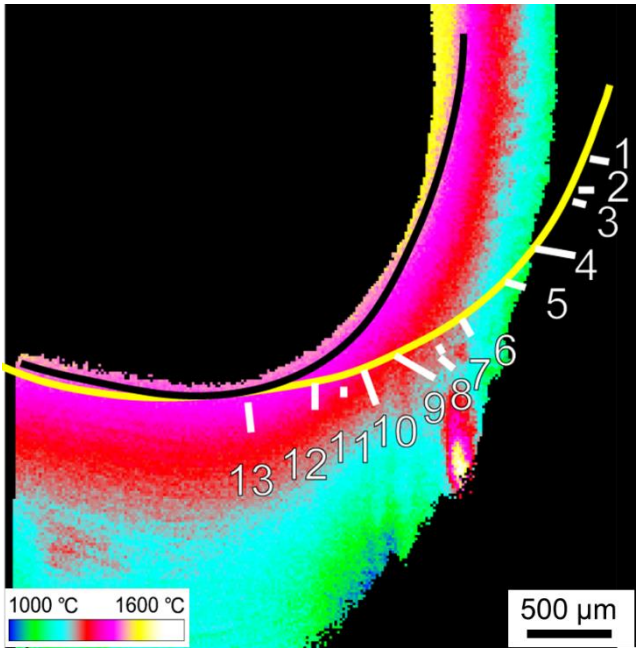

(c) Superimposed image of solidification crack distribution and 2D temperature distribution

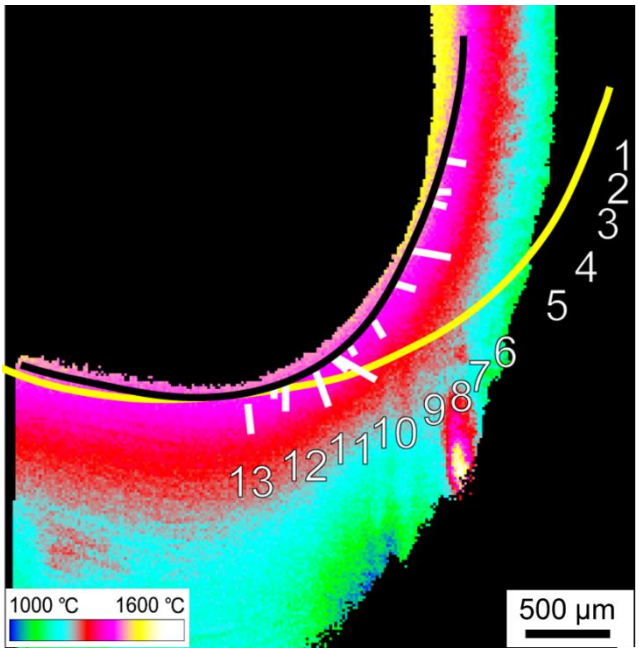

(d) Movement of solidification crack

Fig. 3.28 Measurement of temperature range of solidification crack during LBW at welding speed of 0.2 m/min

Figure 3.29 shows the temperature range corresponding to the solidification crack distribution in Figs. 3.9 and 3.10 during LBW at welding speed of 0.2 m/min under augmented strain of 4.3 %. The temperature range is composed of that of the crack and healing part length, as marked by black bar. However, it is difficult to confirm that the crack which initiates far away from fusion boundary is solidification crack. Thus, in order to obtain the true BTR, the temperature ranges of these cracks are eliminated, such as No. 7 and 8 crack in Fig. 3.29. Because the maximum crack length occurs at the rear center of the molten pool, thus the maximum temperature range appears at the center in the graph. In addition, some longer temperature ranges are at the sides even though owning short crack length as a contribution of high temperature gradient at the sides of the molten pool. The average BTR is 107 °C under the saturated augmented strain of 2.8 and 4.3 % during LBW at welding speed of 0.2 m/min using 2D temperature distribution. Therefore, the BTR could be measured by using Trans-Varestraint test during LBW and 2D temperature distribution.

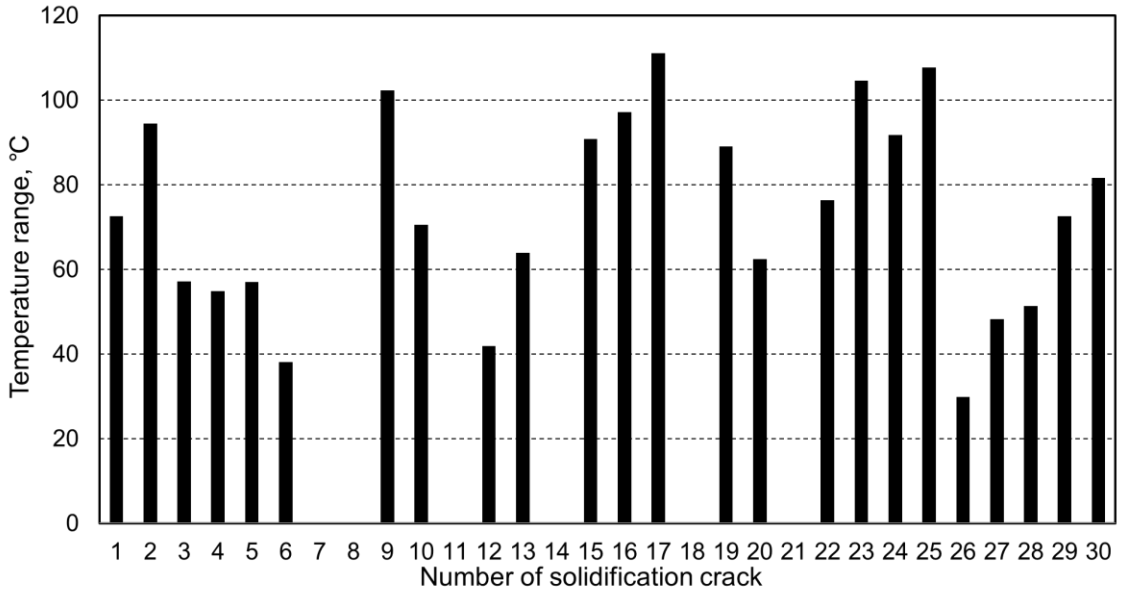

Fig. 3.29 Graph of temperature range of solidification crack during LBW at welding speed of 0.2 m/min under augmented strain of 4.3 %

By comparison, the average BTR using 2D temperature distribution is different from that using the optical fiber radiation thermometer due to different cooling rate. In the case of the Trans-Varestraint test, the crack length is measured from the surface of the specimen. Therefore, only if the temperature profile is obtained from the surface of the specimen, the BTR is more credible. As is mentioned, 2D temperature distribution can measure temperature from the surface, however, the optical fiber radiation thermometer measures temperature profile inside the specimen. Thus, the average BTR of 107 °C using 2D temperature distribution is more credible during LBW at welding speed of 0.2 m/min. However, the temperature range of the crack could be affected by scattered 2D temperature distribution. Thus, in next chapter, the verification of temperature measurement method for measuring the temperature range of the crack will be studied in detail to obtain more precise BTR.

3.7 Ductility Curve using 2D Temperature Distribution

Commonly, the ductility curve could be deduced by combining the temperature range of the maximum crack length with the corresponding augmented strain. However, multiple

tests must be carried out in order to obtain the relatively complete ductility curve tendency. Figure 3.30 shows the ductility curve tendency only using the maximum temperature range from 2D temperature distribution during LBW at welding speed of 0.2 m/min under different augmented strain. The ductility curve tendency can be obtained by drawing line cross the plot value of each maximum temperature range under different augmented strain. And the BTR is the widest temperature range inside the ductility curve. However, no crack specimen is not found so that the critical augmented strain for just causing solidification crack is not clear, as represented using dash line.

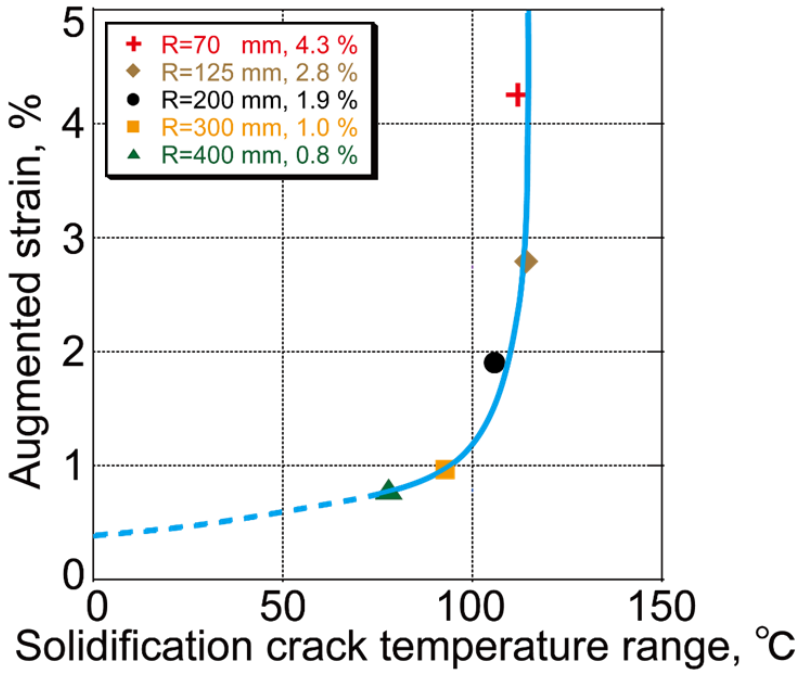

Fig. 3.30 Ductility curve tendency during LBW at welding speed of 0.2 m/min using the maximum temperature range but under different augmented strain

In the case of the Trans-Varestraint at low welding speed, the crack with the maximum crack length occurs at the rear center of the molten pool as a direct contribution of bending conventionally. While, it is considered that other cracks occur with some angles to the welding direction should be forced by the components of ε_x (vertical to the welding direction) and ε_y (parallel to the welding direction), as shown in Fig. 3.31. The red line expresses the fusion boundary and the yellow bar represents the crack length. The augmented strain for each solidification crack could be calculated:

$$\varepsilon = \varepsilon_x cos\theta + \varepsilon_y sin\theta \tag{3.8}$$

where ε_x and ε_y are the strain vertical and parallel to the welding direction measured by using strain gauge at the room temperature respectively, and θ is the angle between solidification crack and welding direction.

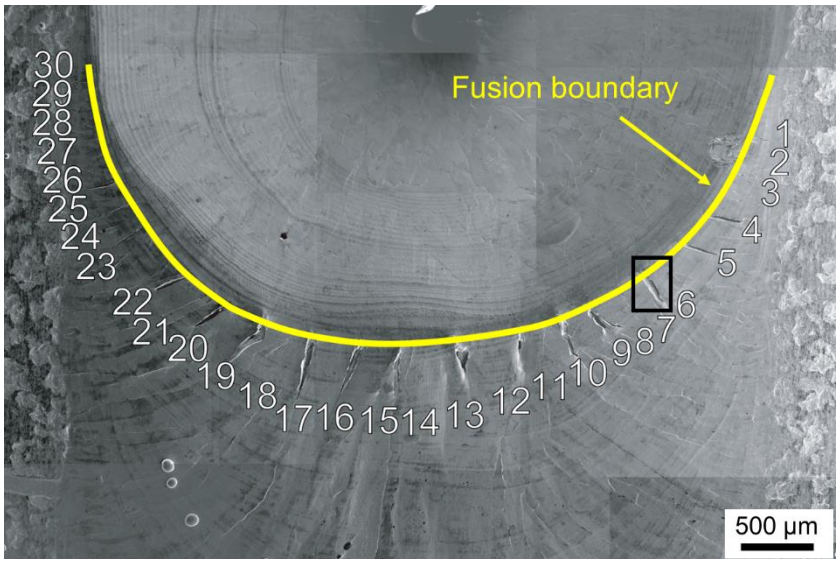

(a) SEM image of solidification crack distribution

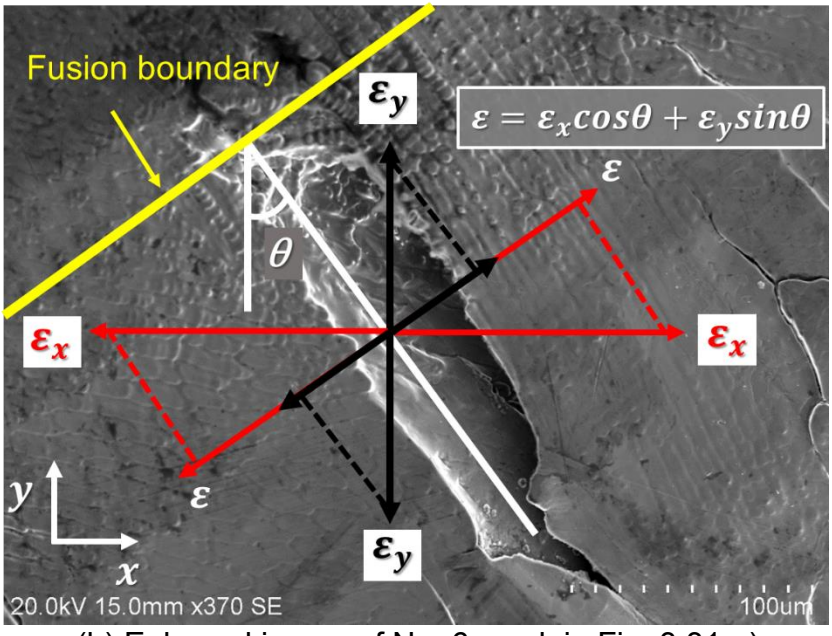

(b) Enlarged image of No. 6 crack in Fig. 3.31 a)

Fig. 3.31 Augmented strain for each solidification crack during LBW at welding speed of 1.0 m/min under augmented strain of 4.3 %

Figure 3.32 shows the ductility curve tendency by combining the temperature range with the augmented strain of each crack from 2D temperature distribution during LBW at welding speed of 0.2 m/min under the saturated augmented strain of 4.3 %. The temperature range of each crack on two specimens with the same condition is plotted on the graph. The tendency is done by drawing the curve covering all of the plot value. Inside the curve, the widest temperature range is the BTR and the occurrence of solidification crack is relatively easy when the strain is higher than the critical augmented strain in its corresponding temperature range during solidification. By comparison, the shapes of two ductility curve tendencies are similar, which proves that the precise ductility curve tendency could be obtained by using only one test based on the use of each crack length and temperature under the saturated augmented strain. However, when the crack occurs vertical to the welding direction the augmented strain is not clear. Therefore, in the future, in order to obtain the precise ductility curve using the Trans-Varestraint test during LBW, this issue should be overcome by improving the technology of measuring local critical strain during the occurrence of solidification crack at high temperature region.

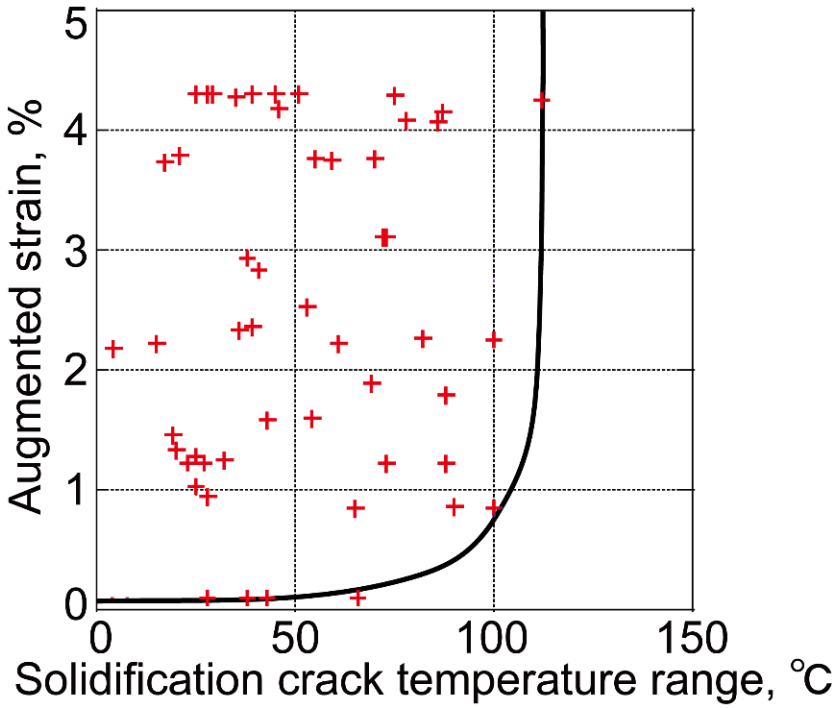

Fig. 3.32 Ductility curve tendency during LBW at welding speed of 0.2 m/min using temperature range of each crack but only under augmented strain of 4.3 %

3.8 Summary

In this chapter, Trans-Varestraint test during LBW and measurement method of 2D temperature distribution were developed and employed originally to evaluate solidification cracking susceptibility. The obtained conclusions are as follows:

1. Trans-Varestraint test during LBW was developed. First, the specimen was fixed on the bending block. When the trailing edge of the molten pool moved to the center of the specimen, the bending strain was applied on the specimen as laser heat source stop, leading to the occurrence of the cracking. Especially, due to high cooling rate during LBW, the fast bending with the speed of about 350 mm/s (yoke movement) was required that testing machine and fiber laser were accurately synchronized. In addition, a high speed camera was set up vertical to the center of the specimen for capturing the molten pool shape after the occurrence of the solidification crack.
2. The number density of solidification crack and total crack length per bead width using LBW were nearly the same as those using GTAW at welding speed of 0.2 m/min. The results showed that the different heat sources between LBW and GTAW had a small influence on the solidification cracking susceptibility at low welding speed of 0.2 m/min.
3. The temperature profile could be obtained by inserting an optical fiber radiation thermometer into the molten pool and the liquidus temperature could be derived from judging the time by setting synchronization between a thermometer and a high speed camera during LBW at welding speed of 0.2 m/min.
4. Measurement method of 2D temperature distribution by using a multi-sensor camera could be employed to measure the temperature range of each crack during LBW at welding speed of 0.2 m/min.
5. The BTR could be measured by using an optical fiber radiation thermometer and 2D temperature distribution during LBW at welding speed of 0.2 m/min, respectively. However, the BTR was more credible using 2D temperature distribution because the measured temperature profile and crack length were both from the surface of the specimen.
6. By combining the Trans-Varestraint test during LBW with 2D temperature distribution, the ductility curve tendency could be obtained by drawing the curve

covering all of the temperature range of the crack only under the saturated augmented stain. In addition, this ductility curve tendency was nearly the same as that using traditional method under different augmented strain.

Chapter 4

Effect of Welding Speed on Solidification Cracking Susceptibility during Laser Beam Welding

4.1 Introduction

In order to improve the efficiency and productivity of the industries during laser beam welding (LBW), one of the important key is to increase welding speed. Solidification behavior and thermal strain depend on the welding speed, thus, an increase in welding speed could influence the change of solidification cracking susceptibility. Therefore, the solidification cracking susceptibility must be under the discussion during LBW at different welding speeds.

High temperature ductility curve composed of the local critical strain and brittleness temperature range (BTR) can quantitative evaluate solidification cracking susceptibility. Generally, solidification crack occurs within the BTR because the ductility decreases in this range. In addition, when the strain is lower than the critical strain during solidification, the crack would not occur. However, when higher than the critical strain, solidification crack tends to occur more easily. Therefore, it is better to study both of the local critical strain and BTR in order to evaluate solidification cracking susceptibility comprehensively and precisely.

Shinozaki group has already developed U type hot cracking test with LBW to measure the local critical strain [4]. They evaluated the effect of different welding speeds on solidification cracking susceptibility of type 310S stainless steel during LBW using U type hot cracking test with in-situ observation [16]. With an increase in welding speeds from 0.4 to 1.6 m/min, the local critical strain tended to decrease. However, the advantage of U type hot cracking test is just to measure the local critical strain but it is no capable of measuring the BTR.

Until now, there is little evaluation method to obtain the BTR during LBW. Therefore, the authors developed laser Trans-Varestaint test in order to obtain the BTR for

evaluating solidification cracking susceptibility precisely, as introduced in Chapter 3. Meanwhile, Saida group also developed laser Trams-Varestraint test and reported that the BTR tended to decrease with increasing welding speeds from 0.6 to 2.4 m/min for type 310S stainless steel [49]. However, the BTR was measured by employing a thermocouple with the relatively lower response rate. Thus, the result was no less accurate by using this method.

Therefore, the objective of this chapter is to obtain the more precise and credible BTR measured by Trans-Varestraint test during LBW and 2D temperature distribution, and finally to evaluate the effect of welding speed on solidification cracking susceptibility quantitatively. First, solidification crack distributions are evaluated after Trans-Varestraint test during LBW at different welding speeds. The solidifying microstructure using liquid Sn quenching is observed for understanding the phenomena of solidification crack distributions at different welding speeds. Then, the number density of solidification crack and total crack length per bead width, as one of the important factors for evaluating solidification cracking susceptibility, are investigated. Next, in order to obtain the BTR, the precise temperature profile must be measured. However, although the optical fiber radiation thermometer with a high response rate is employed, the problem of the temperature measurement still exists. Thus, the measurement method of 2D temperature distribution is also used to measure the true BTR. Due to the scatter temperature distribution, the applicability and accuracy of temperature measurement method of 2D temperature distribution for measuring temperature range of the crack is investigated quantitatively. Then, the precise BTR could be obtained by combining Trans-Varestraint test during LBW with the measurement method of 2D temperature distribution at different welding speeds. Finally, the effect of welding speed on solidification cracking susceptibility for type 310S stainless steel is evaluated during LBW by combining the measured BTR with the local critical strain (Kadoi et al. data [16]), comprehensively.

4.2 Materials Used and Experimental Conditions

Type 310S stainless steel with the dimension of $110^{l} \times 110^{w} \times 5^{t}$ mm was used in order to evaluate solidification cracking susceptibility quantitatively during LBW at different welding speeds. Table 4.1 shows the chemical composition of the used materials. The

welding condition of LBW is shown in Table 4.2. Fiber laser is employed as a heat source. Welding speed is changed from 0.2 to 2.0 m/min as an experimental parameter. Laser powers are 1.0 kW for 0.2 m/min, 1.85 kW for 1.0 m/min, 2.25 kW for 1.5 m/min and 2.5 kW for 2.0 m/min for obtaining half penetration in the thickness direction, respectively. Laser spot size is 0.4 mm (just focus) and laser head is tilted 25° to the welding direction for avoiding interference of a high speed camera setup. Ar gas is blown at 50 l/min onto the surface and rear of the specimen during LBW.

Table 4.1 Chemical compositions of type 310S stainless steel (mass %)

C	Si	Mn	P	S	Ni	Cr	Co	Fe
0.04	0.43	0.96	0.019	0.001	20.13	25.19	0.09	Bal.

Table 4.2 LBW conditions

Welding speed, m/min	0.2	1.0	1.5	2.0
Laser power, kW	1.0	1.85	2.25	2.5
Laser spot size, mm	0.4 (just focus)			
Laser irradiation angle, deg	25			
Ar shielding gas, l/min	50			

4.3 Solidification Crack Distribution

Figure 4.1 shows the SEM image of solidification crack distribution after Trans-Varestraint test during LBW at different welding speeds from 0.2 to 2.0 m/min under augmented strain of 2.8 %. The fusion boundary is represented by using a red line and the number of the crack is presented by using yellow color in the image. Figure 4.2 shows the graph of solidification crack distribution. At low welding speed of 0.2 m/min, the shape of the molten pool is a smooth curve and the longest solidification crack initiates from the trail edge of the backend center of the molten pool, as shown in Figs. 4.1 a) and 4.2 a). While, in the case of high welding speed more than 1.0 m/min, the shape of the molten pool looks like a teardrop. The higher welding speeds lead to more elongated shapes,

from elliptical to teardrop, because of changes, such as the rate and direction, in the heat flow conditions. Moreover, longer solidification crack tends to occur at the sides of the molten pool, as shown in Figs. 4.1 b) - d) and 4.2 b) - d).

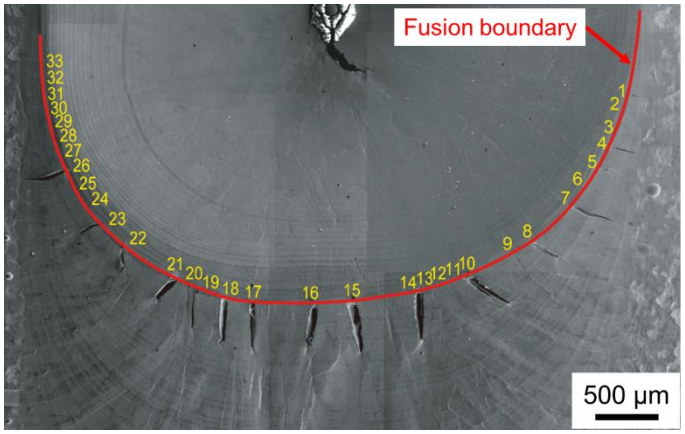

(a) Welding speed of 0.2 m/min

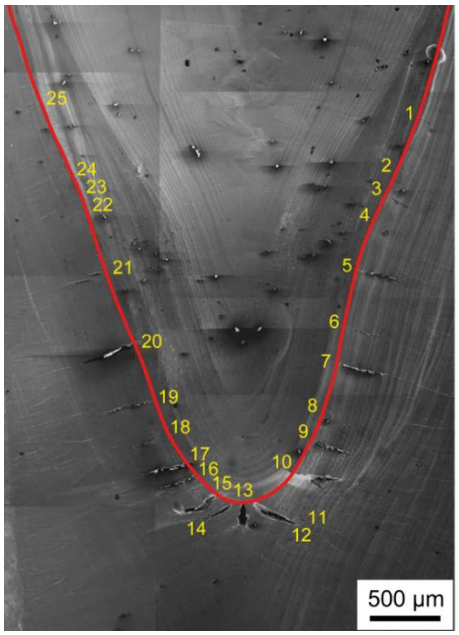

(b) Welding speed of 1.0 m/min

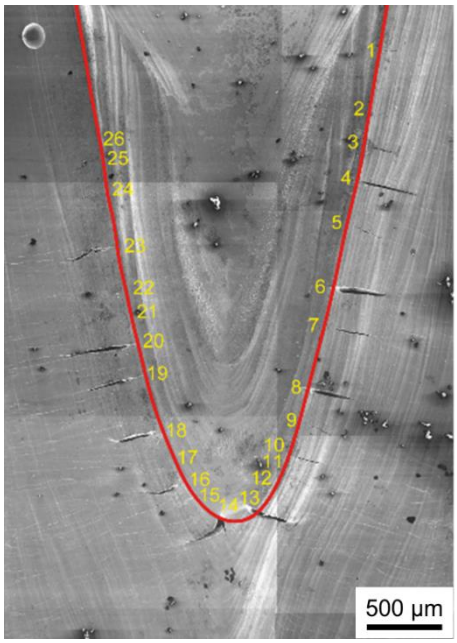

(c) Welding speed of 1.5 m/min

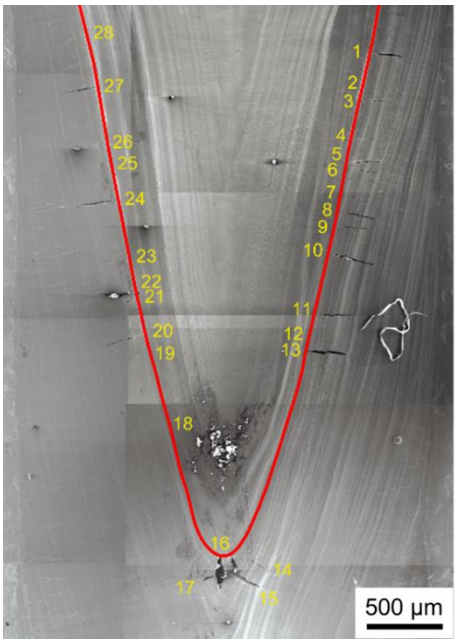

(d) Welding speed of 2.0 m/min

Fig. 4.1 SEM image of solidification crack distribution during LBW at different welding speeds under augmented strain of 2.8 %

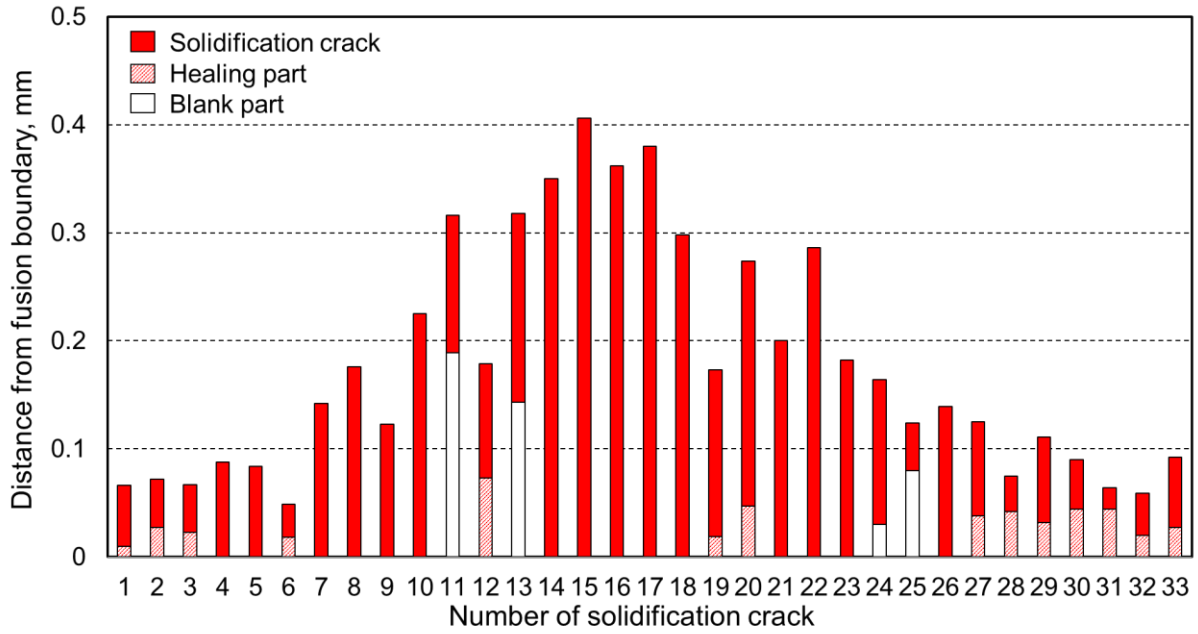

(a) Welding speed of 0.2 m/min

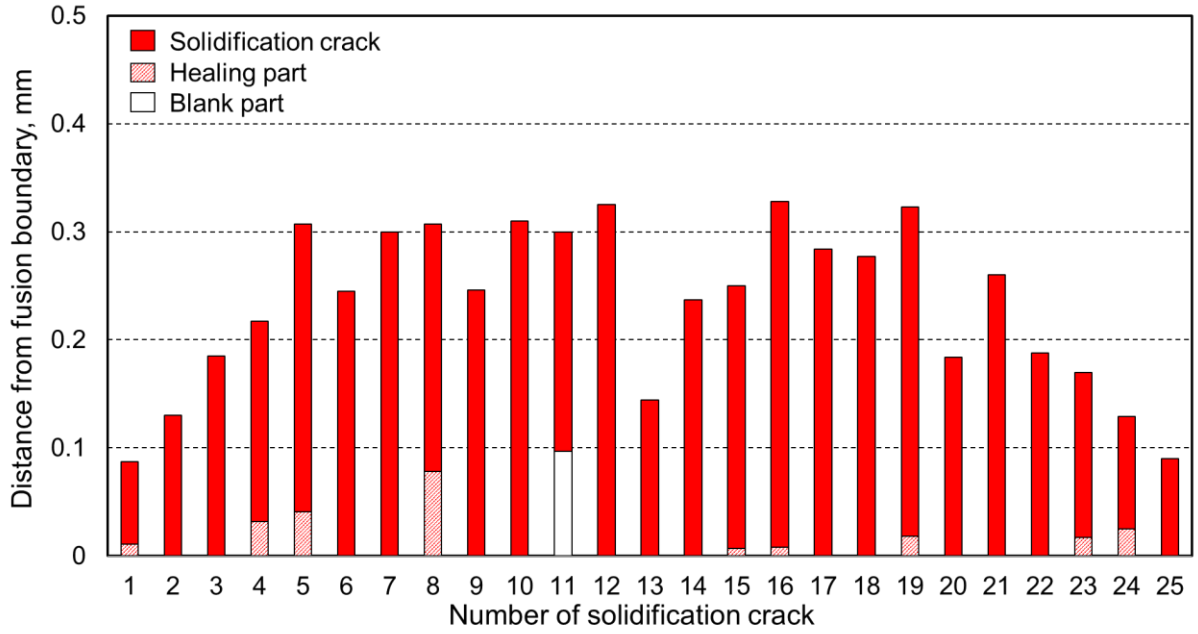

(b) Welding speed of 1.0 m/min

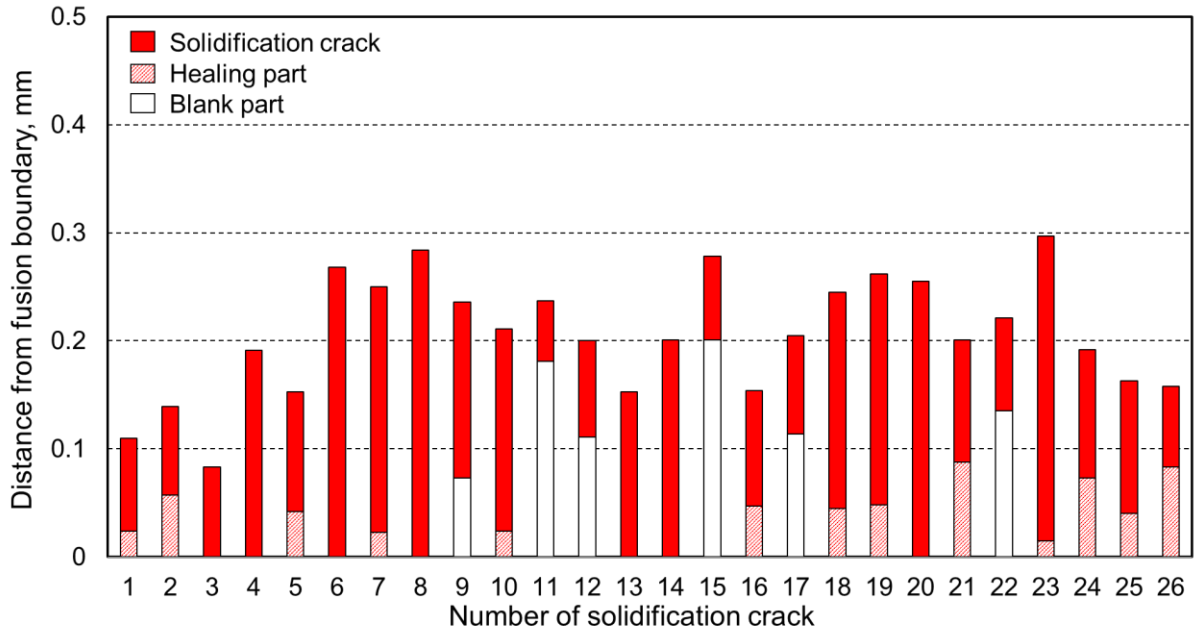

(c) Welding speed of 1.5 m/min

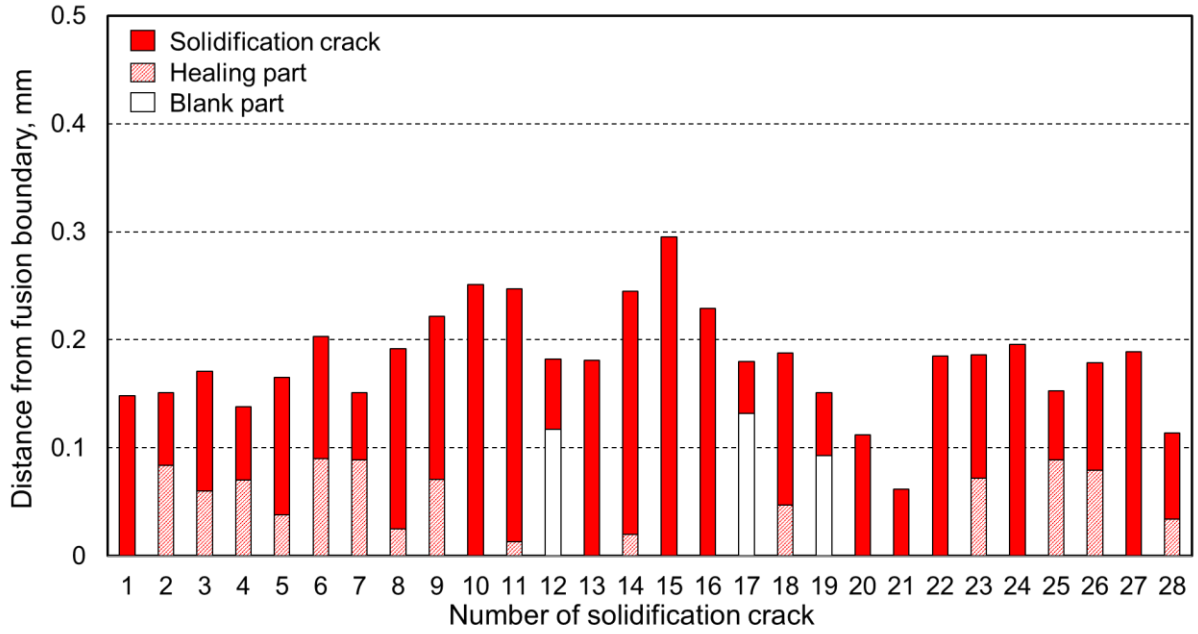

(d) Welding speed of 2.0 m/min

Fig. 4.2 Graph of solidification crack distribution during LBW at different welding speeds under augmented strain of 2.8 %

4.4 Solidifying Microstructure

In order to investigate different phenomena of solidification crack distributions after Trans-Varestraint test during LBW at different welding speeds, the solidifying microstructure is obtained by using liquid Sn quenching. The experimental process is as follows: First, the solidifying microstructure is obtained by pouring liquid Sn toward the trailing edge of the molten pool during LBW. After testing, the specimen is polished by using emery papers and diamond grinding in order to remove the covered liquid Sn and obtain the surface microstructure. Then, the specimen is electrically etched by 10 % oxalic acid for 10 s with 10 V for stainless steel. Finally, the surface of the specimen is observed by using an optical microscope for obtaining the solidifying microstructure.

Figures 4.3 and 4.4 show the solidifying microstructure along the surface and cross the section by liquid Sn quenching during LBW at welding speeds of 0.2 and 1.0 m/min, respectively. During solidification, the dendrite grows along the easy growth direction which is perpendicular to the solid-liquid interface and parallel to the heat flow direction. M. Rappaz et al. reported that the shape of the molten pool could influence the dendrite growth during welding solidification [74]. In Fig. 4.3 a) and b), the shape of the molten pool is a smooth curve and the dendrites grow along the surface during LBW at low welding speed of 0.2 m/min. Cross section solidifying microstructure at the rear center of the molten pool further proves that the dendrites grow along the surface, as shown in Fig. 4.3 c) and d). However, the molten pool changes into a teardrop shape and the tail becomes very shallow at high welding speed of 1.0 m/min, as shown in Fig. 4.4 a) and c) respectively. By combining Fig. 4.4 b) and d), the main direction of dendrites growth is from the bottom to the surface with a large angle to the surface at the rear center of the molten pool, however, at the sides of molten pool some dendrites grow with a small angle to the surface vertical to the fusion boundary. Meanwhile, the similar solidifying microstructures also present at higher welding speeds of 1.5 and 2.0 m/min. Thus, these different dendrite growth types cause that the long solidification crack occurs at the rear center of the molten pool in the case of low welding speed but the solidification crack with longer length appears at the sides of the molten pool in the case of high welding speed using Trans-Varestraint test during LBW.

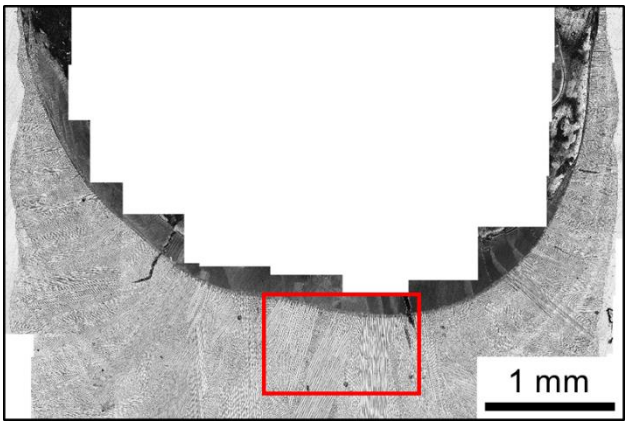

(a) Surface microstructure

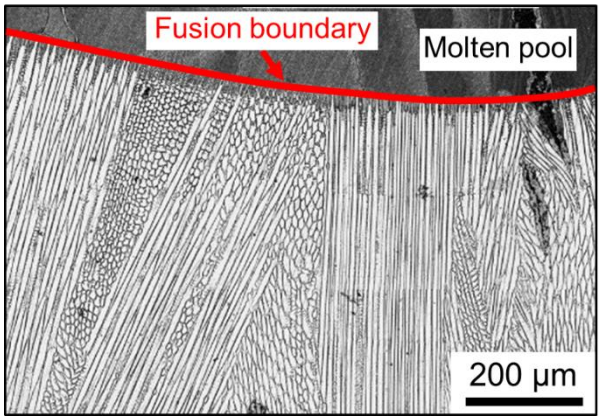

(b) Enlarged image in Fig. 4.3 a)

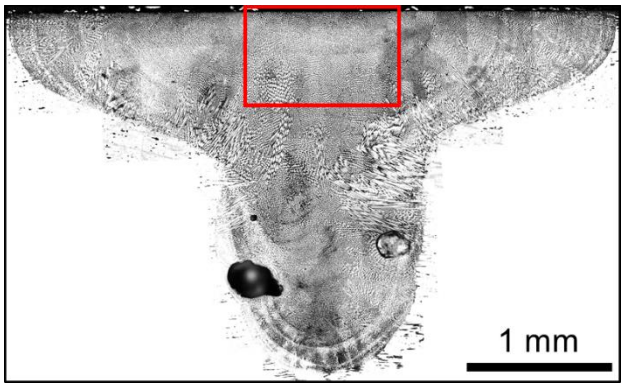

(c) Cross section microstructure

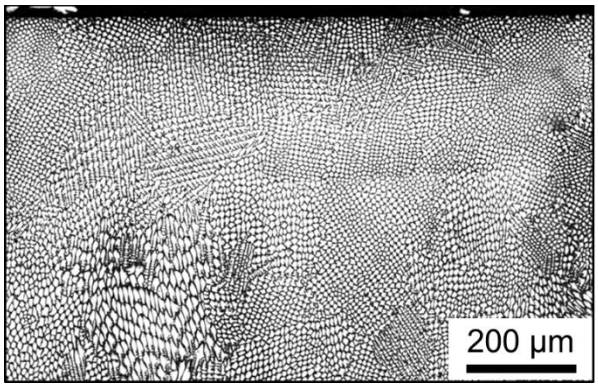

(d) Enlarged image in Fig. 4.3 c)

Fig. 4.3 Solidifying microstructure during LBW at welding speed of 0.2 m/min

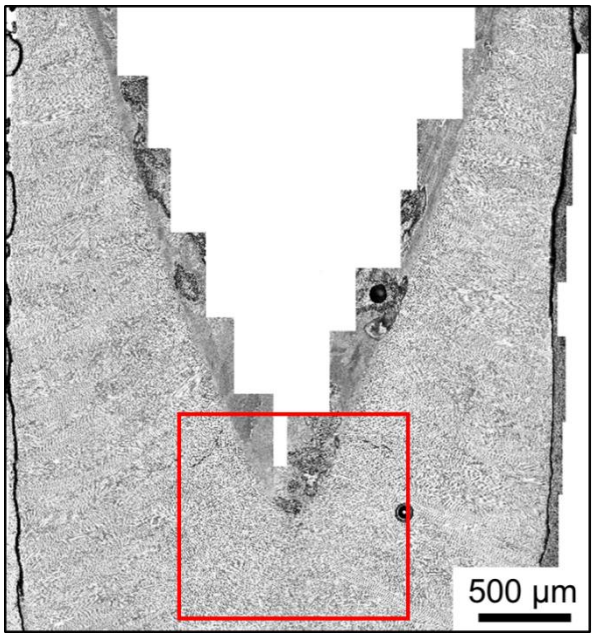

(a) Surface microstructure

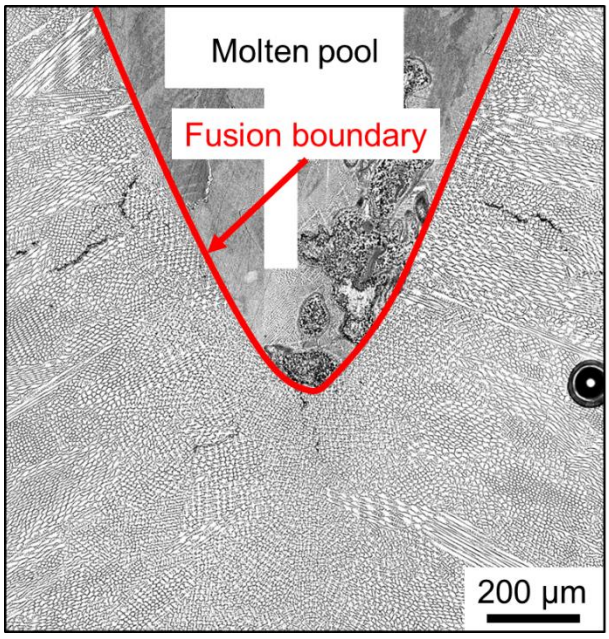

(b) Enlarged image in Fig. 4.4 a)

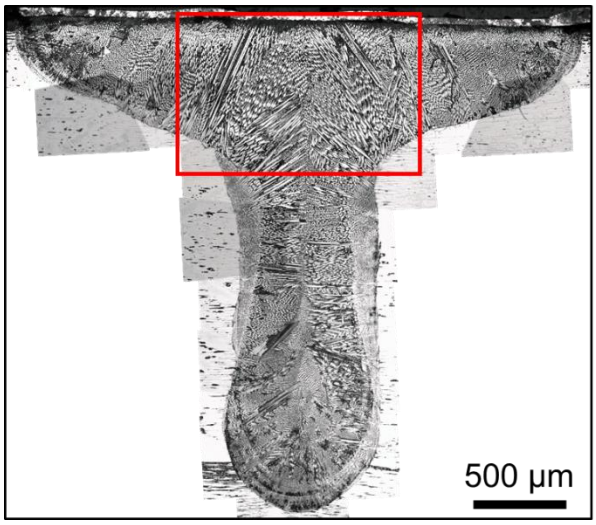

(c) Cross section microstructure

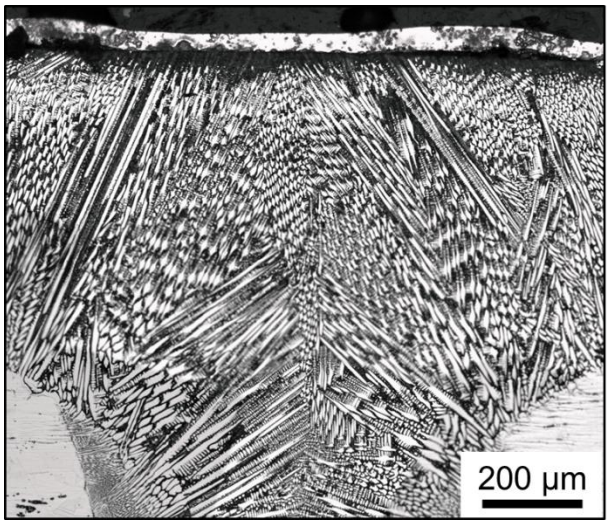

(d) Enlarged image in Fig. 4.4 c)

Fig. 4.4 Solidifying microstructure during LBW at welding speed of 1.0 m/min

4.5 Influence of Welding Speed on Number and Length of Crack

Figure 4.5 shows the number of the solidification crack and total crack length during LBW at different welding speeds from 0.2 to 2.0 m/min. Under low augmented strain of 1.0 %, the number of the solidification crack around the molten pool is around 10 and the total crack length is almost less than 2.0 mm regardless of low welding speed and high welding speed. With increasing augmented strain from 1.0 to 2.0 %, there is obvious rising trend in both the values. When the augmented strain is more than 2.0 %, the tendency of both the values remains unchanged. This means the augmented strain of 2.0 % is the saturated value in this type 310S stainless steel. In addition, a high welding speed tends to decrease in the number of the solidification crack and total crack length, but the difference of both the values is relatively small at different welding speeds from 0.2 to 2.0 m/min. Under the saturated augmented strain, the number of solidification crack is about 30 at welding speed of 0.2 m/min and this value is nearly 25 at high welding speed of 2.0 m/min. While, in the case of the total crack length, the difference of these values is within around 1.0 mm at different welding speeds.

As is mentioned, the number of the solidification crack and total crack length depend on the bead width. Therefore, in order to evaluate solidification cracking susceptibility precisely, the influence of the bead width should be eliminated. Figure 4.6 shows the measured bead width after Trans-Varestraint test during LBW at each welding speed under the saturated augmented strain of 2.8 and 4.3 %. There is a tendency of decrease in the bead width from low welding speed of 0.2 m/min to high welding speed of 2.0 m/min. However, the difference of the bead width is not so obvious at high welding speeds from 1.0 to 2.0 m/min.

Figure 4.7 shows the number of the solidification crack and total crack length divided by the bead width during LBW at each welding speed under the saturated augmented strain of 2.8 and 4.3 %. The number density of solidification crack is approximately 6 and total crack length per bead width is around 1.1 at welding speed of 0.2 m/min. With increasing welding speed from 0.2 to 1.0 m/min, both the values of the number density of the solidification crack and total crack length per bead width have a tendency of increase. However, both the values keep a little fluctuated at welding speeds from 1.0 to 2.0 m/min.

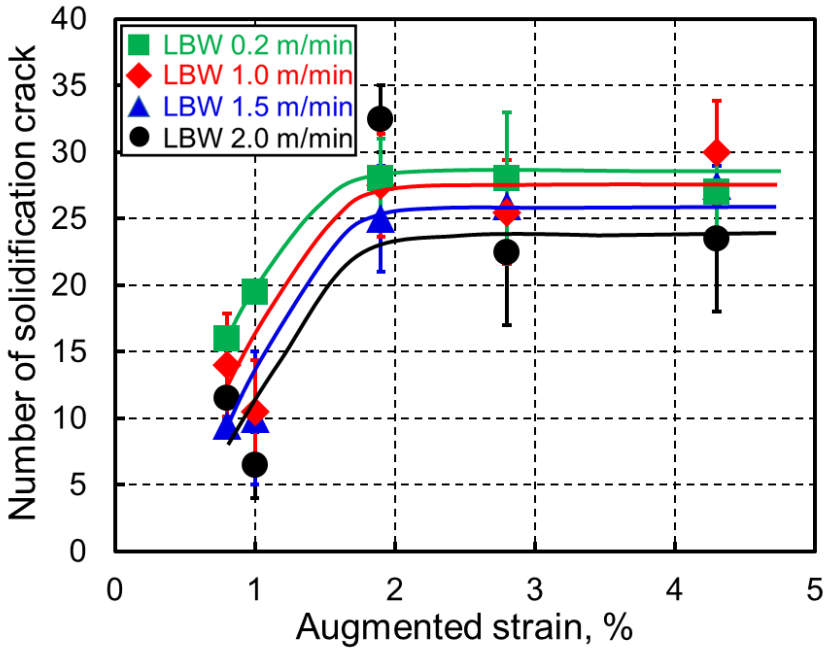

(a) Number of solidification crack

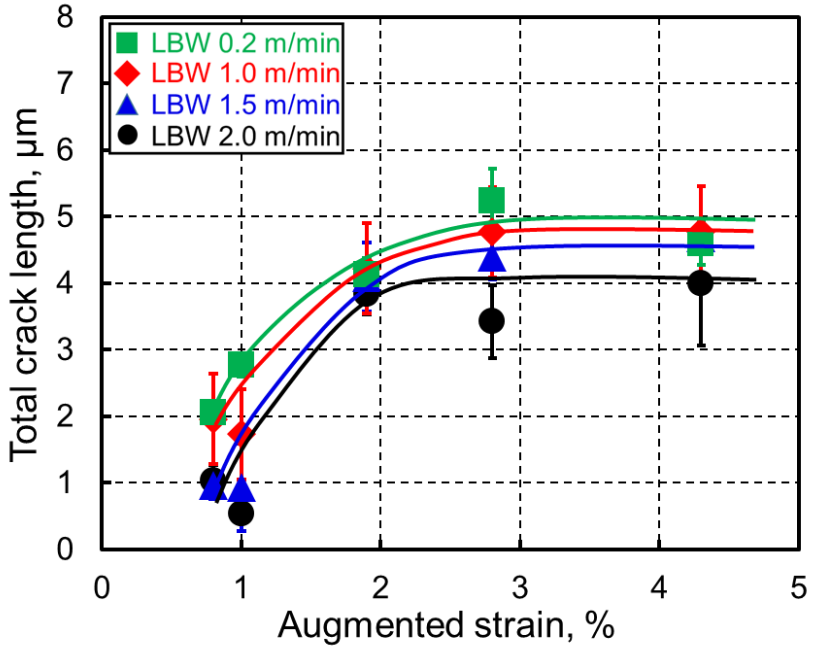

(b) Total crack length

Fig. 4.5 Number of solidification crack and total crack length during LBW at different welding speeds

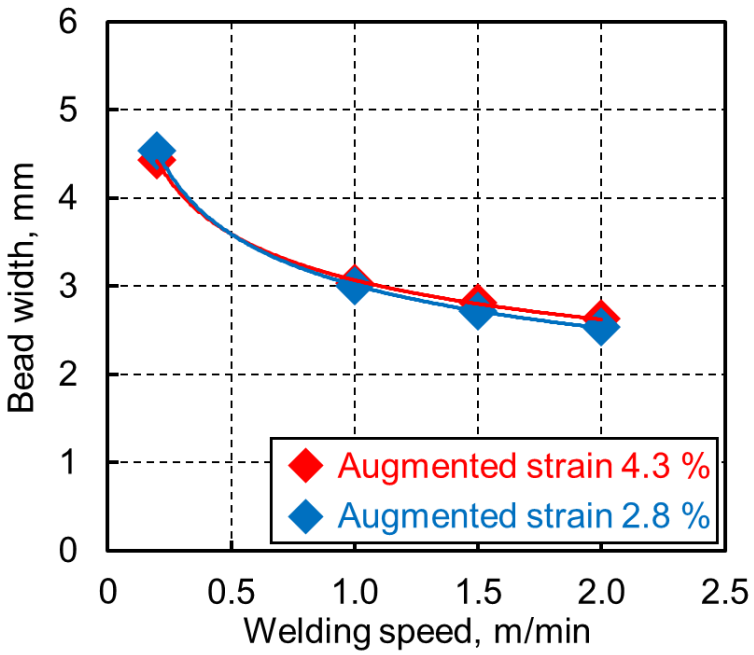

Fig. 4.6 Bead width after Trans-Varestraint test during LBW at different welding speeds

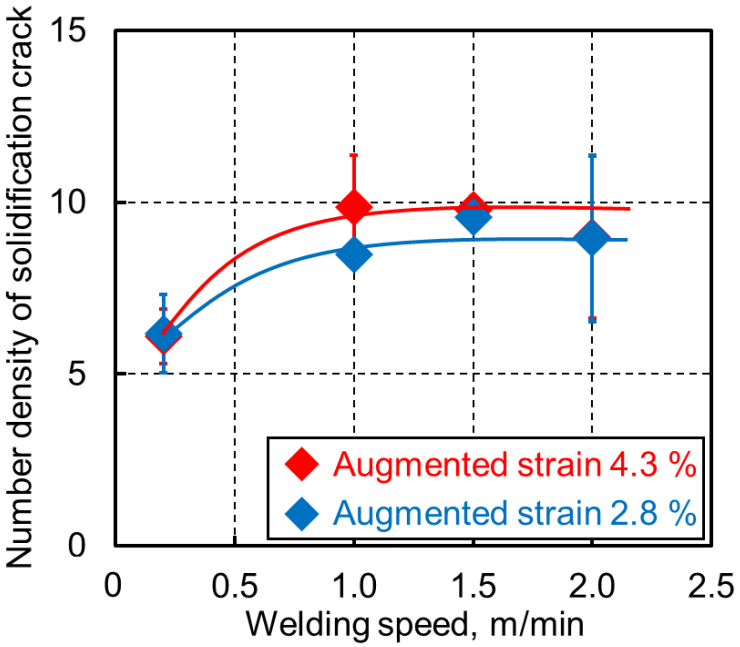

(a) Number density of solidification crack

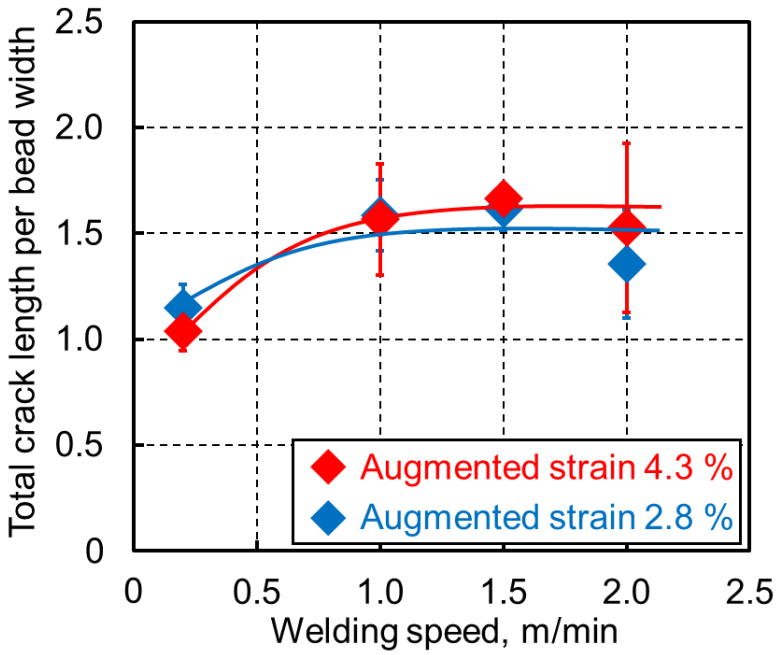

(b) Total crack length per bead width

Fig. 4.7 Number density of solidification crack and total crack length per bead width during LBW at different welding speeds

4.6 Measurement of Temperature Profile during LBW

4.6.1 Using an optical fiber radiation thermometer

In order to obtain the BTR for evaluating solidification cracking susceptibility quantitatively, it is necessary to measure temperature profile during LBW at each welding speed. Until now, there is few studies on measuring the temperature profile directly during LBW at high welding speed. Saida group employed a thermocouple with low response rate to measure temperature during LBW at high welding speed, thus, the result was no less accurate [49]. Thus, the author et al. tried to use an optical fiber radiation thermometer with a high response rate to measure temperature during LBW at each welding speed. The measurement method of the optical fiber radiation thermometer has already been introduced in Chapter 3 and the result shows that the temperature profile can be measured during LBW at welding speed of 0.2 m/min. However, the influence of

high welding speed on the temperature measurement using the optical fiber radiation thermometer still does not be discussed in detail.

Figure 4.8 shows the temperature profiles by inserting the optical fiber radiation thermometer into the molten pool during LBW at welding speed of 1.5 m/min. The sampling frequency of this optical fiber radiation thermometer is just 100 Hz, thus, the plot number of the temperature profile in the solidification temperature range is a little during LBW at high welding speed. By four trials, the temperature profiles are various, emerging two different kinds of cooling curves. Moreover, the liquidus temperature changes from 1405 to 1430 °C and the difference is 25 °C. Therefore, it is hard to measure the precious temperature by inserting the optical fiber radiation thermometer into the molten pool during LBW at high welding speeds.

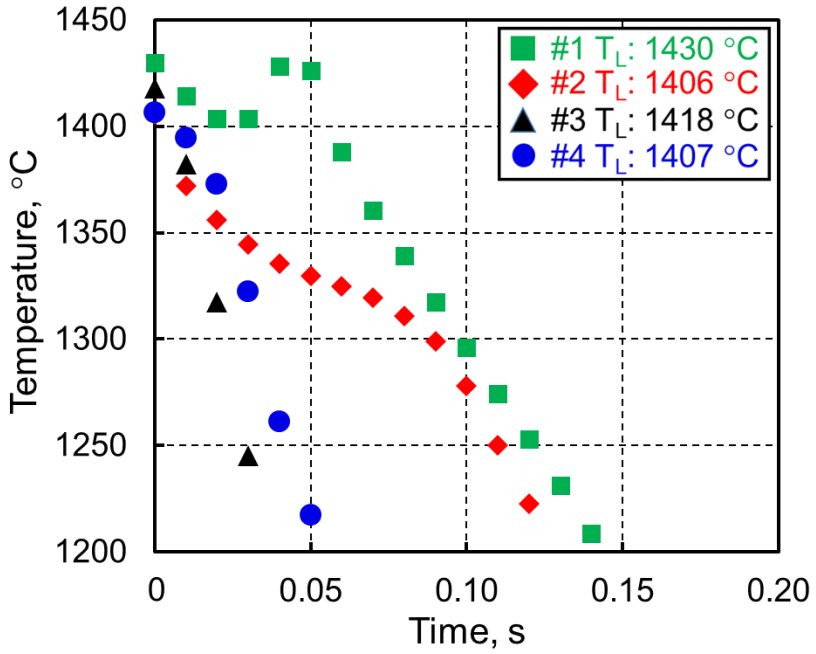

Fig. 4.8 Temperature profiles during LBW at welding speed of 1.5 m/min

In addition, the other problems of the temperature measurement by inserting the optical fiber radiation thermometer into the molten pool are as follows: First, the measured temperature profile is influenced by the size of the measurement tip of the optical fiber radiation thermometer. The molten pool becomes smaller during LBW at high welding

speed. Thus, the measured temperature should be considered as not only liquid metal but also the optical fiber radiation thermometer when inserting it into the narrow and shallow molten pool. In addition, the maximum crack length is around 0.30 mm during LBW at welding speed from 1.0 to 2.0 m/min, but the diameter of the measurement tip of the thermometer is 0.25 mm. Therefore, it is difficult to measure the precious temperature profile during LBW at high welding speed. Second, it is affected by variation of solidification behavior. When inserting the optical fiber radiation thermometer, the solidification behavior around the measurement tip of the thermometer would be deviated from the actual solidification. For example, the ripple line changes into disordered around the measurement tip on the weld bead, as shown in Fig. 4.9. Third, it is restricted to be only one measurement direction that is along welding direction. From the SEM image of solidification crack distribution during LBW at high welding speeds, the longest crack always occurs at the side of molten pool. Thus, in order to measure the real BTR, the temperature range along the maximum crack length should be obtained. However, the optical fiber radiation thermometer has no ability of measuring the temperature profile along any direction.

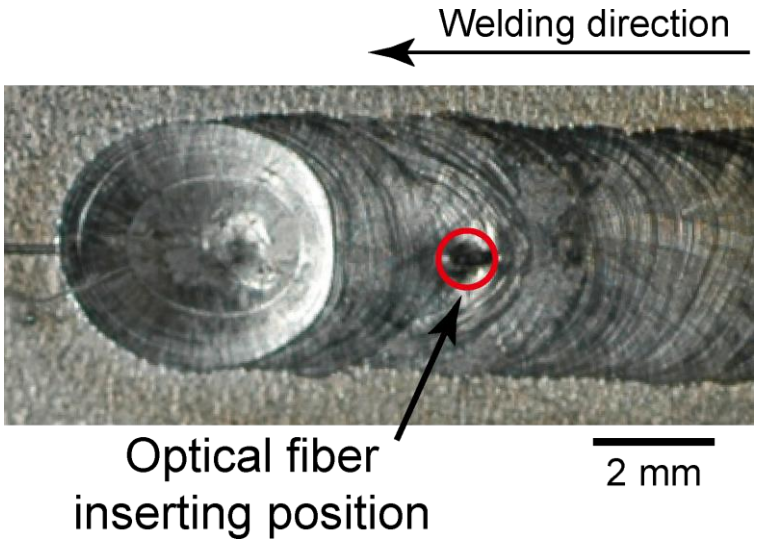

Fig. 4.9 Variation of solidification behavior around measurement tip of the optical fiber radiation thermometer during LBW at welding speed of 0.2 m/min

4.6.2 Using 2D temperature distribution

The above discussion proves that the measurement method of 2D temperature distribution is one of the suitable candidates to measure the true BTR. Sound 2D temperature distribution just can be employed to measure the temperature range of each crack. Thus, in order to select the most suitable 2D temperature distribution, several 2D temperature distribution images are chosen from different frame images at different welding speeds and corresponding temperature gradient along the centerline of the molten pool are compared, as shown in Fig. 4.10. The white line in each image presents the centerline of the molten pool. For each welding speed, 2D temperature distribution images are from intermediate and nearly terminal frame images during the temperature measurement because the molten pool becomes more stable. It can be found that the temperature gradients from different frame images are nearly similar. This result proves that the sound 2D temperature distribution can be obtained using these images and can be employed to measure the temperature range of each crack.

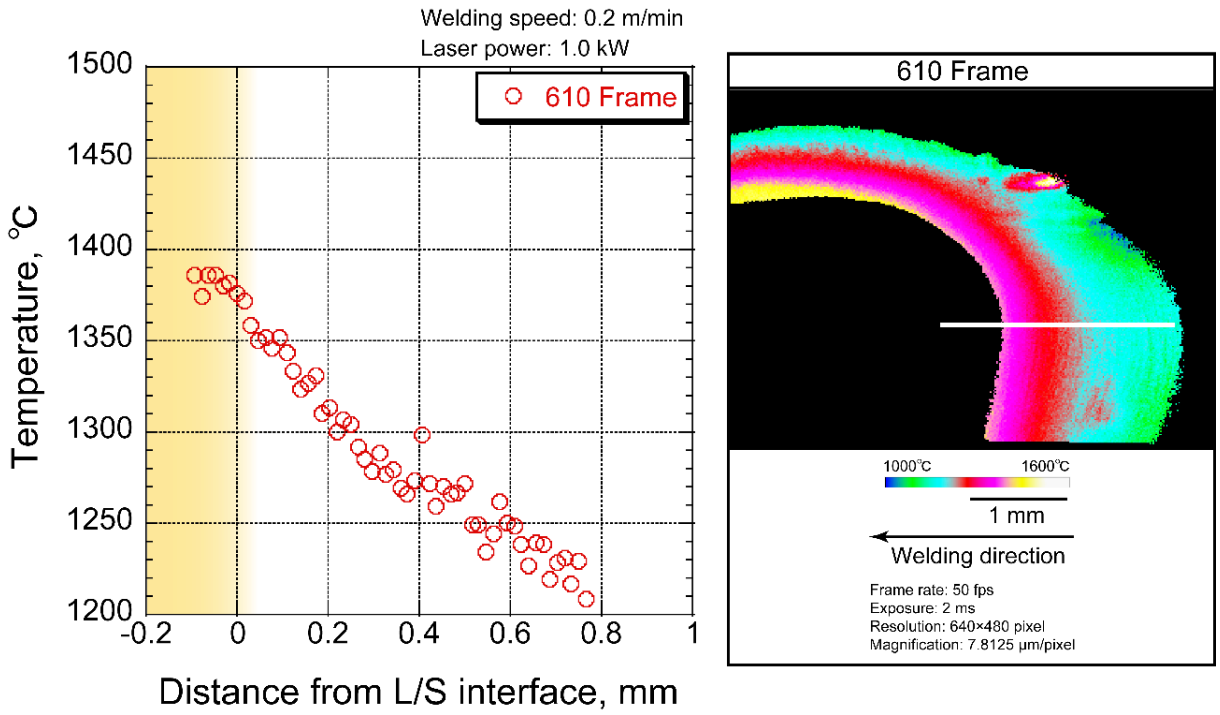

(a) Welding speed of 0.2 m/min

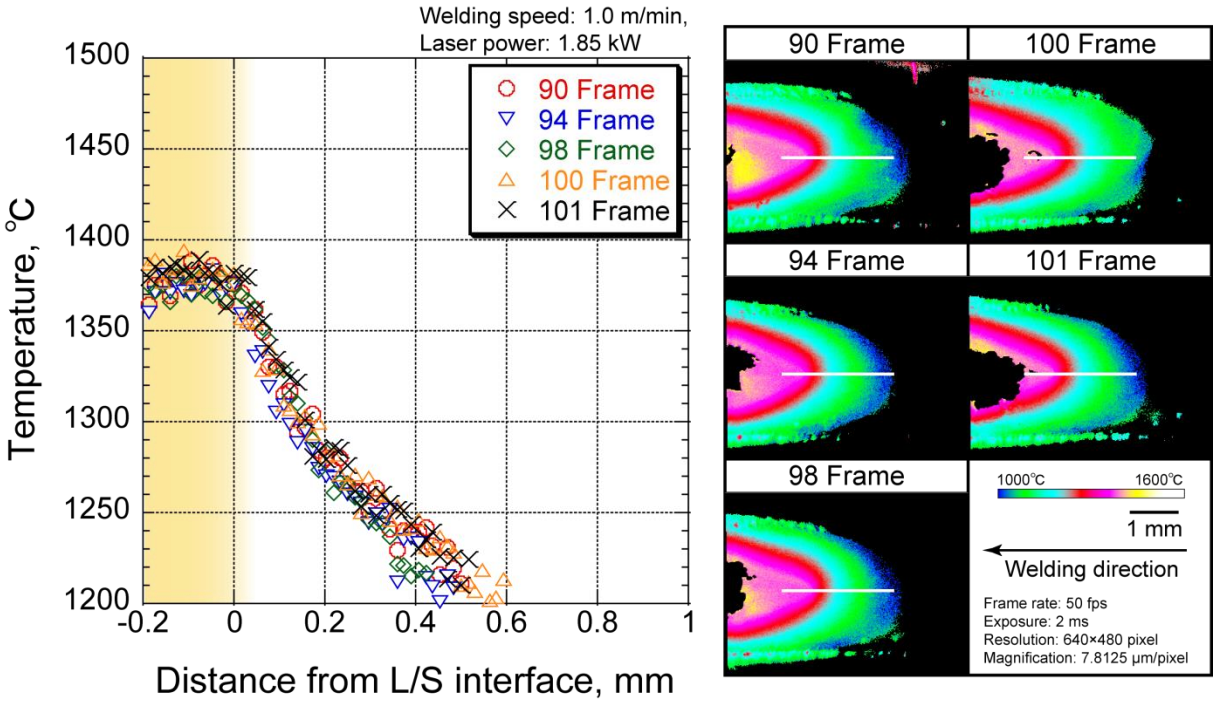

(b) Welding speed of 1.0 m/min

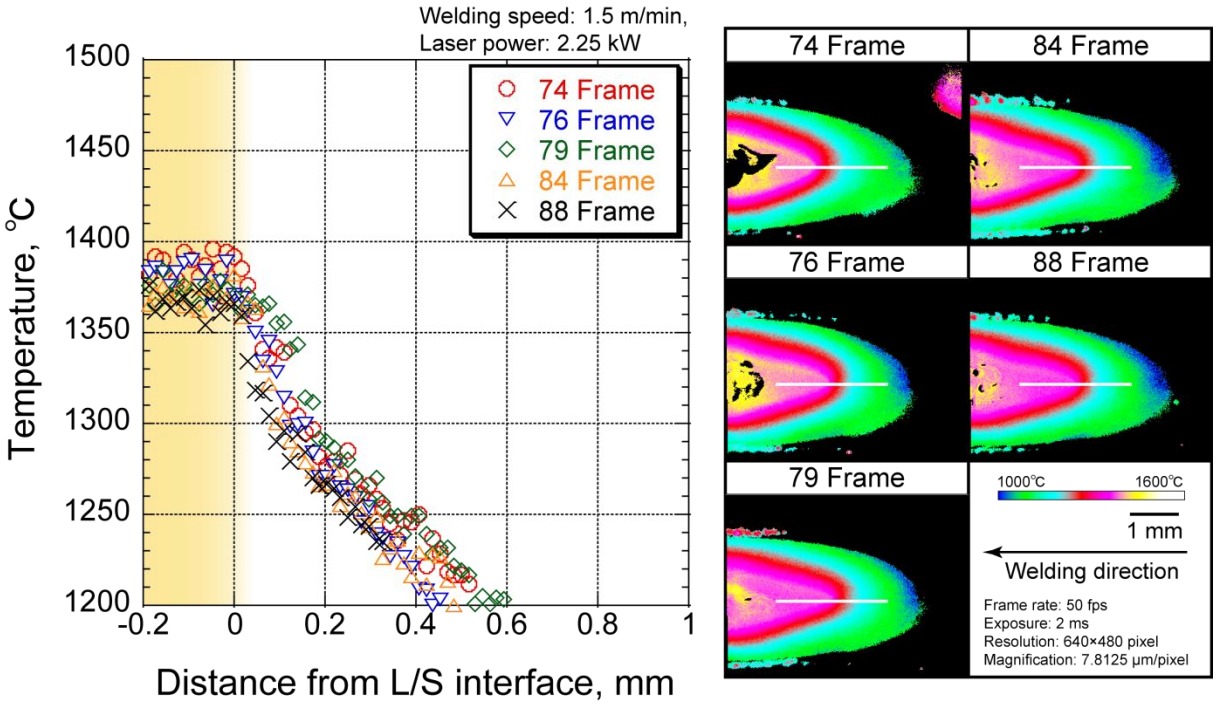

(c) Welding speed of 1.5 m/min

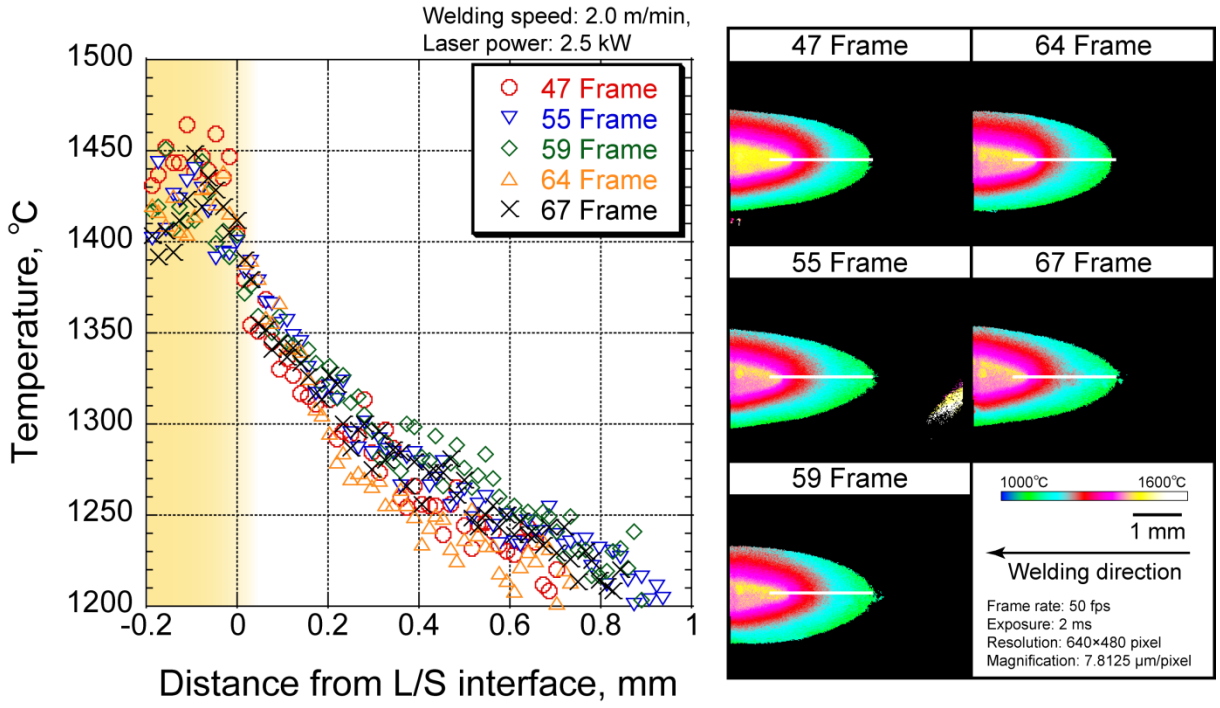

(d) Welding speed of 2.0 m/min

Fig. 4.10 Temperature gradient along the centerline of molten pool using different frame images from the multi-sensor camera during LBW at different welding speeds

4.7 Measurement of BTR using 2D Temperature Distribution

4.7.1 Temperature measurement method of 2D temperature distribution for measuring temperature range of the crack

In order to obtain the true BTR, the applicability and accuracy of the temperature measurement method of 2D temperature distribution must be investigated quantitatively because the measured temperature range of the crack could be affected by the scattered 2D temperature distribution. Theoretically, the temperature range of the crack can be obtained by using temperature gradient of this crack multiplying its length. Therefore, it is necessary to evaluate and verify temperature gradient in the 2D temperature distribution.

Figure 4.11 shows the image about how to verify the temperature gradient in the 2D temperature distribution. The black curve presents the fusion boundary of the molten pool and the yellow bar expresses the position and direction of the measured temperature

gradient which is along the normal direction of the molten pool, as shown in Fig. 4. 11. These temperature gradients can be measured at the different angles to the welding direction from 0 to 90° since the shape of the molten pool is a smooth curve at low welding speed of 0.2 m/min, as is indicated in Fig. 4.11 a). However, due to a teardrop shape of the molten pool at high welding speed of 1.0 m/min, these temperature gradients could be obtained only at the angles to the welding direction of 0° and from 60 to 80° approximately, as shown in Fig. 4. 11 b). Similar results also appear at higher welding speeds of 1.5 and 2.0 m/min.

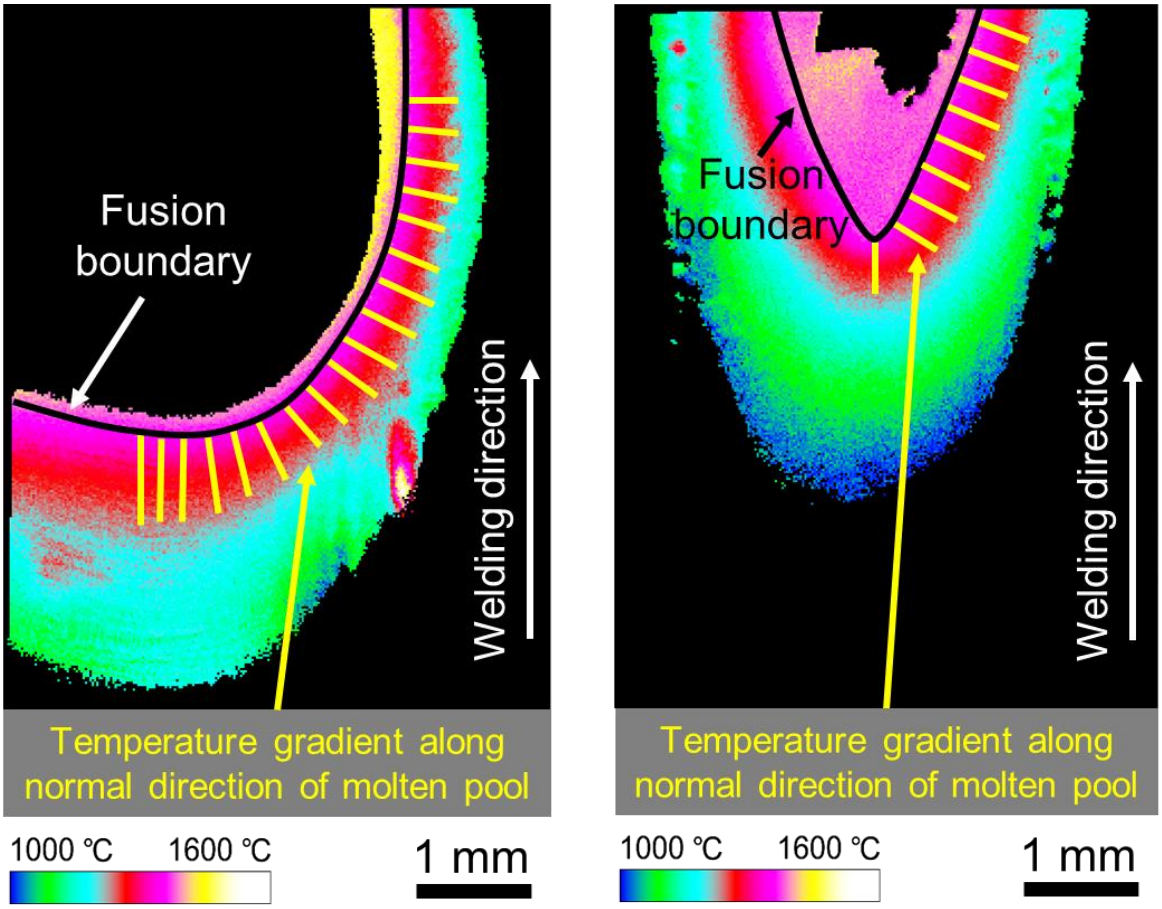

(a) Welding speed of 0.2 m/min (b) Welding speed of 1.0 m/min

Fig. 4.11 Image for measuring temperature gradient along the normal direction of molten pool

Figure 4.12 shows the relationship between the angle to the welding direction and temperature gradient along the normal direction of the molten pool during LBW at each welding speed. In Fig. 4.12, triangle, diamond and square represent the temperature gradients along the normal direction of the molten pool, which are measured vertical to the fusion boundary using different frame images of 2D temperature distribution in the steady state. Moreover, the regression curve is done by using the least square method.

In Fig. 4.12 a), at low welding speed of 0.2 m/min, the temperature gradients can be measured at different angles from 0 to 90°, as is mentioned in Fig. 4.11 a). With increasing the angle, the temperature gradient has a tendency of increase gradually. At the angle of 0°, the value is between 200 and 300 °C/mm. At the angle from 0 to 70°, the value mainly distributes between 300 and 400 °C/mm. At the higher angle from 70 to 90°, the value range is between 400 and 700 °C/mm. In Fig. 4.12 b), at high welding speed of 1.0 m/min, most of the values appear at the angle between 60 and 80° because of a teardrop molten pool, as is mentioned in Fig. 4.11 b). Moreover, the temperature gradient is nearly the same at low angle of 0° and high angle from 60 to 80°. Similar results also appear at higher welding speed of 1.5 and 2.0 m/min. Most of the temperature gradients along the normal direction of the molten pool mainly distribute in the range between 300 and 400 °C/mm approximately.

Figure 4.13 shows the relationship between the angle to the welding direction and the average temperature gradient along the normal direction of the molten pool during LBW at different welding speeds. Except for the average value at the angle of 0 and 90°, the other average values are obtained at each interval of 10°. For example, at welding speed of 0.2 m/min, the average temperature gradient at the angle of 55° is about 370 °C/mm which is the average value of the temperature gradients at the angle from 50 to 60°, as shown in Fig. 4.13. Also, the least square method is employed to analyze the curve fitting for each welding speed. With increasing the angle, the average temperature gradient increases at welding speed of 0.2 m/min. However, at welding speed from 1.0 to 2.0 m/min, the average value is nearly the same at low angle of 0° and high angle from 60 to 80°.

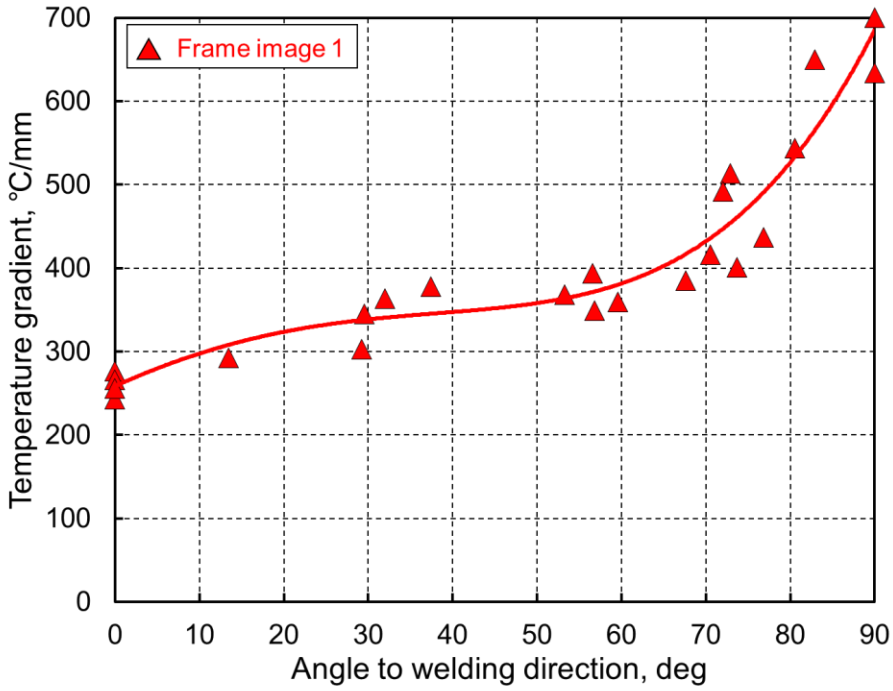

(a) Welding speed of 0.2 m/min

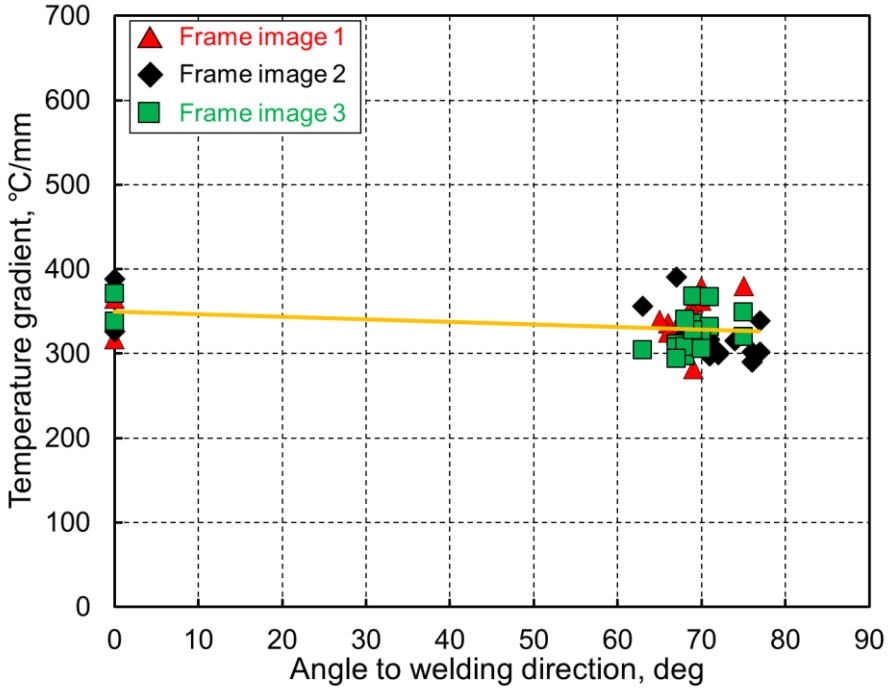

(b) Welding speed of 1.0 m/min

Fig. 4.12 Relationship between the angle to welding direction and temperature gradient along normal direction of molten pool during LBW

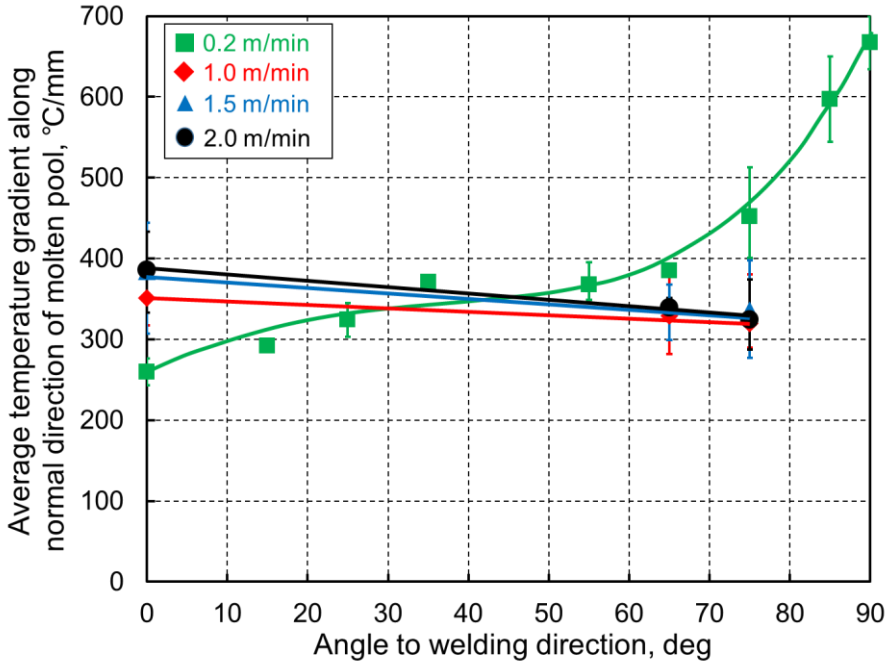

Fig. 4.13 Relationship between the angle to welding direction and average temperature gradient along normal direction of molten pool during LBW for each welding speed

Figure 4.14 illustrates the method to convert solidification crack length for obtaining the temperature range of the crack using the regression curve. Actually, the solidification crack (Black solid line) occurs with the angle θ to the welding direction, however, the crack is not always perpendicular to the fusion boundary, as shown in Fig. 4.1. While, the temperature gradient is along the normal direction of the fusion boundary in the regression curve in Figs. 4.11, 4.12 and 4.13. Thus, the crack should change into the one perpendicular to the fusion boundary, as is illustrated by black dash line. Then, the corresponding conversion length and the angel θ′ to the welding direction could be measured. Finally, the temperature range of each crack can be obtained through the conversion length of the crack multiplying the corresponding temperature gradient at the angel θ′ by using the regression curve.

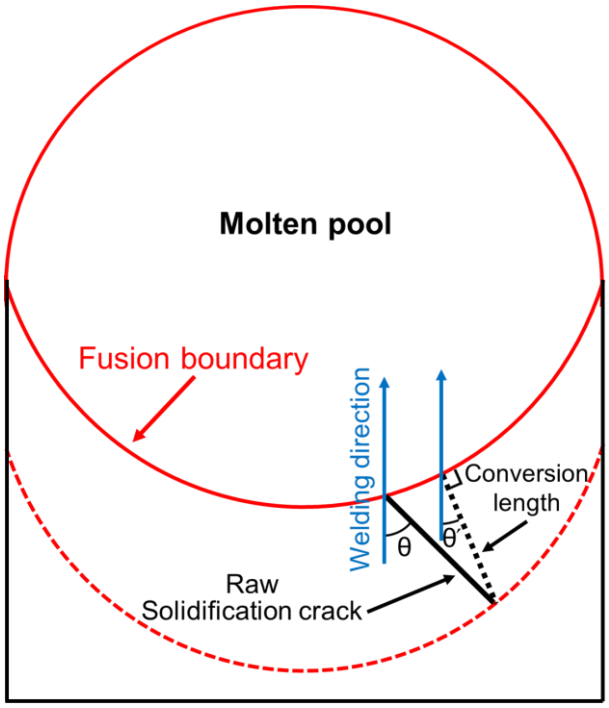

Fig. 4.14 Method to convert the length of solidification crack for obtaining temperature range of the crack

4.7.2 Temperature range of the crack

Figure 4.15 shows the corresponding temperature range of the crack at each welding speed in Figs. 4.1 and 4.2. As is mentioned, the temperature range is composed of that of the crack and healing part length totally marked by the black bar. However, it is difficult to confirm that the crack which initiates far away from fusion boundary is solidification crack. Therefore, in order to obtain the true BTR, the temperature ranges of these cracks are eliminated. At welding speed of 0.2 m/min, the maximum temperature range appears at the rear center of molten pool with the small angle to welding direction, as shown in Figs. 4.15 a) and 4.1 a). However, at high welding speeds, the maximum values distribute at the side of molten pool or with the large angle to the welding direction, as shown in Figs. 4.15 b) - d) and 4.1 b) - d). The maximum temperature ranges are always between 100 and 110 °C during LBW at different welding speeds from 0.2 to 2.0 m/min.

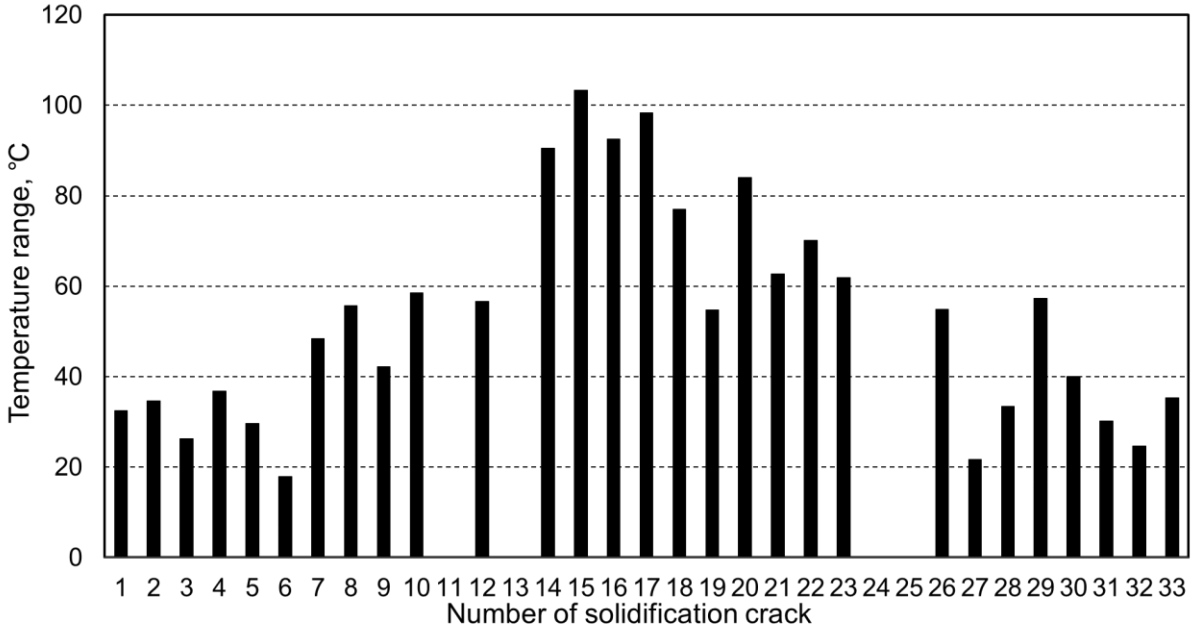

(a) Welding speed of 0.2 m/min

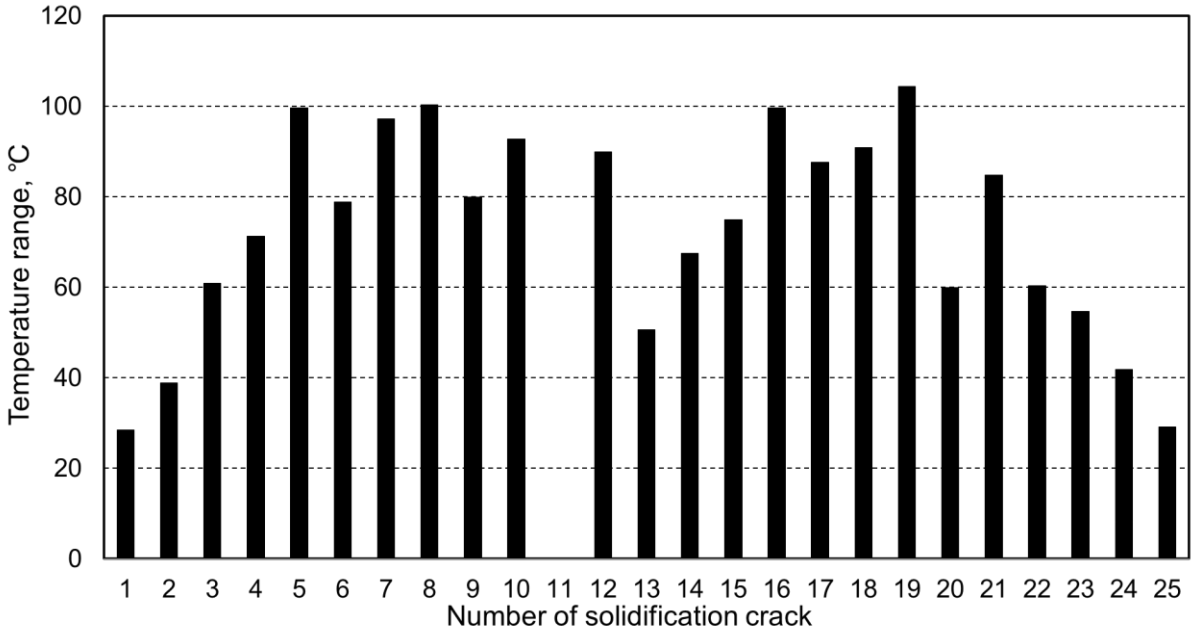

(b) Welding speed of 1.0 m/min

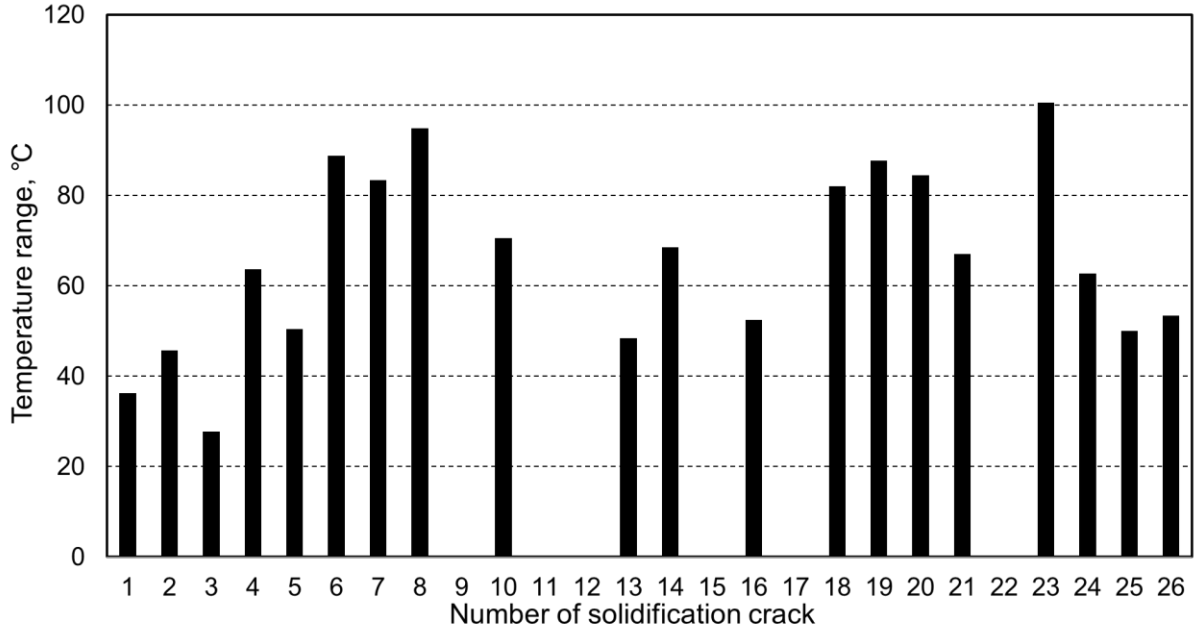

(c) Welding speed of 1.5 m/min

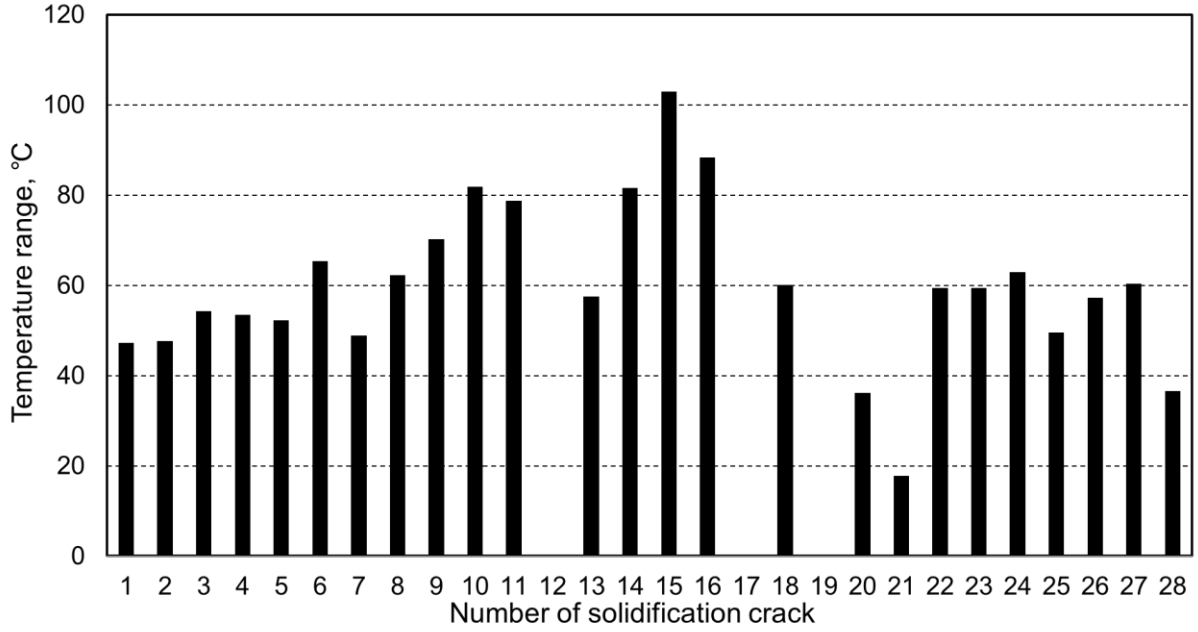

(d) Welding speed of 2.0 m/min

Fig. 4.15 Graph of temperature range of solidification crack during LBW at different welding speeds under augmented strain of 2.8 %

4.8 Ductility Curve for Each Welding Speed

Figures 4.16 and 4.17 shows the ductility curve tendency by combining the temperature range with the augmented strain of each crack from 2D temperature distribution during LBW at different welding speeds under the saturated augmented strain of 2.8 and 4.3 %, respectively. The temperature range of each crack for each welding speed is plotted on the graph in Fig. 4.16 corresponding to those of Figs. 4.1 and 4.15. As is mentioned in Chapter 3, this tendency is drawn by covering all of the plot value. Inside these tendency curves, the widest temperature range is the BTR and this value is almost the same for each welding speed.

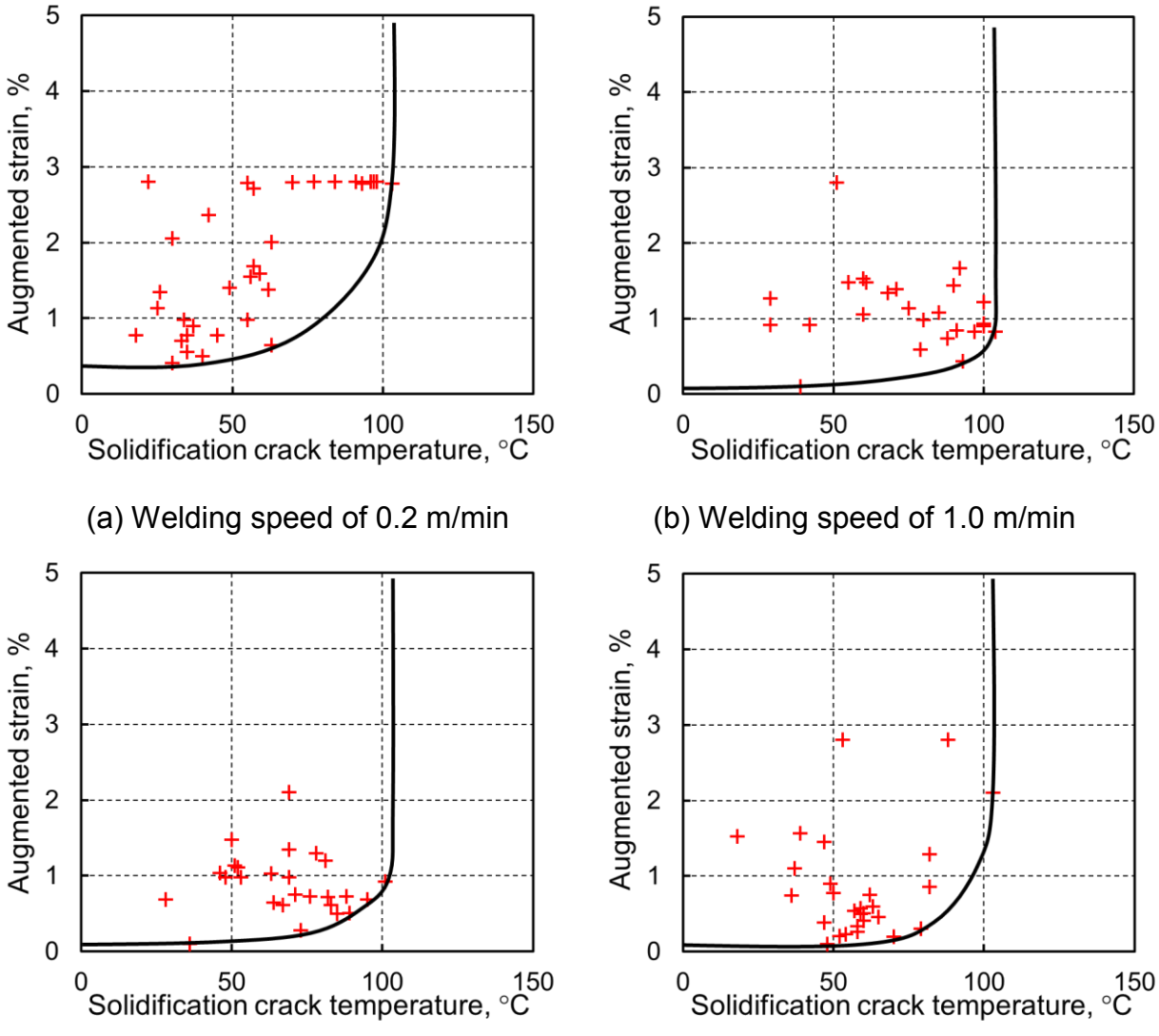

(a) Welding speed of 0.2 m/min

(b) Welding speed of 1.0 m/min

(c) Welding speed of 1.5 m/min

(d) Welding speed of 2.0 m/min

Fig. 4.16 Ductility curve at different welding speeds under augmented strain of 2.8 %

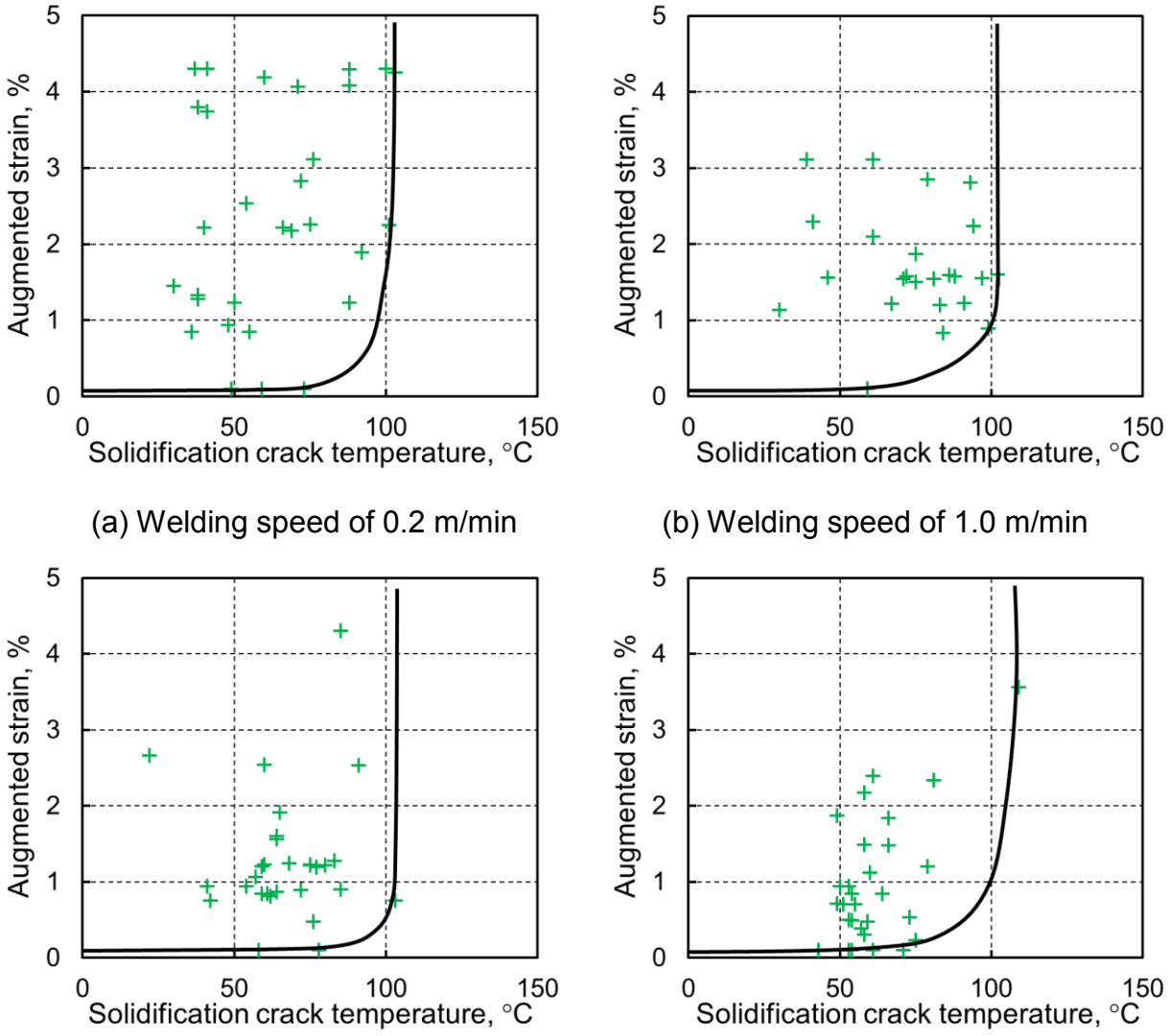

(a) Welding speed of 0.2 m/min (b) Welding speed of 1.0 m/min

(c) Welding speed of 1.5 m/min (d) Welding speed of 2.0 m/min

Fig. 4.17 Ductility curve at different welding speeds under augmented strain of 4.3 %

4.9 Effect of Welding Speed on BTR

Figure 4.18 shows the effect of welding speed from 0.2 to 2.0 m/min on the BTR during laser Trans-Varestraint test under the saturated augmented strain of 2.8 and 4.3 %. The BTR is the average value of the maximum temperature range of the crack under the saturated augmented strain of 2.8 and 4.3 % based on the result like that of Figs. 4.16 and 4.17, and this average value is almost the same at around 102 °C for each welding

speed. The result shows that welding speed from 0.2 to 2.0 m/min has very small influences on the BTR.

Chun et al. reported that the BTR decreased from 133.0 to 123.6 °C with increasing in welding speed from 0.6 to 2.4 m/min during laser Trans-Varestraint test for type 310S stainless steel due to a decrease in the liquidus temperature by undercooling and an increase in the true solidus temperature by inhibiting solidification segregation through calculation [49]. The tendency of the BTR is different from the author's result. However, this difference of BTR with increasing welding speed from 0.6 to 2.4 m/min is around 10 °C and within the deviation of the BTR in this study, as shown in Fig. 4.18. They applied the thermocouple with a low response rate to measure the temperature profile and the longest crack occurred at the side of molten pool during LBW at high welding speeds. In addition, the BTR was measured by using the estimated temperature distribution and conversion length of the longest crack. Thus, it was difficult to measure the BTR along the crack directly at the side of the molten pool. Therefore, the BTR could not be measured precisely using the thermocouple during LBW at high welding speeds due to high cooling rate. By comparison, the author's result has relatively higher reliability and accuracy.

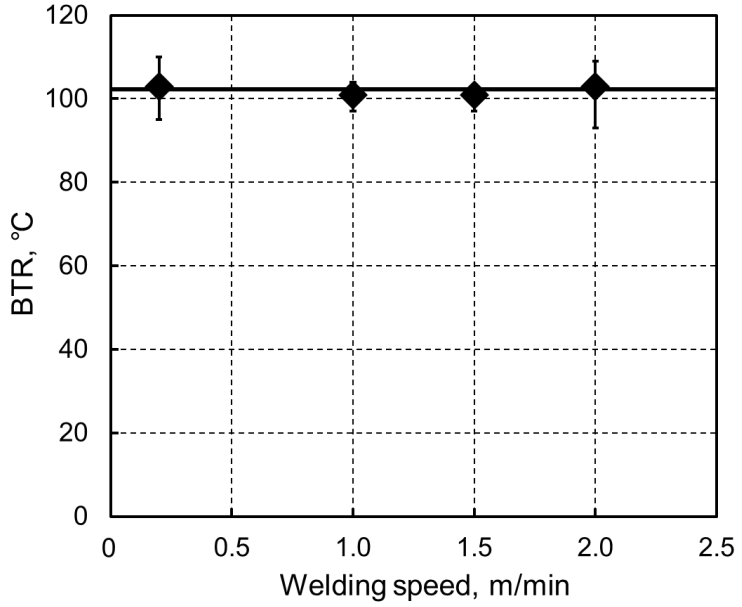

Fig. 4.18 Effect of welding speed on BTR under the augmented strain of 2.8 and 4.3 %

4.10 Effect of Welding Speed on Solidification Cracking Susceptibility

In addition, Shinozaki group [16] has already evaluated the effect of high welding speed on the critical strain of type 310S stainless steel during LBW using U type hot cracking test with in-situ observation, as shown in Fig. 2.9. The result showed that the critical strain at low welding speed of 0.4 m/min was much higher than that at high welding speeds of 0.8 and 1.6 m/min and the critical strain was nearly the same at high welding speeds. As a whole, the critical strain tended to decrease with increasing welding speed.

Comprehensively, high temperature ductility curve composed of the critical strain and BTR can evaluate solidification cracking susceptibility quantitatively and precisely. Figure 4.19 shows the schematic illustration of high temperature ductility curve. The BTR can be measured precisely by using Trans-Varestraint test during LBW and 2D temperature distribution. The measurable critical strain by experiment described as a black slash can be obtained using U-type hot cracking test during LBW, however, due to the healing at the high temperature side and the recovery of the strength at the terminal of the solidification, it is different to measure the critical strain marked as the dash curve. In Fig. 4.19, ε_{min} indicates the lowest value of the ductility curve and the CST presents the critical strain rate of temperature drop. Theoretically, the solidification crack will occur only if the strain rate of temperature drop exceeds the high temperature ductility curve during welding, thus, CST is regarded as a comprehensive index to evaluate solidification cracking susceptibility. However, the critical strain at the terminal of solidification could not be measured directly and the value is estimated, resulting in inaccurate CST. Therefore, in order to evaluate solidification cracking susceptibility precisely, CST′ calculated using ε_{min} divided by the BTR can be employed.

According to the above result, the BTR is nearly the same during LBW at different welding speeds from 0.2 to 2.0 m/min, and ε_{min} has a tendency of decrease with increasing welding speed but the difference is relatively small at high welding speeds. Therefore, CST′ tends to decrease as a whole but the difference is not so large at high welding speeds. In a word, solidification cracking susceptibility of type 310S stainless steel tends to enhance during LBW at different welding speeds from 0.2 to 2.0 m/min but the difference of susceptibility is relatively small at high welding speeds from 1.0 to 2.0 m/min.

It is well known that solidification crack always occur along the solidification grain boundary because of the formation of low-melting residual liquid film along this boundary. Therefore, it is necessary to obtain the morphology and distribution of the residual liquid metal to understand solidification cracking mechanism. However, at present it is hard to measure these morphologies and distributions quantitatively by using the current analytical techniques and instruments, such as liquid Sn quenching method, due to the high cooling rate during LBW. Therefore, in Chapter 5, the simulation as one of the suitable candidates will be employed to predict the morphology and distribution of the residual liquid for understanding solidification cracking mechanism during LBW at different welding speeds.

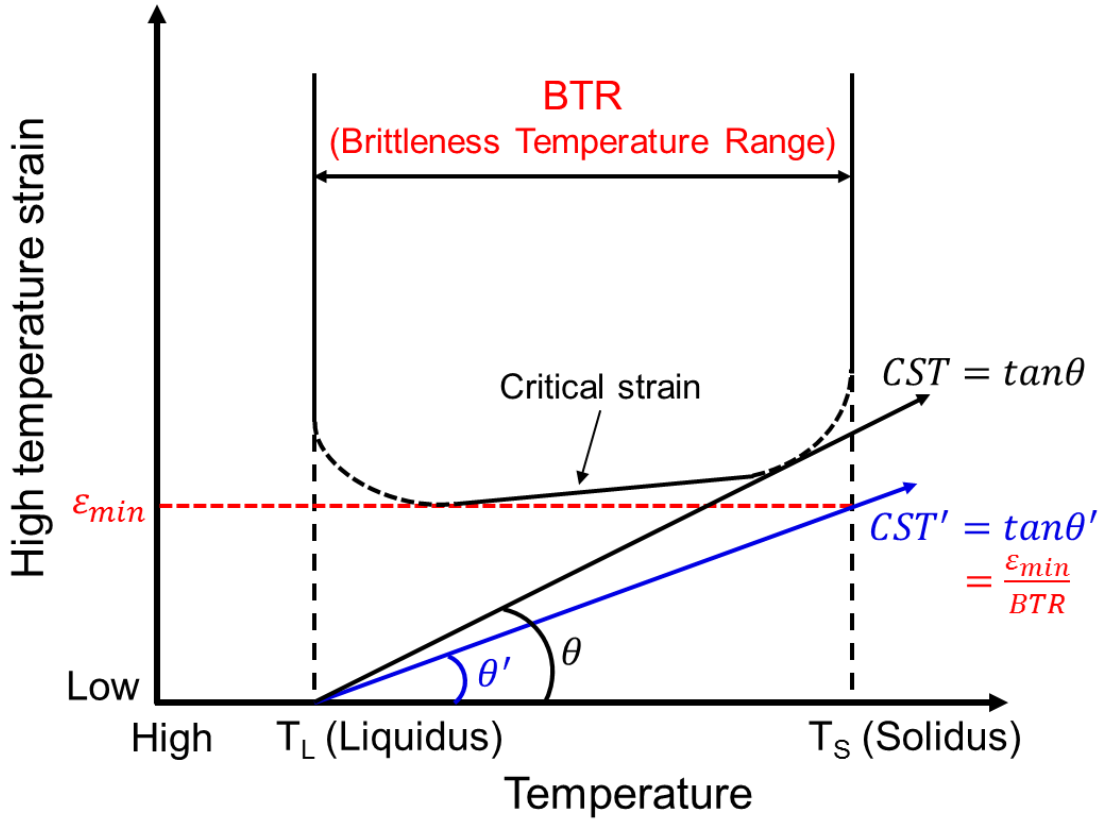

Fig. 4.19 Schematic illustration of high temperature ductility curve

4.11 Summary

In this chapter, temperature measurement method for measuring the temperature range of the crack was verified and discussed in detail. Then, the BTR was obtained by combining Trans-Varestraint test during LBW with the measurement method of 2D temperature distribution at different welding speeds. Finally, solidification cracking susceptibility was evaluated by using the measured BTR and local critical strain (Kadoi et al. [16]). The conclusions are as follows:

1. The longest solidification crack occurred at the rear center of the molten pool during LBW at welding speed of 0.2 m/min, however, the crack with the maximum length tended to appear at the side of the molten pool at high welding speeds from 1.0 to 2.0 m/min. By observing liquid Sn quenched solidification microstructure, the dendrites grew along the surface at low welding speed of 0.2 m/min. However, the main direction of the dendrites growth was from the bottom to the surface at the rear center of the molten pool, but some dendrites grew along the surface at the sides of the molten pool at high welding speeds.
2. The number of the crack and total crack length increased with increasing the augmented strain, but under the saturated augmented strain of 2.0 % both the values kept constant. In addition, both the values had a tendency of decrease with increasing welding speed. The number density of solidification crack and total crack length per bead width firstly increased and then kept stable approximately from low to high welding speed.
3. The 2D temperature distribution could be measured using a multi-sensor camera during LBW at welding speed form 0.2 to 2.0 m/min. In addition, the applicability and accuracy of the 2D temperature distribution measurement method for measuring the temperature range of the crack was evaluated quantitatively to obtain the true BTR. The temperature range of each solidification crack could be obtained using the 2D temperature distribution at different welding speeds. The average BTR was measured using the measurement method of 2D temperature distribution and the average value was almost constant around 102 °C during LBW at welding speeds from 0.2 to 2.0 m/min.

4. Solidification cracking susceptibility could be evaluated comprehensively using the CST′ calculated using ε_{min} divided by the BTR. Because the BTR was almost same at different welding speeds and the ε_{min} was lower at higher welding speeds, the value of the CST′ tended to decrease with increasing laser welding speed. Finally, the result showed that solidification cracking susceptibility had a tendency of increase during LBW at different welding speeds from 0.2 to 2.0 m/min.

Chapter 5

Prediction of Residual Liquid Distribution during Laser Beam Welding using Multi-Phase Field Modeling

5.1 Introduction

As is previously studies, solidification cracking susceptibility of type 310S stainless steel during LBW at different welding speeds has already been evaluated comprehensively by combining the BTR measured by applying Trans-Varestraint test during LBW and the measurement method of 2D temperature distribution, with the local critical strain measured by U-type hot cracking test with in-situ observation [16]. And the tendency of solidification cracking susceptibility seems to enhance with increasing welding speeds from 0.2 to 2.0 m/min during LBW. However, the solidification cracking mechanism is still under the discussion. Generally, solidification crack always occurs along solidification grain boundary, because the solute redistribution can cause a high concentration of the solute and impurity elements along this boundary, resulting in the formation of low-melting residual liquid film along the boundary and further inducing the solidification cracking [8]. In addition, as is mentioned, the BTR and its ductility are the two most important indices to evaluate solidification cracking susceptibility, whereas the morphology and distribution of the residual liquid in the BTR mainly influence these values at the terminal of solidification. For instance, a residual liquid film lowers the ductility, thus the solidification cracking susceptibility becomes higher as a result of the formation of a continuous liquid interface in the BTR [16]. Therefore, it is essential to obtain the morphology and distribution of the residual liquid along the solidification grain boundary for understanding solidification cracking mechanism. However, because of high cooling rate, it is difficult to measure these morphologies and distributions at the terminal of solidification by experimental technological method at present. Therefore, simulation as one of candidates can be used to predict the morphology and distribution of the residual liquid during solidification.

At present, there are several simulation methods for solidification microstructure, such as deterministic method [52], probabilistic method [53-57] and phase field method [58-71]. While, deterministic method does not consider the random phenomena and ignores the crystallographic morphology during dendrite growth [52]. Thus, it is hard to simulate dendrite morphology precisely. In the case of probabilistic method, it can be divided into two types which are Monte Carlo (MC) and Cellular Automaton (CA), respectively [55]. However, MC method lacks of physical basic, such as nucleation and growth of crystalline [54], which results in the difficulty for analyzing physical phenomena quantitatively [55]. Moreover, the simulation result may be a little different from that of experiment using CA method due to consider little macro factors.

While, multi-phase field method (MPFM) based on Ginsberg-Landau theory [58] and giving expression to the influence of diffusion, ordering potential and thermodynamic driving force in terms of differential equations can simulate microstructure evaluation in time and space by the coupling of phase field, temperature field, solute field, and flow field and so on. Thus, it is expected as one of the most useful method to simulate the development of dendrite growth and predict the morphology and distribution of the residual liquid during solidification.

To date, the MPFM was carried out under the condition of low cooling rate, such as casting [12, 13] and GTAW [14, 15]. Moreover, there is little researches on verifying simulation result with that of experiment quantitatively, leading to hard to fit suitable calculation parameters to predict real solidification phenomenon. Fukumoto et al. predicted the dendrite growth of type 304 stainless steel during GTAW and the result was reasonable agreements with the dendrite growth theory, like the Kurz–Giovanola–Trivedi (KTG) model [75, 76], but no compared with experimental result directly [15]. Thus, the aim of this chapter is to use the MPFM to simulate the morphology and distribution of the residual liquid for understanding solidification cracking mechanism under the condition of high cooling rate, like LBW. Moreover, the fracture surface of the solidification crack exhibits a dendrite appearance which is corresponding to the residual liquid distribution [8]. Therefore, the calculation result will also be verified with that of the fracture surface of the solidification crack.

In this chapter, the MPFM is employed to predict the distribution of the residual liquid region and the geometry of type 310S austenitic stainless steel under the condition of high cooling rate during LBW by verifying with experiment and adjusting calculation parameters, such as an interfacial mobility corresponding to a kinetic coefficient in the software, and an anisotropy of interfacial mobility. First, the secondary dendrite arm spacing and primary dendrite tip radius of the calculation are compared with those of experiment and KGT modeling that is a dendritic growth model in order to verify calculation result [75, 76]. Then, the effect of the calculation parameters on residual liquid distribution is investigated. Next, the residual liquid distributions are simulated under different cooling rates by verifying with that of the fracture surface of the solidification crack and optimizing calculation parameters for understanding solidification cracking mechanism. Finally, the effect of cooling rate on the calculation parameters was investigated in order to reveal the suitable parameters to predict real solidification phenomenon under various cooling rates.

5.2 Calculation Method

5.2.1 Multi-phase field modeling

Phase field method is a mathematical model for solving interfacial problems. The interface is described by a steep, but continuous and transition of the phase field variable ϕ between two states. Phase variable ϕ is an ordering variable embodying the physical state of liquid, solid or interface. The variation range of ϕ commonly could be set from 0 to 1. $\phi = 0$ represents the liquid phase and $\phi = 1$ represents the solid phase [59]. The diffuse interface is defined as variable from 0 to 1, as shown in Fig. 5.1. Phase field method can simulate solidification process precisely, which is based on the coupling of phase field, solute field, temperature field or thermodynamics database.

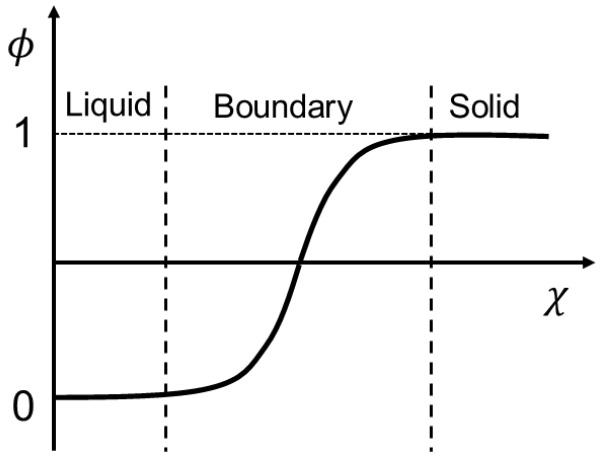

Fig. 5.1 Schematic illustration of phase field interface [15]

Phase field method based on Ginsberg-Landau theory [65, 77], a general model of the free energy can be given as an integral of the density functional over the domain Ω by [78]

$$F(\{\phi_\alpha\}) = \int_\Omega [f^{intf}(\{\phi_\alpha\}) + f^{chem}(\{\phi_\alpha\})] \tag{5.1}$$

where F is the total free energy of the system, ϕ is an ordering variable setting from 0 (liquid phase) to 1 (solid phase), $\{\phi_\alpha\}$ is a function of multiple phase fields and the bracket $\{\ \}$ denotes all phases α and not an individual α, f^{intf} is the interfacial free energy density deduced in the literature [78] and f^{chem} is the Helmholtz free energy density explained in the following part.

According to a detailed derivation from the literature [65], the governing equation for phase field of a i phase can be expressed as [78]

$$\frac{\partial \phi_\alpha}{\partial t} = \sum_{\beta=1}^{v} M_{\alpha\beta} \left\{ \sigma_{\alpha\beta} \left[\left(\phi_\beta \nabla^2 \phi_\alpha - \phi_\alpha \nabla^2 \phi_\beta \right) + \frac{\pi^2}{2\eta^2} \left(\phi_\alpha - \phi_\beta \right) \right] + \frac{\pi}{\eta} \sqrt{\phi_\alpha \phi_\beta} \cdot \Delta G_{\alpha\beta} \right\} \tag{5.2}$$

where ϕ_α and ϕ_β are the phase fields of α and β phases, v is the number of phase, $M_{\alpha\beta}$ is the interfacial mobility, $\sigma_{\alpha\beta}$ is the interfacial energy, η is the interface thickness and $\Delta G_{\alpha\beta}$ is the thermodynamic driving force which can be from a parallel tangent construction [78].

$$\Delta G_{\alpha\beta} = -\left(\frac{\partial}{\partial \phi_\alpha} - \frac{\partial}{\partial \phi_\beta} \right) f^{chem} = \frac{1}{v^m} \left[g_\beta(\vec{c}_\beta) - g_\alpha(\vec{c}_\alpha) - \vec{\tilde{\mu}}(\vec{c}_\beta - \vec{c}_\alpha) \right] \tag{5.3}$$

$$f^{chem} = \frac{g}{v^m} \tag{5.4}$$

$$g(\phi_\alpha, \vec{c}_\alpha) = \sum_{\alpha=1}^{v} \phi_\alpha \, g(\vec{c}_\alpha) \tag{5.5}$$

where v^m is the mean molar volume, g_α and g_β are the chemical free energy densities of α and β phases, $\vec{c}_\alpha = (c_\alpha^1, \dots, c_\alpha^n)$ and $\vec{c}_\beta$ are the phase compositions, and $\vec{\tilde{\mu}}$ is the mixture diffusion potential. If the change of the volume is neglected and it is assumed that the molar volumes of all phases are equal, the Helmholtz free energy density can be replaced by the Gibbs free energy density, as shown in equation (5.4).

Then, the diffusion equation can be given by [78]

$$\frac{\partial \vec{c}}{\partial t} = \nabla \left(\sum_{\alpha=1}^{v} \phi_\alpha D_\alpha \nabla \vec{c}_\alpha \right) \tag{5.6}$$

$$D_\alpha = v^m M_\alpha^{ch} T_\alpha \tag{5.7}$$

$$T_\alpha^{ij} = \frac{\partial \tilde{\mu}_\alpha^i}{\partial c_\alpha^j} = \frac{\partial^2 g_\alpha}{\partial c_\alpha^i \partial c_\alpha^j} \tag{5.8}$$

where $\vec{c} = \sum_{\alpha=1}^{v} \phi_\alpha \vec{c}_\alpha$ is mixture composition, D_α is the diffusion matrix in phase α, M_α^{ch} is the chemical mobility matrix which is the function of the atomic mobility and the local phase composition, T_α is the matrix comprised the derivatives of the diffusion potentials in phase α, i and j are the components, and $\tilde{\mu}_\alpha$ is the phase diffusion potential.

As is known, the phase field and diffusion equations need to be solved by quasi-equilibrium data which could be derived from thermodynamic calculations using database [78]. However, the quasi-equilibrium condition should be solved for each location and each interface cell in every numerical time step [78]. Thus, a multi-binary extrapolation is considered in order to improve calculation efficiency [78]

$$c_\alpha^i = \frac{c^i - \sum_{\rho=1}^{v} \phi_\rho [c_\rho^{i*} - K_{\rho\alpha}^{ij} c_\alpha^{i*} + (\frac{\partial c_\rho^i}{\partial T}) \Delta T]}{\sum_{\rho=1}^{v} \phi_\rho K_{\rho\alpha}^{ij}} \tag{5.9}$$

where c^i is the composition of component i, ρ is an arbitrary reference phase, c_ρ^{i*} is the composition of an arbitrary reference phase in quasi-equilibrium condition, $K_{\rho\alpha}^{ij} = \left(\frac{\partial c_\rho^i}{\partial c_\alpha^j}\right) = T_\rho^{-1} T_\alpha$ is the partition coefficient, $\Delta T = T - T^*$ and T^* is the quasi-equilibrium temperature.

Normally, because of the release of latent heat in the solid-liquid interface during solidification, the effect of temperature distribution should be considered in the calculation, which means coupling temperature field [79]. However, due to an appearance of a steep temperature gradient in this experiment, the latent heat could be disregarded during calculation [80]. Therefore, it is not necessary to couple temperature field actually in this research. And the thermal boundary conditions could be specified using temperature gradient and cooling rate [80].

In this study, MICRESS was employed, which is a commercial software based on the phase field modeling for single-, multi-phase systems and multi-component systems. A thermodynamic database of Fe (TCFE7) and a mobility database of MOBFE2 were applied by direct coupling to the MPFM due to the stable calculation. Meanwhile, a multi obstacle potential was used to the phase field modeling, because it takes into account all of the multi-phase or multi-grain interactions and can correct dihedral angle [65].

When the calculation model during solidification of the LBW was considered, several physical and calculation parameters, such as interfacial energy, anisotropy of the interfacial energy, interfacial mobility, and anisotropy of the interfacial mobility were required. Thus, the anisotropy model should also be considered during calculation.

Normally, the anisotropy function of interfacial energy is given by [15]

$$\sigma(\varphi) = \sigma_{i-j}[1 + \varepsilon_4 \cos(4\varphi)] \tag{5.10}$$

where i and j represent different phases, ε_4 is the anisotropy coefficient. When the value of ε_4 is more than 0.056, the crystal will change into facet [15]. Therefore, in the case of the dendrite growth, ε_4 should set less than 0.056. While, in MICRESS software, the anisotropy of interfacial energy is replaced by the anisotropy of interfacial stiffness because the latter considers a direct matching to the modified Gibbs-Thomson equation for anisotropic interfaces [80]. Therefore, for this reason, the anisotropy of interfacial stiffness equals $15 \times \varepsilon_4$ in the research [80]. In addition, the anisotropy function and relationship are also appropriate for that of the anisotropy of interfacial mobility. In this study, the anisotropies of interfacial stiffness and interfacial mobility from MICRESS software were used.

In addition, material parameters, such as the dendrite arm spacing, cooling rate, and temperature gradient during LBW were required and measured directly by experiment.

5.2.2 Materials used

The material used for LBW was type 310S stainless steel which was solidified as γ single mode during LBW. The chemical composition of the material is shown in Table 1.

Table 5.1 Chemical composition of Type 310S (mass %)

C	Si	Mn	P	S	Ni	Cr	Co	Fe
0.04	0.43	0.96	0.019	0.001	20.13	25.19	0.09	Bal.

5.2.3 Measurement of primary and secondary dendrite arm spacing

In order to set parameters for calculation and verifying the calculation result of the MPFM, the primary and secondary dendrite arm spacing need to be measured by experiment, respectively. Figure 5.2 shows the liquid Sn quenched microstructures during LBW at different welding speeds. The liquid Sn quenched microstructures along the opened cracks directions are at the rear center of the molten pool at welding speed of 0.2 m/min in Fig. 5.2 a), and at the side of the molten pool at welding speed of 1.0 m/min in Fig. 5.2 b), respectively. In Fig. 5.2, the primary and secondary dendrite arm spacing can be measured directly from this liquid Sn quenched microstructure, however, it is difficult to distinguish the residual liquid. Both the values of the primary and secondary dendrite arm spacing for each welding speed are listed in Table 5.2.

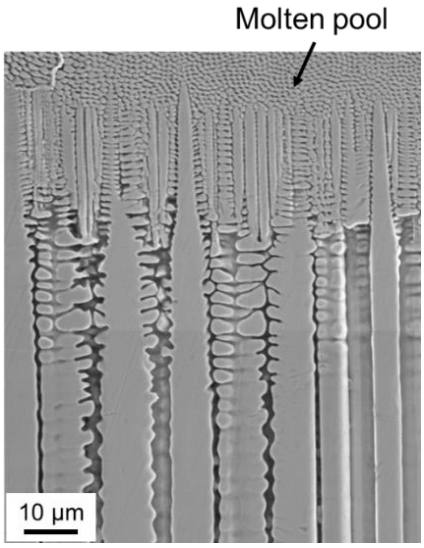

(a) Welding speed of 0.2 m/min

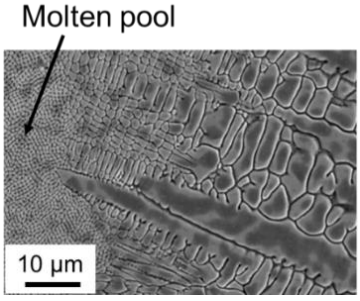

(b) Welding speed of 1.0 m/min

Fig. 5.2 Liquid Sn quenched microstructure during LBW at different welding speeds

Table 5.2 Calculation conditions

Welding speed, m/min	0.2		1.0	1.5
Cooling rate, °C/s	745	848	2665	2896
Temperature gradient, °C/mm	223	254	316	342
Temperature measurement direction	Along centerline of molten pool	Along opened crack		
Primary dendrite arm spacing, μm	10.0		6.0	5.7
Secondary dendrite arm spacing, μm	2.31		1.85	1.85

5.2.4 Measurement of cooling rate and temperature gradient

The solidification cracking phenomenon can be understood by observing the fracture surface of the solidification crack which could be obtained by laser Trans-Varestraint test [50]. Therefore, in order to predict the residual liquid distribution matching that of the fracture surface, the temperature conditions, such as temperature gradient and cooling rate, need to be measured along the crack direction. In this case, the temperature gradient and cooling rate along a crack during LBW are measured directly using 2D temperature distribution, as shown in Fig. 5.3 at welding speed of 1.0 m/min. Figure 5.3 a) shows the solidification crack distribution at the rear center of the molten pool after laser Trans-Varestraint test [50] and the target crack for the temperature measurement is marked by a white circle. Figure 5.3 b) shows an image of 2D temperature distribution for measuring temperature along this target crack which is expressed as a white line. In Chapter 3 and 4, the method to measure temperature gradient has already been introduced and discussed in detail using 2D temperature distribution [81]. Figure 5.3 c) shows the corresponding temperature gradient along the crack using 2D temperature distribution. In addition, positioning the start point of the crack, the cooling rate is measured at different times by using a series of the images of 2D temperature distribution, as shown in Fig. 5.3 d). Due to the frame rate of 50 fps of 2D temperature measurement, the time interval is 0.02 s between each image in Fig. 5.3 d). Finally, the cooling rate and temperature gradient for each welding speed are listed in Table 5.2.

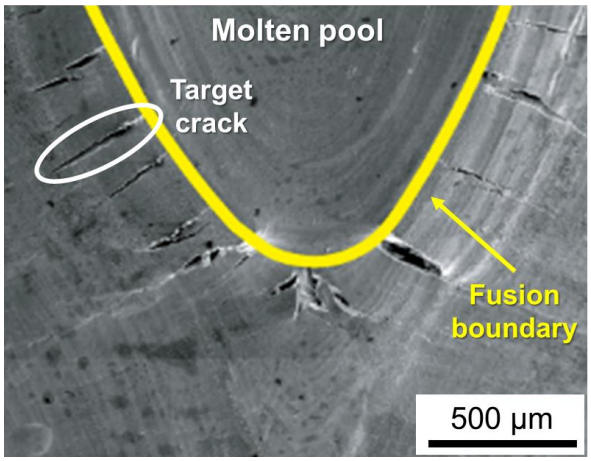

(a) Solidification crack distribution

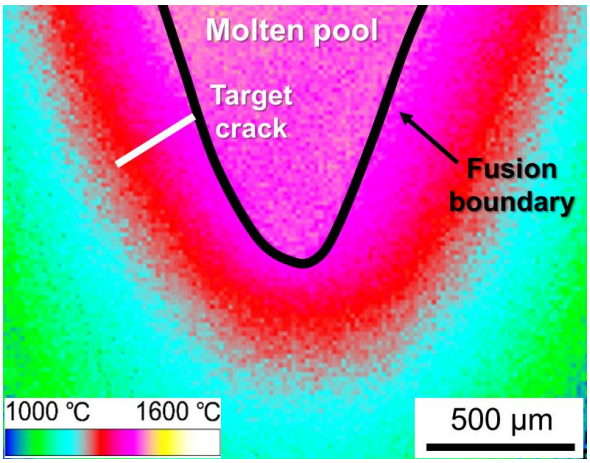

(b) 2D temperature distribution

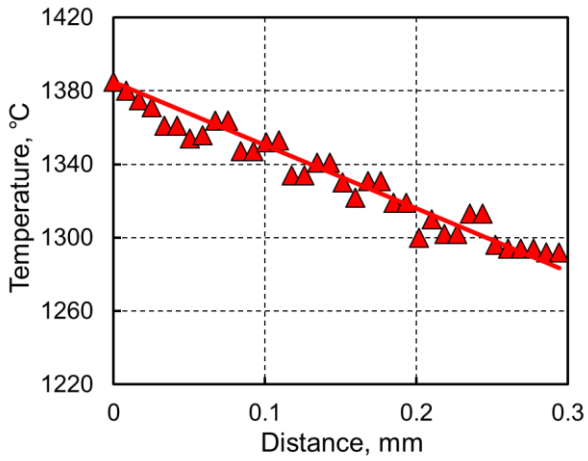

(c) Temperature gradient

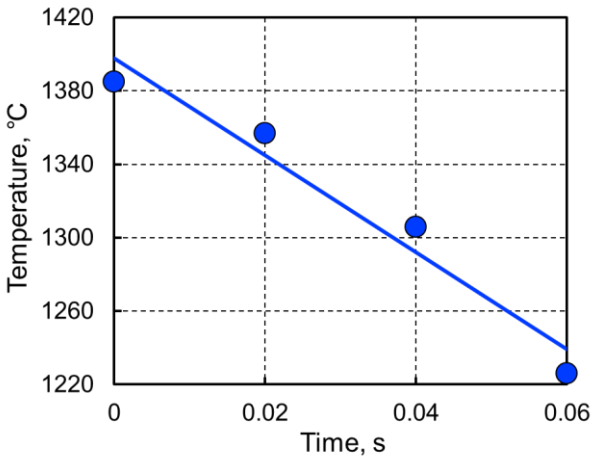

(d) Cooling rate

Fig. 5.3 Measurement of temperature gradient and cooling rate along a crack during LBW at welding speed of 1.0 m/min

5.2.5 Calculation condition

All of the elements in the materials shown in Table 5.1 should be taken into account in the calculation, however, the preliminary calculation revealed that low content induced an instabilities of calculation and it was impossible to finish the solidification due to the divergence of calculation. Therefore, P, S, and Co were removed in this study. Two nucleation grains set at the both corners of a domain area with the measured primary dendrite arm spacing in Table 5.2, as shown in Fig. 5.4. Due to the small secondary

dendrite arm spacing under higher cooling rate in Table 5.2, cell dimension is set to 0.06 μm in order to provide enough resolution and enhance calculation efficiency, and the interface thickness is set to 3 cells.

Table 5.3 shows the parameters between the liquid and solid γ-Fe phase in the case of type 304 during solidification simulation of GTAW from reference paper [15]. Due to relatively good agreement with the solidification theory, the parameters are adjusted based on Table 5.1 in this calculation. Especially, the interfacial energy is 0.30 J/m^2 and the anisotropy of interfacial stiffness is 0.10 because the past research reveals a good simulation result using this value [15]. While, the interfacial mobility and the anisotropy of interfacial mobility as the calculation parameters are changed from 2.5E-10 to 60.0E-10 m^4/J/s and from 0.005 to 0.10, respectively, because these two parameters depends on the cooling rate.

Additionally, the temperature along the centerline of the molten pool in Table 5.2 is used to evaluate the effect of calculation parameters on the secondary dendrite arm spacing and the residual liquid distribution. The other temperature along the opened crack in Table 5.2 is employed to predict the morphology and the distribution of the residual liquid metal, and to verify with experiment for each cooling rate. Moreover, the liquidus temperature is 1385 °C and the initial temperature sets 1395 °C in order to start calculation in a stable environment.

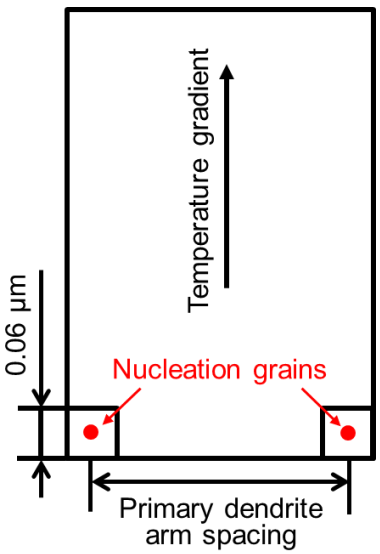

Fig. 5.4 Schematic illustration of a calculation domain area

Table 5.3 Parameters between liquid and solid γ-Fe phase from reference paper [15]

Interfacial energy $\sigma_{L\text{-}\gamma}$, J/m^2	0.30
Anisotropy of interfacial stiffness	0.10
Interfacial mobility $M_{L\text{-}\gamma}$, m^4/J/s	5.0E-10
Anisotropy of interfacial mobility	0.10

5.2.6 Relationship between calculation result and fracture surface of solidification crack

Figure 5.5 shows the schematic illustration of solidification sequence and calculation result. Blue and yellow represent the liquid and solid γ-Fe phases, respectively. According to the solidification theory, a dendrite morphology (Type D) can transform into Type D-F firstly and then a flat fracture (Type F) along the fracture surface of the solidification crack corresponding to the solidification sequence with decreasing temperature [8]. And the critical temperature between Type D-F and Type F is defined as T_B, as shown in Fig. 5.5 a). In Fig. 5.5 b), the primary dendrite tip is observed at the solidification front and the temperature at the primary dendrite tip is assumed as the liquidus temperature T_L. With decreasing temperature, the dendrites grow and secondary dendrite arms appear gradually. In addition, the residual liquid connects directly with the molten pool and the liquid metal can flow freely between adjacent dendrites. Then, continuing to decline temperature until to the temperature T_B, the first point of the bridging of secondary dendrite arms forms which can totally hinder the flow of the residual liquid metal, leading to the formation of the residual liquid film. Thus, from T_L to T_B, this region is regarded as "Residual liquid connecting with molten pool region" expressed as L_P (T_L to T_B). With falling temperature further, the bridging becomes more significant and the residual liquid distributes as film or dot. Finally, the solidus temperature T_S is determined where the last residual liquid appears. Thus, from T_B to T_S, this region is regarded as "Residual liquid film-dot region" expressed as L_{FD} (T_B to T_S). In addition, the total mushy zone experiences from the primary dendrite tip to the last residual liquid during solidification, which is expressed as L_M (T_L to T_S). Because the critical temperature T_B in the solidification

sequence corresponds to those of the fracture morphology and calculation result, the lengths of L_P and L_{FD} equal to those of the region from Type D to Type D-F, and the region of Type F, respectively.

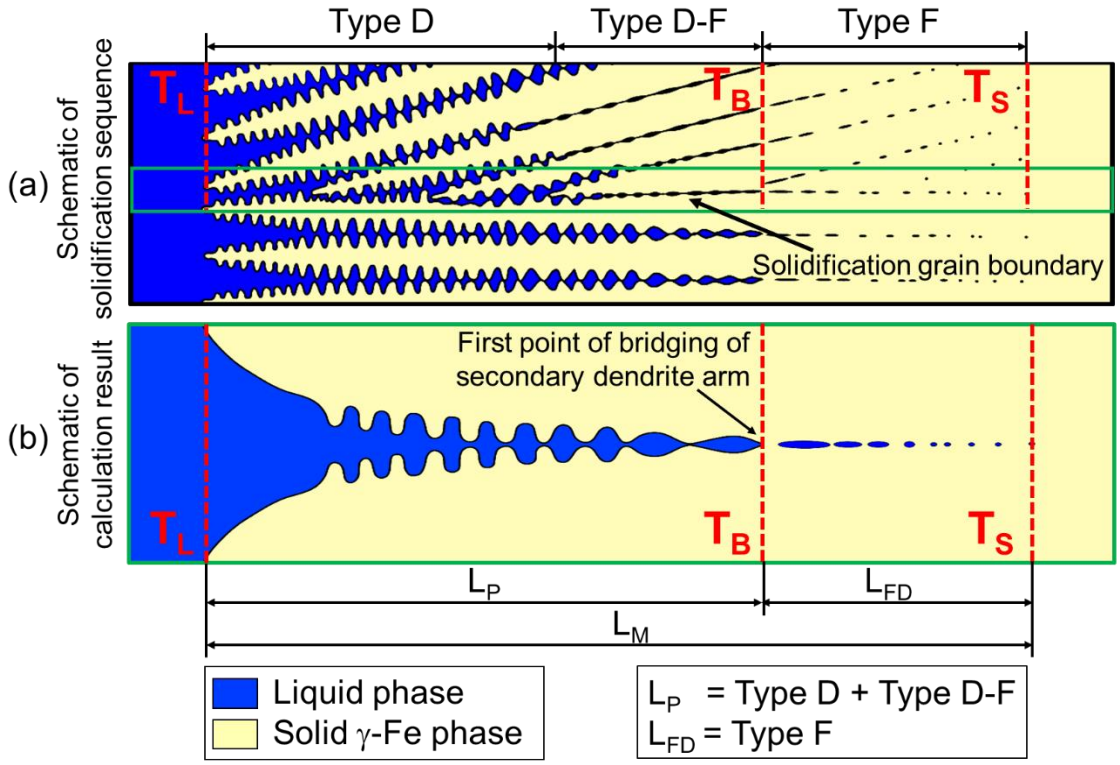

Fig. 5.5 Schematic illustration of (a) solidification sequence and (b) calculation result

In order to verify the calculation result, the predicted residual liquid distribution is compared with the morphology of the fracture surface of the solidification crack with the longer lengths and similar temperature range, as shown in Table 5.4. The cooling rates changed from 848 to 2896 °C/s correspond to the welding speeds from 0.2 to 1.5 m/min, respectively. However, at welding speed of 2.0 m/min, the crack with longer length and temperature range initials at the rear center of the molten pool, and the dendrites grow from the bottom to the surface of specimen. Therefore, it is hard to predict the residual liquid distribution due to only measure 2D temperature distribution of the surface of the specimen. Additionally, the fracture surfaces under different cooling rates are observed, as shown in Figs. 5.6, 5.7 and 5.8.

Figure 5.6 shows the fracture surface at welding speed of 0.2 m/min under cooling rate of 848 °C/s. No. 14 crack marked by circle is chosen for opening due to its longer crack length and temperature range, as shown in Fig. 5.6 a). The left side and right side of opened No. 14 crack are indicated in Fig. 5.6 b) and c), and red curve expresses the fusion boundary. These two images evidence the opened crack is targeted No. 14 crack. Figure 5.6 d) shows the fracture surface of No. 14 crack. The temperature decreases from the left to right side along the crack and the contour line of the crack is drawn using the red line. As is mentioned in Chapter 3, the morphology of the fracture surface of the solidification crack changes from dendrite morphology to hollow characteristic with decreasing temperature. Along the crack, the left side of the fracture surface is near the molten pool at the liquidus temperature T_L. The middle and right lines indicates the start and end hollow position observed by the high magnification SEM image. And the enlarged start and end hollow images are shown in Fig. 5.6 d) marked by the white circle. According to the solidification theory, the start hollow is the same as the first point of the bridging at the temperature T_B and the end hollow means the finish of solidification at the temperature T_S. Therefore, the length of the region from Type D and Type D-F along the crack corresponds to L_P (T_L to T_B) in the calculation result is 180 μm, and the length of the region of Type F along the crack equals to L_{FD} (T_B to T_S) in the calculation result is 170 μm. Moreover, the total solidification crack length is the same as that of L_M (T_L to T_S). Thus, in order to predict the real residual liquid distribution, the length of each residual liquid region should be verified with those of fracture surface.

Table 5.4 Length of opened crack and corresponding temperature range for each cooling rate

Cooling rate, °C/s	848	2665	2896
Length of opened crack, μm	350	275	258
Temperature range of opened crack, °C	89	87	88

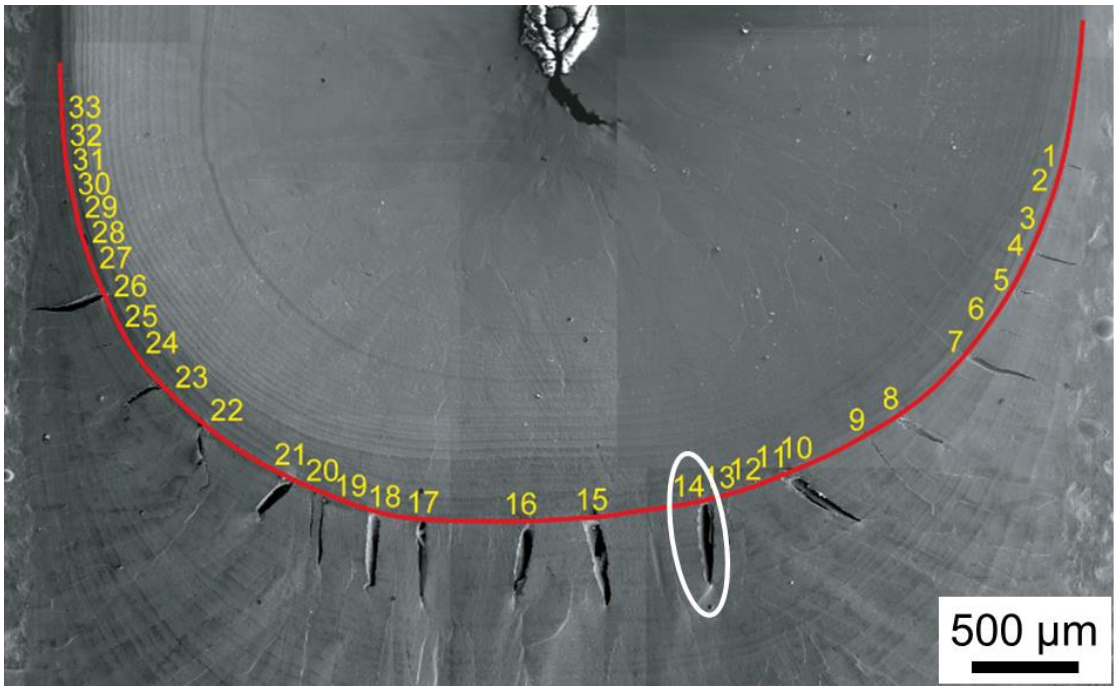

(a) The selected crack for opening

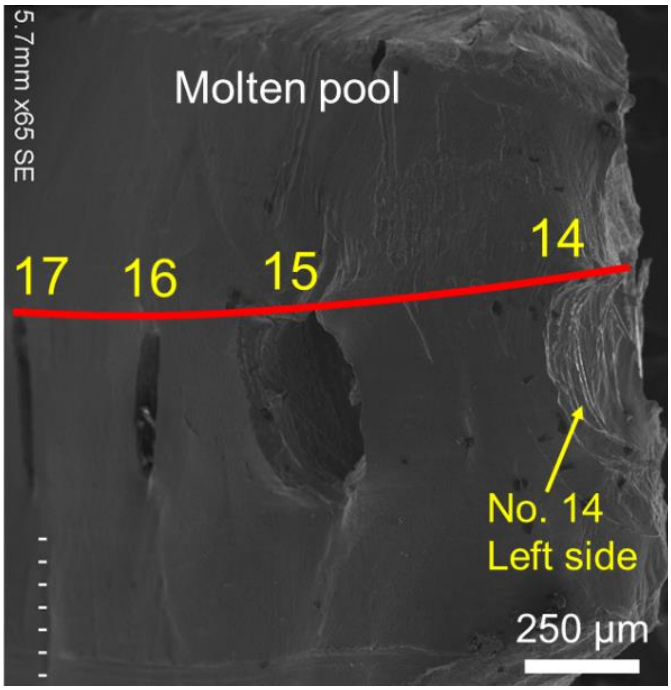

(b) Left side of opened No. 14 crack

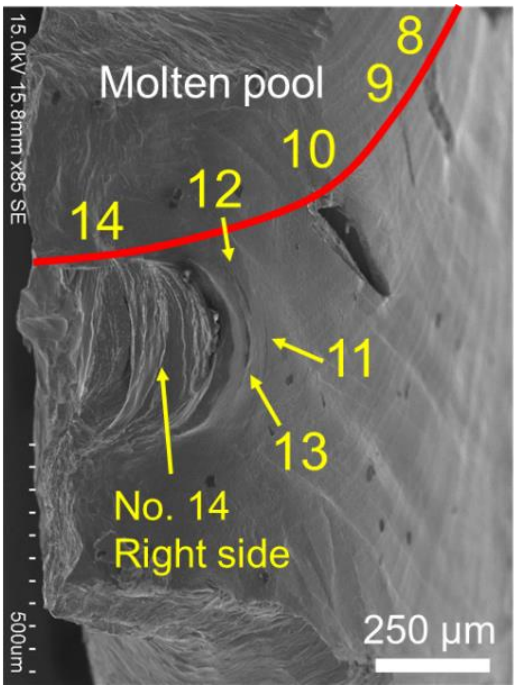

(c) Right side of opened No. 14 crack

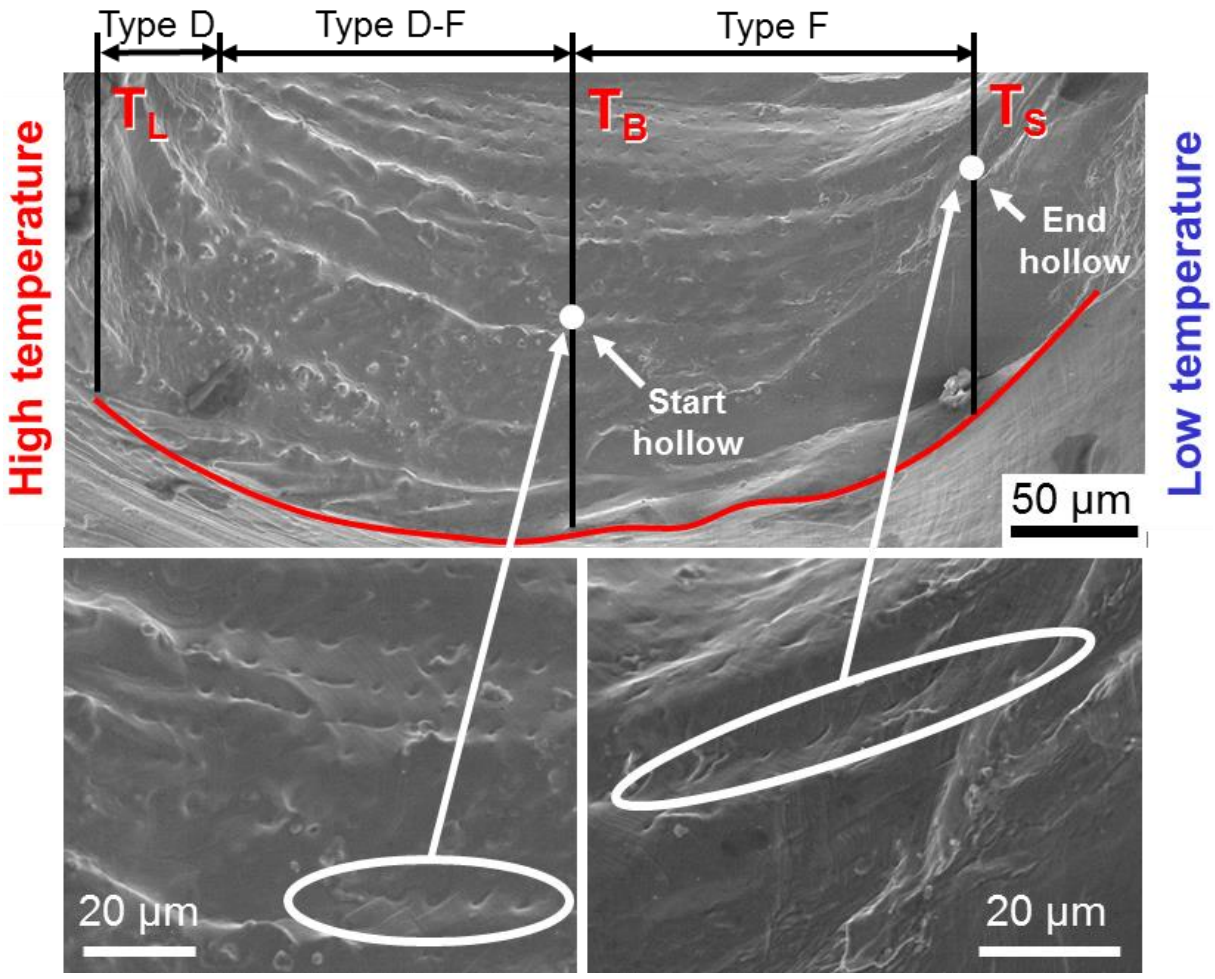

(d) Fracture surface of No. 14 crack

Fig. 5.6 Fracture surface under cooling rate of 848 °C/s

Figures 5.7 and 5.8 show the fracture surface of the solidification crack under cooling rates of 2665 and 2896 °C/s, respectively. In Fig. 5.7, No. 24 crack marked by the white circle is the targeted crack for opening, the corresponding lengths of L_P (T_L to T_B) and L_{FD} (T_B to T_S) are 100 and 175 μm, respectively. In Fig. 5.8, No. 5 crack marked by the white circle is the targeted crack for opening, the corresponding lengths of L_P (T_L to T_B) and L_{FD} (T_B to T_S) are 100 and 158 μm, respectively.

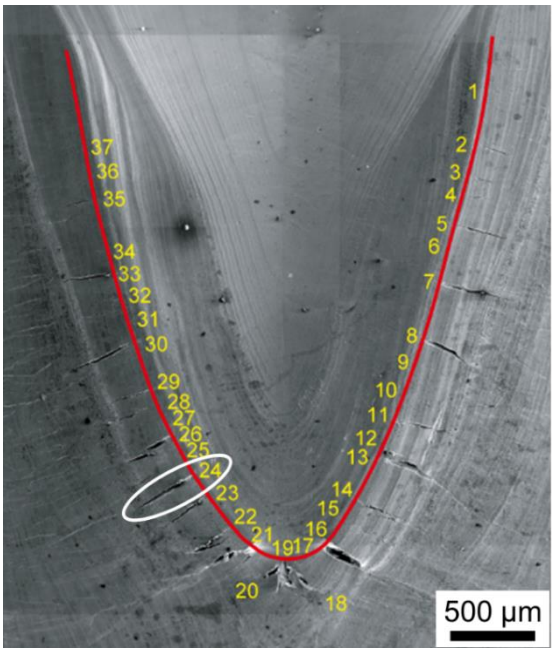

(a) The selected crack for opening

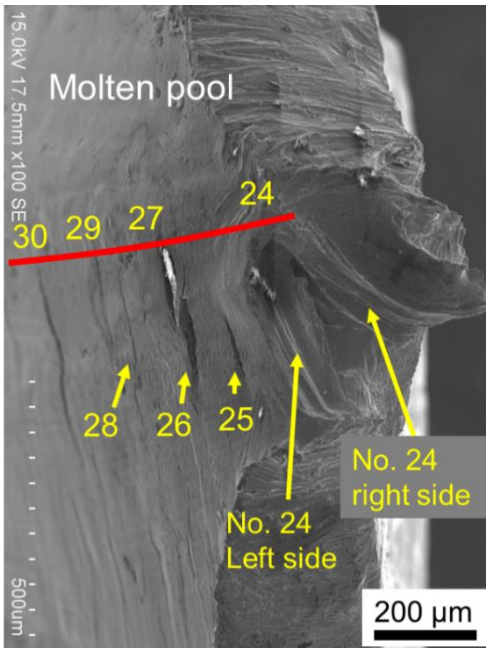

(b) Opened No. 24 crack

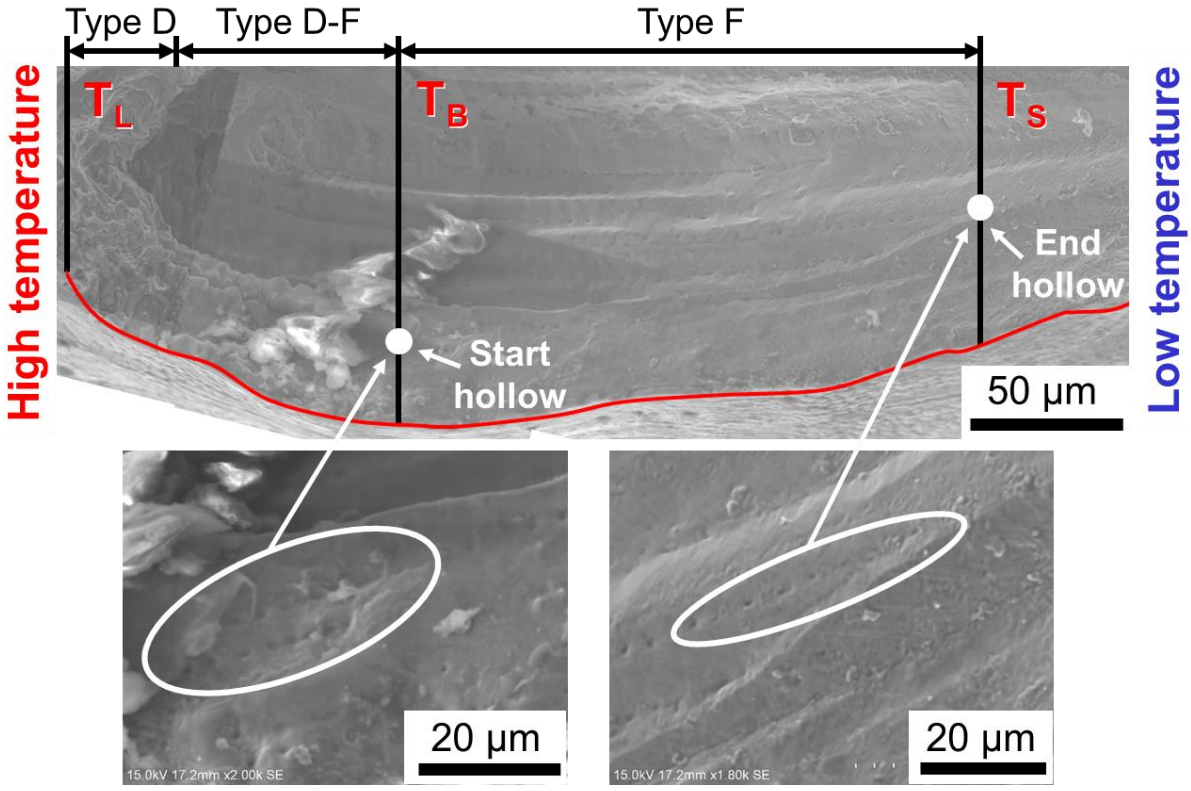

(c) Fracture surface of No. 24 crack

Fig. 5.7 Fracture surface under cooling rate of 2665 °C/s

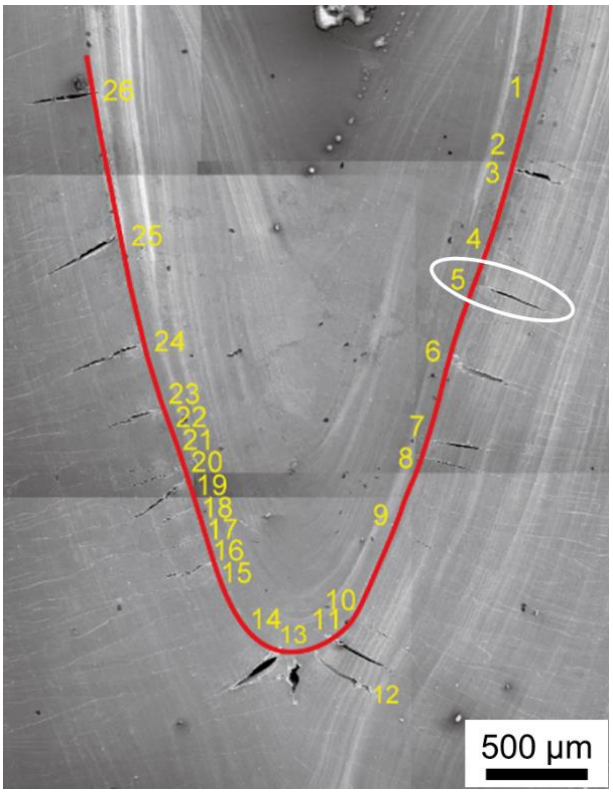

(a) The selected crack for opening

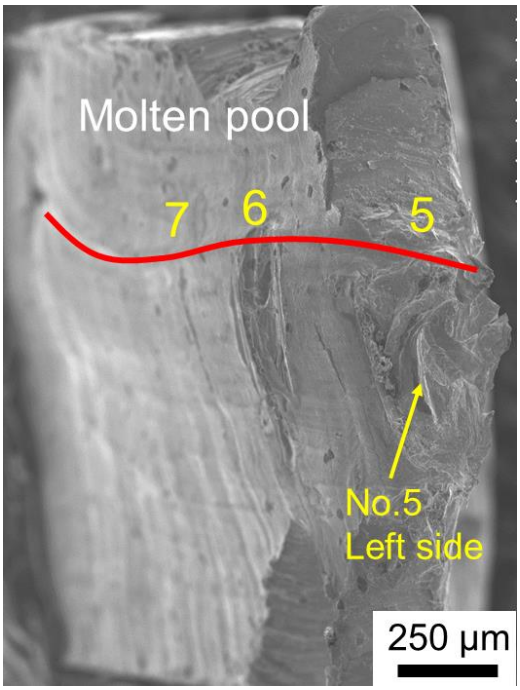

(b) Left side of opened No. 5 crack

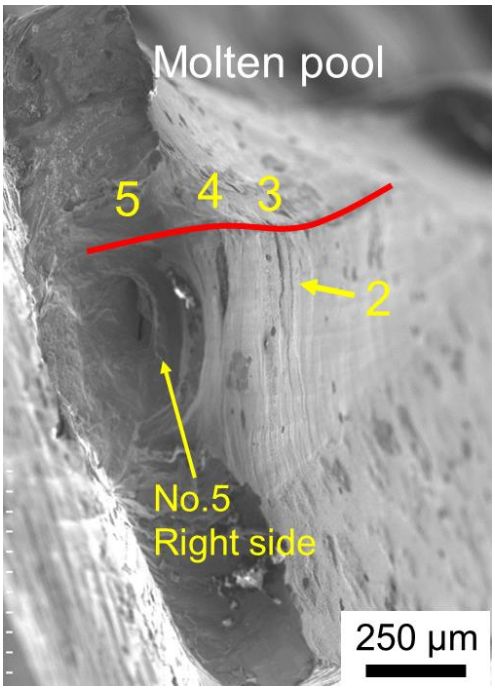

(c) Right side of opened No. 5 crack

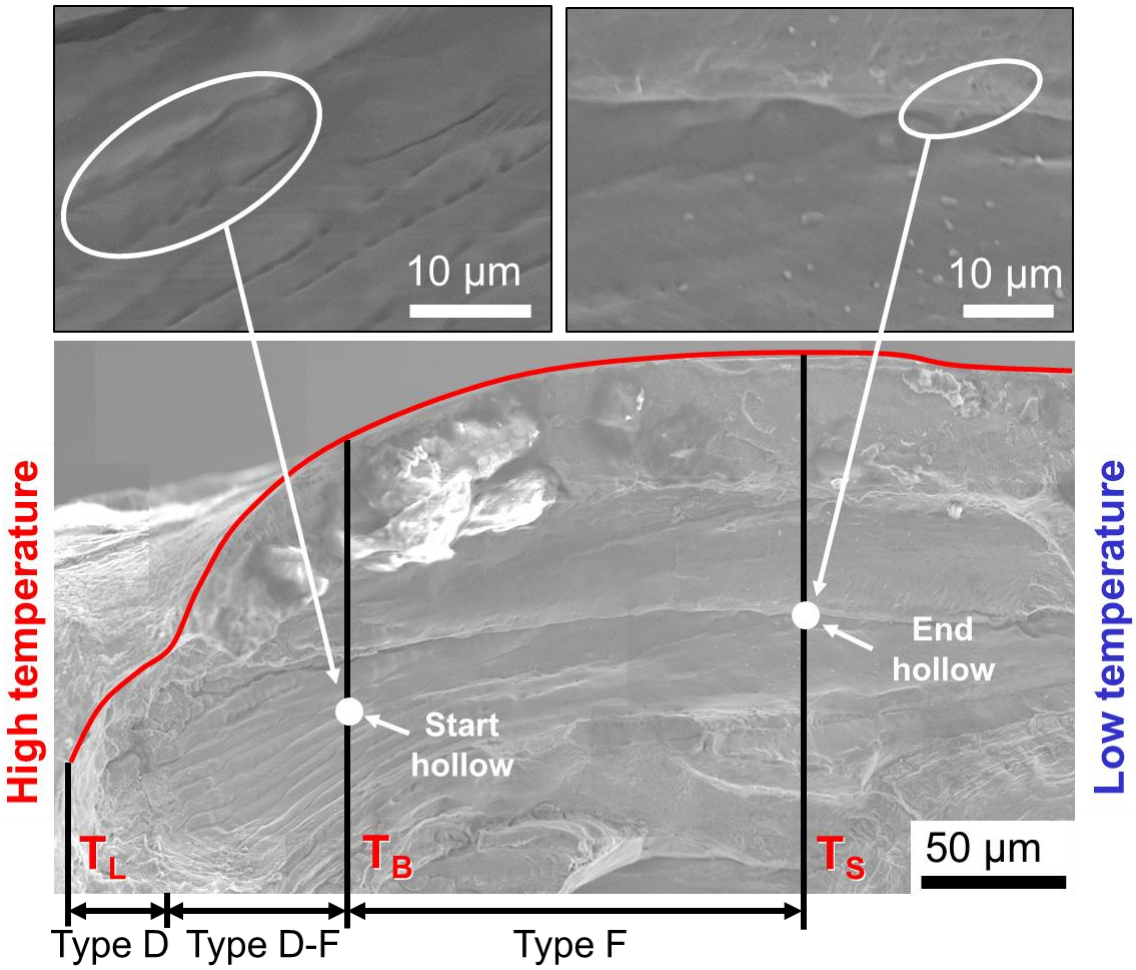

(d) Fracture surface of No. 24 crack

Fig. 5.8 Fracture surface under cooling rate of 2896 °C/s

5.3 Verification with Secondary Dendrite Arm Spacing and Primary Dendrite Tip Radius

In order to verify the calculation result of the MPFM, the secondary dendrite arm spacing and primary dendrite tip radius are compared with those of experiment and KGT modeling [75, 76], respectively. Especially, the KGT model that is a dendritic growth model is also employed to verify calculation result from the solidification theory perspective [75, 76]. The equation is given as:

$$R = 2\pi\sqrt{\frac{D\Gamma}{k\Delta T_0 V}} \tag{5.11}$$

where R is the primary dendrite tip radius, m;

D is liquid interdiffusion coefficient, m^2/s;

Γ is Gibbs-Thompson coefficient, Km;

($\Gamma = \frac{\sigma}{\Delta S_f}$, where σ is interfacial energy, J/m^2; ΔS_f is melting entropy, J/m^3K)

k is partition coefficient;

ΔT_0 is liquidus-solidus range, K;

($\Delta T_0 = \frac{mC_0(k-1)}{k}$, where m is liquid slope, C_0 is initial liquid composition)

V is interface movement velocity, m/s.

Figure 5.9 shows the comparison of the secondary dendrite arm spacing and primary dendrite tip radius under different calculation parameters and cooling rate of 745 °C/s. Figure 5.9 a) shows the comparison under different interfacial mobility and anisotropy of interfacial mobility of 0.10. The secondary dendrite arm spacing and primary dendrite tip radius nearly keep constant under different interfacial mobility. Under the interfacial mobility from 5.0E-10 to 20.0 E-10 $m^4/J/s$, the secondary dendrite arm spacing and primary dendrite tip radius are both close to those of liquid Sn quenched microstructure in Fig. 5.2 a) and KGT modeling.

Figure 5.9 b) shows the comparison under different anisotropies of interfacial mobility and interfacial mobility of 10.0E-10 $m^4/J/s$. The secondary dendrite arm spacing and primary dendrite tip radius tend to decrease with increasing anisotropy of interfacial mobility. However, when the value is more than 0.10, the secondary dendrite arm disappears. The secondary dendrite arm spacing and primary dendrite tip radius are both close to those of experiment in Fig. 5.2 a) and KGT modeling only if the anisotropy of interfacial mobility is around 0.10. Therefore, these tendencies proves that the calculation result has a good agreement with that of not only experiment but also solidification theory by adjusting the suitable calculation parameters within these ranges under cooling rate of 745 °C/s. Thus, it is possible to predict the residual liquid distribution using the MPFM with a relatively high credibility under corresponding condition for each cooling rate.

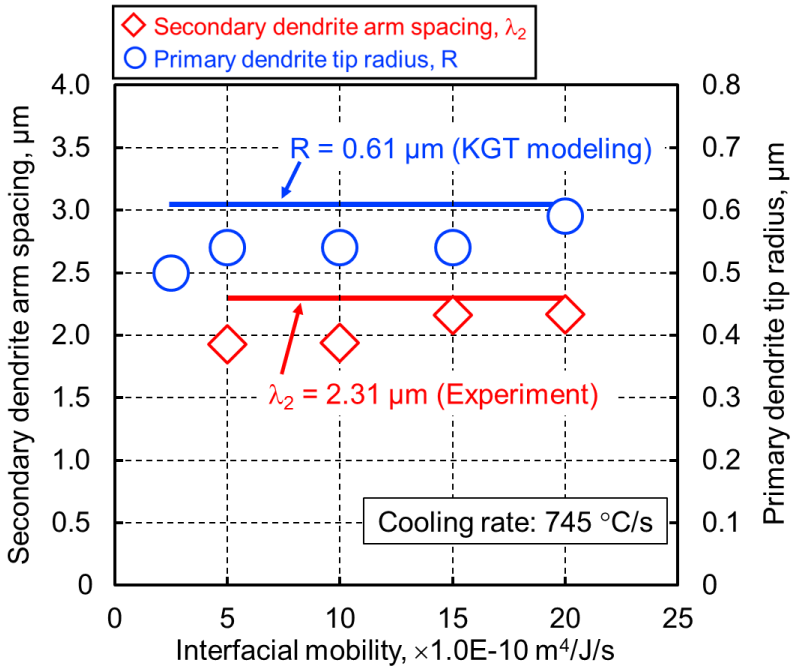

(a) Under different interfacial mobility and anisotropy of interfacial mobility of 0.10

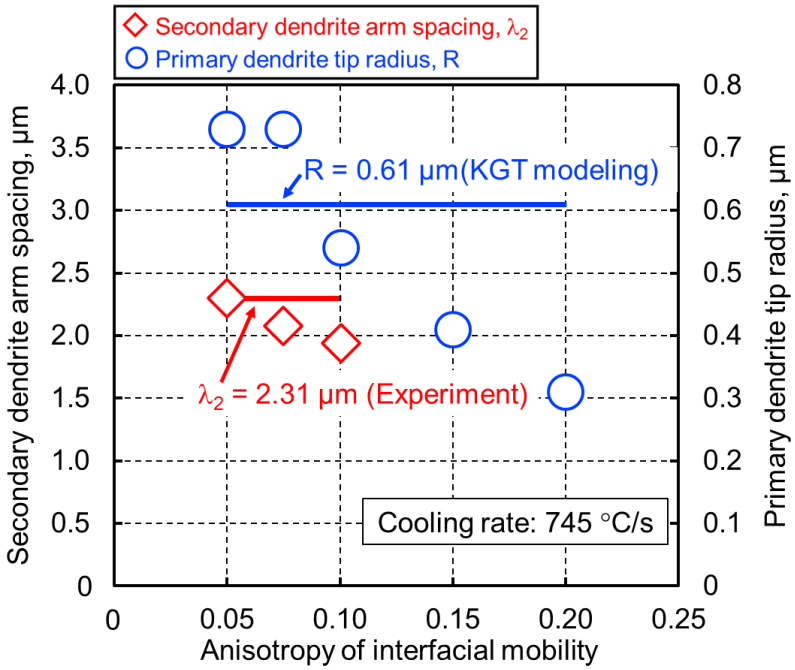

(b) Under different anisotropies of interfacial mobility and interfacial mobility of 10.0E-10 $m^4/J/s$

Fig. 5.9 Comparison of secondary dendrite arm spacing and primary dendrite tip radius under different calculation parameters and cooling rate of 745 °C/s

5.4 Influence of Parameters on Residual Liquid Distribution

5.4.1 Effect of interfacial mobility on residual liquid distribution

Interfacial mobility corresponds to an interface movement velocity attributing driving force or curvature. Theoretically, the interfacial mobility should increase with increasing cooling rate in order to obtain the suitable dendrite morphology during calculation. In reference paper [15], interfacial mobility of 5.0E-10 $m^4/J/s$ is suited to the low cooling rate under 100 °C /s. However, in the case of LBW at welding speed of 0.2 m/min, the cooling rate is 745 °C/s, much higher than that value. Thus, the interfacial mobility should increase reasonably. Table 5.5 shows the parameters under different interfacial mobility changed from 5.0E-10 to 15.0E-10 $m^4/J/s$.

Figure 5.10 shows the residual liquid distribution under different interfacial mobility and cooling rate of 745 °C/s. The number of the residual liquid film and dot is represented in each image. By comparison, the dendrite morphology is nearly the same under different interfacial mobility, as shown in Fig. 5.10. Figure 5.11 indicates the effect of interfacial mobility on the length of the residual liquid region quantitatively under cooling rate of 745 °C/s. The lengths of L_P (T_L to T_B), L_{FD} (T_B to T_S), and L_M (T_L to T_S) increase with increasing interfacial mobility, respectively. According to the solidification theory, the dendrite growth rate is directly proportional to interfacial mobility. While, the high dendrite growth rate can cause an increase in the length of the total mushy zone during solidification, as well as the length of the other residual liquid region. Therefore, the length of each residual liquid region tends to increase with increasing interfacial mobility.

Table 5.5 Parameters under different interfacial mobility

Interfacial energy $\sigma_{L\text{-}\gamma}$, J/m^2	0.30 [15]		
Anisotropy of interfacial stiffness	0.10 [15]		
Interfacial mobility $M_{L\text{-}\gamma}$, $m^4/J/s$	5.0E-10	10.0E-10	15.0E-10
Anisotropy of interfacial mobility	0.10 [15]		

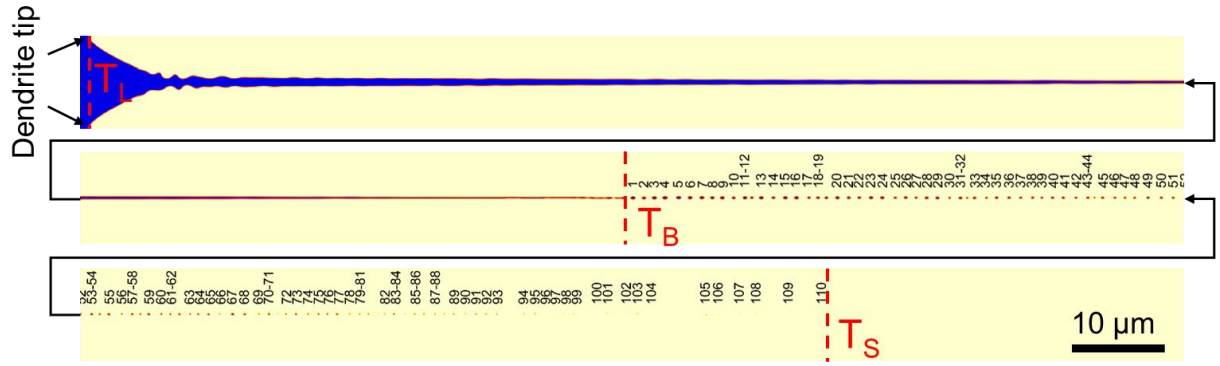

(a) Value of 5.0E-10 $m^4/J/s$

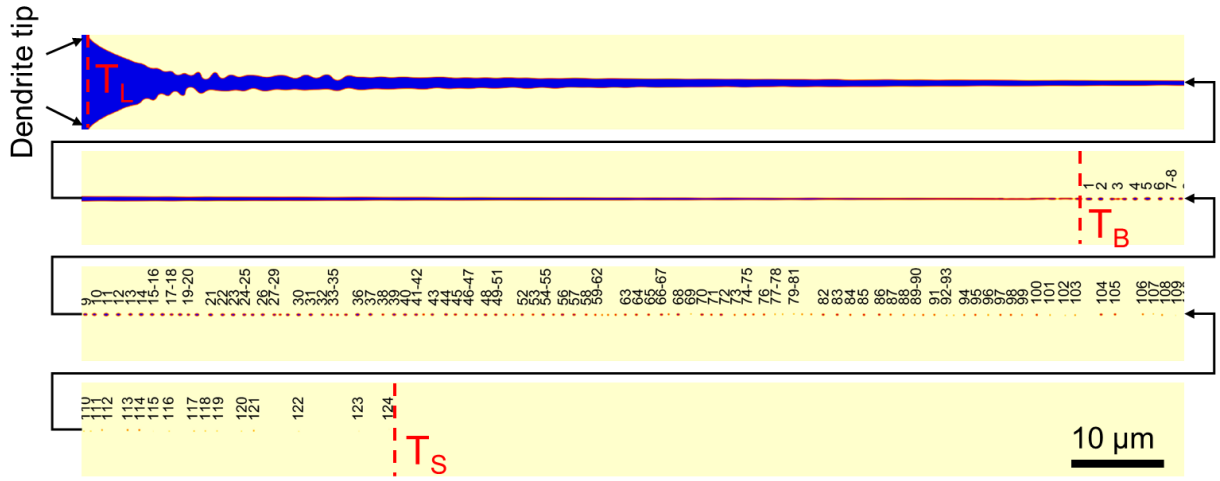

(b) Value of 10.0E-10 $m^4/J/s$

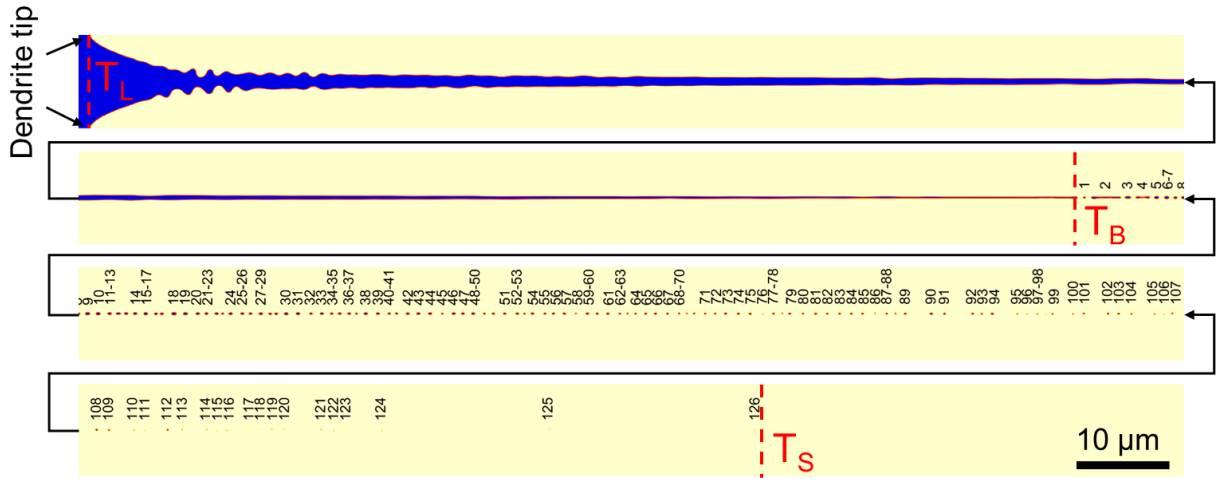

(c) Value of 15.0E-10 $m^4/J/s$

Fig. 5.10 Residual liquid distribution under different interfacial mobility and cooling rate of 745 °C/s

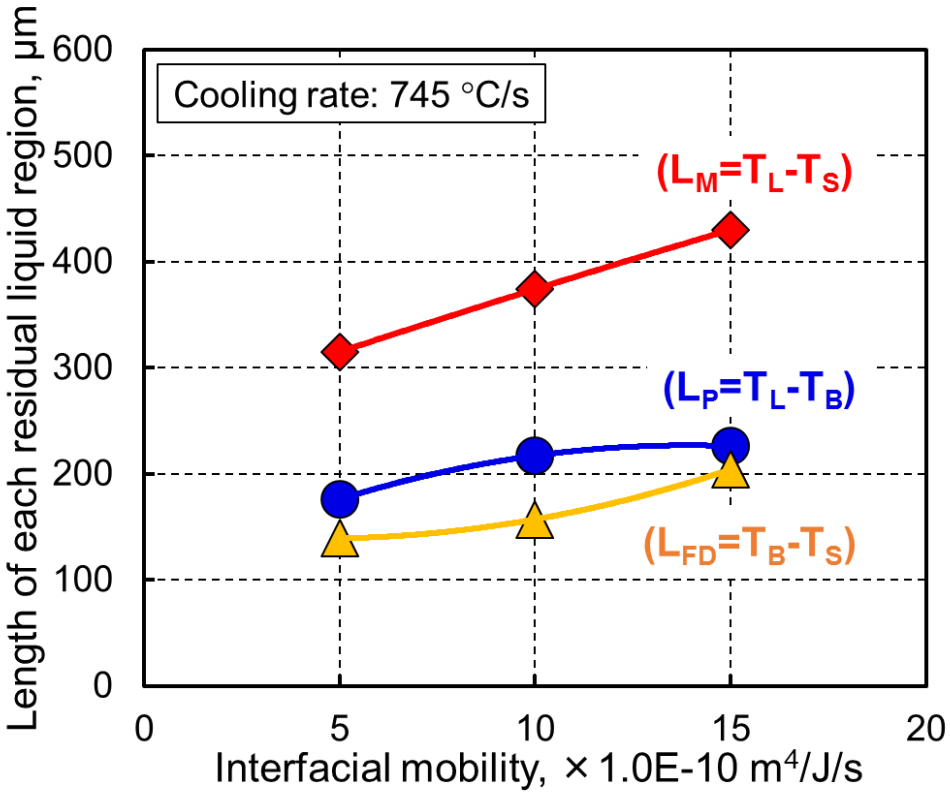

Fig. 5.11 Effect of interfacial mobility on the length of residual liquid region under cooling rate of 745 °C/s

5.4.2 Effect of anisotropy of interfacial mobility on residual liquid distribution

Anisotropy presents the difference degree of interfacial energy, interfacial thickness and interfacial mobility in different directions during solidification, causing the variation of dendrite morphology theoretically. Table 5.6 shows the parameters under different anisotropies of interfacial mobility from 0.05 to 0.20. Figure 5.12 indicates the residual liquid distribution under different anisotropies of interfacial mobility and cooling rate of 745 °C/s. With increasing anisotropy of interfacial mobility, the secondary dendrite arm and primary dendrite tip radius become smaller, and the residual liquid near the temperature T_B changes from film to dot gradually. Figure 5.13 shows the effect of anisotropy of interfacial mobility on the length of the residual liquid region quantitatively under cooling rate of 745 °C/s. With increasing anisotropy of interfacial mobility from 0.05 to 0.10, the

length of L_P (T_L to T_B) increases, however, the lengths of L_{FD} (T_B to T_S) and L_M (T_L to T_S) tend to decrease. In addition, the length of each residual liquid region nearly keep constant when the anisotropy of interfacial mobility is more than 0.10. Similar result also appears under higher cooling rates.

Theoretically, the dendrite morphology strongly depends on the anisotropy of interfacial mobility under high cooling rate [82]. When the anisotropy of interfacial mobility decreases to the low value like 0.05, the difference degree of interfacial mobility between preferred growth direction and other growth directions becomes smaller. The dendrite tends to grow in the way like isotropy, thus, the secondary dendrite arm becomes more significant and the primary dendrite tip radius becomes relatively large, as shown in Figs. 5.12 a) and 5.9 b). Furthermore, the growth of the secondary dendrite arm is conducive to promote the formation of the bridging and save more residual liquid metal in L_{FD} during solidification, resulting in an increase of T_B and a decrease of T_S, as shown in Fig. 5.12. Therefore, the above phenomena leads to a decrease in L_P (T_L to T_B) but an increase in L_{FD} (T_B to T_S) and L_M (T_L to T_S) with decreasing anisotropy of interfacial mobility from 0.10 to 0.05, as shown in Fig. 5.13. On the other hand, when the anisotropy of interfacial mobility is the middle value like from 0.075 to 0.10, this difference degree would enhance in interfacial mobility between preferred growth direction and other growth directions. Therefore, secondary dendrite arm and primary dendrite tip radius becomes smaller gradually, as shown in Figs. 5.12 b), c) and 5.9 b). When the anisotropy of interfacial mobility is the high value like more than 0.10, the similar columnar occurs during growth, as shown in Fig. 5.12 d) and e), inducing to the unchanged residual liquid region distribution, as shown in Fig. 5.13.

Table 5.6 Parameters under different anisotropies of interfacial mobility

Interfacial energy $\sigma_{L\text{-}\gamma}$, J/m^2	0.30 [15]				
Anisotropy of interfacial stiffness	0.10 [15]				
Interfacial mobility $M_{L\text{-}\gamma}$, m^4/J/s	10.0E-10				
Anisotropy of interfacial mobility	0.05	0.075	0.10	0.15	0.20

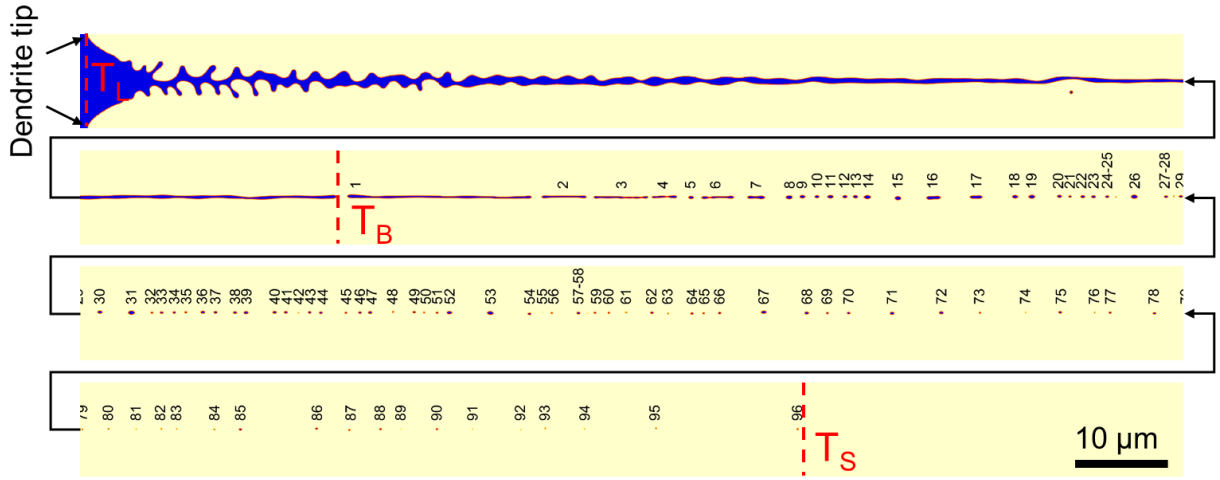

(a) Value of 0.05

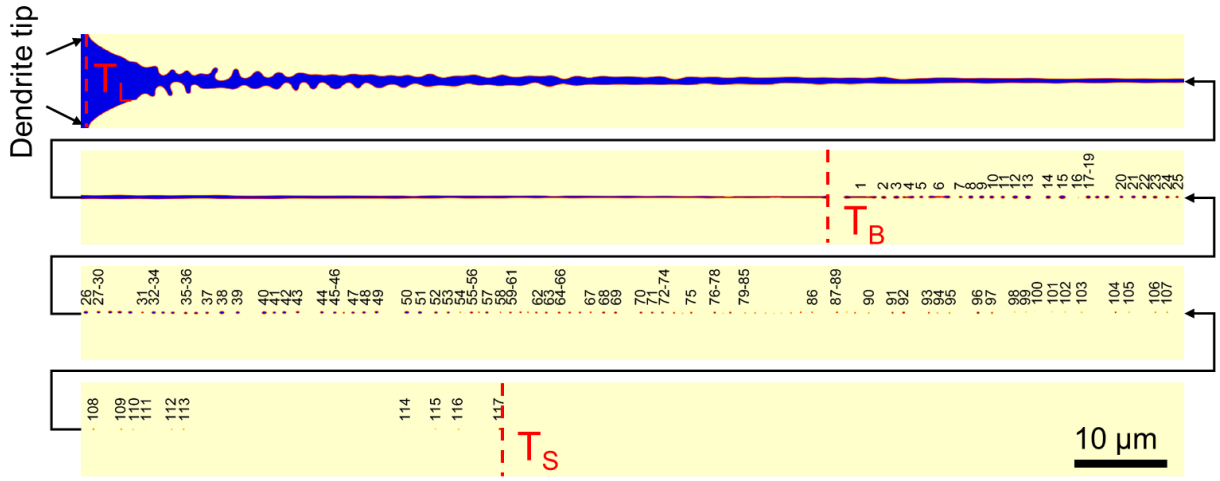

(b) Value of 0.075

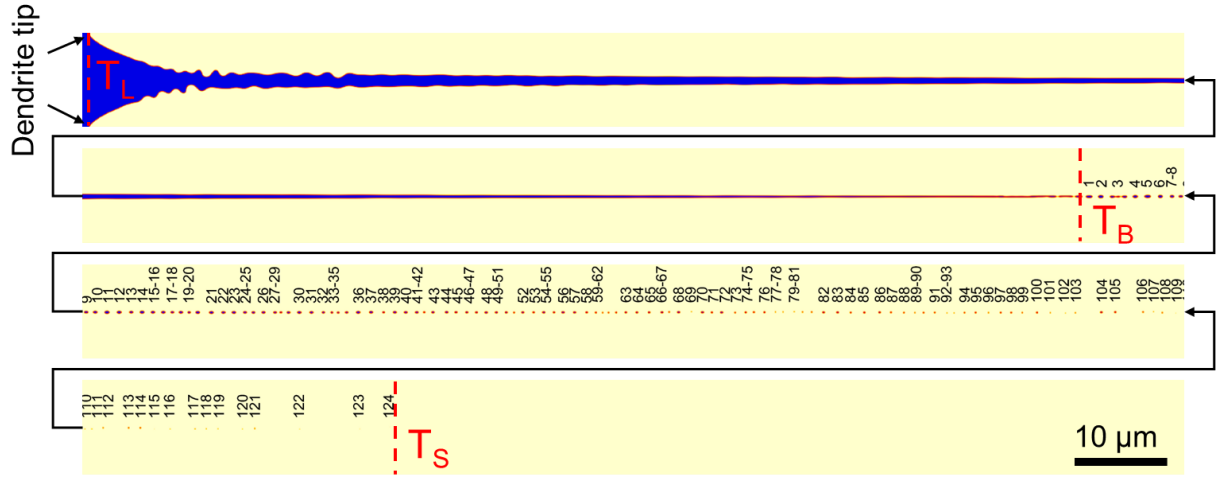

(c) Value of 0.10

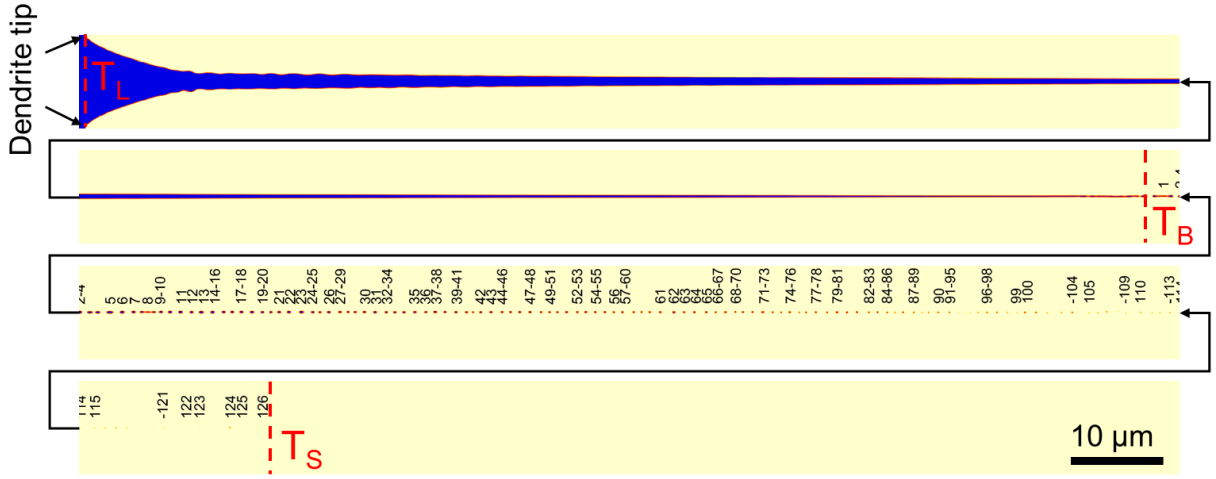

(d) Value of 0.15

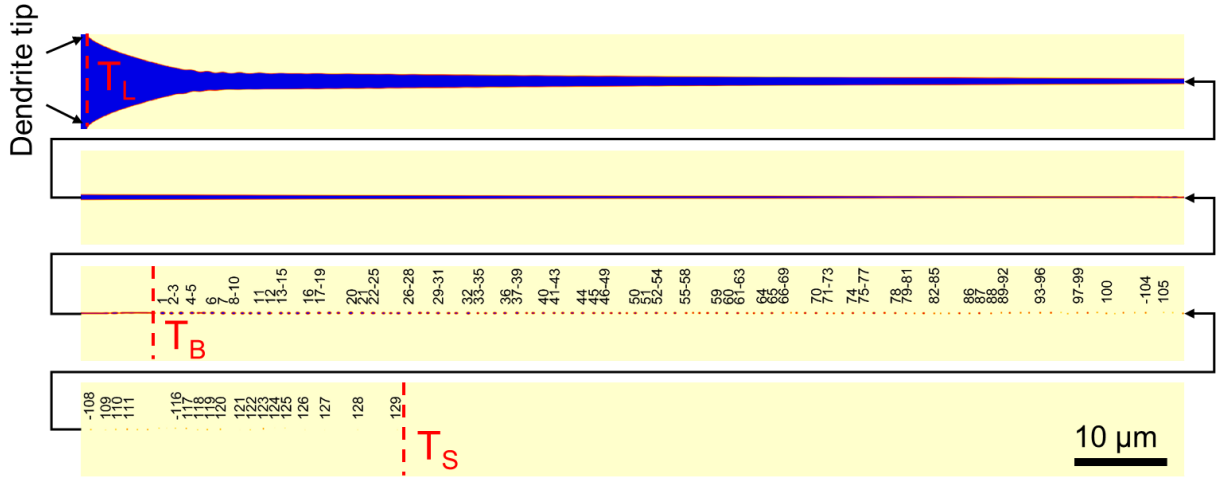

(e) Value of 0.20

Fig. 5.12 Residual liquid distribution under different anisotropies of interfacial mobility and cooling rate of 745 °C/s

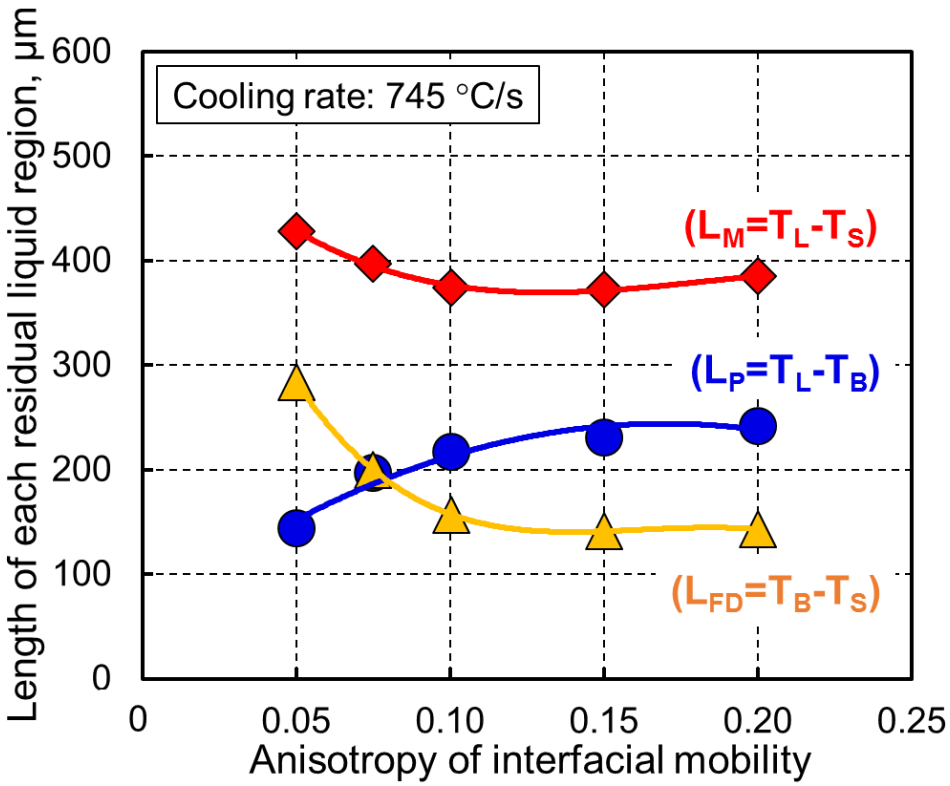

Fig. 5.13 Effect of anisotropy of interfacial mobility on the length of residual liquid region under cooling rate of 745 °C/s

5.4.3 Effect of interfacial energy on residual liquid distribution

Additionally, the effect of the parameters like interfacial energy and anisotropy of interfacial stiffness on the residual liquid distribution are also investigated. Interfacial energy presents the degree of lattice distortion on the curvature of the interface between two phases. Main influencing factors are the curvature of the crystal surface, atomic density on the bare crystal surface, forces on the interface atoms by external medium and so on. Table 5.7 shows the parameters under different interfacial energies changed from 0.10 to 0.40 J/m^2. Moreover, interfacial mobility of 10.0E-10 m^4/J/s is used due to the appearance of relatively more obvious secondary dendrite arm, as shown in Fig. 5.10 b).

Figure 5.14 shows the residual liquid distribution under different interfacial energies and cooling rate of 745 °C/s. With decreasing interfacial energy, the secondary dendrite arm becomes more significant. In addition, the residual liquid film near the temperature

T_B becomes obviously and relatively longer under low interfacial energy. Figure 5.15 indicates the effect of interfacial energy on the length of the residual liquid region quantitatively under cooling rate of 745 °C/s. With increasing interfacial energy from 0.10 to 0.40 J/m^2, the length of L_P (T_L to T_B) has a tendency of increase. However, the lengths of L_{FD} (T_B to T_S), and L_M (T_L to T_S) decrease gradually.

According to the kinetic theory of interface stability [83], the interface stability is affected by not only temperature gradient and concentration gradient, but also interference occurred at the interface during dendrite growth. Any periodic interference can be considered as sinusoidal interference. Thus, the interface stability is determined by the rate of change of the sine wave amplitude with time, the equation is given as,

$$S(\omega) = -T_m \Gamma \omega^2 - \frac{1}{2}(g_S + g_L) + mG_C \frac{\omega_C - (\frac{v}{D})}{\omega_C - (\frac{v}{D})(1-k_0)} \quad (5.12)$$

where $S(\omega)$ decides the interface stability ($S(\omega)$<0 means interface stability and $S(\omega)$>0 means interface instability);

T_m is melting point;

Γ is Gibbs-Thomson coefficient ($\Gamma = \frac{\sigma}{\Delta Sf}$, where σ is liquid-solid interface energy, ΔSf is melting entropy);

ω is vibrational frequency;

g_S means influence of solidus temperature gradient on interface stability;

g_L means influence of liquidus temperature gradient on interface stability;

m is the slope of liquidus;

G_C is liquidus concentration gradient;

ω_C is vibrational frequency of solute;

v is growth rate;

D is liquidus diffusion;

k_0 is partition coefficient.

In the above interface stability equation, the first item is decided by interfacial energy, the secondary item illustrates the influence of temperature gradient and the last item is determined by concentration gradient. Significantly, the interfacial energy item contributes

negative value, which means relative unstable interface could occur under low interfacial energy.

Therefore, with decreasing interfacial energy, the interface changes into more unstable, resulting in the growth of the secondary dendrite arm as shown in Fig. 5.14 a). Then, the bridging becomes more significant as a contribution of the growth of the secondary dendrite arm with declining temperature, causing a decrease in the length of L_P (T_L to T_B). In addition, a mass of the bridging is capable of saving much more residual liquid metal between adjacent dendrites during solidification. Therefore, the lengths of L_{FD} (T_B to T_S), and L_M (T_L to T_S) increases obviously when interfacial energy decreases.

Table 5.7 Parameters under different interfacial energies

Interfacial energy $\sigma_{L\text{-}\gamma}$, J/m^2	0.10	0.20	0.30	0.40
Anisotropy of interfacial stiffness	0.10 [15]			
Interfacial mobility $M_{L\text{-}\gamma}$, m^4/J/s	10.0E-10			
Anisotropy of interfacial mobility	0.10 [15]			

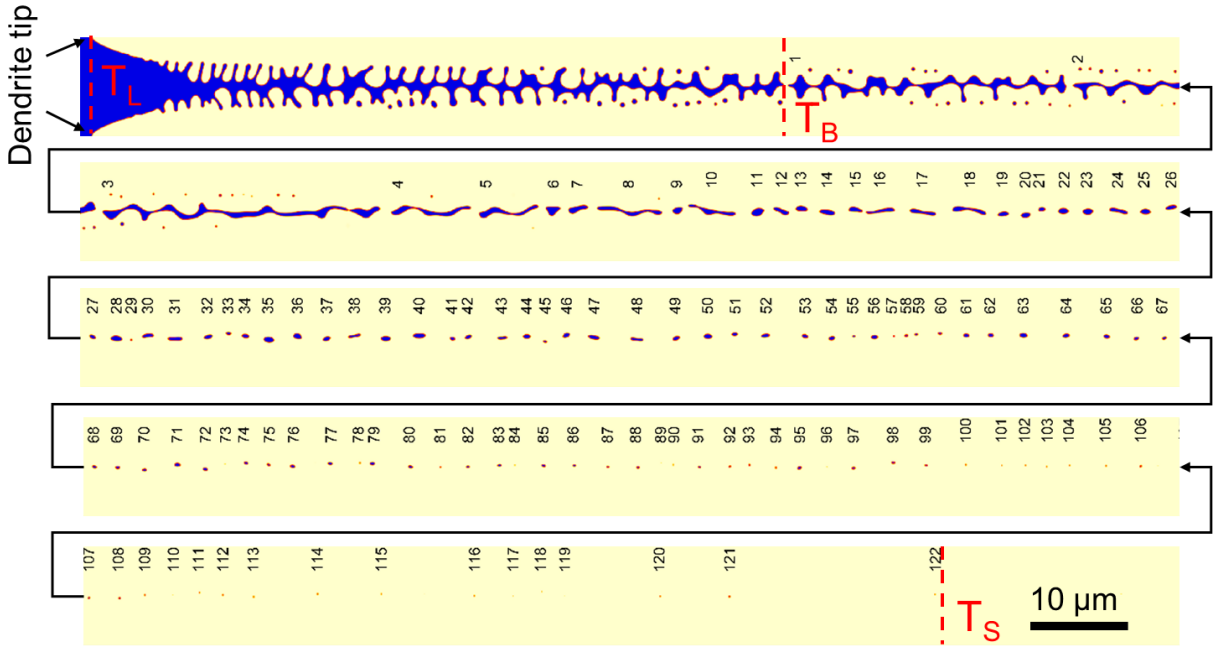

(a) Value of 0.10 J/m^2

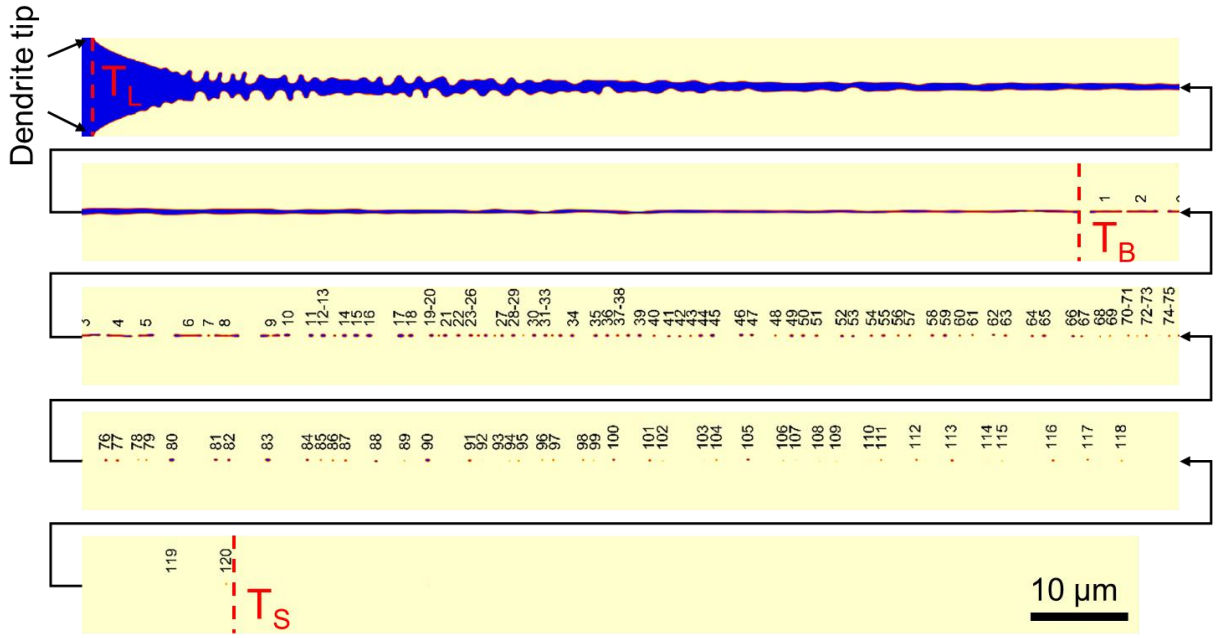

(b) Value of 0.20 J/m^2

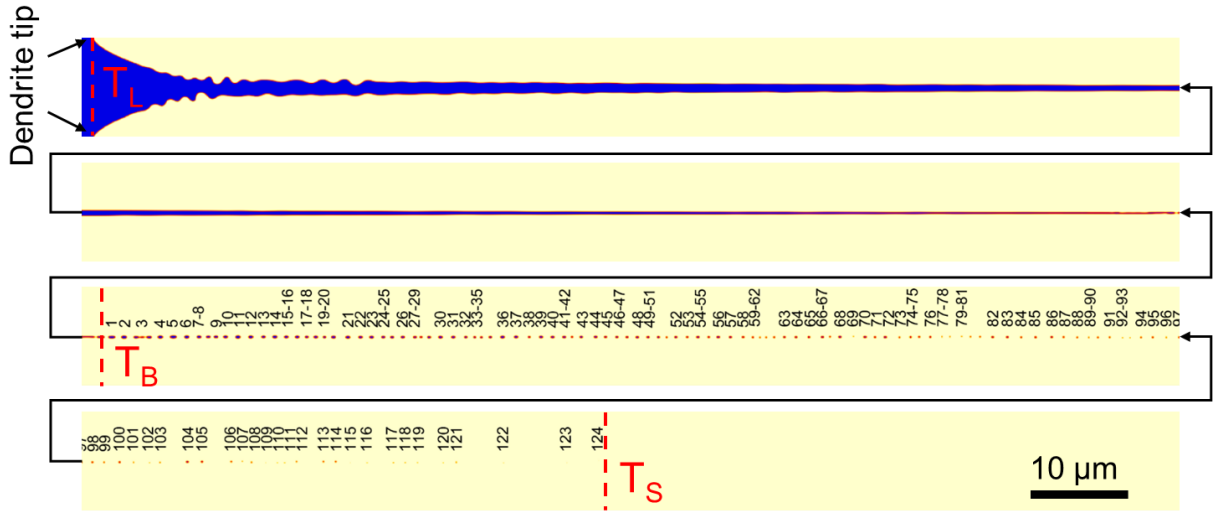

(c) Value of 0.30 J/m^2

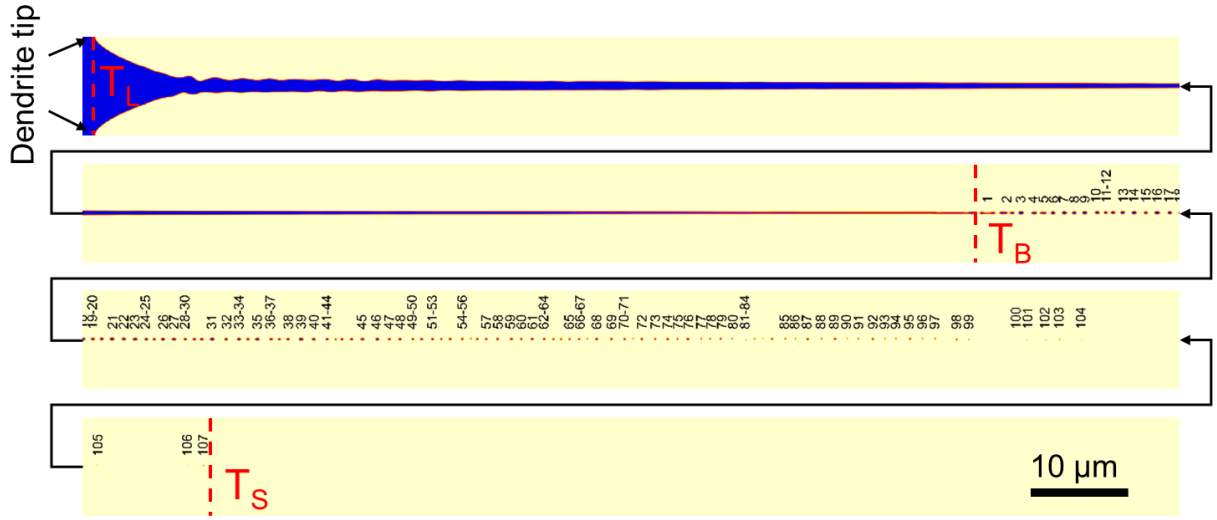

(d) Value of 0.40 J/m^2

Fig. 5.14 Residual liquid distribution under different interfacial energies and cooling rate of 745 °C/s.

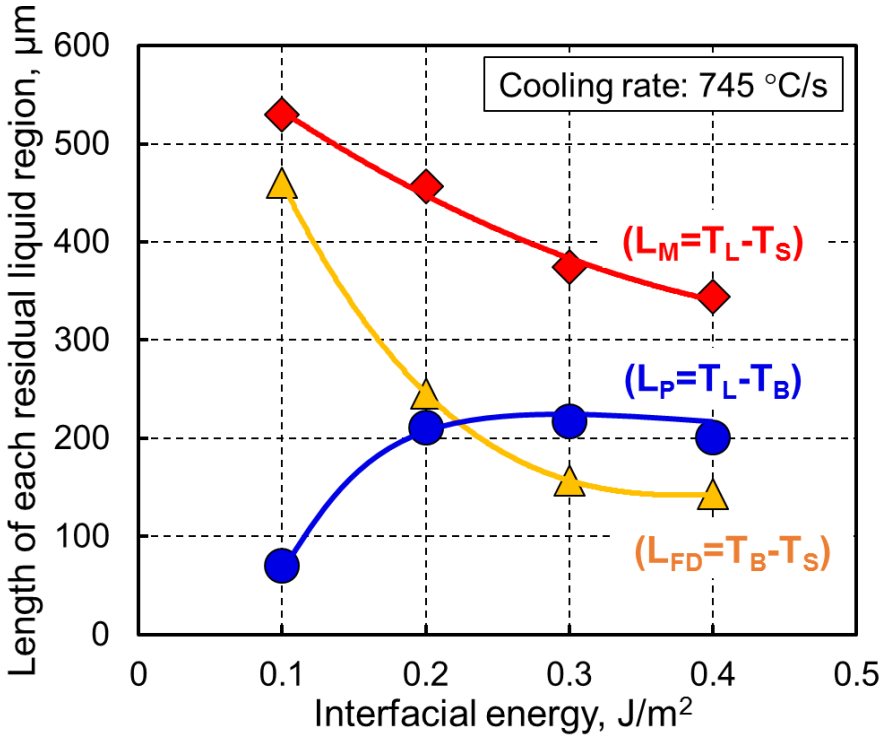

Fig. 5.15 Effect of interfacial energy on the length of residual liquid region under cooling rate of 745 °C/s

5.4.4 Effect of anisotropy of interfacial stiffness on residual liquid distribution

Table 5.8 shows the parameters under different anisotropies of interfacial stiffness varied from 0.025 to 0.50. Figure 5.16 shows the residual liquid distribution under different anisotropies of interfacial stiffness and cooling rate of 745 °C/s. The morphology of primary dendrite tip and secondary dendrite arm is nearly the same under different anisotropies of interfacial stiffness from 0.025 to 0.10. However, from 0.10 to 0.50, the secondary dendrite arm disappears gradually. Figure 5.17 shows the effect of anisotropy of interfacial stiffness on the length of the residual liquid region quantitatively under cooling rate of 745 °C/s. The length of each region is also the nearly same from 0.025 to 0.10 in anisotropy of interfacial stiffness. However, the lengths of L_P (T_L to T_B) and L_M (T_L to T_S) tend to rise slightly, and the length of L_{FD} (T_B to T_S) has a little down with increasing anisotropy of interfacial stiffness from 0.10 to 0.50.

Under high cooling rate, the dendrite morphology is mainly determined by anisotropy of interfacial mobility. However, under low cooling rate, the dendrite morphology is influenced by anisotropy of interfacial stiffness [82]. Therefore, the dendrite morphology and the length of each region are the same as a whole by changing anisotropy of interfacial stiffness, especially in the range from 0.025 to 0.10. While, with increasing the value from 0.10 to 0.50, the influence of interfacial energy in intensity would be amplified, leading to the disappearance of secondary dendrite arm as a result of the occurrence of the stable interface. Thus, it is relatively difficult to form the significant bridging. Thus, the length of L_P (T_L to T_B) increases a little with increasing anisotropy of interfacial stiffness.

Table 5.8 Parameters under different anisotropies of interfacial stiffness

Interfacial energy $\sigma_{L\text{-}\gamma}$, J/m^2	0.30 [15]				
Anisotropy of interfacial stiffness	0.025	0.05	0.075	0.10	0.25
Interfacial mobility $M_{L\text{-}\gamma}$, m^4/J/s	10.0E-10				
Anisotropy of interfacial mobility	0.10 [15]				

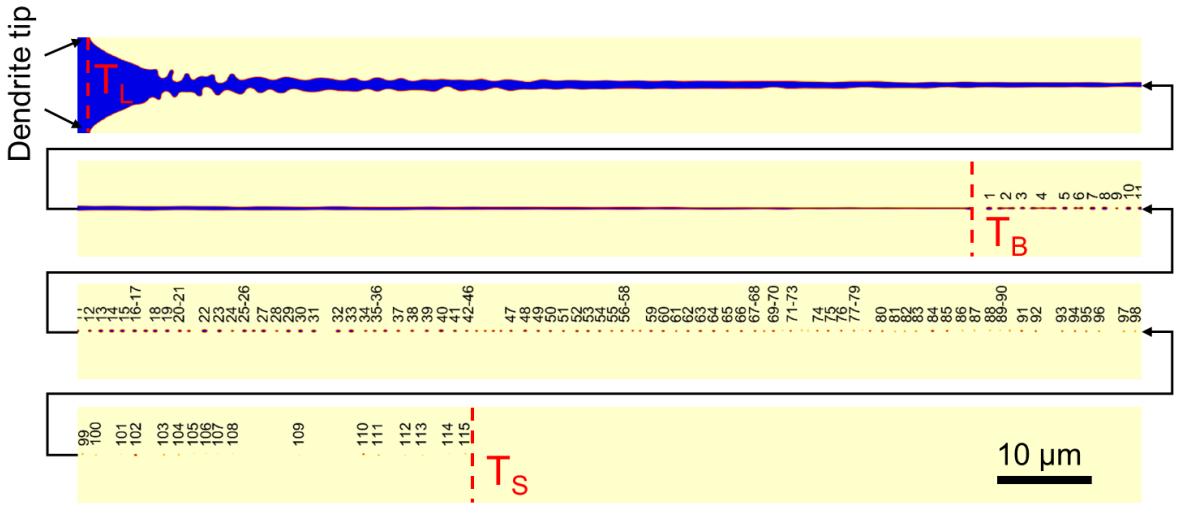

(a) Value of 0.025

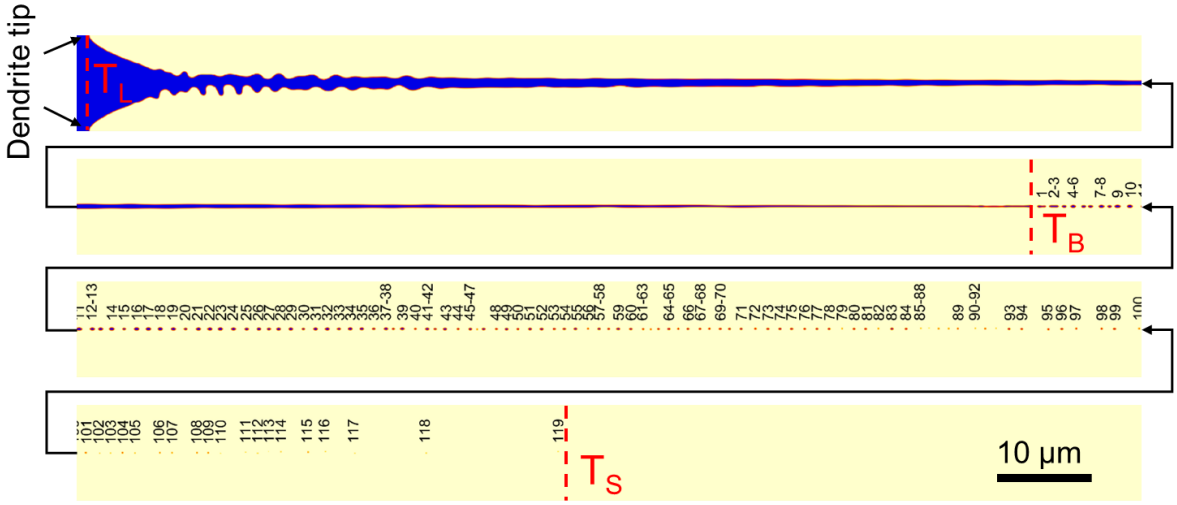

(b) Value of 0.05

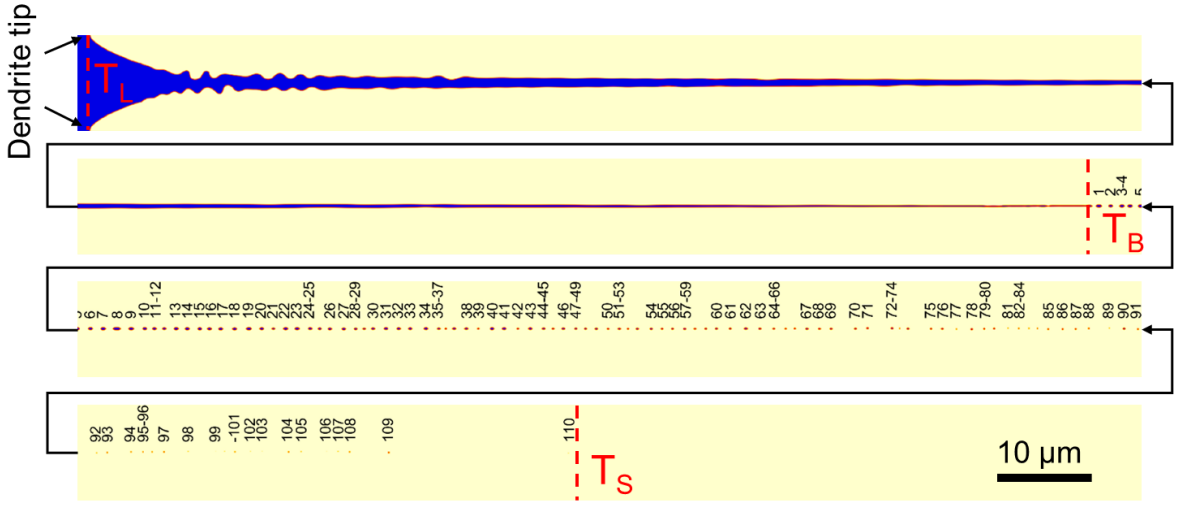

(c) Value of 0.075

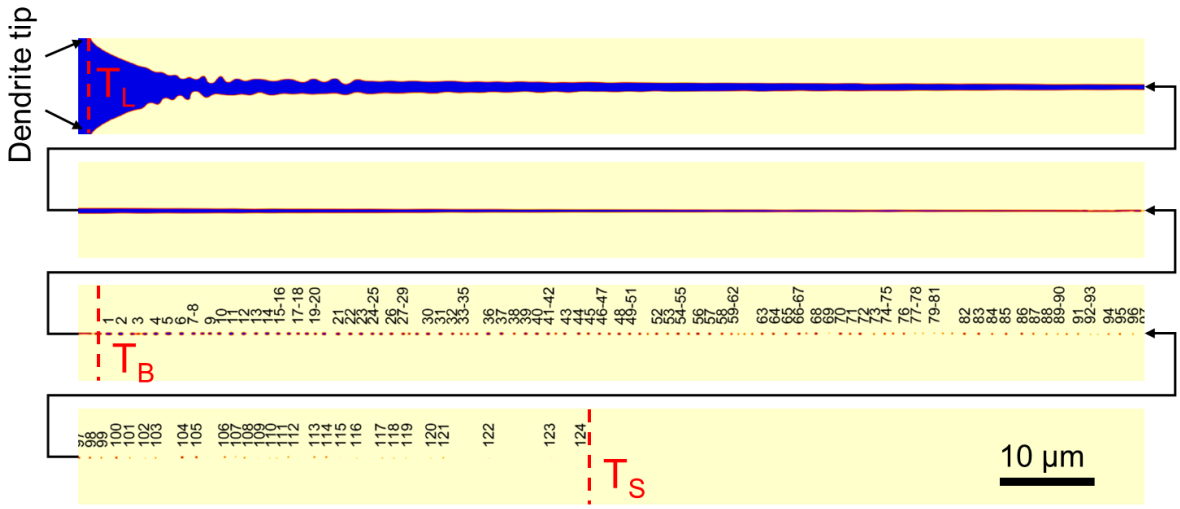

(d) Value of 0.10

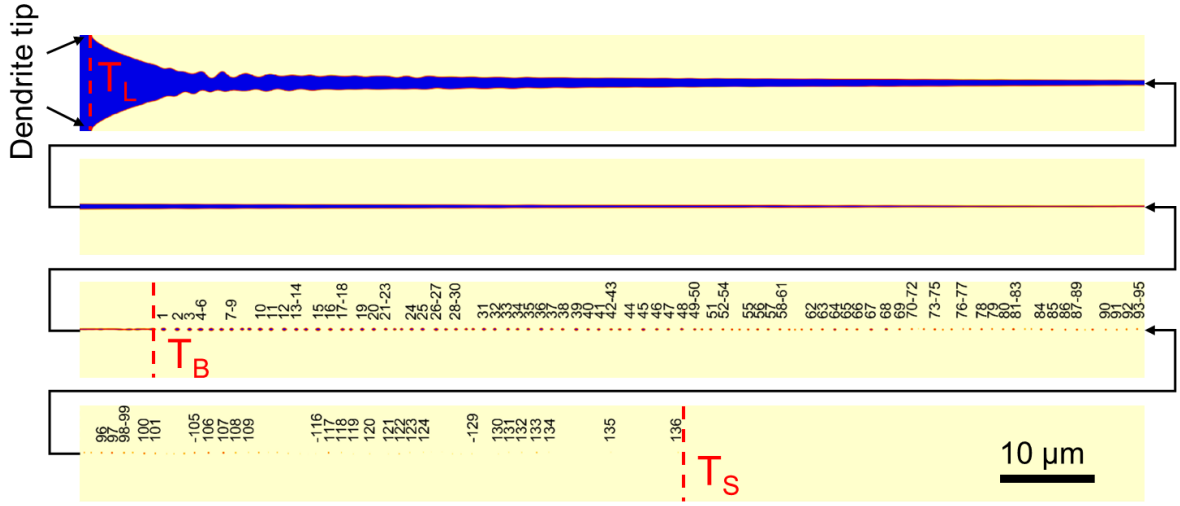

(e) Value of 0.25

Fig. 5.16 Residual liquid distribution under different anisotropies of interfacial stiffness and cooling rate of 745 °C/s

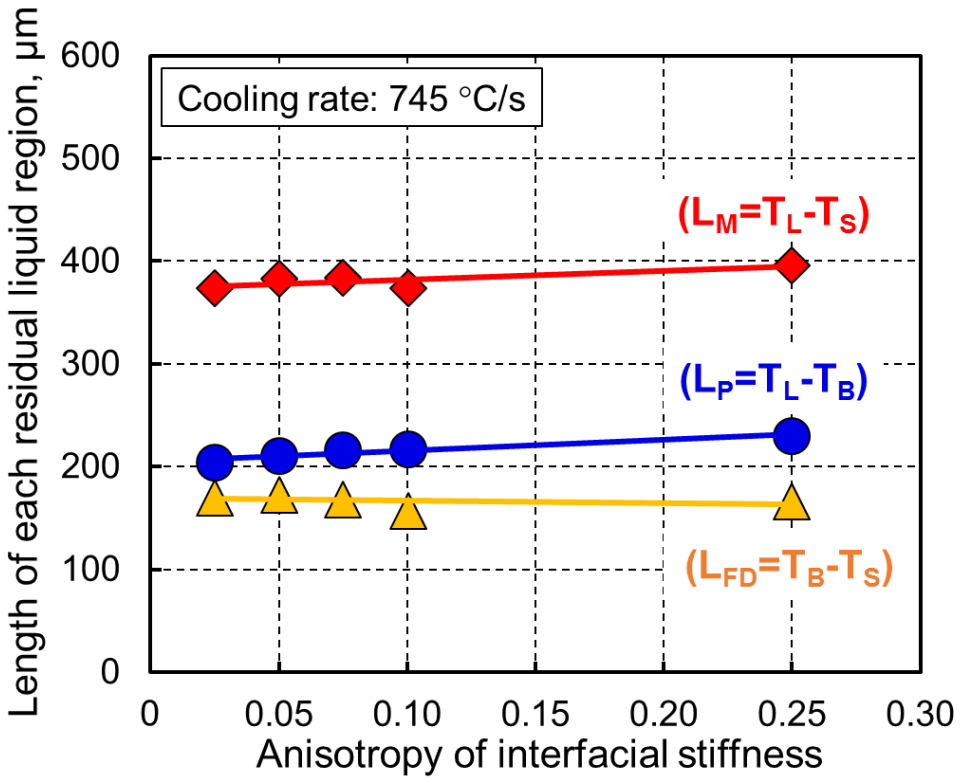

Fig. 5.17 Effect of anisotropy of interfacial stiffness on the length of residual liquid region under cooling rate of 745 °C/s

5.5 Comparison of Residual Liquid Distribution and Experimental Result

In this calculation, interfacial energy of 0.30 J/m^2 and anisotropy of interfacial stiffness of 0.10 are the same as reference paper, because interfacial energy does not depend on the cooling rate, and the effect of anisotropy of interfacial stiffness on residual liquid distribution is relatively small under high cooling rate. Moreover, interfacial mobility and anisotropy of interfacial mobility are adjusted for each cooling rate, respectively.

Figure 5.18 shows the method to obtain the matching residual liquid distribution as that of experiment under cooling rate of 848 °C/s. The blue and yellow bars present the lengths of L_P (T_L to T_B) and L_{FD} (T_B to T_S), respectively. In order to predict the correct residual liquid distribution, the length of each region should be adjusted. According to the above investigations, the length of each residual liquid region keeps constant when anisotropy of interfacial mobility is more than 0.10, thus, the calculation results are obtained firstly by

adjusting interfacial mobility and setting anisotropies of interfacial mobility of 0.10, as shown in Fig. 5.18 a). When the interfacial mobility is 10.0E-10 $m^4/J/s$, the length of L_P (T_L to T_B) in the calculation result is 191 μm which is longer than that of crack (180 μm), and the length of L_{FD} (T_B to T_S) in the calculation result is 144 μm which is shorter than that of the crack (170 μm). As is mentioned, the lengths of L_P (T_L to T_B) and L_{FD} (T_B to T_S) tend to decrease and increase with decreasing anisotropy of interfacial mobility from 0.1 to 0.05, respectively. Therefore, the matching residual liquid distribution can be obtained only if decreasing anisotropy of interfacial mobility and setting interfacial mobility of 10.0E-10 $m^4/J/s$, as shown in Fig. 5.18 b). Finally, the length of each residual liquid region is nearly the same as that of fracture surface under the anisotropy of interfacial mobility of 0.09 and interfacial mobility of 10.0E-10 $m^4/J/s$.

Figure 5.19 shows the comparison of the length of residual liquid region with that of the fracture surface under higher cooling rates of 2665 and 2896 °C/s by changing anisotropy of interfacial mobility. Under cooing rate of 2665 °C/s, when anisotropy of interfacial mobility is 0.0475, even though the length of L_P (T_L to T_B) is a little longer than that of the fracture surface, however, the length of L_{FD} (T_B to T_S) is 175 μm which is the same as the value of the fracture surface, as shown in Fig. 5.19 a). In addition, the result under cooling rate of 2896 °C/s is similar as that of 2665 °C/s. When anisotropy of interfacial mobility is 0.005, even though the length of L_P (T_L to T_B) is a little longer than that of the fracture surface, however, the length of L_{FD} (T_B to T_S) is 160 μm which is nearly the same as the value of the fracture surface (158 μm), as shown in Fig. 5.19 b).

Figure 5.20 shows the final comparison of calculation and experimental result under different cooling rates by adjusting calculation parameters. As a whole, the length of each region in the calculation result is nearly the same as that of the crack for each cooling rate. Therefore, the residual liquid distribution can be predicted by verifying with experimental result. And the corresponding optimized calculation parameters after verification with experiment are shown in Table 5.9.

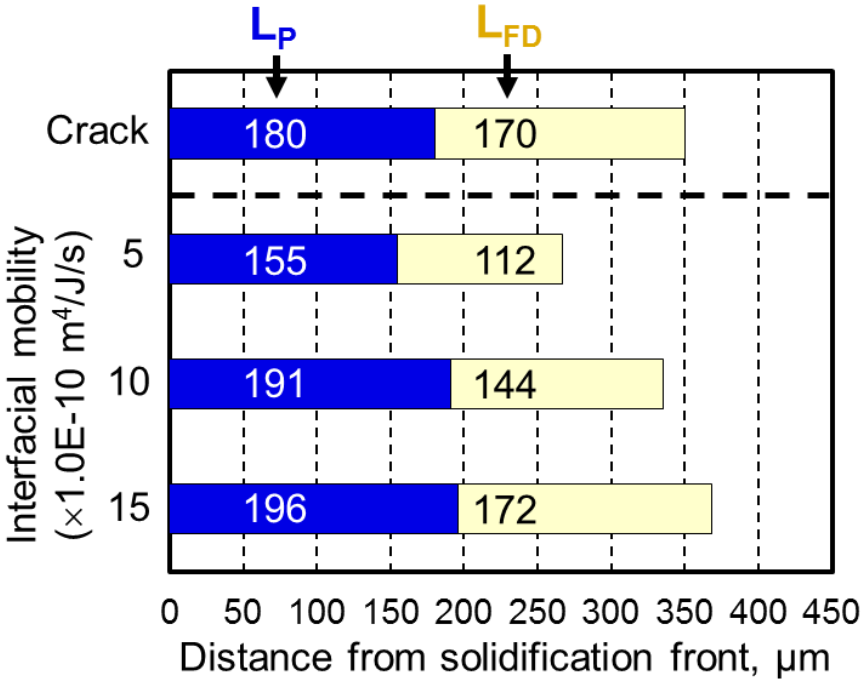

(a) Under anisotropy of interfacial mobility of 0.10

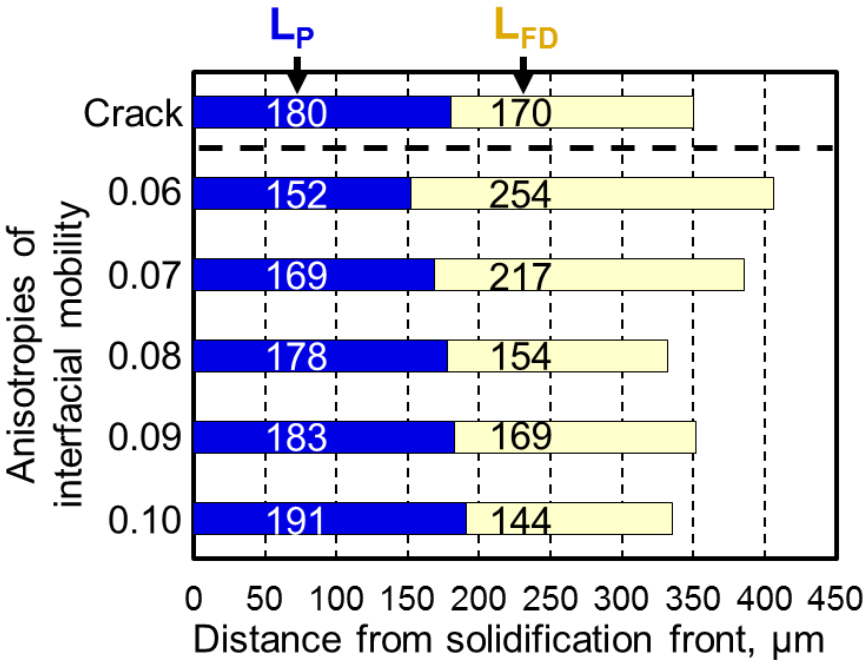

(b) Under interfacial mobility of 10.0E-10 $m^4/J/s$

Fig. 5.18 Length of residual liquid region with compared to the length of fracture surface under cooling rate of 848 °C/s by adjusting calculation parameters

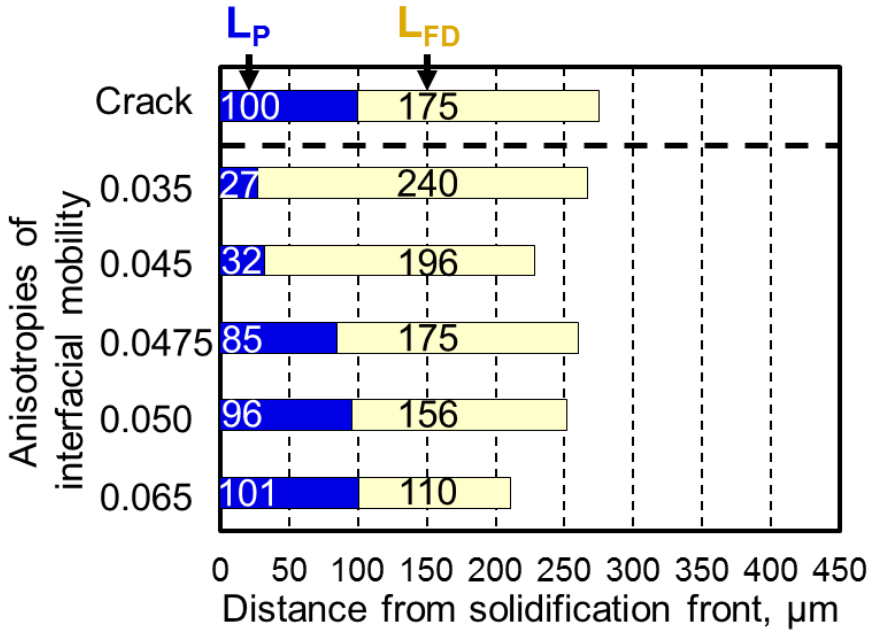

(a) Cooling rate of 2665 °C/s under interfacial mobility of 40.0E-10 $m^4/J/s$

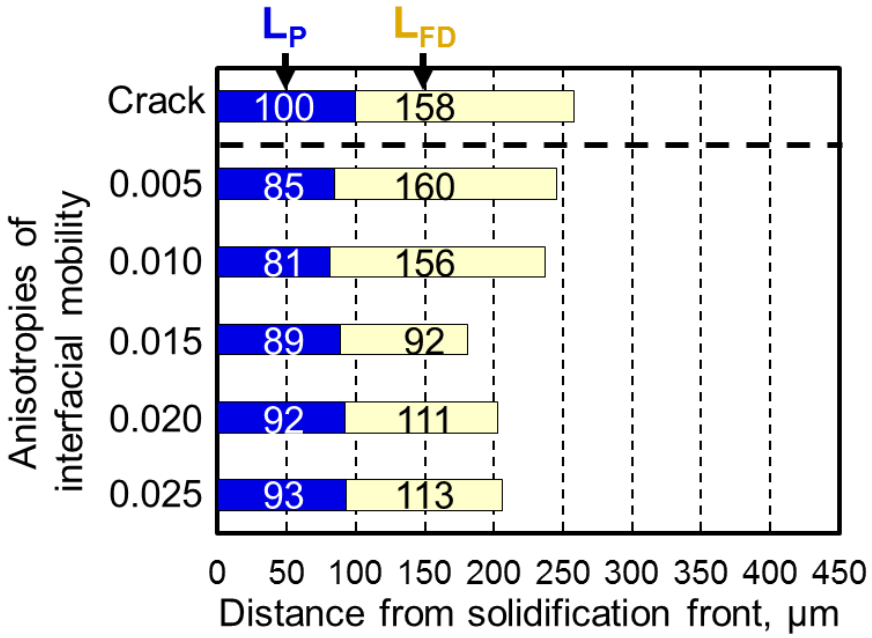

(b) Cooling rate of 2896 °C/s under interfacial mobility of 60.0E-10 $m^4/J/s$

Fig. 5.19 Length of residual liquid region with compared to the length of fracture surface under higher cooling rates of 2665 and 2896 °C/s

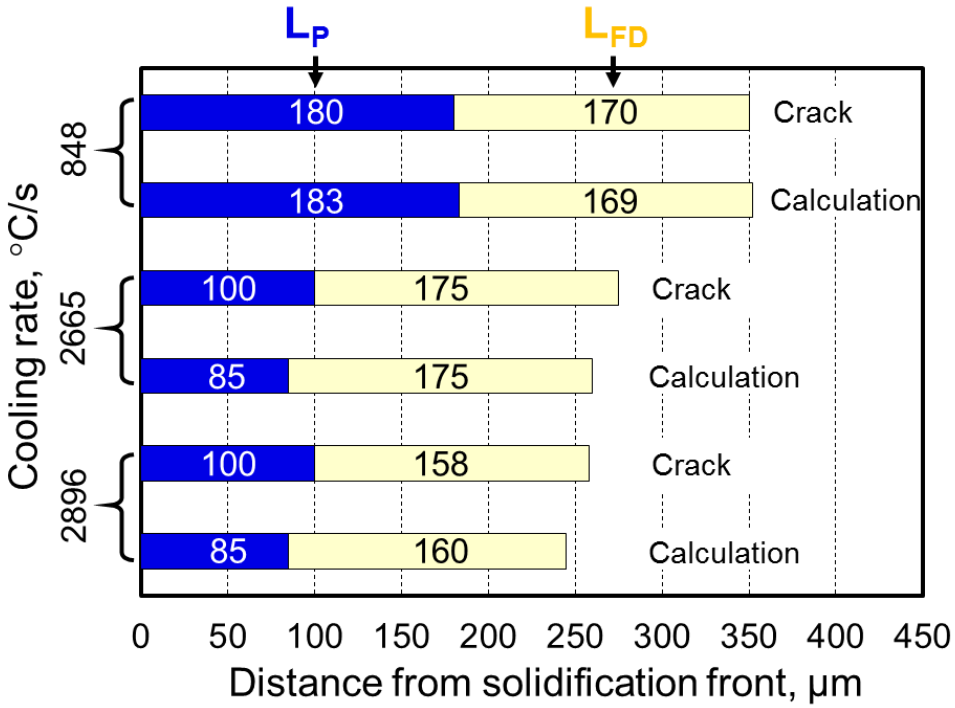

Fig. 5.20 Comparison of length of residual liquid region between calculation and crack for each cooling rate

Table 5.9 Optimized calculation parameters after verifying with experiment results

Cooling rate, °C/s	848	2665	2896
Interfacial mobility, $m^4/J/s$	10E-10	40E-10	60E-10
Anisotropy of interfacial mobility	0.09	0.0475	0.005

5.6 Prediction of Morphology and Distribution of Residual Liquid Metal

Figure 5.21 shows the residual liquid distribution under different cooling rates after verification with experimental result. By comparison, the relatively longer residual liquid film appears just below the temperature T_B under high cooling rates of 2665 and 2896 °C/s compared with those under cooling rate of 848 °C/s, as shown in Fig. 5.21. For each cooling rate, the residual liquid changes from film to dot structure with decreasing temperature and the residual liquid dot structure with isolated morphology distributes at the terminal of solidification.

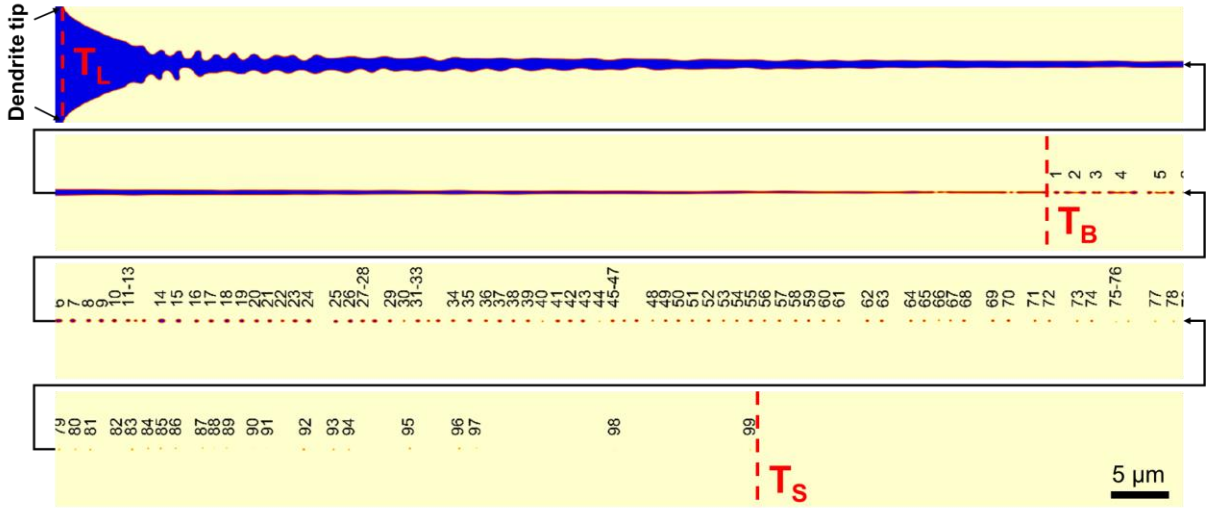

(a) Cooling rate of 848 °C/s

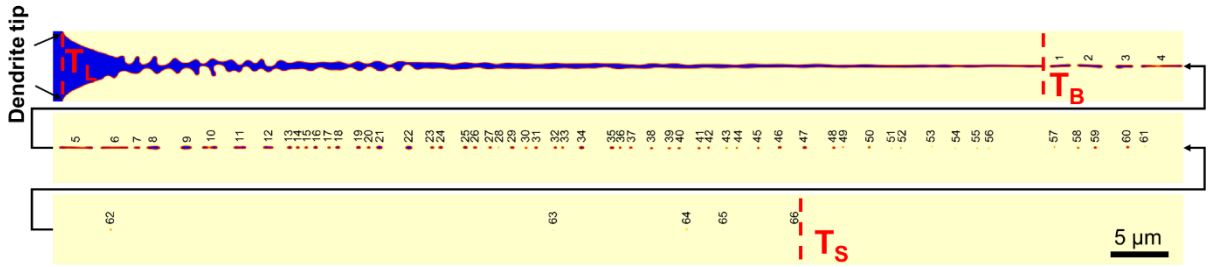

(b) Cooling rate of 2665 °C/s

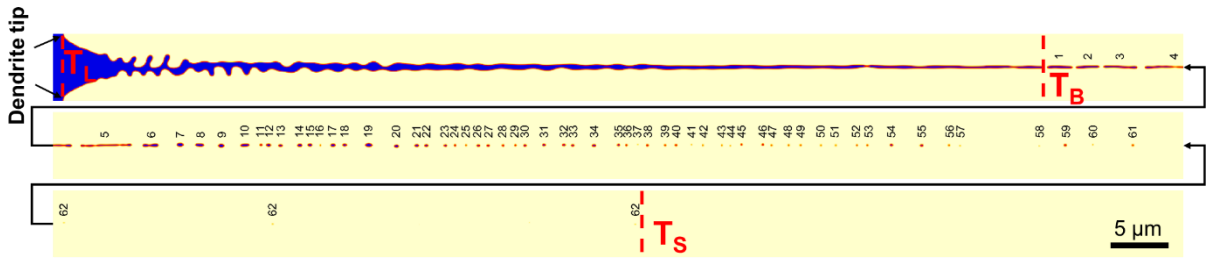

(c) Cooling rate of 2896 °C/s

Fig. 5.21 Residual liquid distribution under different cooling rates after verification with experimental results

5.7 Relationship between Residual Liquid Metal and Solidification Cracking Susceptibility

Figure 5.22 shows the schematic illustration of calculation result and high temperature ductility curve. The high temperature ductility curve is expressed by blue solid line (critical strain by experiment) and dash line (critical strain by estimation). In this calculation result, the L_P (T_L-T_B) is divided into two regions which are the free liquid region from T_L to T_1 and the long continuous film region from T_1 to T_B, respectively. Because the residual liquid between adjacent dendrites directly connects with molten pool and can move freely in the free liquid region from T_L to T_1, the liquid healing will appear easily if crack occurs causing a relatively high critical strain and a low solidification cracking susceptibility. Thus, it is difficult to measure the critical strain in the free liquid region by experiment, as indicated by blue dash line. With decreasing temperature, the secondary dendrite arm grows, which can hinder the movement of the residual liquid and can generate a long continuous film from T_1 to T_B. If the crack occurs, this long continuous film would contribute to a relatively small critical strain and a relatively high solidification cracking susceptibility due to hard to use free liquid near the molten pool to heal the crack.

While, the L_{FD} (T_B-T_S) in the calculation result is also divided into two regions which are isolated film region from T_B to T_2 and dot region from T_2 to T_S, respectively. Due to the formation of the bridging, the residual liquid in the L_{FD} (T_B-T_S) does not connect with the molten pool, therefore, the isolated film and dot exist in the L_{FD}. Because the residual liquid film is isolated in the isolated film region from T_B to T_2, the ductility has a little recovering which would result in a slight increase in the critical strain, however, it is still possible to contribute to a relatively small critical strain if the crack occurs. Continuing to reduce the temperature, the isolated dot will distribute in the dot region from T_2 to T_S, leading to a large improvement in the ductility recovering. Thus, it is difficult to crack and to measure the critical strain in the dot region by experiment, as indicated by blue dash line.

As is mentioned, the BTR depends on the residual liquid metal distribution at the terminal of solidification. Under cooling rates of 848, 2665 and 2896 °C/s, the similar distribution of the residual liquid dot structure at the terminal of solidification contributes to the same value of the BTR.

While, the minimum local critical strain strongly depends on the morphology and distribution of the residual liquid in the region from T_1 to T_2. However, at present it is difficult to decide the critical temperature T_1. In the case of the critical temperature T_2, it can be assumed in the position where the length of the residual liquid is not larger than 0.5 μm because the size of the hollow is around 0.5 μm in the fracture surface of the crack. Thus, in this case, we focus on the region from T_B to T_2 to evaluate the minimum critical strain.

Figure 5.23 shows the prediction of the temperature region from T_B to T_2 for each cooling rate. This region under cooling rate of 848 °C/s is a little smaller (10 °C) than those of high cooling rates of 2665 and 2896 °C/s. And this region is nearly the same (14 °C) under the two high cooling rates. However, as is mentioned, the minimum local critical strain does not depend on the length of the residual liquid region, but depend on the morphology and distribution of the residual liquid in this region. Figure 5.24 shows the schematic image to understand the occurrence of the minimum local critical stain. Compared with the distribution of relatively short residual liquid film or dot in the region from T_B to T_2 in Fig. 5.24 a), lots of relatively long residual liquid film which distribute in the same region from T_B to T_2 in Fig. 5.24 b) would contribute to the smaller minimum critical strain if the crack occurs. Therefore, the obvious and long residual liquid film in the region from T_B to T_2 under high cooling rate of 2665 and 2896 °C/s corresponding to that of welding speeds of 1.0 and 1.5 m/min in Fig. 5.21 b) and c) results in the lower minimum critical strain, while the short residual liquid film with some dots in the region from T_B to T_2 under cooling rate of 848 °C/s corresponding to that of welding speed of 0.2 m/min in Fig. 5.21 a) would cause a relatively high minimum critical strain.

Thus, comprehensively, by considering both the effect of the BTR and local critical strain, the solidification cracking susceptibility of type 310S stainless steel during LBW increases with increasing welding speed as a contribution of similar dot distribution at the terminal of solidification corresponding to that of nearly the same BTR, and obvious and long residual liquid film in the region from T_B to T_2 corresponding to that of the lower minimum local critical strain, as shown in Fig. 2.9.

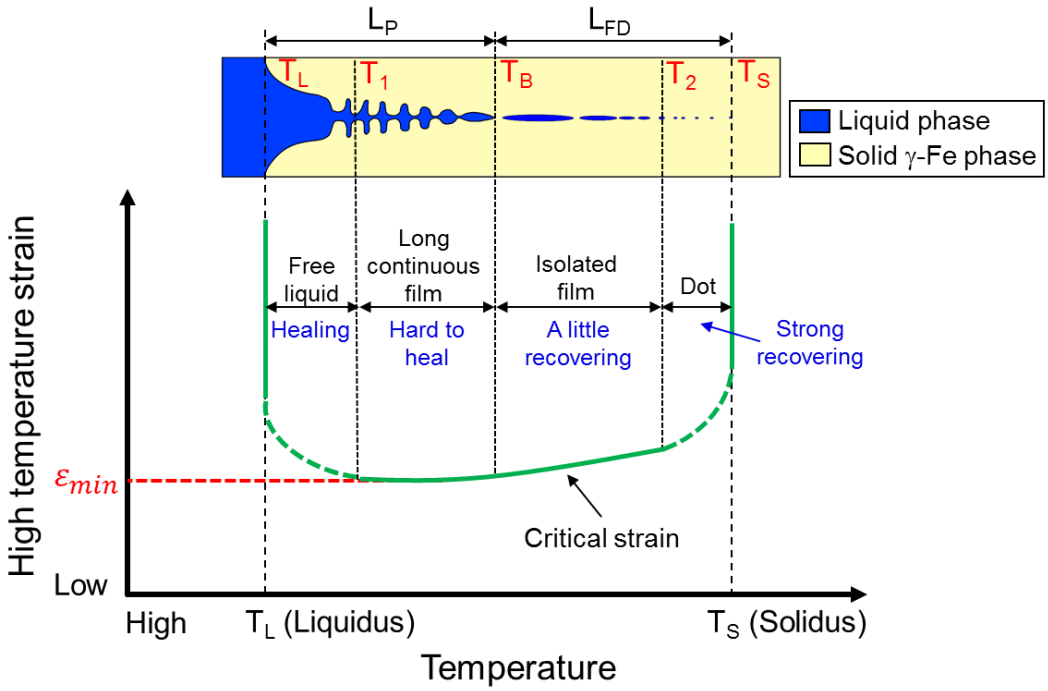

Fig. 5.22 Schematic illustration of calculation result and high temperature ductility curve

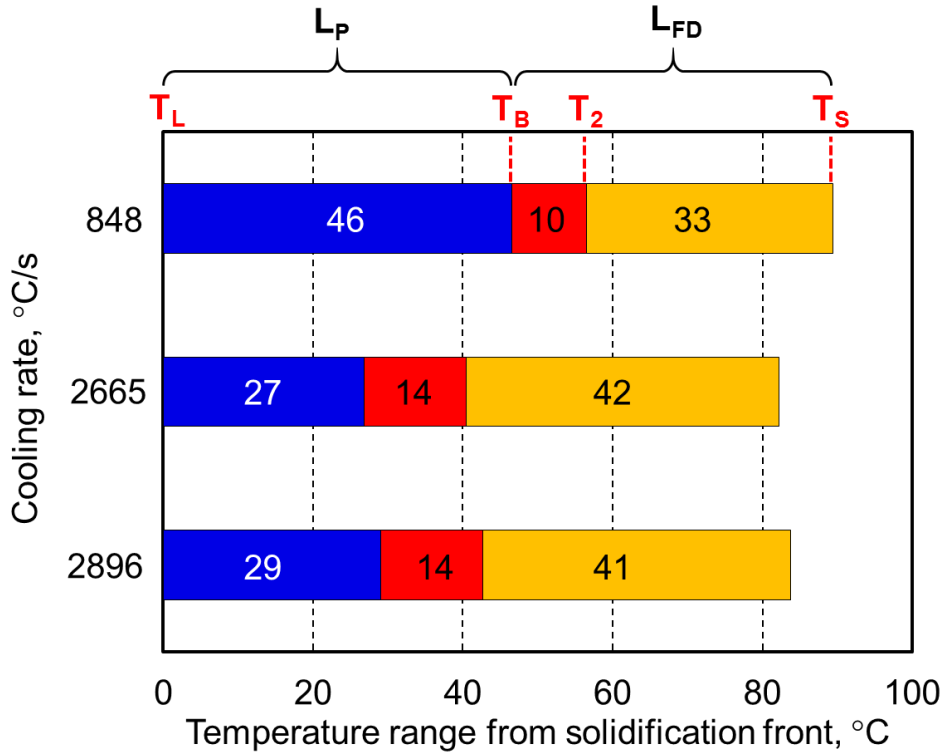

Fig. 5.23 Prediction of the temperature region from T_B to T_2 for each cooling rate

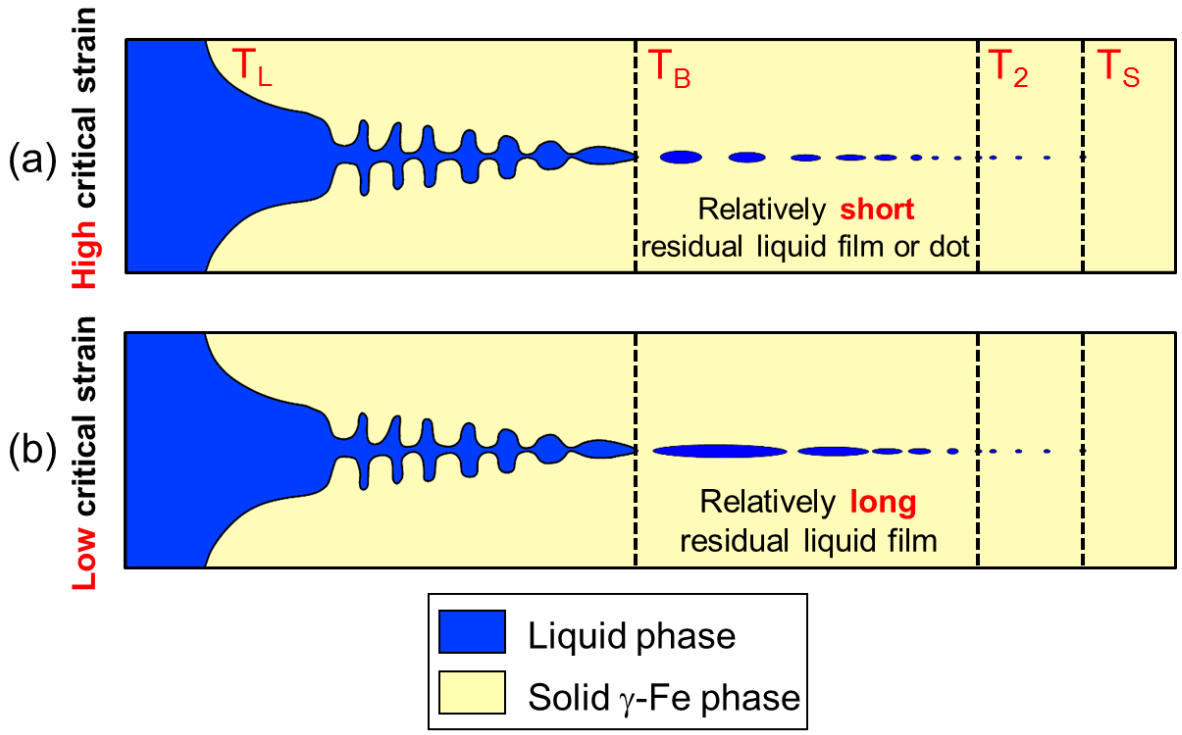

Fig. 5.24 Schematic illustration to understand the occurrence of the minimum local critical strain

5.8 Relationship between Cooling Rate and Calculation Parameters

Moreover, at present there is no studies on the effect of cooling rate on the calculation parameters to simulate real solidification phenomenon compared with that of experiment. Thus, the authors investigate the relationship between cooling rate, interfacial mobility and anisotropy of interfacial mobility by combining this research data and previous research data [15, 84], as shown in Fig. 5.25. The red symbols present the value of this work and the white symbols are the reference values in the case of type 304 stainless steel [15, 84].

The influence of cooling rate on the interfacial mobility is indicated in Fig. 5.25 a). The interfacial mobility increases with increasing cooling rate, because in theory a high cooling rate can induce a high dendrite growth rate which is directly proportional to interfacial mobility. Therefore, the value of the interfacial mobility tends to increase with an increase in cooling rate during calculation.

Figure 5.25 b) shows the effect of cooling rate on the anisotropy of interfacial mobility. The anisotropy of interfacial mobility tends to decrease with increasing cooling rate. Actually, L_P tends to be shorter under higher cooling rates from those of the fracture surface of the crack. Thus, L_P must be shortened in order to obtain the correct residual liquid distribution. Figure 5.26 shows a schematic illustration of the calculated results under different anisotropies of interfacial mobility based on the results in Fig. 5.12. If the anisotropy of the interfacial mobility decreases to a low value as shown in Fig. 5.26 a), the extent of difference in interfacial mobility between the preferred and other growth directions decreases. Thus, the dendrite tends to grow in an isotropic manner, the secondary dendrite arm becomes more significant and the primary dendrite tip radius becomes relatively large, as show in Fig. 5.26 a). The growth of the secondary dendrite arm is beneficial to bridge and save the residual liquid metal in the L_{FD} during solidification. This results in an increase in T_B and a decrease in T_S, causing a decrease in L_P but an increase in L_{FD} and L_M, as shown in Fig. 5.13. If the anisotropy of interfacial mobility has an intermediate value as shown in Fig. 5.26 b), this difference enhances the interfacial mobility between the preferred and other growth directions. Therefore, the secondary dendrite arm and primary dendrite tip radius become smaller, as shown in Fig. 5.26 b). If the anisotropy of interfacial mobility is high as shown in Fig. 5.26 c), the columnar with the similar morphology occurs during growth, resulting in the unchanged residual liquid region distribution, as shown in Fig. 5.13. Therefore, in order to obtain matching residual liquid distribution, the value of the anisotropy of interfacial mobility seems to decrease with an increase in cooling rate.

Finally, based on the above results, these graphs can give a suggestion to fit the reasonable calculation parameters to predict the real solidification phenomenon during calculation under various cooling rates.

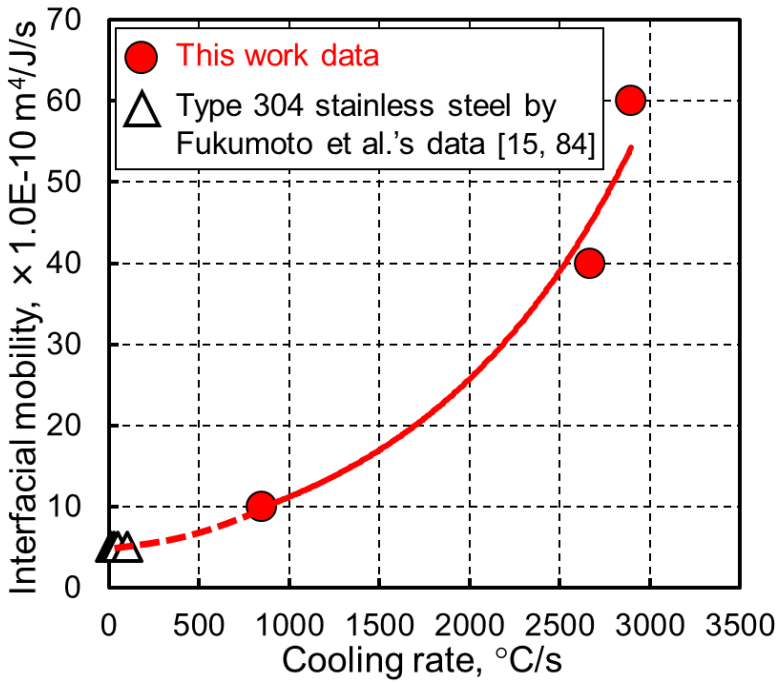

(a) Effect of cooling rate on interfacial mobility

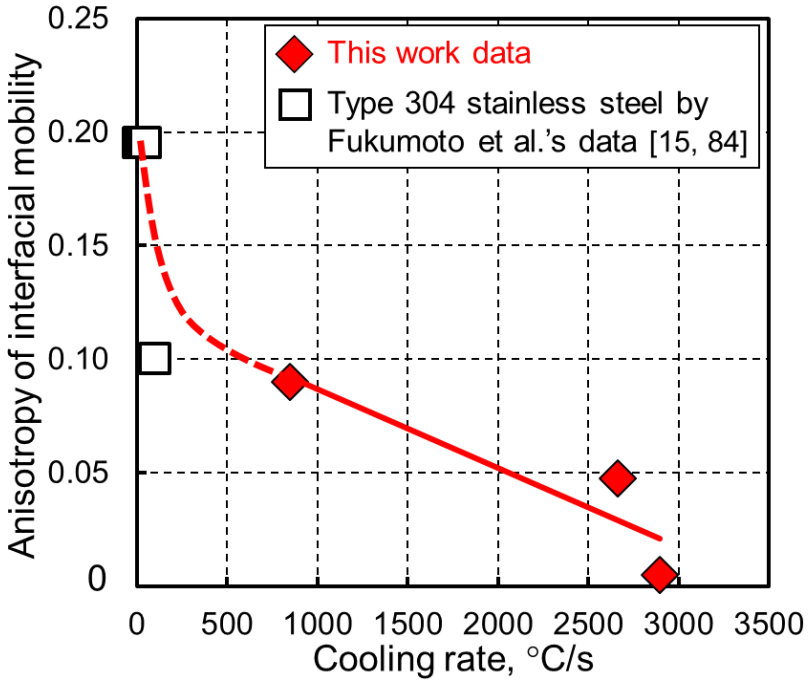

(b) Effect of cooling rate on anisotropy of interfacial mobility

Fig. 5.25 Effect of cooling rate on calculation parameters

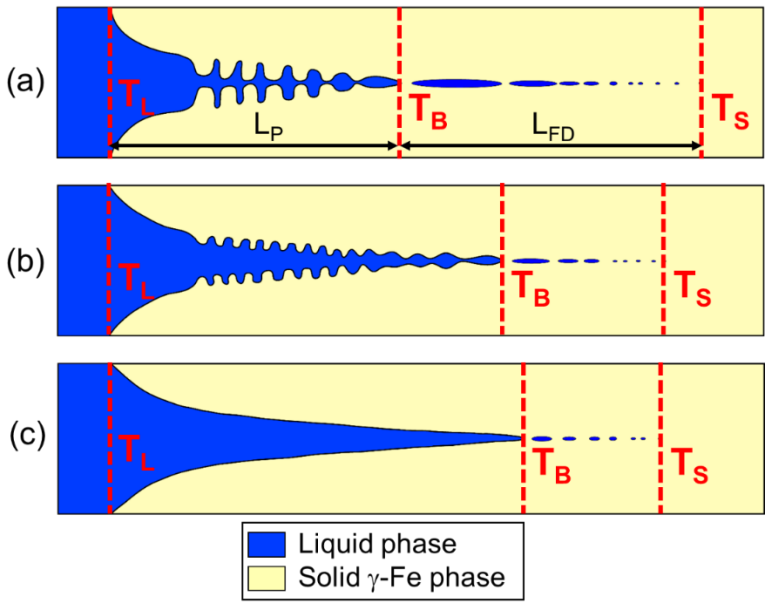

Fig. 5.26 Schematic illustration of calculated results under different anisotropies of interfacial mobility, (a) low value, (b) middle value and (c) high value

5.9 Summary

In this chapter, the morphology and distribution of the residual liquid under different cooling rates were calculated using the MPFM to predict the real solidification phenomenon and understand solidification cracking mechanism during LBW at different welding speeds. The conclusions are as follows:

1. The calculated secondary dendrite arm spacing and primary dendrite tip radius by adjusting the calculation parameters, such as the interfacial mobility and the anisotropy of interfacial mobility, had agreement with those of liquid Sn quenched microstructure and KGT modeling, respectively. The result showed that it was feasible and trustworthy to use this MPFM to further predict the morphology and distribution of the residual liquid.
2. The effect of the parameters, such as the interfacial mobility, the anisotropies of interfacial mobility, the interfacial energy and the anisotropy of interfacial stiffness, on the length of the residual liquid region was investigated quantitatively. With increasing the interfacial mobility, the lengths of L_P (T_L to T_B), L_{FD} (T_B to T_S) and L_M (T_L to T_S) increased, because the dendrite growth rate was directly proportional to

the interfacial mobility. In addition, with increasing the anisotropy of interfacial mobility, the length of L_P (T_L to T_B) increased but that of L_{FD} (T_B to T_S) and L_M (T_L to T_S) tended to decrease, because the dendrite morphology strongly depended on the anisotropy of interfacial mobility under high cooling rate, which could influence the variation of the residual liquid region. Then, according to the kinetic theory of interface stability, with increasing the interfacial energy, the length of L_P (T_L to T_B) increased but those of L_{FD} (T_B to T_S) and L_M (T_L to T_S) tended to decrease because the interface stability depended on the interfacial energy. Moreover, with increasing the anisotropy of interfacial stiffness, the length of each residual liquid region approximately kept constant.

3. In order to verify calculation result, the fracture surface of the solidification crack was observed. The length of the residual liquid region in the calculation result was nearly the same as that of the fracture surface by adjusting calculation parameters, like the interfacial mobility and the anisotropy of interfacial mobility. Therefore, the residual liquid distribution could be predicted precisely by verifying with experiment and optimizing calculation parameters.
4. According to the predicted result, the distribution of the similar residual liquid dot at the terminal of solidification under different cooling rates contributed to nearly the same BTR during LBW at different welding speeds. However, the appearance of the relatively long residual liquid film in the region from T_B to T_2 under higher cooling rates lead to a decrease in the minimum local critical strain during LBW at higher welding speeds. Therefore, these comprehensive factors caused an increase in the solidification cracking susceptibility of type 310S stainless steel during LBW at different welding speeds from 0.2 to 2.0 m/min.
5. With increasing cooling rate, the interfacial mobility increased because a high cooling rate could induce a high dendrite growth rate that was directly corresponding to the interfacial mobility, while the anisotropy of interfacial mobility tended to decrease because different cooling rates could cause the change of the dendrite morphology that strongly depended on the anisotropy of interfacial mobility. Finally, based on this study it is possible to apply the recommended calculation parameters to predict real solidification phenomenon under various cooling rates.

Chapter 6

Summary and Future Work

The final purpose of the present research was to develop a systematic method to evaluate solidification cracking susceptibility quantitatively and predict residual liquid distribution in order to understand the mechanism of the susceptibility during LBW. By combining the Trans-Varestraint test during LBW with the measurement method of 2D temperature distribution, the BTR could be measured precisely. In addition, with the aid of the MPFM, the morphology and distribution of the residual liquid were predicted. Therefore, based on the above and previous results, solidification cracking susceptibility was evaluated comprehensively and the mechanism was understood.

To beginning with, the background of this study, the objective and construction of the thesis were discussed. The relative researches on solidification cracking susceptibility and the simulation of solidification microstructure were reviewed and summarized.

The Trans-Varestraint test during LBW was developed in order to evaluate solidification cracking susceptibility quantitatively. For comparison, the traditional Trans-Varestraint test during GTAW was also employed at the same welding speed of 0.2 m/min. The similar values in the number density of solidification crack and total crack length per bead width revealed that there was a little influence on solidification cracking susceptibility by using different heat sources between LBW and GTAW. Then, in order to obtain the BTR during LBW, an optical fiber radiation thermometer was employed to measure the temperature profile at welding speed of 0.2 m/min. However, there were some problems when using a thermometer especially at high welding speed. Thus, the measurement method of 2D temperature distribution by using a multi-sensor camera was employed to measure the temperature range of each crack. Finally, the BTR could be obtained by using 2D temperature distribution, which was the maximum temperature range of the crack. Moreover, the ductility curve tendency was tried to be completed by drawing the curve covering all of the temperature range of the crack.

Then, the effect of welding speed on solidification cracking susceptibility was evaluated for type 310S stainless steel during LBW. The solidification crack distribution was investigated and understood by using liquid Sn quenched microstructure at different welding speeds. In addition, there was a detail discussion on the problem of the temperature measurement by inserting an optical fiber radiation thermometer into the molten pool at high welding speeds. In order to obtain the precise BTR, the applicability and accuracy of the measurement method of 2D temperature distribution was investigated quantitatively. Finally, the precise BTR could be obtained and was nearly the same at around 102 °C during LBW at welding speeds from 0.2 to 2.0 m/min. However, the local critical strain tended to decrease with increasing welding speed according to the previous research. By combining both the effect of the BTR and local critical strain, the results showed that the solidification cracking susceptibility of type 310S stainless steel increased during LBW with increasing welding speed from 0.2 to 2.0 m/min.

Next, the MPFM was employed to predict the residual liquid distribution for understanding solidification cracking mechanism during LBW at different welding speeds. By comparison, the calculated secondary dendrite arm spacing and primary dendrite tip radius were in agreement with that of liquid Sn quenched microstructure and KGT model, respectively. The influence of interfacial mobility, interfacial energy, anisotropies of interfacial mobility and interfacial stiffness on the length of the residual liquid region was investigated quantitatively. Meanwhile, the solidification cracks were opened and observed to verify the calculation result based on the length of each residual liquid region. And the calculated result was nearly the same as that of experiment for each cooling rate corresponding to the welding speed. Therefore, the residual liquid distribution could be predicted precisely by verifying with experiment and optimizing calculation parameters, like interfacial mobility and its anisotropy. Based on the predicated solidification phenomenon, the distribution of the similar residual liquid dot at the terminal of solidification under different cooling rates contributed to nearly the same BTR during LBW at different welding speeds. However, the relatively long residual liquid film in the region from T_B to T_2 under higher cooling rates caused a decrease in the minimum local critical strain during LBW at higher welding speeds. Therefore, these comprehensive factors contributed to an enhancement in the solidification cracking susceptibility of type 310S

stainless steel during LBW at different welding speeds from 0.2 to 2.0 m/min. Moreover, based on this study, with increasing cooling rate, the interfacial mobility and the anisotropy of interfacial mobility tended to increase and decrease, respectively. Finally, it is possible to apply the recommend calculation parameters to predict real solidification phenomenon under various cooling rates by referring this relationship between cooling rate and calculation parameters.

In the future, the measurement method of 2D temperature distribution need to be improved further. At present, 2D temperature distribution is obtained just during LBW, but not during Trans-Varestraint test. Transient temperature distribution during the occurrence of solidification crack need to be measured in order to obtain the BTR through the most direct method. However, the relative studies need to be investigated quantitatively, such as the effect of bending on 2D temperature distribution and the achievement of high resolution image and so on. Moreover, the present augmented strain is measured at the room temperature. Thus, by developing in-situ observation further, a new evaluation method need to be improved in order to measure the local critical strain at high temperature range during LBW. After that, a high temperature ductility curve with high precision could be obtained.

Until now, the MPFM is employed for the prediction of the residual liquid distribution of type 310S stainless steel under high cooling rate, like LBW, to understand solidification phenomenon and solidification cracking mechanism. However, for the dissimilar materials welding, the solidification cracking mechanism is still unclear, which also strongly depends on the residual liquid distribution at the terminal of solidification. Therefore, in order to understand solidification phenomenon and solidification cracking mechanism of dissimilar materials welding, it is necessary to predict the residual liquid distribution under different chemical compositions based on the modeling and parameters of this calculation result.

Acknowledgements

I would like to express my sincere gratitude to Professor Kenji Shinozaki for his great guidance and insight throughout this study. He gave me full support not only on my research, but also on my life and career, which has played an important role in both of my professional and personal development. I would also like to thank to Assistant Professor Kota Kadoi. He gave me so much positive help on the research and accumulation of the knowledge, and I have learnt so much from him. In addition, I would also like to thank to Associate Professor Motomichi Yamamoto. He gave me so much positive help on the key issues of research and my life, and I have learnt so much from him. Moreover, I would like to express my heartfelt thanks to Professor Kazuhiro Matsugi, Professor Atsushi Sugeta and Professor Gen Sasaki for their suggestions.

I would like to thank the past members of my research group: Mr. Shuntaro Sakoda and Mr. Maki Iwata. In addition, I would also like to thank to Mr. Shotaro Yamashita for considerable assistance and help in my experiments and life. I would like to thank to Dr. Rittichai Phaoniam, Dr. Warinsiriruk Eakkachai, Mr. Shuai Gao, Mr. Guan Wang and Mr. Yifu Liu for giving suggestions and help in my research and life. Moreover, I would also like to thank all the past and present members of Materials Joining Science and Engineering Laboratory, in Department of Mechanical System Engineering, Hiroshima University, for their enthusiastic help to both of my life and study.

I would like to thank my parents for their support and encouragement during my study. And I would like to express my special but heartfelt gratitude to my wife, she always gives me positive support and encourage to overcome difficulties within these years.

Finally, I would like to thank to China Scholarship Council for three and half years scholarship to support my research and life in Japan.

References

[1] T. Koseki, H. Inoue, H. Morimoto and S. Ohkita. Prediction of solidification and phase transformation of stainless steel weld metals, Nippon Steel Technical Report, 1995, 65, 33-40.

[2] S.V. Kuryntsev and A.Kh. Gilmutdinov. Welding of stainless steel using defocused laser beam, Journal of Constructional Steel Research, 2015, 114, 305-313.

[3] M. Yonemura, T. Osuki, H. Terasaki, Y. Komizo, M. Sato and A. Kitano. In-situ observation for weld solidification in stainless steels using time-resolved X-ray diffraction, Materials Transactions, 2006, 47(2), 310-316.

[4] K. Shinozaki, M. Yamamoto, A. Kawasaki, T. Tamura, P. Wen. Development of evaluation method for solidification cracking susceptibility of Inconel600/SUS347 dissimilar laser weld metal by in-situ observation, Materials Science Forum, 2008, 580-582, 49-52.

[5] S. Kou. Welding Metallurgy, 2003, John Wiley & Sons.

[6] T. Senda, F. Matsuda, G. Takano, K. Watanae, T. Kobayashi and T. Matsuzaka. Studies on solidification crack susceptibility for weld metals with Trans-Varestraint test (1)- Investigation for commercially used constructional metals and alloys, Quarterly Journal of the JWS, 1972, 41(6), 709-723.

[7] T. Senda, F. Matsuda and G. Takano. Studies on solidification crack susceptibility for metals with Trans-Varestraint test (2)- Investigation for commercially used aluminum and aluminum alloys, Quarterly Journal of the JWS, 1973, 42(1), 48-56.

[8] J.C. Lippold and D.J. Kotecki. Welding Metallurgy and Weldability of Stainless Steels, 2005, John Wiley & Sons.

[9] M. Militzer. Phase field modeling of microstructure evolution in steels, Current Opinion in Solid State and Materials Science, 2011, 15, 106-115.

[10] W.J. Boettinger, J.A. Warren, C. Beckermann and A. Karma. Phase-field simulation of solidification, Ann. Rev. Mater. Res., 2002, 32, 163-194.

[11] G.J. Schmitz, B. Bottger, J. Eiken, M. Apel, A. Viardin, A. Carre and G. Laschet. Phase-field based simulation of microstructure evolution in technical alloy grades, Int. J. Adv. Eng. Sci. Appl. Math., 2010, 2(4), 126-139.

[12] D. J. Seol, K. H. Oh, J. W. Cho, J. Lee and U. Yoon. Phase-field modelling of the thermos-mechanical properties of carbon steels, Acta Materialia, 2002, 50, 2259-2268.

[13] Y. Xie, H. Dong and J. Dantzig. Growth of secondary dendrite arms of Fe-C alloy during transient directional solidification by phase-field method, ISIJ International, 2014, 54(2), 430-436.

[14] W.J. Zheng, Z.B. Dong, Y.H. Wei, K.J. Song, J.L. Guo and Y. Wang. Phase field investigation of dendrite growth in the welding pool of aluminum alloy 2A14 under transient conditions, Computational Materials Science, 2014, 82, 525-530.

[15] S. Fukumoto and I. Hiroshige. Evaluation of microstructure formation in SUS304 by multi-phase-field method, Quarterly Journal of the JWS, 2011, 29(3), 197-203.

[16] K. Kadoi, A. Fujinaga, M. Yamamoto and K. Shinozaki. The effect of welding conditions on solidification cracking susceptibility of type 310S stainless steel during laser welding using an in-situ observation technique, Weld World, 2013, 57, 383-390.

[17] J. Adamiec. The influence of construction factors on the weldability of AZ91Z alloy, Archives of Metallurgy and Materials, 2011, 56, 769-778.

[18] J. Adamiec and A. Kierzek. Hot cracking of ZRE1 alloy in constant joint stiffness condition, Archives of Foundry Engineering, 2010, 10, 151-156.

[19] D.D. Nage and V.S. Raja. Examination of crater crack formation in Nitrogen-containing austenitic stainless steel welds, Welding Research, 2007, 104-112.

[20] J. Adamiec. Influence of design factors on weldability of the AZ91Z alloy, Archives of Foundry Engineering, 2010, 10, 339-344.

[21] M. Katoh, K. Nishio and S. Mukae. A comparison of the conventional and reverse houldcroft type hot cracking tests in A5052 aluminum alloy sheet, Quarterly Journal of the JWS, 1994, 12(2), 179-185.

[22] L. Kolarik, K. Kovanda, M. Valova, P. Vondrous and J. Dunovsky. Weldability test of precipitation hardenable aluminum alloy EN AW 6082 T6, MM Science Journal, 2011, 242-246.

[23] L. Kolarik, K. Kovanda, M. Valova, P. Vondrous and J. Dunovsky. Houldcroft weldability test of aluminium alloy EN AW 6082 T6, Scientia Agriculturae Bohemica, 2012, 43(1), 14-21.

[24] S.A. Rizvi, S.P. Tewari and W. Ali. Weldability of steels and its alloys under different conditions – A review, International Journal of Science, Engineering and Technology Research, 2013, 2(3), 539-550.

[25] S.A. David and J.J. Woodhouse. Weldability test for thin sheet materials, Welding Research, 1987, 129-134.

[26] T.W. Nelson, J.C. Lippold, W. Lin and W.A. Baeslack. Evaluation of the circular patch test for assessing weld solidification cracking, Part 1- Development of a test method, Welding Research Supplement, 1997, 110-119.

[27] M.G. Mousavi, C.E. Cross and O. Grong. Effect of scandium and titanium-boron on grain refinement and hot cracking of aluminum alloy 7108, Science and Technology of Welding and Joining, 1999, 4(6), 381-388.

[28] Y. Arata, F. Matsuda, K. Nakata and I. Sasaki. Solidification crack susceptibility of aluminum alloy weld metals (Report 1)- Characteristics of ductility curves during solidification by means of the Trans-Varestraint test, Transactions of JWRI, 1976, 5(2), 53-67.

[29] Y. Arata, F. Matsuda and S. Katayama. Solidification crack susceptibility in weld metals of fully austenitic stainless steels (Report 2)- Effect of ferrite, P, S, C, Si and Mn on ductility properties of solidification brittleness, Transactions of JWRI, 1977, 6(1), 105-116.

[30] F. Matsuda, H. Nakagawa, S. Katayama and Y. Arata. Solidification crack susceptibility in weld metals of fully austenitic stainless steels (Report 6)- Effect of La or REM addition on solidification crack resistance, Transactions of JWRI, 1982, 11(1), 79-94.

[31] F. Matsuda, H. Nakagawa, S. Ogata and S. Katayama. Fractographic investigation on solidification crack in the Varestraint test of fully austenitic stainless steel- Studies on fractography of welded zone (3), Transactions of JWRI, 1978, 7(1), 59-70.

[32] F. Matsuda, H. Nakagawa, S. Katayama and Y. Arata. Solidification crack susceptibility in weld metals of fully austenitic stainless steels (Report 8)- Effect of Nitrogen on cracking in SUS 304 weld metal, Transactions of JWRI, 1983, 12(1), 89-95.

[33] I. Varol, W.A. Baeslack and J.C. Lippold. Characterization of weld solidification cracking in a duplex stainless steel, Metallography, 1989, 23, 1-19.

[34] S. Katayama, T. Fujimoto and A. Matsunawa. Correlation among solidification process, microstructure, microsegregation and solidification cracking susceptibility in stainless steel weld metals, Transactions of JWRI, 1985, 14(1), 123-138.

[35] C.P. Chou and C.H. Lee. The evaluation of hot crack susceptibility of Fe-30Mn-10Al-XC weld metal by using Varestraint test, Scripta Metallurgic A, 1989, 23, 1109-1114.

[36] A.C. Lingenfelter. Varestrint testing of Nickel alloy, Welding Research Supplement, 1972, 430-436.

[37] F.M.L. Arantes and R.E. Trevisan. Experimental and theoretical evaluation of solidification cracking in weld metal, Journal of Achievements in Materials and Manufacturing Engineering, 2007, 20(1-2), 407-410.

[38] T. Senda, F. Matsuda, G. Takano, K. Watanabe, T. Kobayashi and T. Matsuzaka. Fundamental investigations on solidification crack susceptibility for weld metals with Trans-Varestaint test, Transaction of the J.W.S., 1971, 2(2), 45-66.

[39] H. Kihara and F. Matsuda. Varestraint test for hot crack susceptibility of HY-type high strength steels, Transactions of JWRI, 1973, 2(2), 83-95.

[40] Y. Arata, F. Matsuda and S. Saruwatari. Varestraint test for solidification crack susceptibility in weld metal of austenitic stainless steels, Transactions of JWRI, 1974, 3(1), 79-88.

[41] G.M. Goodwin. Development of a new hot-cracking test- the sigmajig, Welding Research Supplement, 1987, 33-38.

[42] J.C. Lippold, S.S. Shademan and W.A. Baeslack. The effect of specimen strength and thickness on cracking susceptibility during the sigmajig weldability test, Welding Research Supplement, 1996, 81-92.

[43] F. Matsuda, H. Nakagawa, K. Nakata, H. Kohmoto and Y. Honda. Quantitative evaluation of solidification brittleness of weld metal during solidification by means of in-situ observation and measurement (Report 1)- Development of the MISO technique, Transactions of JWRI, 1983, 12(1), 65-72.

[44] F. Matsuda, H. Nakagawa, H. Kohmoto, Y. Honda and Y. Matsubara. Quantitative evaluation of solidification brittleness of weld metal during solidification by in-situ observation and measurement (Report 2)- Solidification ductility curves for steels with the MISO technique, Transactions of JWRI, 1983, 12(1), 73-80.

[45] P. Wen, K. Shinozaki, M. Yamamoto, Y. Senda, T. Tamura and N. Nemoto. In-situ observation of solidification cracking of laser dissimilar welded joints, Quarterly Journal of JWS, 2009, 27(2), 134-138.

[46] K. Shinozaki, P. Wen, M. Yamamoto, K. Kadoi, Y. Kohno and T. Komori. Effect of grain size on solidification cracking susceptibility of type 347 stainless steel during laser welding, Transactions of JWRI, 2010, 39(2), 136-138.

[47] W.F. Savage and C.D. Lundin. The Varestraint test, Welding Journal, 1965, 44(10), 433-442.

[48] J.N. DuPont, J.C. Lippold and S.D. Kiser. Welding Metallurgy and Weldability of Nickel-base Alloys, 2009, John Wiley & Sons.

[49] E.J. Chun, H. Baba, K. Nishimoto and K. Saida. Development of laser beam welding Transverse-Varestraint test for assessment of solidification cracking susceptibility in laser welds, Met. Mater. Int., 2015, 21(3), 543-553.

[50] D. Wang, S. Sakoda, K. Kadoi, K. Shinozaki and M. Yamamoto. Investigation of evaluation method for hot cracking susceptibility of 310S stainless steel during laser welding using Trans-Varestraint test, Quarterly Journal of the JWS, 2015, 33(2), 39-43.

[51] P. Wen. Evaluation of Solidification Cracking Susceptibility by In-situ Observation and Prediction of its Occurrence during Laser Welding, 2009, Ph. D. Dissertation of Hiroshima University, Japan.

[52] B. Liu and Q. Xu. Advances on microstructure modeling of solidification process of shape casting, Tsinghua Science and Technology, 2004, 9(5), 497-505.

[53] J. Gao and R.G. Thompson. Monte Carlo simulation of solidification, The Minerals, Metals & Materials Society, 1997, 77-86.

[54] P. Zhu and R.W. Smith. Dynamic simulation of crystal growth by Monte Carlo method-1 model description and kinetics, Acta Metal. Mater., 1992, 40(4), 683-692.

[55] X. Liu, Q. Xu, T. Jing and B. Liu. Simulation of microstructures in solidification of aluminum twin-roll casting based on CA, Transactions of Nonferrous Metals Society of China, 2009, 19, 422-427.

[56] H.W. Hesselbarth and I.R. Gobel. Simulation of recrystallization by Cellular Automata, Acta Metall. Mater., 1991, 39(9), 2135-2143.

[57] P.R. Rios, J.C.P.T. de Oliveira, V.T. de Oliveira and J.A. de Castro. Comparison of analytical models with Cellular Automata simulation of recrystallization in two dimensions, Materials Research, 2005, 8(3), 341-345.

[58] T. Biben. Phase-field modes for free-boundary problems, European Journal of Physics, 2005, 26, 47-55.

[59] R.S. Qin and E.R. Wallach. A phase-field model coupled with a thermodynamic database, Acta Materialia, 2003, 51, 6199-6210.

[60] G. Caginalp. Stefan and Hele-Shaw type models as asymptotic limits of the phase-field equations, Physical Review A, 1989, 39(11), 5887-5896.

[61] A.A. Wheeler, W.J. Boettinger and G.B. McFadden. Phase-field model for isothermal phase transitions in binary alloys, Physical Review A, 1992, 45(10), 7424-7439.

[62] S.G. Kim, W.T. Kim and T. Suzuki. Interfacial compositions of solid and liquid in a phase-field model with finite interface thickness for isothermal solidification in binary alloys, Physical Review E, 1998, 58(3), 3316-3323.

[63] S.G. Kim, W.T. Kim and T. Suzuki. Phase-field model for binary alloys, Physical Review E, 1999, 60(6), 7186-7197.

[64] T. Suzuki, M. Ode, S.G. Kim and W.T. Kim. Phase-field model of dendritic growth, Journal of Crystal Growth, 2002, 237-239, 125-131.

[65] I. Steinbach, F. Pezzolla, B. Nestler, M. Seebelberg, R. Prieler, G.J. Schmitz and J.L.L. Rezende. A phase field concept for multiphase systems, Physica D, 1996, 94, 135-147.

[66] H. Garcke, B. Nestler and B. Stinner. A diffuse interface model for alloys with multiple components and phases, SIAM J. Appl. Math., 2004, 64(3), 775-799.

[67] D.U. Furrer. Application of phase-field modeling to industrial materials and manufacturing process, Current Opinion in Solid State and Materials Science, 2011, 15, 134-140.

[68] T. Takaki. Phase-field modeling and simulations of dendrite growth, ISIJ International, 2014, 54(2), 437-444.

[69] B. Bottger, M. Apel, B. Santillana and D.G. Eskin. Relationship between solidification microstructure and hot cracking susceptibility for continuous casting of low-carbon and high-strength low-alloyed steels- A phase-field study, Metallurgical and Materials Transactions A, 2013.

[70] D. Zhao, T. Jing and B. Liu. The effects of phase-field parameters on grain growth morphologies in the solidification, Materials Transactions, 2003, 44(3), 367-371.

[71] C. Zhu, B. Liu, T. Jing and W. Feng. Dependence of dendritic side-branches on parameters in phase-field simulations, Materials Transactions, 2005, 46(1), 15-19.

[72] S. Yamashita, M. Yamamoto, K. Shinozaki, K. Kadoi, K. Mitsui and H. Usui. In-situ temperature measurement using a multi-sensor camera during laser welding, Quarterly Journal of the Japan Welding Society, 2015, 33(2), 93-97.

[73] S. Yamashita, A. Fujinaga, M. Yamamoto, K. Shinozaki, K. Kadoi, K. Mitsui and H. Usui. In-situ temperature measurement using monochrome high-speed sensors during laser welding, Quarterly Journal of the Japan Welding Society, 2013, 31(4), 78-81.

[74] M. Rappaz, S.A. David, J.M. Vitek and L.A. Boatner. Development of microstructures in Fe-15Ni-15Cr single crystal electron beam welds, Metallurgical transactions A, 1989, 20A, 1125-1138.

[75] W. Kurz, B. Giovanola and R. Trivedi. Theory of microstructural development during rapid solidification, Acta Metall., 1986, 34(5), 823-830.

[76] W. Kurz and D.J. Fisher. Fundamentals of solidification. Aedermannsdorf, Trans. Tech. Publication, 1989, 293.

[77] N. Provatas and K. Elder. Phase-field methods in materials science and engineering, 2010, Wiley-VCH.

[78] J. Eiken, B. Bottger and I. Steinbach. Multi-phase field approach for multicomponent alloys with extrapolation scheme for numerical application, Physica. Rev. E, 2006, 73(6), 066122-1 – 066122-9.

[79] R.Z. Xiao, G.S. An, C.S. Zhu, Z.P. Wang and S.Y. Yang. Comparative analysis of isothermal and non-isothermal solidification of binary alloys using phase-field model. Transactions of Nonferrous Metals Society of China, 2014, 24, 3639-3644.

[80] MICRESS group. User Guide Version 6.1, Volume 2, Running MICRESS, 66-81.

[81] D. Wang, S. Sakoda, S. Yamashita, K. Kadoi, K. Shinozaki and M. Yamamoto. Measurement of BTR during laser Trans-Varestraint test using 2D temperature measurement- Investigation of hot cracking susceptibility during laser welding (Part 2). Preprints of the National Meeting of JWS, 2015, 96, 20-21.

[82] E.A. Brener. Influence of kinetic effects on the growth of a two-dimensional dendrite, Sov. Phys. JETP, 1989, 69(1), 133-137.

[83] W.W. Mullins and R.F. Sekerka. Stability of a planar interface during solidification of a dilute binary alloy, Journal of Applied Physics, 1964, 35(2), 444-451.

[84] S. Fukumoto and S. Nomoto. Microstructure simulation for solidification of stainless steel by multi-phase-field model, J. Japan Inst. Metals, 2009, 73(7), 502-508.

Published or Accepted Papers in Regards to This Thesis

1. **D. Wang**, S. Sakoda, K. Kadoi, K. Shinozaki and M. Yamamoto. Investigation of evaluation method for hot cracking susceptibility of 310S stainless steel during laser welding using Trans-Varestraint test, Quarterly Journal of the Japan Welding Society, 2015, 33, (2), 39-43. (Chapter 3 & 4)
2. K. Kadoi, **D. Wang** and K. Shinozaki. Solidification cracking susceptibility during laser welding and the high-accuracy evaluation, Journal of the Japan Welding Society, 2016, 85, (6), 13-18. (Chapter 3 & 4)
3. **D. Wang**, K. Kadoi, K. Shinozaki and M. Yamamoto. Evaluation of solidification cracking susceptibility for austenitic stainless steel during laser Trans-Varestraint test using 2D temperature measurement. (Accepted by ISIJ International) (Chapter 3 & 4)
4. **D. Wang**, K. Kadoi and K. Shinozaki. Prediction of residual liquid distribution of austenitic stainless steel during laser beam welding using multi-phase field modeling. (Accepted by ISIJ International) (Chapter 5)
5. **D. Wang**, S. Sakoda, K. Kadoi, K. Shinozaki and M. Yamamoto. Investigation of evaluation method for hot cracking susceptibility of 310S stainless steel during laser welding using Trans-Varestraint test, The international symposium on visualization in joining & welding science through advanced measurements and simulation (Visual JW 2014), 2014, V(1), 163-164. (Chapter 3 & 4)

Presentations

1. **D. Wang**, K. Kadoi and K. Shinozaki. Prediction of solidification microstructure of austenitic stainless steel during laser welding using multi-phase field modeling- Investigation of hot cracking susceptibility during laser welding (Part 3), National Conference of Japan Welding Society, Spring, 2016, Osaka, Japan.
2. **D. Wang**, S. Sakoda, S. Yamashita, K. Kadoi, M. Yamamoto and K. Shinozaki. Evaluation of solidification cracking susceptibility for type 310S stainless steel using laser Trans-Varestraint test and 2D temperature measurement, The 7th International Congress on Laser Advanced Materials Processing, 2015, Kitakyusyu, Japan.
3. **D. Wang**, S. Sakoda, S. Yamashita, K. Kadoi, K. Shinozaki and M. Yamamoto. Measurement of BTR during laser Trans-Varestraint test using 2D temperature measurement- Investigation of hot cracking susceptibility during laser welding (Part 2), National Conference of Japan Welding Society, Spring, 2015, Tokyo, Japan.
4. K. Kadoi, S. Sakoda, **D. Wang**, K. Shinozaki and M. Yamamoto. Solidification cracking susceptibility for dissimilar weld metal of austenitic metals, National Conference of Japan Welding Society, Autumn, 2015, Hokkaido, Japan.
5. **D. Wang**, S. Sakoda, K. Kadoi, K. Shinozaki and M. Yamamoto. Investigation of evaluation method for hot cracking susceptibility of 310S stainless steel during laser welding using Trans-Varestraint test, The International Symposium on Visualization in Joining & Welding Science through Advanced Measurements and Simulation (Visual JW 2014), 2014, Osaka, Japan.
6. S. Sakoda, **D. Wang**, K. Kadoi, M. Yamamoto and K. Shinozaki. Investigation of evaluation method for Trans-Varestraint test with laser welding- Investigation of hot cracking susceptibility during laser welding (Part 1), National Conference of Japan Welding Society, Autumn, 2014, Kurobe, Japan.